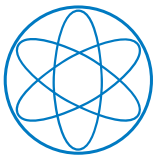

Technische Universität München

Physik Department

Theoretische Physik T37

Friction of Soft Matter at the Nano-Scale

Aykut Erbaş

Dissertation

Technische Universität München
Physik Department
Theoretische Physik T37

Friction of Soft Matter at the Nano-Scale

Aykut Erbaş

Vollständiger Abdruck der von der Fakultät für Physik der Technischen Universität München zur Erlangung des akademischen Grades eines

Doktors der Naturwissenschaften (Dr. rer. nat.)

genehmigten Dissertation.

Vorsitzender:		Univ.-Prof. Dr. Matthias Rief
Prüfer der Dissertation:	1.	Univ.-Prof. Dr. Roland Netz, Freie Universität Berlin
	2.	Univ.-Prof. Dr. Ralf Metzler, Universität Postdam

Die Dissertation wurde am 22.11.2011 bei der Technischen Universität München eingereicht und durch die Fakultät für Physik am 16.12.2011 angenommen.

Contents

List of Figures

Abstract

Amontons' classical friction law states that the resistive force against the motion of a sliding macroscopic object on a surface is proportional to the applied external normal force. Recent advances in nanotribology and single-molecule experiments have revealed that at nanoscopic scales, conventional laws do not apply due to the adhesive forces and thermal fluctuations, and these laws should be reviewed. This work focuses on the friction dynamics of nano-soft matter, which plays an important role in the biological machinery and is accessible by single-molecule experiments. In the first part of this work, the friction of laterally pulled single peptides over planar H-terminated non-polar and hydroxylated polar substrates are put under investigation in the presence of water using extended Molecular Dynamics (MD) simulations and the stochastic Fokker-Planck equation. Since the stiffness of the surface-peptide matrix affects the hydrogen bonding, we also discuss the friction experienced by a peptide in a peptide bundle as a function of a confinement parameter, which is the number of neighbouring chains in the bundle. We show that the friction of hydrogen-bonded matter obeys a simple equation in the biologically relevant low-velocity viscous regime: The friction force is proportional to the number of hydrogen bonds, the sliding velocity, and a friction coefficient per hydrogen bond γ_{HB}. The value of γ_{HB} is extrapolated from simulations by mapping on the stochastic model. The γ_{HB} turns out to span a range from $\gamma_{\mathrm{HB}} \simeq 10^{-11}$ kg/s, for parallel or perpendicular pairs of polyglycines, to $\gamma_{\mathrm{HB}} \simeq 10^{-6}$ kg/s, for a denser bundle of 7 polyglycines. At the polar surfaces, $\gamma_{\mathrm{HB}} \simeq 10^{-8}$ kg/s, which coincides with that in a bundle of 5 peptides. Our findings can explain the confinement dependent slowing observed in single-molecule experiments. To interpret these experiments precisely, hydrodynamic friction, which is particularly important in experiments utilizing nano-scale beads or nanowires, should be considered. Hence, in a related project, the transient compressible Navier-Stokes equation is solved analytically to obtain the frequency-dependent friction response functions for spherical, cylindrical and planar geometries in an unbounded fluid, with finite slip length. For high driving frequencies, the flow pattern is dominated by the diffusion of vorticity and compression. On the other hand, for low frequencies, the compression propagates in the form of sound waves which are exponentially damped at a screening length larger than the sound wave length. In the propagative regime, the hydrodynamic-friction response of spheres and cylinders exhibits a high-frequency resonance when the particle size is of the order of the sound wave length. A distinct low-frequency resonance occurs at the boundary between the propagative and diffusive regimes.

Zusammenfassung

Amontons' klassisches Reibungsgesetz sagt voraus, dass die Widerstandskraft gegen die Bewegung eines auf einer Oberfläche gleitenden makroskopischen Gegenstandes proportional zur extern angelegten Normalkraft ist. Neuere Entwicklungen in der Nanotribologie und Einzelmolekülexperimente haben gezeigt, dass konventionelle Reibungsgesetze auf der Nano-Skala aufgrund von Haftung und thermischen Fluktuationen nicht gültig sind und daher überarbeitet werden müssen. Schwerpunkt dieser Arbeit ist die Reibungsdynamik nanoskopischer, weicher Materie. Sie spielt in der Biologie eine wichtige Rolle und kann in Einzelmolekülexperimenten quantifiziert werden. Im ersten Teil der Arbeit wird die Reibung einzelner Peptide auf hydrophoben und hydrophilen Oberflächen untersucht. Hierfürwerden Molekulardynamik-Simulationen und eine stochastische Beschreibung basierend auf der Fokker-Planck-Gleichung verwendet. Da die Steifigkeit der Oberflächen - Peptid-Matrix die Ausbildung von Wasserstoffbrücken beeinflusst, wird außerdem die Reibung eines Peptids innerhalb eines Peptid-Bündels behandelt. Es wird gezeigt, dass im biologisch relevanten Bereich niedriger Geschwindigkeiten die Reibungskraft proportional zur Geschwindigkeit, zur Wasserstoffbrückenanzahl und zu einem Wasser-stoffbrücken-Reibungskoeffizienten γ_{HB} ist, der vom kollektiven Charakter der Bindungsbrüche abhängt. γ_{HB} wird hierbei aus der Übertragung von Simulationsergebnissen auf das stochas-tische Modell gewonnen und nimmt Werte von 10^{-11} kg/s für einzelne Polyglycin-Paare bis zu 10^{-6} kg/s für dichte Peptid-Bündel an. Auf der hydrophilen Oberfläche entspricht γ_{HB} mit 10^{-8} kg/s dem Wert in einem Bündel aus fünf Peptiden. Diese Ergebnisse liefern eine Erklärung für die Verlangsamung von Prozessen bei räumlicher Einschränkung, die in Einzelmolekülexperimenten beobachtet wird. In solchen Experimenten, in denen häufig Kugeln oder Drähte auf der Nano-Skala zum Einsatz kommen, sind auch hydrodynamische Effekte von großer Bedeutung. Im zweiten Teil der Arbeit wird daher die zeitabhängige, kompressible Navier-Stokes-Gleichung in einer unbegrenzten Flüssigkeit mit endlicher Slip-Länge analytisch gelöst. Dies erlaubt die Berechnung von frequenzabhängigen Reibungs-Antwortfunktionen für verschiedene Geometrien: Kugeln, Zylinder und Ebenen. Bei hohen Frequenzen wird das Strömungsprofil durch die Diffusion von Wirbeldichte und Kompression dominiert. Bei niedrigen Frequenzen hingegen breitet sich die Kompression in Form von Schallwellen aus, die exponentiell gedämpft werden, wenn die Abschirmlänge größer als die Schallwellenlänge ist. In diesem propagativen Regime zeichnet sich die Reibungs-Antwortfunktion von Kugeln und Zylindern durch eine Hochfrequenz-Resonanz aus, wenn die Partikelgröße in in den Bereich

der Schallwellenlänge kommt. Es existiert darüber hinaus eine Resonanz bei niedrigen Frequenzen an der Grenze zwischen dem diffusiven und dem propagativen Regime.

Chapter 1

Introduction and outline

1.1. A historical overview of friction

The definition of friction can be summarized simply by three words; 'resistance to motion'. However, apart from its compact and simple definition, the microscopic origins of friction itself has not been totally agreed-upon [1]. As pointed out by Persson [2], just because it is one of the first topics in freshmen courses, that does not mean that the problem was already solved. The friction is mostly invoked to occur between sliding macroscopic solid bodies, namely as dry friction. However, the arms of friction phenomena enclose many fields of modern science from earthquake analysis [3], lubrication technology [4] to orthopaedics [5]. Although these application fields have been advanced in the last century, the concept of friction in the course of civilization can be easily traced back to Neanderthal men, who, maybe, a little bit by chance, slid two flint stones or to ancient Egyptian engineers, who used oil-based lubricants to decrease the friction of large building blocks [6]. However, the first scientific investigation of the friction is attributed to Leonardo da Vinci (1452-1519), who firstly realized that the friction is independent of the apparent contact area. He also investigated the friction using inclined surfaces and various setups, a few of them shown in Fig. 1.1, which also slightly resembles the medieval racking machines [7]. His experiments convinced him to conclude that doubling the weight of a sliding object doubles the friction regardless of contact length and breadth. He also tentatively added that each object should experience a friction equal to 1/4 of its own weight. This number was the first recognition of a friction coefficient. However, since da Vinci's setups were limited to certain materials such as smooth and polished surfaces, his coefficient was far from being universal. In the era of industrial age, friction had been put under investigation in more detail: Guillaume Amontons (1663-1706) conducted friction experiments on sliding blocks. Unlike da Vinci who looked into the friction against the initiation of the motion, Amontons focused on the kinetic friction. His idea was that the friction is due to the roughness (asperities) at the contact region of two surfaces, and arises when these roughnesses on adjoining surfaces ramp up on each other. Following, Euler (1707-1783) supported Amontons' arguments. Coulomb (1736-

1806) also brought friction experiments to a further level, and performed experiments with varying ambient conditions such as temperature or humidity. His experiments also underlined the ageing effects, which suggest a higher static friction as the contact time is increased. Coulomb also showed that the sliding friction is independent of sliding velocities as long as the velocity is not too high or too low, and combined his results with his predecessors' findings in a single equation [2].

$$\mu \equiv \text{Macroscopic friction coefficient} = \frac{\text{Friction force}}{\text{Normal force}} = \frac{F_\text{f}}{F_\text{N}}, \tag{1.1}$$

which is also commonly referred as the Amontons' law in the literature [8–12]. Intriguingly, this simple equation explains the friction for a wide range of velocities and normal forces successfully and furthermore confirms da Vinci's observation of friction being independent of positioning of the object on the surface (see Fig. 1.1). The reason of its success had to wait for a quantitative explanation until 1950s: Bowden and Tabor measured the electrical conductivity between two non-adhesive metal surfaces pressed to each other. They concluded that the connectivity, hence, the area of real contact linearly increases with the pressing force and is orders of magnitude lower than the apparent contact area in the case of dry friction [4]. Thus, Eq. (1.1) holds its validity. Their explanation was based on the plastic, i.e., non-reversible, deformations of asperities and not valid for elastic deformation or adhesive contacts [9], particularly at the single asperity level [10, 13]. However, the distinction between the real and apparent contact areas has been widely accepted [2].

After almost 500 years since Eq. (1.1) was first seeded, there is no simple answer why Amontons' equation gives reasonable friction coefficients for a diversity of systems [9]. Actually, in this work, we will neither tackle with validity of the Amontons' law nor concentrate on one of those systems for which it work flawlessly. On the contrary, we rather focus on the regimes which Eq. (1.1) fail to explain: For instance, adhesive contacts exhibit friction even if the normal forces are absent or less than adhesive forces [9, 14, 15]. Similarly, when the sliding velocity tends to vanish, thermal excitations lead to a creep motion, i.e., a friction linearly dependent on the velocity [16–18]. A more problematic situation arises when the scales of sliding objects are of comparable dimensions to the range of inter-molecular interactions [19, 20]; even if we accept either a linear or non-linear dependence of the surface area on the normal force, the definition of the area for a nano-scale contact, e.g., for a molecule, is obviously not clear.

1.2. Friction at nano-scales

The origin of the friction between two objects is due to interaction of interfacial atoms; atoms at the contact regions interact via electromagnetic forces, rotate, sometimes displace, vibrate, and, in a simple picture, these vibrations are converted to heat through phonons. Given the fact that the number of atoms at the contact is of order of the Avagadro number, $\mathcal{N}$, basically, the macroscopic friction coefficient μ in Eq. (1.1) counts for all interactions between atoms at the contact. This is equivalent to integrating out all

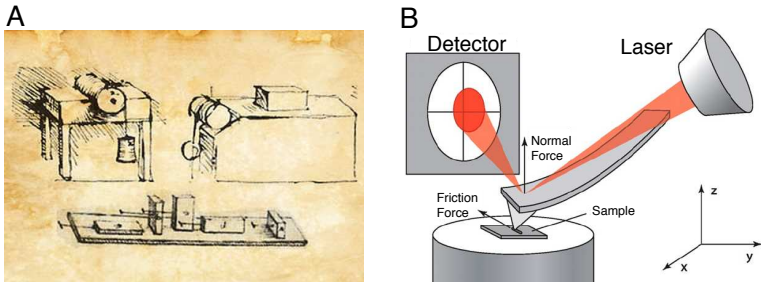

Figure 1.1.: *Evolution of tribological experiments A) Sketches of Leonardo da Vinci's setups for friction experiments from his notebooks, Codex Atlanticus and Codex Arendul [2], which are currently parts of the Biblioteca Ambrosiana and the British Library, respectively. B) AFM setup to measure the friction at nano-scale contacts; a nanometer-size tip is dragged on the surface, whose bending is measured via deflection of a laser. The friction force is recorded as the force constant times the bending of the AFM tip. Adapted from Ref [21].*

degrees of freedom (responsible for the dissipation) to describe the sliding system with only one degree of freedom: the position of the sliding object. Such an approach can also be naively viewed as a renormalization process with an analogy to spin systems [22].

Since the friction and dissipation are purely due to the inter-atomic and inter-molecular interactions [2], it is not surprising that conventional continuum models similar to Eq. (1.1), essentially based on the decimation of inter-atomic interactions, are not successful to explain friction at atomic or molecular levels [19, 23]. For instance, a single adatom or a molecule diffusing on a surface experiences basically zero-normal force but due to the adhesive effect of the surface, the friction is non-zero [24–26], which is out of the reach of Eq. (1.1). Furthermore, a monolayer of adsorbed atoms can exhibit different friction behaviors depending on whether surfaces are commensurate, i.e., thin-film atoms exactly register to minima of the effective surface potential, or incommensurate [12, 15, 27, 28]. Not only adhesion at nano-scales, but also the existence of thermal fluctuations provokes violations of the Amontons' law: When sliding velocities are much slower than the conventional velocities, at any non-zero temperature, the friction will be velocity dependent and tends to zero as the velocity vanishes [2, 16, 17]. Actually, sliding occurring at extremely low velocities even causes questioning of the static friction in macroscopic systems [29, 30].

Controversies between continuum models and friction at nano-scales have further surfaced parallel to the recent experimental and computational developments in nanotribology [20, 31]. With advanced techniques such as atomic-force microscopy (AFM), schematically depicted in Fig. 1.1, a diamond or a silicon tip can mimic one single asperity [21, 32, 33], and concurrently, computer simulations can reproduce these systems [19, 32, 34, 35]. Furthermore, the AFM setups have also been used to peel off or drag single molecules across the surfaces [36, 37]. Besides AFM, to probe the friction properties of angstrom-thick films, special tools such as the surface-force apparatus (SFA) have been developed [20, 38–41]. Readers, who have further interest in recent

tribological experiments, may consult Ref[21]. Findings of numerous friction studies, particularly those on the single asperities and on single molecules, have improved our understanding of and control the friction at nano-scales; single asperity simulations [34] and experiments [42] revealed a transition in friction behavior from linear regime in normal force (obeying Eq. (1.1)) to a non-linear regime depending on the adhesion. Similarly, contact vibrations [40], effect of the moisture [13, 43, 44] or surface chemistry of contacts [10, 11, 45–48], e.g, hydrogen bonding, have been shown to drastically change the the friction dynamics.

With the wave of new experiments and new tribological applications, new theories have also emerged to deal with the cases that cannot be expianed by Eq. 1.1; in the presence of adhesive contacts such as hydrogen bonds (HBs) and for low sliding velocities, the crossover to linear friction, where friction force becomes proportional to sliding velocity, is described by Schallamachs phenomenological model [8, 39, 49], which treats the stochastic breakage and rebinding of individual adhesive bonds. Likewise, at low velocities, thermally assisted friction was modelled by rate equations [16–18]. On the other hand, to introduce frictional history, rate-state theories, particularly for the static friction, have been proposed [50].

1.3. Friction of soft-matter: Single molecule friction

In the previous section, our discussion on friction is mostly confined to the friction of solid samples, e.g., AFM tips, or metallic surfaces. However, as imposed by the first sentence of this thesis, wherever there is a motion, friction arises, with certain exceptions being excluded. Certainly, soft-matter is not in the list of exceptions. At this point, maybe what we mean by "soft-matter" should be explained briefly; mesoscopic molecular groups whose conformations can easily be altered by thermal fluctuations. Their hardness and melting points are low compared to metals. Accordingly, liquid water or a protein molecule fulfils our definition of soft-matter. Soft-matter, except water, is the most abundant in biological systems, which contains its own bio-machinery to sustain animation. Naturally, this machinery also experiences friction as most man-made devices do. Actually, one of the aims of modern tribology is to infer how the nature adapts itself to optimize or benefit from this phenomenon: [1, 2]; proteins stay in their folded state due to dissipative barriers and unfold if these barriers are lowered by either external or internal effects. Cells bound to other cells via highly adhesive units such as Cadherins [51], or white blood cells adhered to the interior of blood vessel are driven to the peripheral tissues after multi-step control of the friction [52].

In mesoscopic bio-systems, friction manifests itself either in the diffusion coefficient or in dissipative barriers. Hence, measuring these quantities to infer the friction, particularly at the single molecule level, requires very accurate and advanced experimental techniques. In fact, recent single-molecule studies have opened this door. The diffusivity of single DNA molecules adsorbed on cationic bilayers or mica surfaces has been determined using video microscopy [26, 53], from which the friction coefficient can be inferred using Einstein's relation. The velocity-dependent friction of adsorbed polymers has been

probed in single-molecule AFM studies by pulling single molecules over substrates [36]. Other scenarios in which single molecule friction could be determined are forced slippage between complementary DNA strands [54] and the driven motion of kinesin on microtubules [55]. Some insight into the single-molecule friction was provided by Molecular Dynamics (MD) simulations of adsorbed peptides on surfaces; while adhesive free energies on hydrophobic and hydrophilic surfaces are roughly equal and amount to a few k_BT per residue, where k_BT is the thermal energy, the surface friction coefficients are wildly different [56, 57].

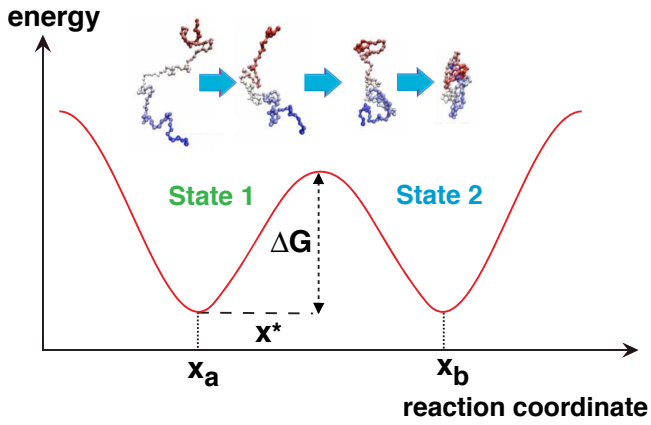

Figure 1.2.: *Illustration of reaction coordinate approach for protein folding problems: A barrier located at $x = x*$ with a height ΔG separates two minima, which correspond to, for a protein, folded and unfolded states.*

At first glance, friction may be thought of as a result of relative motion of two separate objects. This is not entirely true if we stick to our definition of friction, "resistance to motion"; in bio-machinery, mesoscopic units, such as proteins or RNA, also experience friction during their folding/unfolding transitions. This friction is a combination of internal resistance of corresponding structures and the friction due to ambience, e.g., water viscosity [58–60]. Luckily, recent single molecule experiments can probe that type of friction behavior; AFM setups can apply forces on proteins until they are unfolded with piconewton precision [37, 61, 62], or likewise, single molecules can be pulled apart using laser-trapped beads, to which pulled molecules are attached [63–66]. Clearly, the results generated by these single-molecule studies cannot be interpreted using models similar to Eq. 1.1. Instead, to deduce the information from these experiments, rate equation approaches, which combine the strength of adhesive junctions, i.e., the equilibrium adhesive free energy, and kinetics are commonly used. The idea of the rate equation is to project all degrees of freedom involved in the transition, e.g., from folded to unfolded states, along a well-defined reaction coordinate while all other degrees of freedom are coupled to a heat bath. Along this 1D reaction coordinate, native states are represented by minima and separated by a barrier with a height ΔG as depicted in Fig. 1.2. The basic idea is that, for any system (including a quasi-particle) to swap in between its native states, this

barrier should be overcome. Kramers' theory predicts the rate of escape in terms of ΔG and a pre-factor as [67]

$$k = \frac{D\omega^2}{2\pi} e^{\frac{\Delta G}{k_{\mathrm{B}}T}}, \tag{1.2}$$

where the exponential is the Arrhenius factor. The prefactor in the front is the rate in the absence of the energy barrier. The prefactor is the product of the characteristic curvature of the energy landscape given in Fig. 1.2, ω, and the diffusion coefficient, D, (or inverse friction coefficient) along the 1D reaction coordinate [68, 69]. For proteins, this prefactor determines the so-called speed-limit for folding in the absence of free-energetic barriers, $\Delta G \to 0$ [58, 70], which means that the transition is completely driven by the diffusion. Now the key question to answer is that what determines the diffusion (inverse friction) coefficient.

Forces in mesoscopic bio-systems may be grouped as hydrophobic and hydrophilic forces, which are also responsible for the observed friction and rupture forces observed in single-molecule experiments. Interplay of hydrophobic and hydrophilic forces are rather complicated due to complex structures of bio-systems. However, there are certain systems that individual effects can be probed: For peptides pulled on surfaces, it has been shown that, on the hydrophobic surfaces, the friction is very low compared to the hydrophilic surfaces [57]. On the other hand, secondary and tertiary structures of proteins or RNA like molecules are stabilized by hydrophilic interactions, more precisely by hydrogen bonding, and it is the main reason of the high force peaks in the pulling experiments [63, 71, 72]. All those bring us to the conclusion that the high friction and adhesion in corresponding systems are due to the hydrogen bonding, which are of notable contribution in the corresponding energy landscapes, i.e., in the diffusion coefficients, as we just discussed above.

HBs originate from the electrostatic interactions in between a hydrogen atom and two other more electronegative atoms. Although the characterization of these bonds can vary from system to system, for biologically relevant problems, mostly intermediate type HBs with a free energy of 3-20 $k_{\mathrm{B}}T$ are at present [73]. Indeed, in the bio-machinery, to maintain the reversibility of adhesion and to adjust the level of friction, interactions less stronger than covalent bonds but also resistive enough to hold structures jointly are needed. As an ideal candidate, HBs with their environment-dependent energy levels and distinct directionality are optimally suited for the controlled assembly of macromolecular complexes. More strikingly, they can act in groups and resist against high external forces where it is necessary, or act one-by-one [74–77]. Besides their essential role in *in vivo* systems, their unique properties have also inspired researchers to design synthetic polymeric systems with enhanced features, such as self-healing [78] or adaptive networks [79].

Indeed, the influence of hydrogen bonding in certain systems can be probed experimentally through the force-extension curves of pulling experiments, variation of the rotational diffusion of solutes [80] or the friction between surfaces [45, 46]. However, to disentangle the friction contribution from a single HB in these mesoscopic experiments is rather complicated and difficult. This is mainly due to the fluctuations in the number of HBs, the cooperativity between HBs, or due to the orientational dependence of HBs. On the

other hand, atomic *in silico* models of the pre-mentioned systems, i.e., MD simulations, can be ideal tools to infer and concentrate on the HB dynamics.

Understanding the friction of hydrogen-bonded matter at the single-molecule level is clearly important by itself, but also sheds light on the viscous kinetics of protein folding, ligand-receptor binding, viscoelastic properties of polymeric networks as well as selective transport in complex biological media. But more interestingly, HB friction is also particularly important to determine the boundaries between continuum friction theories and friction in nano-soft matter.

1.4. Hydrodynamic friction at the low Reynolds number level

As we underlined previously, friction arises from atomic interactions at the contact region. For a sphere embedded in an unbounded fluid, the resistive force follows from collisions between the solvent particles and the sphere. Integrating out solvent collisions leads to the well-known Navier-Stokes equation [2]. However, describing the motion through a differential equation is only one half of the problem. The other half, solving this equation, is another task.

The solution of the Navier-Stokes equation has been plaguing scientists and engineers from diversity of fields since they were first written down in 1851. This marvellous equation, which has changed the course of many countless modern engineering applications, such as aeroplane industry, heating systems, etc., can successfully describe the fluid motion down to nano-scales. Contrary to their wide application areas, after almost 150 years, still they can only be solved by employing numerical methods or by accepting certain assumptions. Therefore, even at the time being, their solution is a great challenge for mathematicians and physicists. One of the pioneering paces to solve the Navier-Stokes equations was taken by Sir Gabriel Stokes; in 1848, he first published his work on the steady motion of a sphere, then following, in 1851 he came with his successful work on the non-steady motion of a sphere [81]. In his works, he accepted a set of assumptions i) no-slip condition ii) incompressible fluid and iii) vanishing Reynolds number, which also gave this sections its name. The dimensionless Reynolds number ($\mathcal{R}$), quantifies the relative importance of inertial forces to viscous forces. Stokes assumed that inertial forces are less significant at the vicinity of the sphere and derived his time-dependent solution for a sphere in an unbounded fluid. He also attempted to solve the same problem for a cylinder. However, his approach precluded him to reach a solution. Later, Oseen corrected the Stokes' assumption by counting inertial terms in an approximated way and obtained a solution for the cylinder problem. A detailed review on the solution of Stokes' equation can be found in Ref [82].

The Reynolds number, which pops up through the dimensional analysis of the Navier Stokes equation, is a combination of the system parameters, $\mathcal{R} = VL\rho_0/\eta$; the characteristic velocity V, the length L of the moving object, the density ρ_0 and the viscosity η of the surrounding ambience. As we briefly illustrate in Fig. 1.3 with representative sketches, in many engineering applications, ($\mathcal{R}$) being quite larger than unity hinders

us to use an approach similar to that of the Stokes'. However, as the dimensions and the velocities go below the macroscopic limits, the validity of a Stokes type of approach intensifies, e.g., in the swimming problem of a bacteria, $\mathcal{R}$ is much smaller than unity, hence, inertia is of a negligible effect to describe the corresponding motion of bacterium. Not only in the hydrodynamic motion of micro swimmers, but also recent interests and improvements on the biological and material sciences have opened another gate for the application of low $\mathcal{R}$ hydrodynamics: In the consideration of nano-micro sized systems, it has been realized that hydrodynamic interactions are as equivalently important as other physiochemical conditions, and luckily these systems are characterized by $\mathcal{R} << 1$.

In the last decade, the necessity of considering hydrodynamics has implied itself particularly in the field of microrheology, which uses micron-sized spheres to probe the local dynamic response of small volumes to applied forces, some of them illustrated in Fig. 1.4. Laser-trapped silicon beads, magnetic beads or discs driven by external fields can be counted as a few examples among many. The microrheology particularly has become a useful tool to investigate the viscoelastic behavior of complex fluids such as biopolymer solutions, composites and complex interfaces [83, 84]. Alternatively, the thermal mean displacement of spheres obtained from diffusing wave spectroscopy, interferometry, laser deflection or video-tracking is connected to the friction response function via the dissipation-fluctuation theorem and essentially yields equivalent information on the linear response level [85–88]. Not only for spheres, but knowing the hydrodynamic forces acting on small cylinders is also important for the development of advanced sensors and actuators [89–91]. For instance, ferromagnetic nanowires driven by external magnetic fields have been used to investigate anisotropic features of complex fluids and interfaces [92]. In many applications, the Stokes' equation for an incompressible fluid with the no-slip boundary condition is used, but it was recognized early on that compressibility effects are crucial to describe certain phenomena [93–95]. In addition, a finite slip length, which is in the nanometer range for planar hydrophobic surfaces [96] and for curved objects shows an intricate dependence on flow direction and flow speed [97, 98], can have drastic effects on the dynamics of nanometer size objects and thus has to be included in the treatment as well.

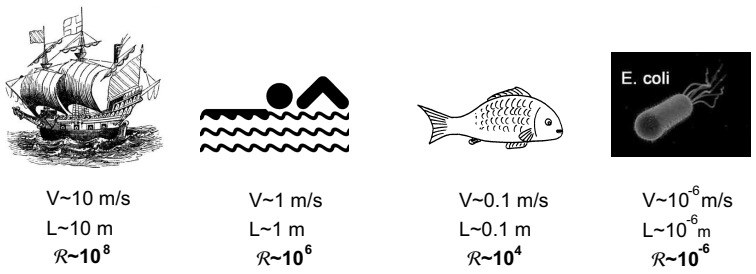

Figure 1.3.: *Illustration of Reynolds numbers from macroscopic to mesoscopic systems. Reynolds number ($\mathcal{R} = VL\rho_0/\eta$), where $\eta/\rho_0 = 10^{-6}$ m^2/s for water, is defined as the ratio of the product of typical system velocity and length to the kinematic viscosity.*

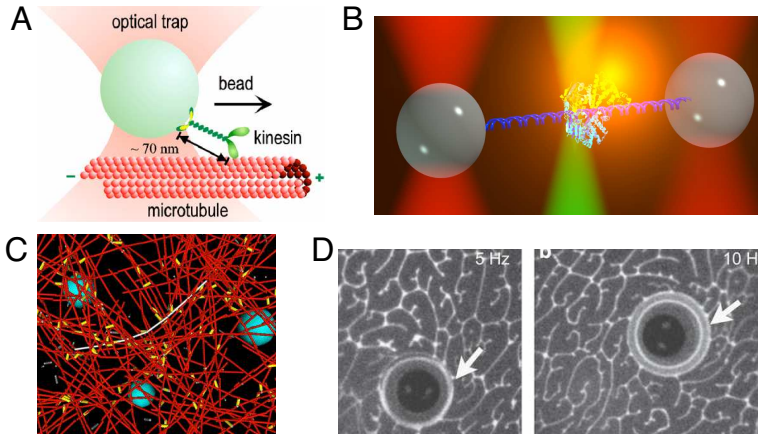

Figure 1.4.: *Some examples for the experimental methods, in which micron to nano-sized beads are used to probe forces or local viscoelastic behavior; A) A laser-trapped bead probes the friction between a microtubule and a kinesin, adapted from WWW source: http://www.stanford.edu/group/blocklab/kinesin/kinesin.html, B) two laser-trapped beads pull apart a protein, adapted from Ref [99], C) through power spectrum of nanameter-size beads, local viscolelastic properties of complex networks can be measured, adapted from WWW source: http://celldynamics.org/celldynamics/research/cortexmodel/index.html, D) micron-sized magnetic cylinders (buttons) probe the surface viscoelastic properties of lipid monolayers, adapted from Ref [100].*

1.5. Thesis Outline

The main object of this thesis is to understand friction in certain mesoscopic bio-systems, and to provide its connection to corresponding single-molecule experiments. To be able to do this, extended all-atom MD simulations, a stochastic probability theory and various mathematical tools such as the Green's function approach for solving differential equations are extensively used. In those manners, this work can be regarded as a combination of computational and analytical methods.

The chapters are organized to support and complete each other's results and conclusions, except the very last chapter, Chapter 6, which may stand for itself. Each chapter begins with its own introduction section, in which the main motivation and related previous studies are briefly discussed. Each chapter also ends with a discussion and conclusion section at its end.

In Chapter 2, we start with a detailed description of MD methodology, which is default for the rest of this work unless noted otherwise. Water bulk systems are used to test our simulation setups. In the following sections, the friction of short peptides on the non-polar (hydrophobic) and polar (hydrophilic) surfaces are focused for various pulling velocities. The pulling is applied via harmonic spring systems, which mimic the AFM setups. Additionally, the effect of normal forces and the concentration of surface-polar groups on the friction forces are discussed in detail.

The common problem of MD simulations are limited time and system sizes due to the limited computational sources [77, 101]. For non-equilibrium simulations, this limitation is mainly emphasized in terms of prescribing experimentally adapted-pulling velocities. Hence, in Chapter 3, firstly, we introduce a non-linear Fokker-Planck description to extrapolate our results towards the vanishing velocity limit. Following, the surface-peptide friction data from Chapter 2 is re-addressed and fitted by the Fokker-Planck solution. This leads to a HB friction coefficient at the linear-response level. Finally, the collective HB ruptures and their effects on the HB friction are examined.

A system containing a single peptide pulled on the polar surfaces is discussed in Chapter 2. This system forms an intermediate HB matrix in between the peptide-peptide and surface-surface geometries. In Chapter 4, we discuss the friction of a single peptide due to the neighbouring peptides. First of all, the friction between two periodic elongated peptides is discussed. Secondly, we focus on the friction in peptide bundles. At last, the friction between two perpendicular peptides are discussed.

In Chapter 5, we revise the data from Chapter 2 to focus on the peptide motion on the non-polar surfaces. The effect of non-polar surface anisotropy, frictional dissipation mechanisms and the conformation of peptides on the non-polar surfaces are studied in detail. Also, the monomer mobilities on all surfaces and in pure bulk water are compared.

In the last chapter, Chapter 6, we switch gears and focus on the analytical solution of the transient Navier-Stokes equation. Using the Green's function approach, firstly, the velocity field for a point source is obtained. Later on, using this solution, velocity fields and frequency-dependent friction forces for planes, spheres and cylinders are calculated and analysed in great detail.

In the summary section, we review all the work presented in the thesis and underline connections among all chapters. We also discuss some possible issues, which may be a guidance for future studies.

Chapter 2

Peptide friction on polar and non-polar surfaces

Recent advances in single-molecule experiments have enabled to probe the friction and adhesion of macro-molecules at various surfaces; pulling a protein off a hydrophobic surface with AFM (atomic force spectroscopy) [36], single DNA diffusion on cationic bilayers or mica surfaces [26, 53] or the driven motion of kinesin on microtubules [55] can be counted among many examples. These studies bridge the gap between conventional (macroscopic) friction laws and friction between adhesive contacts [11]. Due to mesoscopic system sizes, some of these experiments also have been studied using all-atom Molecular Dynamics (MD) simulations. For instance, MD simulations reproduced the desorption forces of a spider silk protein on the non-polar surfaces [56]: In this study, authors also hypothesized that while the adhesive free energies on the non-polar and polar surfaces are roughly equal and amount to a few $k_{\mathrm{B}}T$ per residue, the surface friction coefficients are wildly different [56, 57]. Due to the formation of hydrogen bonds (HBs) between the polar surface and the molecules, the underlying mechanism of the friction on the non-polar and polar surfaces is vastly different. MD simulations can be re-addressed to elucidate origins of the surface-peptide friction; the dissipation mechanisms and the response of the peptide to external forces can be studied for a wide variety of peptides and surfaces.

In the following first, we describe the computational methods of our MD simulations in fine detail and then perform tests. To test our simulation setups, we investigate the relatively well-studied bulk friction of short peptides. Then, the effect of the surface rigidity and of pulling geometry is discussed together with the related scaling arguments. After completing tests, secondly, the lateral motion of various single peptides by using, to our knowledge, the slowest pulling velocities down to $V \sim 10^{-2}$ m/s is focused: The friction of single polypeptide chains on polar OH-covered surfaces, which are capable of forming HBs, and non-polar H-terminated surfaces with and without external normal forces will be considered. Finally, we discuss the stick-slip motion of a single peptide on the polar surfaces. and close the chapter with the discussion section.

2.1. Methods

2.1.1. Computational methods

In the current work, a system which consists of water, a diamond slab and a short peptide is simulated using the Gromacs MD package [102]. The force field chosen is Gromos96 [103], which accounts for all bonding and non-bonding interactions. All simulations are performed using periodic boundary conditions. The solvent is modelled via up to 3000 SPC (Single Point Charge) water molecules [104]. The peptide is placed on the diamond surface before adding water into the system.

Run parameters

All simulations are performed under $N_s P_z A T$ conditions, namely with constant particle number in the system N_s, a constant pressure P in $\hat{z}$-direction, constant surface area A and a constant temperature T of 300 K. Durations of simulations vary between 10 ns and 1 μs to obtain proper displacements of the peptide with a integration step of 2 fs. An initial energy minimization procedure is applied using the steepest descent algorithm to diminish unwanted contacts between atoms. Also, each system is equilibrated for 1 ns. For temperature and pressure control, Berendsen's method [105] is used. The bulk water compressibility is set to $\kappa_z = 4.5 \times 10^{-5}$ bar^{-1} for the $\hat{z}$-direction. For long range Coulombic interactions, the Particle-Mesh Ewald [106] method is employed. For the cut-off distance of non-bonded Coulomb and Lennard-Jones interactions, 0.8 nm and 0.9 nm are tested, and no significant difference is observed for the studied quantities. Therefore, for computational efficiency, 0.8 nm is used. All covalent bonds involving hydrogen atoms are constrained using the LINCS algorithm. Also, at each 20-50 steps, the neighbouring list of each atom for non-bonded interactions are updated. Note that updating at each single step is checked and does not yield a difference in related properties.

To investigate the friction forces, a setup which mimics an AFM experiment is prepared: A 2-dimensional harmonic spring in $\hat{x}$ and $\hat{y}$-directions is attached to the center of mass of the first amino acid of the polypeptide and pulled always in the $\hat{x}$-direction with velocities chosen between $V = 10^{-2}$ m/s and $V = 100$ m/s. (We note that the lowest velocity is determined by computational capacity, and that the upper value is limited by the desorption of the peptide off the surface.) In doing so, the spring applies on the first terminal group of the peptide a harmonic force $(k\Delta x,\ \ \lambda k\Delta y,\ \ 0)$, where k is the force constant of the spring (units of k is 1 kJ/(nm^2 mol) $\simeq$ 1.7 pN/nm), λ is 1 or 0 for polar and non-polar surfaces, respectively. For non-polar surface simulations, we set $\lambda = 0$, namely the peptide is allowed to move in the $\hat{y}$-direction as well. This is done since very low friction forces drive the non-pulled parts of the peptide also in $\hat{y}$-direction even if the pulling is applied in the $\hat{x}$-direction due to the anisotropy at the non-polar diamond surface. Δx and Δy are the spring extensions in $\hat{x}$ and $\hat{y}$-directions. The largest force constant is k=1350 pN/nm, and the smallest is k=3 pN/nm. The spring constant is chosen in a way that the tip position advances the position of the pulled group, and the spring extensions are smaller than half of the box length in the pulling direction.

For studying the normal or homogeneous lateral forces on peptides, a constant force on each atom including hydrogen atoms is applied in the $-\hat{z}$ or $\hat{x}$-directions, respectively. To obtain an equal force on each atom, each individual atom is accelerated inversely proportional to its mass.

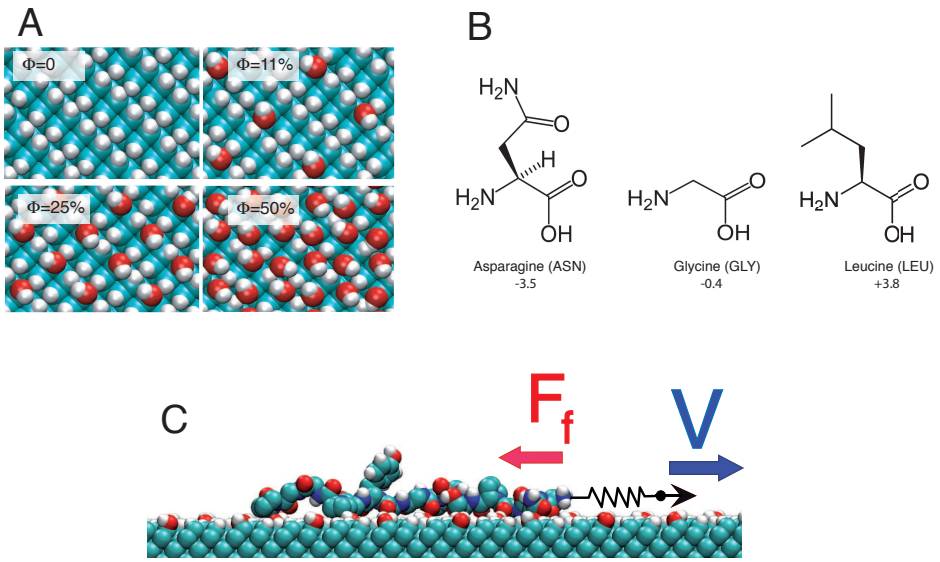

Figure 2.1.: *A) (100) surfaces of diamond slabs used in our MD simulations:* $\Phi = 0\%$ *hydrogen terminated non-polar surface,* $\Phi = 11\%$ *OH-covered polar surface,* $\Phi = 25\%$ *and* $\Phi = 50\%$ *OH-covered polar surfaces. Red and cyan spheres represent oxygens and carbons atoms, respectively, and white spheres are hydrogen atoms. B) Atomic structure of asparagine, glycine and leucine amino acids used in simulations and their hydropathy index. Corners without labels correspond to carbons atoms. The higher the hydropathy index, the more hydrophobic (non-polar) the amino acid is. C) N=15 spider silk is pulled on* $\Phi = 11\%$ *OH-covered polar surface.*

Surfaces and simulations boxes

For surface simulations, the total height of the simulation box is taken at least 5 nm. Since the system under consideration is periodic in all directions, effectively the system considered here is a peptide between two surfaces. Hence, various heights up to 8 nm are tested, but no difference in the relevant quantities, such as friction force or HBs, is observed.

The default dimensions of diamond slabs used in simulations are summarized in Table 2.1. For simulations performed on the polar surface, smaller diamonds compared to those used for non-polar surfaces are taken due to the high friction forces on the polar surface. No significant difference between the simulations on larger and smaller polar surfaces is observed for the friction force or HB population. For the non-polar surface, (001) surface of the diamond slab is saturated completely by hydrogen atoms with partial charges $q_H = 0$ and $q_C = 0$. At the polar surface, a fraction of the dangling bonds are

saturated by OH groups to obtain different surfaces with $\Phi = 11\%, 25\%$ and $\Phi = 50\%$ OH-coverage levels, e.g., for $\Phi = 50\%$ surface, on which half of the hydrogen atoms on the non-polar surface are replaced with OH groups. In Fig. S2.1, (100) surfaces of all diamond slabs are shown. For the partial charges of COH, the parameters of a serine residue is used ($q_{\mathrm{C}} = 0.266$ e, $q_{\mathrm{O}} = -0.674$ e and $q_{\mathrm{H}} = 0.408$ e). Also, by fixing the position of all diamond atoms, inelastic non-polar diamonds are constructed, but they are only used to obtain the data shown in this supplementary information text. All data in the main text are obtained on elastic surfaces. Since the friction forces on non-polar surfaces are too small compared to polar surfaces, to prevent any effects due to gaps between two adjacent periodic diamond slabs, slabs are made continuous in all lateral directions. For polar surface, these gaps do not affect the result.

For the water bulk simulations, due to the long-range nature of hydrodynamic forces, in designing the cubic simulation boxes, the distance between two periodic images of polypeptides is taken minimum 10 times the experimentally predicted hydrodynamic radius $R_{\mathrm{H}} = 0.027 \times M_{\mathrm{r}}^{0.5}$ nm [107], where M_{r} is molecular weight (rescaled with $1/12$ of the mass of one carbon atom). The sizes of the simulations boxes are given in Table 2.1.

Peptides

One of the peptide sequences we study is a part of the repeated units of the mildly hydrophobic polypeptide C_{16} of ADF-4 *Areneus diadematus* silk protein. This protein is composed of 16 repeating segments each, of which comprises 35 amino acids. For computational efficiency, only the terminal part between residues 21-35, NQGPSGPG-GYGPGGP, of one single segment is simulated, where N, Q, G, P, S and Y correspond to asparagine, glutamine, glycine, proline, serine and tyrosine amino acids, respectively. Beside spider silk, which is non-homogeneous, homogeneous peptide chains with polymerization degrees between N=6 and N=22 are also studied: The smallest amino acid, glycine, asparagine, mainly hydrophilic and leucine with a hydrophobic side chain are used. Note that to gain computational efficiency, hydrogen atoms bonded to C_α atoms are removed, and their masses are added to that of C_α. Since CH group is non-polar, this does not effect the properties, e.g., hydrogen bonding, investigated here.

Data analyses

The spring extension in the $\hat{x}$-direction times the spring constant is recorded as the total friction force F_{f} averaged over time. Also, except noted otherwise, quantities presented in this paper are averaged with respect to time. All error bars are calculated via block averaging and shown only when they are larger than the symbol of the related data point. To calculate an experimentally more relevant quantity, the friction coefficient γ, from the friction force data,

$$\gamma \equiv \frac{F_{\mathrm{f}}}{V} = \frac{F_{\mathrm{f}}}{N^{\nu} V} = \mu^{-1} = \frac{k_{\mathrm{B}} T}{D} \tag{2.1}$$

Table 2.1.: *Sizes of the diamond slabs and of water boxes used in the surface-peptide and water bulk MD simulations, respectively.*

Peptide	N	System	Size ($L_x \times L_y \times L_z$) (nm^3)
spider silk	15	polar diamond	$6 \times 3 \times 1.8$
glycine	6	polar diamond	$6 \times 3 \times 1.8$
glycine	11	polar diamond	$6 \times 3 \times 1.8$
glycine	22	polar diamond	$12 \times 3 \times 1.8$
asparagine	11	polar diamond	$6 \times 3 \times 1.8$
leucine	11	polar diamond	$6 \times 3 \times 1.8$
spider silk	15	non-polar diamond	$8 \times 4 \times 1.8$
asparagine	3	non-polar diamond	$7 \times 4 \times 1.8$
asparagine	6	non-polar diamond	$7 \times 4 \times 1.8$
asparagine	11	non-polar diamond	$7 \times 4 \times 1.8$
asparagine	15	non-polar diamond	$7 \times 4 \times 1.8$
asparagine	20	non-polar diamond	$9 \times 9 \times 1.8$
asparagine	3	water bulk (small)	$4 \times 3 \times 3$
asparagine	3	water bulk (large)	$10 \times 10 \times 10$
asparagine	6	water bulk (small)	$5 \times 4 \times 4$
asparagine	6	water bulk (large)	$12 \times 12 \times 12$
asparagine	11	water bulk (small)	$6 \times 5 \times 5$
asparagine	15	water bulk (small)	$8 \times 5 \times 5$
asparagine	15	water bulk (large)	$15 \times 15 \times 15$

is used, where ν is the system dependent scaling exponent and V is the pulling (or drift) velocity in the pulling (drift) direction. Here μ and D are monomer mobility and diffusion coefficient, respectively.

Counting HBs

OH and NH groups are taken as donors, O and N atoms are always regarded as acceptors. HBs are counted with respect to two criteria [108] as depicted in Fig. 2.2);

I . The distance-angle criteria: The Acceptor - Donor - Hydrogen angle θ should be equal or smaller than $\theta = 30^o$, and the distance between the donor and acceptor atoms should be smaller than $d = 0.35$ nm,

II . The distance-only criteria: The distance between the donor and acceptor atoms should be shorter than $d = 0.35$ nm. Angular dependence is ignored.

2.1.2. Testing simulation setups: friction in bulk water

Before conducting pulling simulations on surfaces, to test our simulation setups, we perform extensive simulations for asparagine chains in bulk water. From the pulling force, we deduce the bulk water friction coefficients, which allow us to compare our results with experimentally available diffusion constants of amino acids (AA) in bulk water [107, 109, 110]. Furthermore, the obtained friction forces and corresponding friction

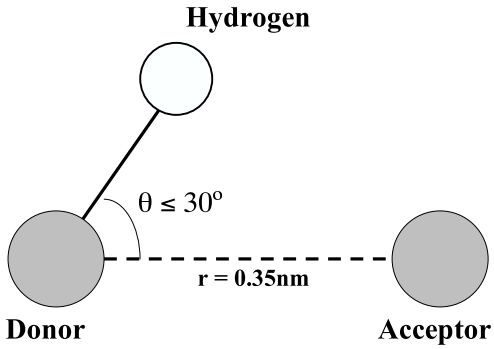

Figure 2.2.: *Geometrical definition of the hydrogen bond used throughout this work.*

coefficients for bulk water will be used to quantify those for various surfaces in the following chapters. For polymers adsorbed on surfaces different scaling rules appear in the literature; for DNA molecules on lipid membrane a scaling of N^{-1} was reported [26]. Experiments with PEG (Polyethylene glycol) on hydrophobic surfaces report a scaling of $N^{-3/2}$ [111]. A computational work suggested N^{-1} and $N^{-3/4}$ for corrugated and flat surfaces, respectively [112] The latter obeys 2-D Zimm statistics where the entire polymer is accepted as a Stokes sphere and the hydrodynamics involves. Due to the diversity of scaling arguments and the length of peptides considered here being shorter, we performed simulations with polymerization degrees of N=3, 6 and N=15 polyasparagine to obtain a proper scaling for our problem. In Fig. 2.3A, we show the friction coefficients for a fixed pulling velocity $V = 1$ m/s in bulk water. The friction coefficients are compatible with $N^{3/5}$ Zimm scaling for large simulations boxes, spheres in Fig. 2.3A, as expected for a non-draining polymer. But note that for smaller simulation boxes (black diamonds), deviations occur and the data are better fitted by a scaling linear in N, indicative of Rouse scaling, which might be due to the fact that small simulation boxes do not allow for long-range hydrodynamic effects to fully build up. Besides, the polymer chains are too short to deduce any scaling with reasonable certainty, so we are content with stating that the friction increases with the polymerization index N in a way that is compatible with Zimm scaling for large simulation boxes and with Rouse scaling for small simulation boxes. We also conducted a free-drift simulation for an N=3 polyasparagine chain and deduced the mobility from the Einstein relation $\gamma_{\mathrm{N}} = k_{\mathrm{B}}T/(6t\Delta r^2)$, where Δr^2 is the mean square displacement of the peptide in 3D and given in Fig. 2.3B as a function of time. Note that the displacement data become very noisy for long times. A least-square fit (solid line in Fig. 2.3B, together with the error limits indicated by dotted lines) gives a bulk friction coefficient value of $\gamma_{\mathrm{N}} = 3 \times 10^{-12}$ kg/s as indicated in Fig. 2.3A by a star. The equilibrium friction coefficient agrees within its error with the values obtained from the pulling simulations of the same system with $V = 1$ m/s. Extrapolation of all data according to the $N^{3/5}$ Zimm scaling down to N=1 gives a monomeric friction coefficient in bulk water of $\gamma_0 \approx 2 \times 10^{-12}$ kg/s. Since the SPC water model underestimates

the water viscosity considerably [113], we rescale the experimental monomeric friction coefficient according to $\gamma'_{\rm exp} = \gamma_{\rm exp} \times \eta^{\rm SPC}/\eta^{H_2O}$, where the experimental water viscosity is taken as $\eta^{\rm H_2O} = 10^{-3}$ kg/(ms) and the SPC water viscosity is $\eta^{\rm SPC} = 0.4 \times 10^{-3}$ kg/(ms) [113]. After this rescaling, our γ_0 value agrees well with the experimental result (purple square) [107] in Fig. 2.3.

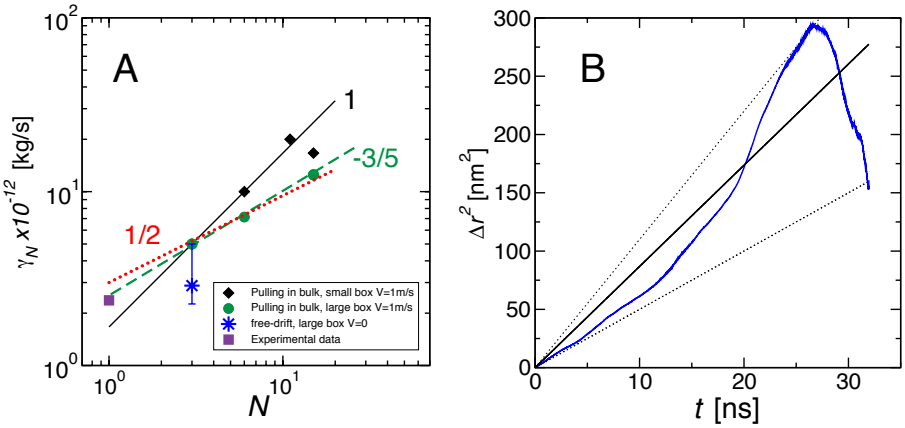

Figure 2.3.: *Peptide friction in bulk water: A) Friction coefficient of asparagine chains versus polymerization degree N. For the diamond and sphere symbols, the pulling velocity is $V = 1$ m/s and the friction coefficient is calculated via $\gamma_N = F_f/V$. The data point indicated by a blue star is obtained from the mean-square displacement of a freely diffusing chain, see (B). The various lines indicate power laws according to Rouse scaling $\gamma_N \sim N$, Zimm scaling for a swollen chain $\gamma_N \sim N^{3/5}$, and Zimm scaling for an ideal chain $\gamma_N \sim N^{1/2}$. The friction coefficient per monomer (N=1) is obtained via extrapolation as $\gamma_{N=1} \equiv \gamma_0 \approx 2 \times 10^{-12}$ kg/s, with only small dependence on the precise scaling law used. The experimental (purple square) value is obtained via viscosity rescaling, $\gamma'_{exp} = \gamma_{exp} \times (\eta^{SPC}/\eta^{H_2O})$ [107, 113]. B) Mean square displacement of an asparagine peptide with N=3 at $V = 0$, used to calculate the data point (star) in (A). The solid line is a least-square fit, dotted lines denote the error bounds.*

2.1.3. Terminal pulling versus homogeneous force, elastic versus inelastic Diamond

We conducted simulations on the non-polar surfaces for asparagine chains with varying lengths between N=3 and N=20, results are shown in Fig. 2.4A. In addition to pulling on one peptide terminus and measuring the pulling force by the extension of the pulling spring, which is the method used to obtain all friction throughout this work and called "terminal pulling", we in addition perform simulations where we apply a constant lateral force of F_L=1.25 pN per monomer in the $\hat{x}$-direction, which we refer to as "homogeneous force method". The constant force value induces a drift velocity of the order of V=1 m/s and thus allows to compare the resulting friction coefficients. The results from both different methods (Fig. 2.4A) agree very well, which shows that the terminal pulling introduces no artifacts. By freezing all degrees of freedom of the substrate carbon atoms,

a completely inelastic diamond is obtained. As shown in Fig. 2.4A, the friction coefficient on the inelastic diamond surface (red diamonds) is slightly higher compared to the elastic surface (black triangles). This might be due to the smaller surface corrugation on the elastic surface, although in principle one could have expected an increased friction on the elastic surface due to an additional dissipation mode that is related to phononic degrees of freedom in the diamond. Although our polymerization degrees are too small to quantify scaling laws, from Fig. 2.4A, both Rouse scaling proportional to N and a $N^{3/4}$ Zimm law seem to be compatible with the data. The Rouse scaling includes no hydrodynamics while the Zimm scaling treats the hydrodynamics. The question to what extent hydrodynamics are screened by a nearby surface is a subtle one that depends on the precise separation from the surface [114]. If we extrapolate our data to N=1, we obtain monomer friction coefficients $\gamma \simeq 1.5 \times 10^{-12}$ kg/s for Rouse scaling and $\gamma \simeq 2 \times 10^{-12}$ kg/s for Zimm scaling. The small difference between the two different extrapolation techniques is not significant, and both values are very close to the water bulk friction coefficient γ_0 given previously, which reflects that on the non-polar surface friction due to water dominates, as we demonstrate in Fig. 2.5.

Fig. 2.4B shows the ratio of the radii of gyration in the $\hat{x}$ and $\hat{y}$-directions for asparagine chains as a function of N. In terminal pulling simulations, particularly for chains $N > 11$, the chain elongates along the pulling direction, while for the homogeneous force scenario, no preferential direction is present. For $N < 11$, in both terminal-pulling and homogeneous-force cases, the peptide shows roughly isotropic conformations on the non-polar surface. This can also be appreciated from snapshots of N=11 polyasparagine in Figs. S2.4C and D: Here, the top and side views of the peptide for two separate time frames are shown for the homogeneous force simulations in C and for the terminal pulling simulations in D.

We note that the monomeric friction coefficients on the non-polar surface reported here are smaller than those reported previously [57] $\gamma \simeq 3.3 \times 10^{-12}$ kg/s, which were obtained by extrapolation using Rouse scaling. The difference is due to a structural gap between periodic images on the hydrophobic diamond surface that was present in the previous simulation setup [57]. In our present simulation setup we make sure that the diamond surface presents no inhomogeneity at the simulation box boundaries, and hence, our friction forces are lower. Although, choosing a rigid diamond help to gain in computational power, due to the possible effect of fluctuations of the diamond atoms and for a more precise description of the problem, for non-polar surface simulations we mainly use the elastic diamond throughout this work. Also we should again underline that for both polar and non-polar surfaces, terminal pulling method is used except noted otherwise. Note that due to the existence of OH groups, polar surfaces should be always elastic.

2.2. Lateral pulling of peptides

In our simulations, fragments of spider silk peptides and different home-peptides consisting of up to $N = 22$ amino acids (AA) are pulled laterally over various polar and non-polar

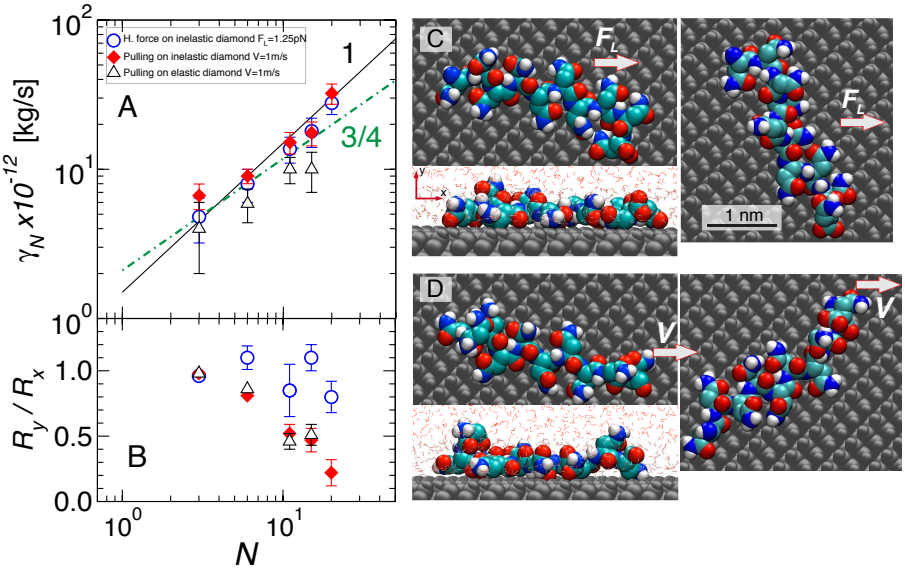

Figure 2.4.: *Peptide friction on the non-polar $\Phi = 0$ surface: A) Friction coefficient of asparagine chains versus polymerization degree N from terminal pulling simulations and homogeneous force simulations, obtained from $\gamma_N = F_f/V$. The system sizes are given in Table 2.1. The friction coefficient per monomer (N=1) extrapolates to a value of $\gamma \approx 2 \times 10^{-12}$ kg/s when using the $N^{3/4}$ scaling. For the inelastic diamond surface, the positions of all substrate atoms are fixed, the resulting friction coefficients are slightly higher. B) The ratio of the radii of gyration in $\hat{x}$ and $\hat{y}$-directions, same notation as in (A). Snapshots of the N=11 asparagine peptide C) for homogeneous force simulations, where the lateral force per monomer is $F_L = 1.25$ pN, and D) for terminal pulling simulations with $V = 1$ m/s. In the top views, water molecules are not shown for clarity. $F_N = 0$ for all cases.*

diamond surfaces. Surfaces with typical area 6 nm × 3 nm are designed and characterized by the fraction Φ of surface OH groups, we compare results for $\Phi = 0, 11, 25$ and 50%. To attain a proper statistics, the simulations are performed up to a time duration at which a proper peptide displacement, which is in our case at least the fully-stretched size of the corresponding polypeptide, is obtained at corresponding surfaces. However, pulling velocities are chosen to allow us to approach to the linear response regime. At polar surfaces, for the sake of computational time, we mainly sample our velocities on $\Phi = 11\%$ surface on which higher pulling velocities compared to $\Phi = 50\%$ and $\Phi = 25\%$ surfaces can be simulated. To keep the peptide adsorbed on a highly OH covered surface e.g., on $\Phi = 50\%$ OH covered surface and to prevent any desorption off the surface get difficult and more time demanding [115]; for instance, for the $\Phi = 50\%$ case, pulling velocities have to be ten times slower than those used for $\Phi = 11\%$ OH covered surface implying a similar scaling in the computational time. Also, note that $\Phi = 11\%$ OH coverage of the diamond surface is more closer to experimental oxidation levels [116].

2.2.1. Velocity dependence of friction forces

In Fig. 2.5A, we show the friction force per aa, F_f/N, for a $N = 15$ spider-silk fragment on non-polar $\Phi = 0\%$ (triangles) and polar $\Phi = 11\%$ (spheres) surfaces as a function of the pulling velocity V. Note that for slow velocities, $V < 1$ m/s, error bars for the friction forces are larger. These large error bars can be attributed to simulation durations: We believe that these differences disappear for longer simulation times since error bars decreasing with increasing displacements, e.g., for $V_x = 5$m/s, more sufficient displacements are obtained in a shorter time compared to $V = 0.1$m/s. For the non-polar surface, equilibration is not an issue [57], and the peptide chain glides smoothly over the surface and the total friction force (solid triangles) grows linear with V, as denoted by the solid line. Thus the friction is in the viscous regime, and the friction coefficient per AA is given by $\gamma_0 = F_f/(NV) \simeq 10^{-12}$ kg/s, very close to the value in bulk water, as deduced from our simulations in Section 2.1.2 and from experiments. The corresponding hydrodynamic radius R_H defined by the Stokes relation, $\gamma_0 = 6\pi\eta R_H$, is $R_H \simeq 0.1$ nm and thus of the order of the spatial extent of a single aa. Note that the surface friction on the non-polar surface is dominated by water friction, as follows by comparing the surface friction contribution F_f^{surf} (due to forces on the peptide from surface atoms, open triangles) and the total friction force F_f (which is the sum of all forces coming from surface *and* water atoms, full triangles). On the polar $\Phi = 11\%$ surface the behavior is completely different: For low velocities around $V \sim 0.1$ m/s, friction forces are more than 100-fold higher compared to the non-polar surface and the system is far from the viscous regime, in other words, F_f is not linearly proportional to V. For velocities $V < 10$ m/s the total friction (solid circles) is dominated by force contributions from the surface (open circles), for higher velocities for both polar and non-polar surfaces, relative contributions of the water increases with increasing pulling velocity as shown in Fig. 2.5A, and the solvent becomes the main source of the friction (solid circles and triangles).

In Fig. 2.5B we show the number of HBs per aa, N_{HB}/N, for the spider silk peptide (black circles). HBs are defined by the combined Luzar-Chandler angle and distance criterion [108]. The data indicate that for pulling velocities below $V \approx 1$ m/s, N_{HB} is not affected by the pulling and roughly $N_{HB}/N \simeq 0.35$, close to the equilibrium value obtained at $V = 0$ (included at the left in the graph). Indeed, for larger velocities, N_{HB} decreases, which is responsible for the maximum in F_f in Fig. 2.5A. The data for a N=11 polyglycine chain, indicated by triangles, exhibit similar behavior but saturate at a slightly higher value of N_{HB}/N for low V due to the lack of bulky side chains; the effect of the side chains will be discussed in Section 2.3 in more detail.

Comparison of time scales

A decreasing N_{HB} observed in Fig. 2.5 under high pulling rates imposes a time analysis: In equilibrium, a HB is expected to survive a time τ_0. When the pulling starts, another time scale emerges, $\tau_{HB} = a_{HB}/V$, where the typical HB extension length scale is $a_{HB} \simeq 0.1$ nm. As a_{HB}/V approaches τ_0, HBs feel the imposed shear rate and break. Our minimum and maximum pulling velocities $V = 0.01$ m/s and $V = 50$ m/s, a_{HB}/V values correspond

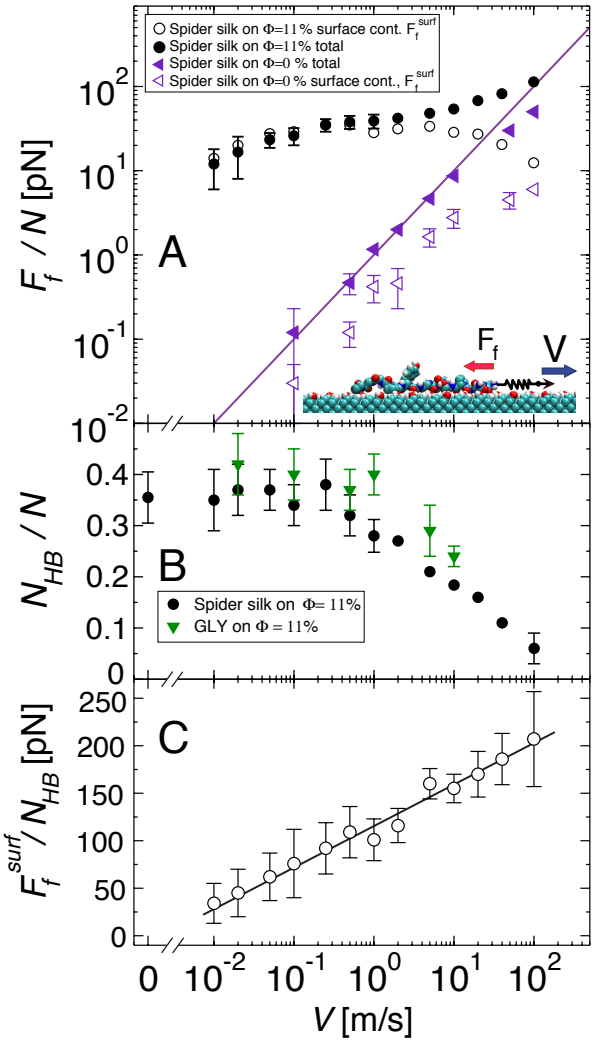

Figure 2.5.: *A) Friction force per residue F_f/N versus pulling velocity V for $N = 15$ spider silk peptide on $\Phi = 11\%$ polar (solid spheres) and $\Phi = 0\%$ non-polar diamond surfaces (solid triangles), open symbols denote the surface friction F_f^{surf}/N without the solvent contribution. Inset represents the simulation system. Straight line indicates the linear viscous law $F_f/N = \gamma_0 V$ with monomeric friction coefficient $\gamma_0 = 10^{-12}$ kg/s on the non-polar surface. B) Number of surface-peptide HBs per residue N_{HB}/N on $\Phi = 11\%$ polar surface for $N = 15$ spider silk and $N = 11$ polyglycine. C) Surface friction force per HB, F_f^{surf}/N_{HB}, for spider silk on $\Phi = 11\%$ polar diamond, straight line corresponds to Eq.* (2.2).

to roughly, 10 ns and 2 ps, respectively, both of which are longer than reported life times of a HB, which is less than 1 ps for HB clusters in water [108]. Hence, a HB might break and reform without feeling the shear rate. Nevertheless, the mechanism behind the decrease in N_{HB} displayed in Fig. 2.5 incorporates the pulling velocity as well: In simulations, positions of the donor, acceptor and hydrogen atoms are recorded, and HBs

are evaluated with respect to the angle-distance criteria given before. At any instant, the geometry formed by these three atoms may obey either the required angle rule $\theta \leq 30^o$ or the distance rule $d \leq 0.35$ nm (see Fig. 2.2) but not both at the same time. Then we do not count corresponding conformation of these three atoms as an HB. However, the more time these three atoms spend obeying either of the rules, the higher the chance for them to satisfy both rules due to the existence of fluctuations. If we define a probability of HB formation $P_{\rm HB}$, this probability will be $P_{\rm HB} \sim \tau_{\rm HB}$ since pulling slower enhances the chance of the angle-distance criteria being met for this donor-acceptor-hydrogen set. Hence, for high pulling velocities $P_{\rm HB} \sim V^{-1} \to 0$, the donor-acceptor-hydrogen set cannot meet angle-distance criteria, and the less number of HB can form. As a result, the HB stemmed friction decreases on polar surfaces.

For slow velocities, the situation is different; since the shear rates are also small, HB ruptures will be governed mostly by the thermal effects. This can be justified by comparing $N_{\rm HB}$ for velocities below $V \simeq 1$m/s, for which $N_{\rm HB} \simeq 0.3$, and for $V = 0$ with $N_{\rm HB} = 0.35$. Since these two values are close to each other, it can be concluded that thermally-controlled HB breakage mechanism is dominant in the system up to a critical pulling velocity $V_{\rm HB} = a_{\rm HB}/\tau_0$ [117], which is of the order of $V_{\rm HB} \sim 1$ m/s even if the intrinsic HB life time is taken $\tau_0 \sim$100 ps. Actually, this crossover velocity at around $V_{\rm HB} \simeq 1$ m/s, above which $N_{\rm HB}/N$ significantly decreases, can also be inferred from Fig. 2.5B for both N=15 spider silk and N=11 polyglycine.

Crossover to the viscous regime

The surface friction contribution on the polar surface shown in Fig. 2.5A shows a maximum at a velocity of about $V \simeq 1$ m/s, a phenomenon known from adhesive friction between polymeric and soft interfaces and rationalized by the converse velocity dependencies of the number of adhesive contacts and the friction contribution per adhesive contact [8, 39]. One could therefore be led to think that for $V < V_{\rm HB}$, simulations are in the linear regime where the friction force is simply proportional to V. However, in Fig. 2.5C, we demonstrate the surface friction force data from Fig. 2.5A, rescaled by the number of HBs, to show perfect scaling

$$F_{\rm f}^{\rm surf}/N_{\rm HB} \simeq F_0 \ln(V/V_0) \tag{2.2}$$

with $F_0 = 19.0$ pN and $V_0 = 0.0023$ m/s over the whole velocity range probed in the simulations. A logarithmic velocity dependence of rupture and friction forces is the signature of force-assisted thermal crossing of energetic barriers [8, 39, 76]. The velocity scale V_0 is 440 times lower than the crossover velocity $V_{\rm HB} \simeq 1$ m/s for the average HB population, which illustrates that there is a slow time-scale involved. Therefore, reaching the viscous regime, i.e., $V < V_0$, is a serious issue in biomolecular MD simulations [77, 101] To reach a distance of 2 nm at a pulling speed of V_0, the simulation time is 1 μs, which for large systems is a considerable task. At larger pulling speeds $V > V_0$, the pulling-force induced changes of the free energy landscape produce non-linear effects. In the simplest scaling-type derivation of Eq. (2.2), one writes the life time of an HB as

$\tau \simeq \tau_0 e^{(U-a_0F)/k_BT}$, where U is the activation energy, F_f the externally applied force, τ_0 the intrinsic time scale and a_0 a typical distance characterizing the barrier position. Denoting the velocity as $V \simeq a_0/\tau$, one obtains Eq. (2.2) with $F_0 = k_BT/a_0$ and $V_0 = (a_0/\tau_0)e^{-U/k_BT}$. With the fit value $F_0 = 19$ pN we immediately obtain $a_0 = k_BT/F_0 \simeq 0.2$ nm on the order of the HB bond length (but note that the meaning of a_0 is actually more abstract, see below). Further setting $\tau_0 \sim a_0^2\gamma_0/k_BT$, i.e., associating the intrinsic time scale with the diffusion time over a typical distance a_0, and using for the intrinsic friction the value $\gamma_0 \simeq 10^{-12}$ kg/s valid for AA diffusion in bulk and at the hydrophobic surface, we conclude $e^{U/k_BT} \sim 10^4$. Thus the energy scale is predicted to be of the order $U \simeq 10k_BT$, in considerable excess of the free energy of a single HB of the order of 2-3k_BT [118] which hints at strong cooperativity of HB friction, in accord with previous HB rupture studies [74] In the linear force regime, $a_0F/k_BT < 1$, time scales are predicted to be slowed down by a factor of $\tau/\tau_0 \sim e^{U/k_BT} \sim 10^4$ at the polar surface, including the viscous friction coefficient in the low-velocity limit $V < V_0$, in rough agreement with the data in Fig. 2.5A. Although $V_0 \simeq 0.002$ m/s is small for common MD simulations, it is orders of magnitude larger than typical velocities in molecular biology or single-molecule experiments [74, 77, 101, 119], which are in the μm/s range. In Chapter 3, we will later introduce a more general model that contains Eq. (2.2) as a special case and allows to robustly extrapolate simulation data into the $V \ll V_0$ limit. In doing so, we will be able to obtain a viscous friction coefficient per HB.

2.2.2. Stick-slip motion

So far, we focused on the time average values of the friction force. However, for equal average friction forces, the motion of the peptide might exhibit either sliding or stick-slip like behaviors. Therefore, in Fig. 2.6A, for fixed pulling velocity $V = 1$ m/s, we compare time traces of the total friction force and the displacement of the terminal pulled group for N=15 spider silk on all different surface polarities used in our simulations, $\Phi = 0, 11\%, 25\%$ and $\Phi = 50\%$. The average friction forces for the three polar surfaces are similar, as displayed by dashed lines in Fig. 2.6A. and stick-slip events (force peaks) are clearly visible. As shown in Fig. 2.6A, stick-slip events are also visible in the time trace of the displacement of the pulled group. On the other hand, on the non-polar surface, as shown in Fig. 2.6B, the average friction force is much smaller due to the lack of HBs, the friction force on an non-polar surface is much smaller than on a polar surface. Nevertheless, the peptide still exhibits thermal fluctuations of the instantaneous force around its mean on the non-polar surface. These force fluctuations on the non-polar surface in Fig. 2.6B are related to peptide conformational changes as displayed in Fig. 2.6C: Here, we display the radius of gyration of the peptide in the directions parallel ($R_{g,x}$) and perpendicular to the pulling direction ($R_{g,y}$): due to the low friction on the non-polar surface, the peptide undergoes frequent stretching and rotational fluctuations, as visualized with snapshots in Fig. 2.4.

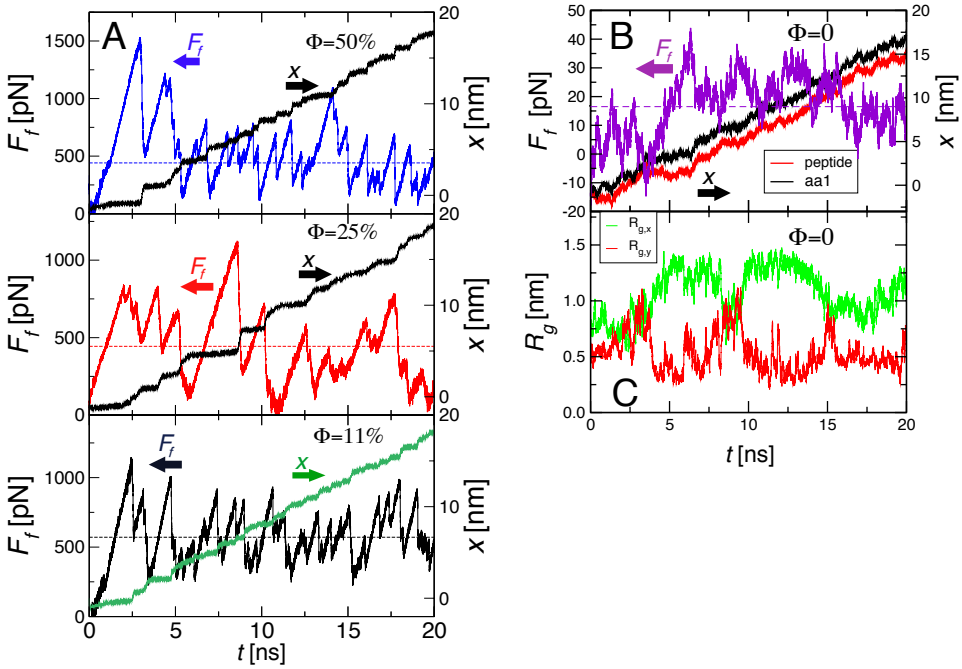

Figure 2.6.: *Time traces of the displacement of the pulled amino acid group, $x(t)$, and the friction force, $F_f(t)$, for a N=15 spider silk peptide pulled with $V = 1$ m/s on A) three polar $\Phi = 11\%, 25\%$ and $\Phi = 50\%$ surfaces, and B) on the non-polar $\Phi = 0$ surface. C) Radius of gyration of the peptide, R_g, in $\hat{x}$ and $\hat{y}$ directions on the non-polar $\Phi = 0$ surface. aa1 refers to the terminal AA.*

Relation between hydrogen bonding and stick-slip

As we have discussed in the previous paragraph, strong stick-slip behaviour is observed on the OH-covered polar surfaces. Indeed, HBs between the surface and the polar groups of the peptides results in force-time traces similar to that of two- sliding mica surfaces [120]. To show this relation between HBs and measured spring forces, in Fig. 2.7A, B and C, we show time traces of the displacement of the pulled group for N=15 spider silk peptide at $V = 10^{-2}$ m/s, for N=22 polyglycine at $V = 0.1$ m/s and for N=11 polyglycine at $V = 0.5$ m/s, all on a $\Phi = 11\%$ surface. Slip events, which manifest themselves in the displacement trajectories, are zoomed in and compared with the behavior of N_{HB}: Each forward jump in displacement is accompanied by a decrease in N_{HB} for all chains and for all velocities. Note that this drops in the HB number are quite similar to the stick-slip phenomena in boundary lubrication [121].

We should also note that stick-slip events observed for our peptide-surface motion are of stochastic nature, e.g., displacement jumps or force peaks are not regular or periodic. It is mainly because OH groups on the surface are spatially fixed whereas due to the dangling atoms and conformational changes, peptide inter acceptor/donor distances are

not totally fixed.

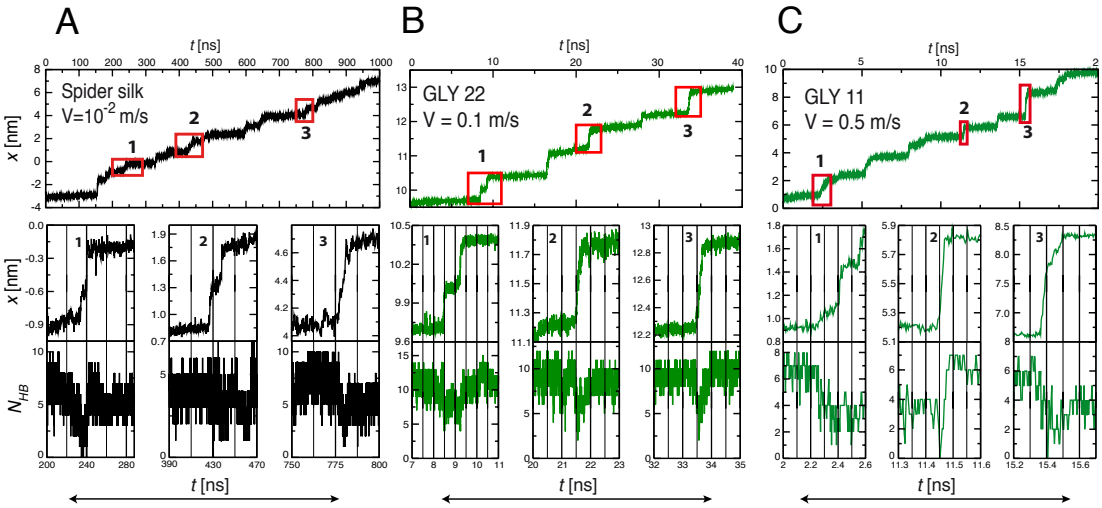

Figure 2.7.: *Trajectories of the displacement of the terminally pulled amino acid as a function of time: A) Data for the N=15 spider silk peptide with a pulling velocity of $V = 10^{-2}$ m/s on a $\Phi = 11\%$ OH-covered polar surface. In the magnified time windows the displacement is compared to HB number trajectories. B) Similar analyses for the N=22 polyglycine pulled with $V = 0.1$ m/s, and C) for N=11 polyglycine pulled with $V = 0.5$ m/s on the same surface.*

Force along the pulled peptide

To illustrate the stick-slip type of motion, the displacement of the terminal group is always shown. In this point whether entire peptide moves in this fashion or not might attract questions. To ensure that not only the terminal amino acid but the whole peptide undergoes a stick-slip type of motion, in Fig. 2.8 the displacements and velocities of three amino acids along the spider silk peptide pulled with $V = 0.05$ m/s on $\Phi = 11\%$ OH-covered polar surface are displayed as a function of the simulation time. It is convincing that all three of these monomers follow a stick-slip type motion. Note that the reason of the noise for 15th amino acid is due to the linear decrease of the stretch-force away from the pulled group. This might be explained by a simple bead model of N monomers connected by N-1 connectors: Consider that this bead is pulled from first bead, for which $i = 1$, where i is the bead index. In steady motion the stretch-force on the connector between ith and $(i+1)th$ beads can be written as $T_i = (N - i)F$, where F is the force acting on each single bead. Thus, the stretch-force between 14th and 15th beads is lower than those between 7th and 8th. Note that no hydrodynamics is involved in this model.

Binomial velocity distribution

The existence of a stick-slip regime can also be identified from the velocity distribution of the pulled group: For a stick-slip regime, the velocity distribution should be binomial

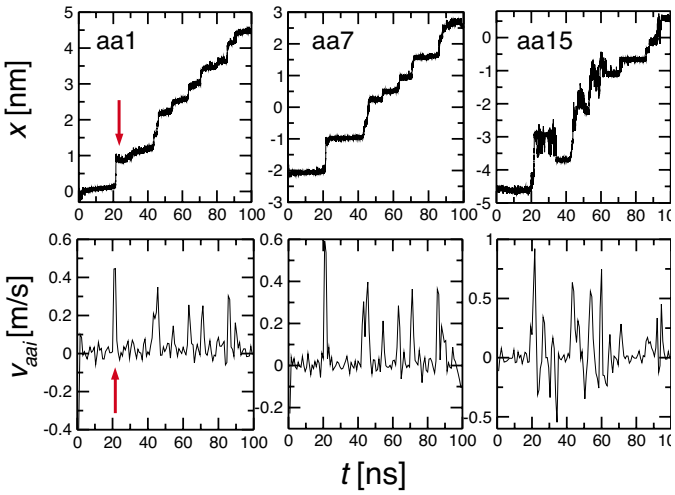

Figure 2.8.: *Displacements and velocities of first, middle and the last amino acids of N=15 spider silk peptide on $\Phi = 11\%$ OH covered polar surface as a function of simulation time. The peptide is pulled from the first amino acid with $V = 0.05$ m/s. $F_N = 0$. The jumps in the last (15th) amino acid are due to weakening stretching force at the trail of the pulled peptide. 1st amino acid is asparagine, 7th and 15th are proline amino acids.*

since the peptide either stays sticked or slips. To illustrate this, in Fig. 2.9, the velocity distribution for the terminal group of the spider silk is given for a bin size of 2ns. For the slowest pulling rate of $V = 0.05$ m/s, the peptide spends more time in stick (pinned) state and undergoes local position fluctuations ensuing a peak at zero velocity as can be seen in Fig. 2.9. Nevertheless, there is still a finite probability for the peptide to move with higher velocities corresponding to the slip regime. For instance, in Fig. 2.9, the arrow indicates the slip event at $v_{aa} \approx 0.6$ m/s, which is also marked in Fig. 2.8 by an arrow. For $V = 5$ m/s, the velocity distribution has a peak around $V = 5$ m/s, and no finite probability out of the main distribution hill unlike $V = 0.05$ m/s shows up. To emphasize this situation in Fig. 2.9, we also show the absolute value of probability times velocity, which is proportional to the displacement in the time window.

2.3. Effect of normal forces on peptide friction

In the macroscopic world, Amonton's law, $F_\mathrm{f} = \mu F_\mathrm{N}$, which states that the friction force is proportional to the normal force F_N and a constant μ of order unity, but in particular is independent of sliding velocity and apparent contact area, very successfully describes friction in the absence of adhesion and for not too low sliding velocities [8, 9]. However, down to nanoscopic scales, due to existence of adhesive forces, it is possible to observe violations from the macroscopic law [9, 12, 34]. Particularly, at the single molecule level, where a clear definition of the contact area is difficult, a closer look to the friction behavior is necessary. For instance, how external normal forces act on a single polypeptide and

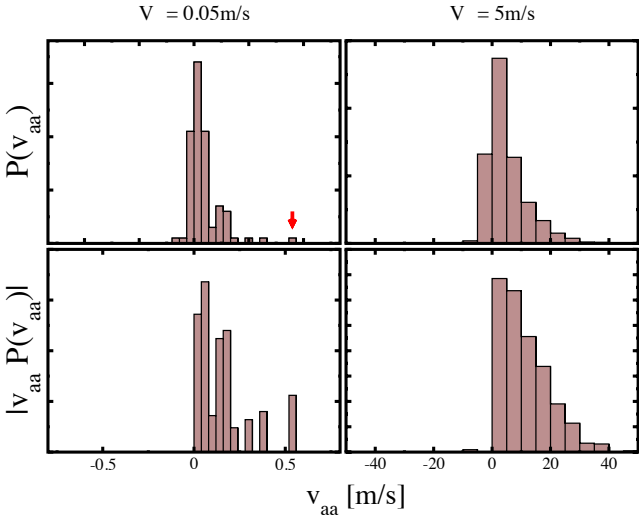

Figure 2.9.: *Normalized velocity distribution and the velocity times distribution function for the terminal amino acid of spider silk peptide on $\Phi = 11\%$ OH covered polar surface. Pulling velocities are $V = 0.05$ m/s and $V = 5$ m/s with simulation run-times 100 ns and 40 ns, respectively. The size of bins is 2 ns for both distributions. The red arrow indicates the specific slip event also shown in Fig. 2.8 by a red arrow. $F_N = 0$.*

change its friction and its configuration on various surfaces is unclear.

In this section, in order to test the influence of normal forces on the single-molecule friction, we apply an acceleration on each peptide atom inversely proportional to its mass, which amounts to a force that uniformly pushes the peptides onto the surface. Note that experimentally, normal forces have been realized in single-molecule studies by osmotic pressure techniques [122]. In Fig. 2.10A, the friction force per aa, F_f/N, obtained on surfaces with four different OH group concentrations, $\Phi = 0, 11, 25$ and $\Phi = 50\%$, is displayed as a function of normal force per AA ranging up to $F_\mathrm{N}/N = 420$ pN for fixed pulling velocity $V = 0.5$ m/s. The higher F_N/N, the larger the friction force F_f/N, but the behavior differs from the Amontons law in that i) the friction saturates for large F_N/N, and ii) the friction is non-zero for $F_\mathrm{N}/N \to 0$. We also observe that F_f/N saturates as Φ increases, and that on the non-polar surface, $\Phi = 0\%$, friction is negligibly small even for large F_N compared to that on the polar surfaces. For the non-polar surface, indicated by triangles in Fig. 2.10A, the friction force per amino acid is roughly $F_\mathrm{f}/N \approx 0.8$ pN at zero-normal force. With increasing normal force, the friction force increases to $F_\mathrm{f}/N \approx 2$ pN when $F_\mathrm{N}/N = 420$ pN is applied. This is roughly a two-fold increase compared to the zero-normal force case. In between these two limits, the friction force on the non-polar surface shows a weak increase with increasing normal force. On the three polar surfaces with OH concentrations of $\Phi = 11\%, 25\%$ and 50%, the friction force is of the order of $F_\mathrm{f} = 35$ pN when $F_\mathrm{N}/N < 30$ pN. This is far larger than the previous result obtained on the non-polar surface under equivalent normal forces. When $F_\mathrm{N}/N \leq 30$ pN, the normal force has a minor effect on the friction force on polar surfaces. However, for

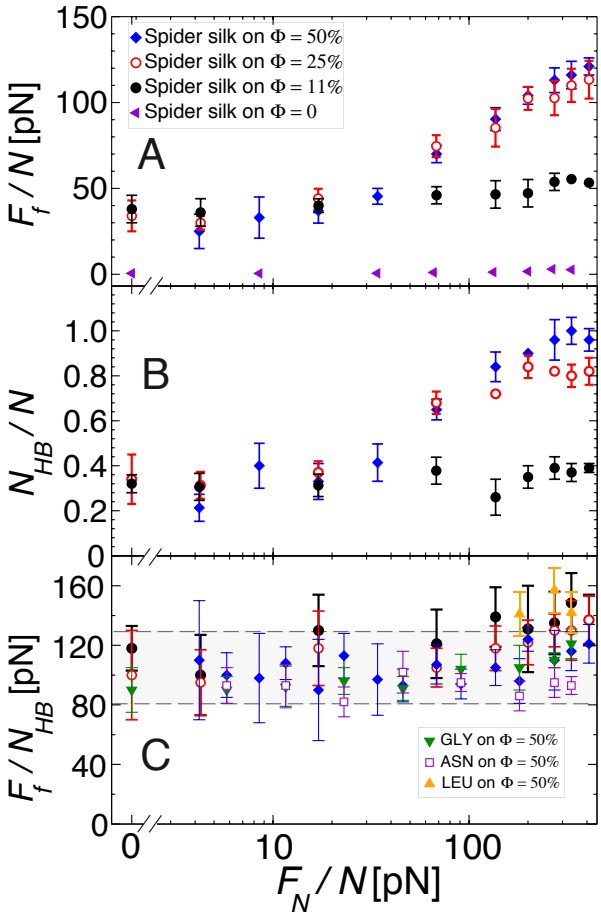

Figure 2.10.: *Effect of normal force: A) Friction force F_f/N, B) number of surface-peptide HBs N_{HB}/N, and C) friction force per HB F_f/N_{HB} versus normal force per residue F_N/N. Data are shown for $N = 15$ spider silk on $\Phi = 0, 11\%, 25\%$ and 50% OH-covered surfaces and in C) also for $N = 11$ polyglycine, polyasparagine and polyleucine for $\Phi = 50\%$. Pulling velocity is $V = 0.5$ m/s for all cases. The dashed lines are guide to the eyes.*

higher normal forces, at polar surfaces, the friction force exhibits a concentration specific behavior: For $\Phi = 25\%$ (circles) and $\Phi = 50\%$ (diamonds) surfaces, the obtained friction forces are very close to each other within the error range. For both surfaces, an increase of the friction force is observed with increasing normal force for the normal forces below $F_N/N \simeq 100$ pN. With higher normal forces, this increase slows down but still continues up to the highest studied normal force of $F_N/N = 420$ pN. For the third polar surface with $\Phi = 11\%$ OH coverage, the friction force also increases with increasing normal force, but the increase is less strong than those observed for $\Phi = 25\%$ and $\Phi = 50\%$, and never exceeds $F_f/N = 60$ pN even for the highest normal force $F_N/N = 420$ pN. In Fig. 2.10A, it is evident that the friction force saturates for larger Φ where higher enough normal forces are applied, e.g., at $F_N/N = 120$ pN, a sudden increase in the friction force from

the concentrations $\Phi = 11\%$ to $\Phi = 25\%$ is observed. Conversely, the same situation does not continue for higher values of Φ; the friction forces for $\Phi = 25\%$ and $\Phi = 50\%$ are almost equal when $F_N/N = 120$ pN. Note that for the normal forces $F_N/N \leq 10$ pN, on $\Phi = 50\%$ surface the friction force is slightly lower compared to that on $\Phi = 11\%$ surface. We attribute this to the partial desorption of the peptide, resulting in a decrease in the friction force.

Saturation of friction at high OH concentrations

Fig. 2.10B shows that the HB number, N_{HB}, versus normal force data largely parallels the friction force versus normal force data as shown in Fig. 2.10A. This suggests to consider the friction force per HB, F_f/N_{HB}, which is plotted in Fig. 2.10C. Here we add, in addition to the spider-silk data in Fig. 2.10A and B, data for N=11 polyglycine, polyasparagine and polyleucine on a $\Phi = 50\%$ surface (which will be further discussed below): the data for all peptides on different surfaces fall within a force range around $F_f/N_{HB} \simeq 100$ pN for the complete F_N/N range and can be fitted by a single line parallel to the force axis. To understand this behavior, in Fig. 2.11A, the friction force and N_{HB} are given as a function Φ for various normal forces chosen particularly among those displaying significant alteration with surface OH concentration in Fig. 2.10A and B. For zero concentration, which corresponds to a non-polar surface, trivially $N_{HB} = 0$ for all normal forces $F_N/N = 17$ pN, 70 pN and 270 pN considered here, however, friction forces obtained for these three normal forces are non-zero. As we increase the surface OH concentration, HBs begin to form between the peptide and the surface. For the lowest normal force of $F_N/N = 17$ pN, both the friction force and N_{HB} exhibit plateaus at roughly $F_f/N \approx 45$ pN and $N_{HB}/N \approx 0.4$, respectively, for non-zero Φ values. Indeed, similar behaviors are also observed for higher normal forces as shown in Fig. 2.11A, e.g., for $F_N/N = 70$ pN. However, in this case the plateau behavior shows up at a higher concentration, $\Phi = 25\%$, above which the friction force is around $F_f/N \approx 75$ pN regardless of increasing Φ. Also, for $F_N/N = 270$ pN, a plateau at roughly $F_f/N \approx 110$ pN appears. For the HB number, we obtain similar regimes observed for the friction force as shown in Fig. 2.11A: For higher normal forces, above a threshold value of Φ, which is specific to the applied normal force, N_{HB} is less modulated by Φ. The difference in N_{HB} and F_f/N indicates that low normal forces cannot push the peptide towards the surface completely after displacing some water. This emphasizes that for low normal forces, surface OH concentration becomes irrelevant in determining the friction force as N_{HB} does not change drastically with the concentration, which is also consistent with Fig. 2.10A and B. The saturation of HB number and force observed in Fig. 2.11A can be explained by the HB formation capacity of the peptide molecule due to its limited number of NH and OH groups: Even if surface OH groups are available to form more HBs, the limiting factor is the number of donors/acceptors on the peptide. This situation is illustrated in Fig. 2.11B: For the lowest surface OH concentration, HBs are rare as can be seen by visual inspection. As the concentration increases, more HBs appear, however, this trend does not persist for very high surface OH concentrations. To clarify the insight, in Fig. 2.11B, we depict this mechanism for these three surfaces.

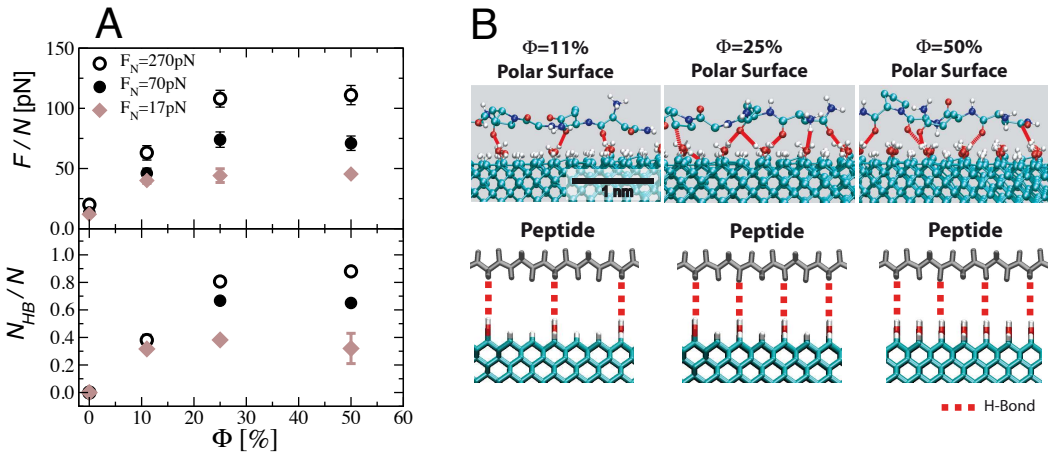

Figure 2.11.: *A) The average friction force and the average number of surface-peptide HBs per amino acid versus surface concentration, Φ, under various normal forces per amino acids for N=15 spider silk peptide at $V = 0.5$ m/s. B) Illustration of HB formation between peptide and polar surfaces with arbitrary snapshots taken from three different simulations of spider silk (N=15) on $\Phi = 11\%, 25\%$ and $\Phi = 50\%$ OH-covered polar diamond surfaces. Applied total normal force per monomer $F_N/N = 135$ pN. The peptide is pulled from left to right from the terminal group which is an asparagine amino acid. Spheres represent hydrogen, oxygen, nitrogen and carbon atoms. The dashed lines indicate HBs obtained by using the angle-distance criteria given in the text between surface OH groups and the peptide NH or OH groups.*

A closer look at the surface-peptide interactions

As we have discussed so far, there is a direct correlation between the friction forces on the polar surfaces and the strong non-covalent interactions, namely HBs. In the previous section, we show that the reason of the increase is the increasing number of HBs. This means that the peptide also changes its conformation under external forces and these changes lead to a higher N_{HB}. To further investigate the peptides' conformational response to the external forces, in Fig. 2.12, we check the distance between C^{α} atoms and the diamond surface: we observe that further increase of F_{N} on $\Phi = 50\%$ OH covered polar diamond eliminates any partial desorption of the peptide off the surface. The peptide approaches to the surface ensuing an increase in the N_{HB}. Actually, since the spider silk fragment comprises of mainly glycine monomers (7 out of 15), the main contribution to the N_{HB} comes from the backbone groups of the spider silk fragment. To illustrate this, in Fig. 2.12 contributions of the side chain and the backbone to N_{HB} are given separately for two criteria given before. HBs between the backbone and the surface are dominant to side chain HBs for all normal forces considered here, and both contributions reach almost a saturation level for normal forces around $F_{\mathrm{N}}/N \simeq 200$ pN as shown in Fig. 2.12. However, we should note that for a peptide mainly composed of hydrophilic side chains, for high enough normal forces, the side chain HBs can be dominant as we will show later. Also note that, as shown in Fig. 2.12, N_{HB} is increasing regardless of the criteria used for HBs. As a consequence of decreasing vertical distance, which is the reason of increasing

N_{HB}, the peptide-surface interaction energy also decreases as shown again in Fig. 2.12. Here, the short-range Coulomb and Lennard-Jones energies per monomer are calculated separately within a cut-off radius of $r = 0.8$ nm: The closer the peptide is, the lower the interaction energies are. We should note that the ongoing increase in Lennard-Jones energy for the normal force $F_{\mathrm{N}}/N \simeq 400$ pN might be due to hard-core r^{-12} term of the Lennard-Jones potential between the peptide and the surface atoms. Another important point to underline is that the increase of the surface-peptide HB number, N_{HB}, is due to flattening of the peptide. As the peptide forms more HB with the polar surface, it forms less HBs with the water as shown in Fig. 2.13. Although, the partition of HBs change with increasing normal forces, the total number HBs, which is the sum of surface-peptide and water-peptide HBs, is almost constant regardless of normal forces and corresponds to 3 HBs per amino acid as indicated by blue circles in Fig. 2.13.

2.3.1. Home-peptides

In the previous sections, the spider silk protein, which is composed of different amino acids, has been used to investigate the friction dynamics of polypeptides. However, to understand the effect and contributions of distinctive properties of amino acids, homo-monomer chains should also be considered. In Fig 2.14, F_{f}/N and N_{HB}/N for N=11 polyglycine, polyasparagine and for polyleucine obtained on $\Phi = 50\%$ OH covered surface as a function of F_{N}/N are also shown for $V = 0.5$ m/s: For the normal forces below $F_{\mathrm{N}}/N \simeq 90$ pN, the friction forces do not change significantly as the normal force is increased, and the highest friction force is observed for polyglycine as can be seen in Fig. 2.14. This is because the polyglycine chain stays adsorbed on the surface for $V = 0.5$ m/s. Contrarily, the strongly hydrophobic polyleucine chain suffers from desorption off the surface unlike polyglycine (that is why we have less number of data points for polyleucine). For the normal forces $F_{\mathrm{N}}/N \geq 90$ pN, the polyleucine chain partially binds to the surface and less desorption occurs. On the other hand, the polyasparagine with the hydrophilic carboxamide side chains binds to the polar surface, and no desorption occurs for the whole range of normal forces considered here. However, still partial desorption of polyasparagine is observed during the simulations with $F_{\mathrm{N}}/N \leq 90$ pN. We should note that for $F_{\mathrm{N}}/N \leq 90$ pN, the peptide chains have a desorption tendency on $\Phi = 50\%$ OH covered surface except polyglycine for the pulling velocity of $V = 0.5$m/s. This tendency is higher for the polyleucine and polyasparagine chains. One reason for this is that the larger side chains of leucine and asparagine monomers compared to that of glycine make it difficult to reach the equilibrium on this OH covered polar surface for our simulation durations with $V = 0.5$ m/s. Thus, even though asparagine is more hydrophilic than others (meaning more HB with the polar surface), its friction force is lower than that of glycine due to its dangling out-of-equilibrium carboxamide side chains as can be seen in Fig. 2.14. Note that for much slower pulling velocities $V \ll 0.5$ m/s and for lower concentrations of surface OH groups, we expect complete adsorption of these peptides as justified by the data shown in Fig. 2.5 for the spider silk peptide on $\Phi = 11\%$ surface.

On the other hand, for the normal forces above $F_{\mathrm{N}}/N \simeq 90$ pN, no desorption is observed for none of the peptide chains. The friction force increases with the normal

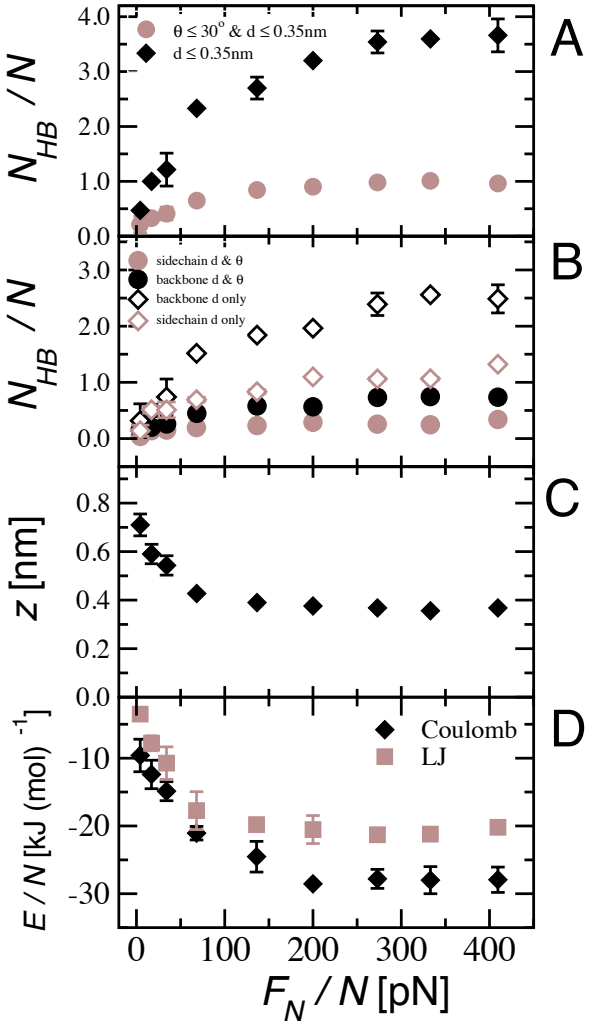

Figure 2.12.: *Detailed surface interactions for N=15 spider silk, A) Average number of HBs per AA obtained via the distance-angle ($\theta \leq 30^o$ and $d \leq 0.35$ nm) and the distance-only criteria ($d \leq 0.35$ nm), B) the side chain and backbone contributions to the latter, C) the average vertical distance between C^α atoms of the peptide and the diamond surface, which is taken with respect to surface C atoms and D) the average surface-peptide (Coulomb and Lennard-Jones) energies per AA for $\Phi = 50\%$ OH covered polar surface as a function of the normal force per amino acid for N=15 spider silk. The pulling velocity is $V = 0.5$ m/s. The Coulomb energy includes only short range contributions within a cut-off distance of $r = 0.8$ nm. Note that in simulations full Coulomb energies including long range contributions are used.*

force and around $F_N/N \simeq 400$ pN reaches almost a saturation level for all peptide chains as shown in Fig. 2.14. Around $F_N/N \simeq 90$ pN, a crossing occurs, and the friction force for polyasparagine becomes larger than that for polyglycine as shown in Fig. 2.14. This transition is due to the increasing contribution of asparagine side chains and backbones

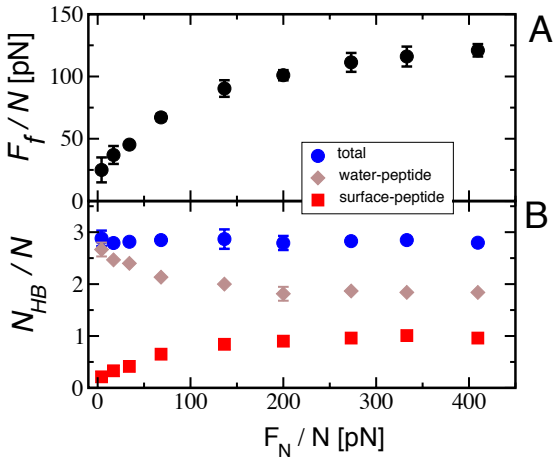

Figure 2.13.: *Partition of HBs for N=15 spider silk A) Friction force and B) average number of HBs per AA as a function of normal force per amino acid on $\Phi = 50\%$ OH-covered polar surface for N=15 spider silk. The pulling velocity is $V = 0.5$ m/s. Diamonds, squares and spheres indicate surface-peptide HBs, water-peptide HBs and the sum of two contributions, respectively. HBs are counted with respect to the distance-angle criteria given in the text.*

into the total N_{HB} with increasing normal forces as illustrated in Fig. 2.14C. This figure shows the separate contributions to N_{HB} from the side chains and backbones of all three corresponding homo-peptide chains. In the following two sections, we analyse the effect of backbone and side chains on hydrogen bonding in detail and classify HBs according to acceptor/donor atoms.

Side Chain and backbone contributions

As shown in Fig. 2.14A, at around $F_{\mathrm{N}}/N \simeq 90$ pN, the friction force for polyasparagine becomes larger than for polyglycine. This crossover is due to the increasing contribution of asparagine side chain HBs with increasing normal force, as illustrated in Fig. 2.14C. The number of HBs from the asparagine backbone also increases with rising normal force, but always stays below the backbone contribution obtained with glycine. For the entire normal force range, the polar side chains of polyasparagine form more HBs with the surface than its backbone groups. Although both polyglycine and polyleucine have equal number of polar groups on their backbones, polyglycine forms more HBs with the surface. Apparently, the large non-polar polyleucine side chains block the polar backbone groups from forming HBs. Increasing normal force pushes the polyleucine backbone towards the surface, and the backbone polar groups finally form HBs with the surface for normal forces $F_{\mathrm{N}}/N \geq 90$ pN, as shown in Fig. 2.14C.

Donor/acceptor contributions

In the geometrical definition of an HB given in Fig. 2.2, the atom which is covalently bonded to the H atom is called the donor, and the third atom is termed acceptor. On

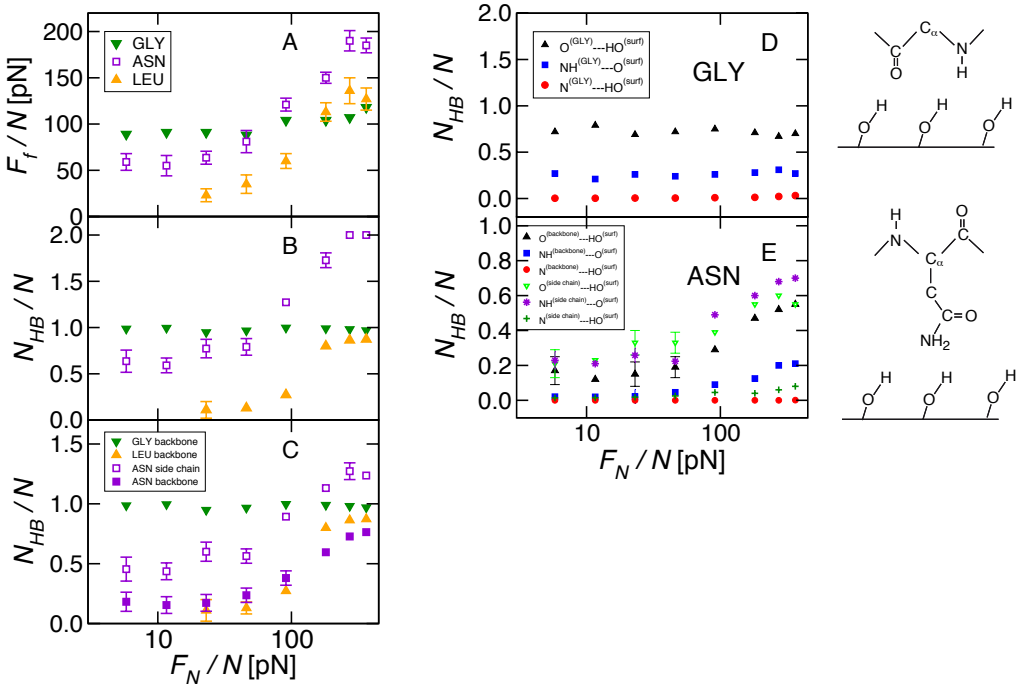

Figure 2.14.: *Friction forces and HB number for N=11 polyglycine (GLY), polyasparagine (ASN) and polyleucine (LEU) homo-peptide chains, A) friction force, B) surface-peptide HB number, C) HB contributions from peptide side chains and the backbone D) from all possible donor and acceptor combinations for N=11 polyglycine and E) for N=11 polyasparagine versus rescaled normal force. All data on the* 50% *OH-covered diamond and the pulling velocity* $V = 0.5$ *m/s. Note that polyglycine and polyleucine have no polar side chain groups.*

the peptide and on the surface, we have various donors and acceptors for HB formation: On the peptide backbone, both O and N atoms can operate as acceptors. The same N atoms can also act as a donor via the NH group. On the surface, the O atom can both be an acceptor and a donor. This means that the backbone (i.e., glycine) can form 3 different types of HBs: NH-O, O-HO and N-HO, where the hyphen denotes a HB. In Fig.2.14D, we show all of these HBs for an N=11 polyglycine chain as a function of the applied normal force. In turns out that the main contribution to N_{HB} is due to 2 types of HBs: NH-O and O-HO. The N atom contributes negligibly as an acceptor to N_{HB}, as shown in Fig. 2.14D. This finding is interesting in light of the value of $a \approx 0.18$ nm for the periodicity of the corrugated potential obtained from the non-linear fitting in the main text, since the average distance of O atoms and NH groups along the backbone is roughly 0.18 nm, which will become more meaningful in the discussion of HB friction in Chapter 5. In Fig.2.14E, we show the results of a similar analysis also for N=11 polyasparagine. Similar to polyglycine, N-HO type HBs have a negligible weight in N_{HB}.

2.3.2. Orientational transition under normal force

As we noted before, polyasparagine has polar side chains, but all these side chains fully contribute to the total number HBs, only when f$F_N/N \geq 100$ pN as shown in Fig. 2.14. For $F_N/N \leq 100$ pN, the N=11 polyasparagine side chains still can form HBs. However, due to the zig-zag order of N=11 polyasparagine, left-handed and right-handed side chains, as depicted in Fig. 2.15C, do not bind isotropically. This is because,the N=11 chain has 5 left-handed and 6 right-handed side chains. When $F_N/N \leq 100$ pN, the polypeptide binds to the surface OH groups through 6 right-handed side chains. As the normal force is increased, the chains is flattened and both right and left-handed side chains bind to the surface. To quantify this behavior, in Fig. 2.15A, we look into the vertical distances between the surface and the asparagine side chains on the $\Phi = 50\%$ OH-covered surface for the velocity of $V = 0.5$ m/s. The center of mass distances of the right-handed z_1 and the left-handed z_2 side chains to the diamond surface are calculated separately, and their difference is given as a function of F_N/N in Fig. 2.15A. For $F_N/N \leq 90$ pN, $(z_1 - z_2)$ difference is higher, which indicates that the asparagine plane is tilted with respect to the surface normal. It is because HB formation is mainly due to the 6 right-sided groups, which are closer to the surface. When F_N/N is increased, the other side chains, previously away from the surface, approach to the surface and contribute to the HB formation together with the backbones. We also demonstrate this situation with two snapshots shown in the inset of Fig.2.15A. Also, in Fig.2.15D, we show two arbitrary snapshots from the same simulation whose data given in Fig.2.15A for $F_N/N = 11.6$ pN. These snapshots explicitly reveal that 5 left-handed side chains dangle in the bulk water whereas other 6 right-handed (or a few of them for this normal force) form HBs with the surface.

Strictly note that this orientational effect emerges as a result of the chain having an odd polymerization degree, N=11, and relatively short size: In the case of an even number of monomers, e.g., N=10, the total normal force would act on both left and right sides of the polypeptide equally. In that case, we can speculate that the binding of side chain polar groups would be more random, either from left or right, and no tilting of the entire chain would be observed. Secondly, a polyasparagine chain having a persistence length equivalent to 5-6 monomers (N=6 polyasparagine cannot collapse as shown in Fig. 2.4), N=11 polyasparagine does not collapse or bend and mostly preserves its "rod-like" configuration on the surface. As a result, this relatively stiff molecule does not desorb off the surface completely unless all HBs break at once. Also, the same effect helps the peptide move laterally on the surface as a single block. As the chain gets longer, this effect should decrease or vanish.

We can also hypothesize that in the case of a hetero-peptide chain composed of polar asparagine and other non-polar monomers, the chain can bind to a polar surface through polar groups of asparagine and exhibits an asymmetric configuration at the surface.

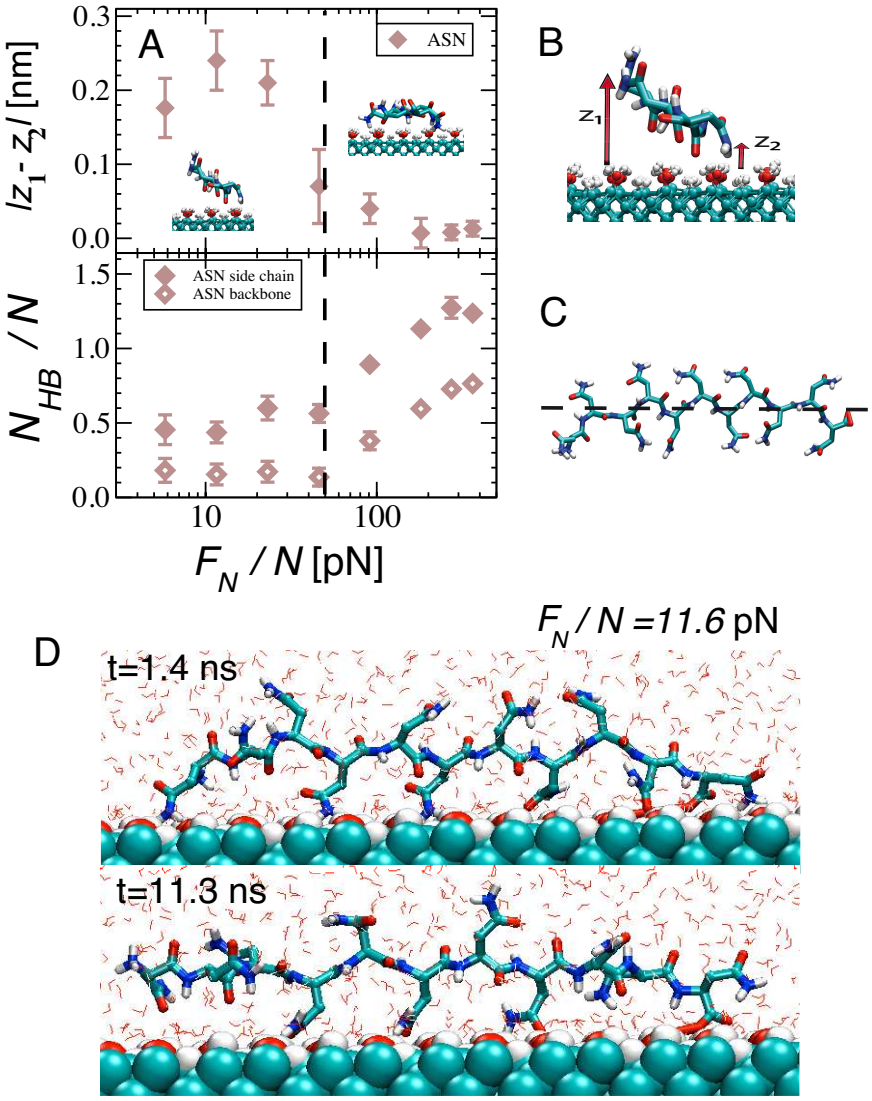

Figure 2.15.: *The average vertical distance difference of center of mass of side chains located at the right and left side of N=11 polyasparagine and the contribution to N_{HB} from backbone and side chain versus normal force per amino acid on $\Phi = 50\%$ OH-covered polar surface. The pulling velocity is $V = 0.5$ m/s. HBs are counted with respect to the angle-distance criteria given in Chapter 2. For snapshots, a few front (from pulling direction) monomers are shown.*

2.4. Conclusion and remarks

In this chapter, using MD simulations, we focus on the friction dynamics of short peptides. In turns out that on polar surfaces, which are capable of forming HBs with the pulled peptides, friction forces are 100-fold higher than those observed on non-polar surfaces. Our findings support the early *in silico* works [123] and experimental finding [45]. As reported previously [123], we also struggled with the difficulty to reach the linear level

friction forces on polar surfaces due to commonly referred computational limits [119, 124].

We also test the effect of normal forces on friction of laterally pulled peptides. We show that increasing normal forces increases the number of atoms of the peptide in contact with the surface. In turn, if approaching groups are polar, normal forces lead to higher friction forces via increasing HB number. As known from macroscopic friction theories, for multi-asperity contact the friction force is $F_{\mathrm{f}} \sim F_{\mathrm{N}}$, and for single asperity contacts, $F_{\mathrm{f}} \sim F_{\mathrm{N}}^{2/3}$. The latter relation actually stems from the fact that the real contact area A_{real} scales as $A_{real} \sim F_{\mathrm{N}}^{2/3}$ and $F_{\mathrm{f}} \sim A_{\mathrm{real}}$. However, in the current problem, we have a polypeptide molecule in contact with a surface, and it is not clear how to define a contact area. Recently, Mo et al. [34] have shown, using a full atomistic model of a AFM tip, that in atomistic scales even a single asperity exhibits roughness and the friction force $F_{\mathrm{f}} \sim A_{\mathrm{real}} = A_{atomic} N_c$, where A_{atomic} is atomic contact area and N_c is number of atoms in contact with the surface. Additionally, for an adhesive contact, A_{real}, namely N_c is non-linear function of F_{N}. Hence, the friction force is a non-linear function of F_N. This problem resembles our case since, as shown in 2.10A, the friction force is a sublinear function of the normal force. Since the ratio of friction force and the number of surface-peptide HB is almost constant for a given pulling velocity, then we write $F_{\mathrm{f}} \approx f_{\mathrm{HB}} N_{\mathrm{HB}}$, where $f_{\mathrm{HB}} = F_{\mathrm{f}}/N_{\mathrm{HB}}$ and is given in Fig. 2.10C. This figure is one of most important result in this work and shows that regardless of amino acid type or surface OH concentration, for a given pulling velocity, friction force distributed into HBs on average equally. Actually, in the following chapter, we use this result to define a more general friction coefficient per HB.

We also demonstrated that increasing friction force by increasing HBs is limited by HB formation capacity of peptides. This means that increasing OH concentration on the surface cannot increase the friction forces once all polar group of adsorbed molecule are saturated by hydrogen bonding. However, since the peptide-surface HB number is determining factor of friction, choosing a more hydrophilic peptide drives the friction force to higher values or vice versa.

As a final remark, we should note, in experiments, friction forces on polar surfaces are reported to be lower than those on non-polar surfaces [25, 111, 125], which contradict our findings. Actually, we observe in our simulations that for OH coverage levels higher than $\Phi = 25\%$, polypeptides desorp off the surface, and they either float ≈ 1 nm above the surface or bind to the surface via 1 or 2 HBs. This is particularly highlighted for N=11 polyleucine, which has no non-polar side chain. This observation can explain the low friction on polar surfaces; molecules cannot bind to the surfaces completely as we have shown here. However, if surface OH levels are decreased down to, e.g., $\Phi \leq 11\%$ as we have here, then we expect very high friction forces, as a result, much lower diffusion coefficients.

Chapter 3

Hydrogen bond friction coefficient

One of the aims of single molecule studies, i.e., protein folding, dDNA/RNA stretching, lateral or vertical pulling of macromolecules on polar surfaces via AFM, is to deduce to equilibrium parameters of corresponding systems, e.g., rates or free energy barriers [37, 62, 71, 76, 126]. Hydrogen bonds (HBs), which are basically the building blocks for those systems and one of the reasons of high force-extension peaks observed in pulling experiments [51, 76], are of notable contribution to the corresponding energy rates considering isoenergetic processes [127], i.e., in the absence of free energy barriers. This means that elucidating the dynamics of HB ruptures, particularly when the act in unison, is a key step to understand the intrinsic time scales of many biologically relevant transitions. To infer the dynamics properties of a single HB via mesoscopic experiments are difficult due to coupled hydrophobic effects, collectivity of multiple HBs and, of course, due to fluctuations in HB number (HB number and collectivity can be coupled), etc. At this level, MD simulations can be employed to understand these effects in qualitative as well as quantitative manner. On the other, due to computational limitations, systems sizes and time scales will be bounded to certain levels. Hence, the system chosen for the MD study should form an ideal layout for the investigation of HBs and also, if it is possible, to be available for experiments. Readily, our peptide-surface systems introduced in the previous chapter fulfil these requirement: pulling a well-defined unstructured peptide chain on a well-defined OH-covered polar surface is an ideal system to unravel the HB dynamics in aqueous media or in confinement. A HB between a peptide and a polar surface provides a more stable and simple geometry compared to internal HBs in a protein globule or in between DNA strands with the differences in the stiffness of HB matrix being noted. Another advantage of using an unstructured peptide chain for MD simulations is that one does not have to worry about biased effect of MD simulations, e.g., the effect of force fields on folding patterns, etc.

In Chapter 2, we show that the main contribution to the friction force on the polar surface is due to hydrogen bonding. In a straight forward manner, friction force data presented previously as a function of velocity allow us to define a friction coefficient per monomer, $\gamma \equiv F_{\mathrm{f}}/(VN)$, on polar surfaces. However, considering structural diversity of

amino acids and complex motifs of which they can form in various systems from helices to strands, a friction coefficient per monomer will be unable to serve as an universal, e.g., system independent, parameter. Hence, in this chapter, we use our conclusion and data from Chapter 2, and define a friction coefficient per HB. Since pulling rates imposed by MD simulations do not allow us to use velocities introduced in experimental setups, which are orders of magnitude lower, we also employ a probability-based model and extrapolate our data to the vanishing force limit. Extrapolations give us the velocity independent, namely viscous, friction coefficient per HB. The workflow of this chapter is as follows: firstly, we present our friction force data as a function of the friction force for various polypeptides pulled on polar surfaces. Following, an equation for the friction coefficient is derived and used to fit our data. Via these fits, we obtain our zero-force friction coefficient per HB. Furthermore, energy scales imposed by our fit equation and analysis of trajectories imply to consider the collective breakage of HBs as also reported for sheered beta-sheets [74].

3.1. Stochastic model for hydrogen bond friction

In Fig. 2.10A and B of Chapter 2, we show that there is a strong correlation between the friction forces on polar surfaces and peptide-surface HB number. Furthermore, Fig. 2.10C shows us that, for a given pulling velocity, average friction force per HB is independent of the monomer type or the surface OH concentration. Spurred by this scaling, we define a friction coefficient per HB as

$$\gamma_{\mathrm{HB}} \equiv F_{\mathrm{f}}/(V N_{\mathrm{HB}}^{\mathrm{eq}}), \tag{3.1}$$

which is shown in Fig. 3.1 as a function of rescaled friction force F_{f}/N for N=11 polyglycine (A) and N=15 spider silk (B). Here, regarding Fig. 2.10B, since the viscous regime ($V < V_0 \simeq 0.002$ m/s) occurs much below the crossover velocity $V_{\mathrm{HB}} \simeq 1$ m/s (above which N_{HB} depends on V), we can safely use $N_{\mathrm{HB}}^{\mathrm{eq}}$, i.e., the equilibrium value of N_{HB} for $V < V_{\mathrm{HB}}$, in order to extract the linear friction coefficient. From Fig. 3.1, it is clear that neither for spider silk nor for polyglycine, the linear-response level, i.e., viscous regime is not reached for our pulling velocities. As we have discussed also in Chapter 2, one needs velocities around $V_0 \simeq 0.002$ m/s to observe the onset of the linear-response plateau, along which γ_{HB} does not depend on the force. In order to reliably extrapolate the data to $F_{\mathrm{f}}/N \to 0$ (and thus to $V \ll V_0$) one needs a theory that encompasses both non-linear and linear friction regimes. Therefore, we introduce a simple stochastic model that describes the full velocity dependence of the friction per HB and allows robust extrapolation of simulation data into the relevant viscous regime for $V < V_0$. Our model is motivated by two observations i) Although the scaling law in given in Chapter 2 by Eq. (2.2) allows to hand-wavingly extract the viscous friction coefficient, it does not describe the crossover from logarithmic to linear friction around $V \simeq V_0$. ii) The more general Schallamach model [8, 39] yields this crossover but contains a handful of fit geometrical parameters, such as the area or the thickness of the junction [39], which are hard to describe for a HB or for an amino acid.

We adopt an early model for the hindered diffusion of a protein along its one-dimensional folding reaction coordinate [68], we consider a single particle in a sinusoidal potential,

$$U(x) = mU_{\mathrm{HB}}\frac{(\cos[2\pi x/a]-1)}{2}, \tag{3.2}$$

where U_{HB} denotes the HB free energy and the cooperativity factor m measures how many HBs break collectively, as depicted schematically in Fig. 3.2A. Now, we derive a friction coefficient for the particle moving along this energy landscape, Eq. 3.2 from the closed-form solution of the Fokker-Planck equation [68, 128]. Fokker-Planck solution, which gives probability of finding the single particle at position x, can be solved exactly for any harmonic potential. The reader can find the full steady-state solution of the Fokker-Planck equation in the Appendix section of this work. At this point, we further continue to introduce the collectivity factor by using Fokker-Planck friction coefficient, whose detailed derivation is also shown in the Appendix section. Suppose there are N monomers, each making a hydrogen bond with the surface, so that a total of $N_{\mathrm{HB}}^{\mathrm{eq}} = N$ HBs form between the peptide and the surface, each moving within its own potential that has a height of U_{HB}, and all moving at a mean velocity V. In the absence of collectivity, and using the definition in Eq. (A.7), the friction coefficient per HB would be given as

$$\frac{\gamma_{\mathrm{HB}}}{\gamma_0} = 1 + \Psi\left(\frac{aF_{\mathrm{f}}}{k_{\mathrm{B}}TN_{\mathrm{HB}}^{\mathrm{eq}}}, \frac{U_{\mathrm{HB}}}{k_{\mathrm{B}}T}\right). \tag{3.3}$$

The main point here is that the total friction force F_{f} produced by all $N_{\mathrm{HB}}^{\mathrm{eq}}$ HBs is equally distributed among the HBs, so that the force per HB is $F_{\mathrm{f}}/N_{\mathrm{HB}}^{\mathrm{eq}}$. When we now introduce collectivity, such that m HBs act in a coherent manner, the friction coefficient per HB reads

$$\frac{\gamma_{\mathrm{HB}}}{\gamma_0} = \frac{N}{N_{\mathrm{HB}}^{\mathrm{eq}}} + \frac{1}{m}\Psi\left(\frac{maF_{\mathrm{f}}}{k_{\mathrm{B}}TN_{\mathrm{HB}}^{\mathrm{eq}}}, \frac{mU_{\mathrm{HB}}}{k_{\mathrm{B}}T}\right). \tag{3.4}$$

Here, γ_0 is the solvent friction, which is taken as $\gamma_0 = 10^{-12}$ kg/s (see Chapter 2). The first term on the right side of Eq. (3.4) reflects the total solvent friction that is not included in the potential, which is proportional to the number of monomers N divided by the number of HBs. The second term on the right side of Eq. (3.4) is due to the friction caused by a quasi-particle consisting of m HBs that move coherently in a corrugated potential with an amplitude of mU_{HB}. The $1/m$ prefactor of the Ψ term is due to the fact that γ_{HB} is defined as the friction coefficient per HB. Again we assume that the total friction force F_{f} is equally shared among all quasi-particles (each consisting of m HBs); there are $N_{\mathrm{HB}}^{\mathrm{eq}}/m$ such quasi-particles, which explains the scaling of the force-dependent argument of Ψ.

In Fig. 3.1B, Eq. (3.4) fits spider silk data quite accurately for $mU_{\mathrm{HB}} = 13.8k_{\mathrm{B}}T$, $a = 0.18$ nm and $m = 3$ (solid black line), for polyglycine in Fig. 3.1A the fit yields slightly adjusted parameters (green solid line). These numbers roughly agree with the scaling-type interpretation of the fit in Fig. 2.5C. The dotted and broken black/green lines denote equally acceptable fits and thus allow to estimate the error in the fit values, the red lines demonstrate that the periodicity a corresponds to a shift along the F_{f}/N

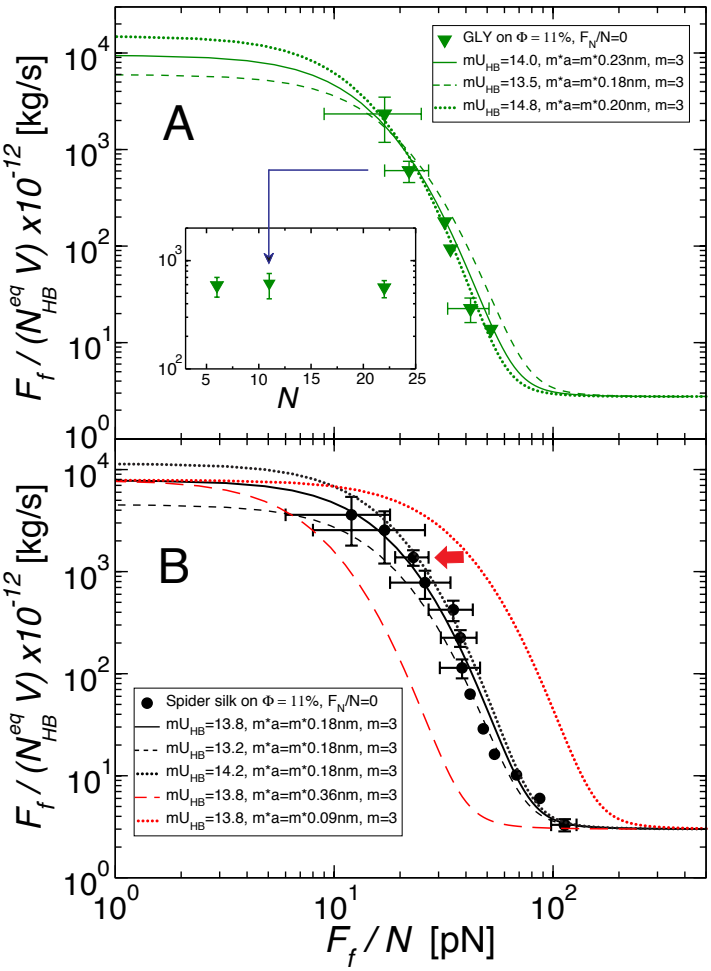

Figure 3.1.: *Comparison of the simulation data for the friction coefficient per equilibrium-HB-number, $\gamma_{HB} = F_f/(VN_{HB}^{eq})$, with the Fokker-Planck solution given in Eq. 3.4 as function of F_f/N. A) $N = 11$ polyglycine for $\Phi = 11\%$ with N_{HB}^{eq} =4, B) $N = 15$ spider silk for $\Phi = 11\%$, N_{HB}^{eq} =5. The data marked by the red arrow is studied in more detail in Fig. 3.5. The inset of (A) shows γ_{HB} versus N for polyglycine and $\Phi = 11\%$ for fixed pulling velocity V =0.1 m/s.*

axis and can be determined with high accuracy. Extrapolation to the limit of $F_\mathrm{f} \to 0$ gives only slightly different values for γ_HB for the two peptides, so we conclude that the viscous friction coefficient per HB is quite generally given by $\gamma_\mathrm{HB} \simeq 10^{-8}$ kg/s. Due to the exponential dependence on mU_HB in the double limit $mU_\mathrm{HB}/k_\mathrm{B}T \gg 1$ and $maF_\mathrm{f}/k_\mathrm{B}TN_\mathrm{HB}^\mathrm{eq} \to 0$, Eq. 3.4 reduces to

$$\gamma_\mathrm{HB} \simeq \frac{\Psi}{m} \simeq \frac{e^{mU_\mathrm{HB}/k_\mathrm{B}T}}{\pi m^2 U_\mathrm{HB}/k_\mathrm{B}T}, \tag{3.5}$$

which indicates that apart from the combination mU_HB, the cooperativity factor by itself, m, is subfluent and influences the functional form of Ψ only mildly (effect of m will

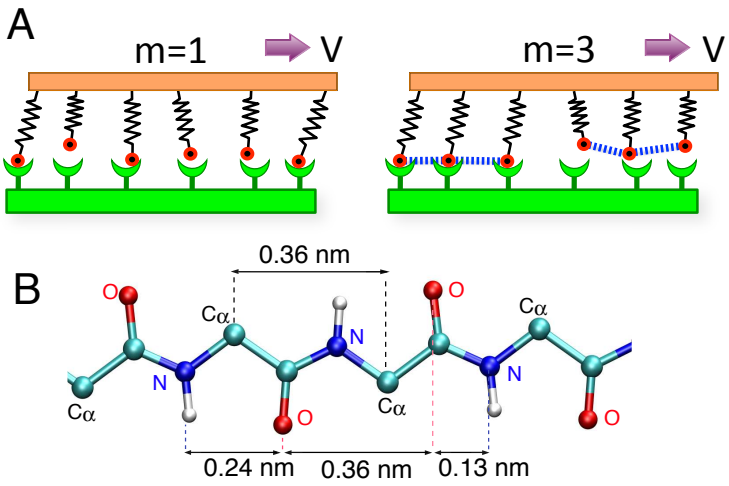

Figure 3.2.: *Illustration of surface-peptide hydrogen-bonding A) In the absence of cooperativity, $m = 1$, HBs act independently; for finite cooperativity factor $m = 3$, three HBs break and reform collectively. B) Per residue there are two main HB contributors on the backbone, the oxygen and the hydrogen connected to the nitrogen; the average distance between HB forming groups is 0.18 nm.*

be discussed in detail in next section). The factor m is introduced mainly to reconcile the surprisingly high value of mU_{HB} with the known (considerably smaller) HB free energy [118], and suggests that m HBs break and form cooperatively upon diffusion of the peptide. It is a-priori not clear whether the activation energy U_{HB} is given by the HB free energy in vacuum, easily reaching $10k_{\mathrm{B}}T$, or by the HB free energy in water, more of the order of 2-3$k_{\mathrm{B}}T$ [118], since HB donors and acceptors are shielded from ambient water by the presence of the peptide on the surface. Assuming an HB activation free energy of $U_{\mathrm{HB}} \simeq 5k_{\mathrm{B}}T$, we arrive at a cooperativity factor $m = 3$, close to what has been seen in force-induced breakage of HB assemblies [74]. To show that finite-size effects are not important and in particular that the cooperativity is not set by the system size, we in the inset of Fig. 3.1A show γ_{HB} for polyglycine of varying size $N = 6, 11$ and $N = 22$ at fixed pulling velocity $V = 0.1$ m/s. The distance between two OH groups on the $\Phi = 11\%$ polar surface is roughly 1 nm, the fit result for the periodicity length scale, $a \simeq 0.18$ nm, turns out to match the distance between HB forming groups on a peptide chain, as shown in Fig. 3.2C. This suggests that when two HB forming surfaces slide against each other, the one with the smaller periodicity will set the effective periodicity a.

Onset of the linear (viscous) regime

In Chapter 2, Fig. 2.5C, we fit the force versus velocity data with a logarithmic scaling law, $F_{\mathrm{f}} \simeq F_0 ln(V/V_0)$, which is an indication of thermally assisted bond breakages.

However, as we noted before, this logarithmic relation cannot explain the onset of linear regime. Indeed, the Fokker-Planck solution can describe both the linear and logarithmic dependence of our data as shown in Fig. 3.1. To emphasize this, in Fig. 3.3, we fit our data with $V(F_\mathrm{f})$ obtained from the inversion of Eq. 3.4 (see Appendix A.2) together with the logarithmic scaling and a linear fit. It is clear that the Fokker-Planck solution can encompass both regimes successfully. Also, note that here we show surface forces per HB, however, for a peptide pulled on the polar surface, most of the friction is due to surface, i.e., $F_\mathrm{f} \simeq F_\mathrm{f}^\mathrm{surf}$. The Fokker-Planck solution analytically leads to the logarithmic scaling for $aF_\mathrm{f} > k_\mathrm{B}T$. Readers, who might be interested in the mathematical connection between the Fokker-Planck solution and the logarithmic scaling law, may consult Appendix A.2 for a complete derivation.

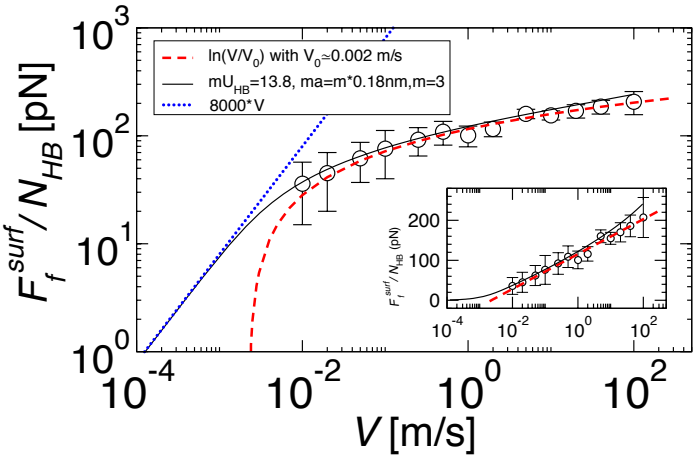

Figure 3.3.: *The surface friction force per hydrogen bond versus pulling velocity for the N=15 spider silk peptide, same data as shown in Fig. 2.5, is fitted with both the logarithmic scaling law Eq.* (A.20) *and the full Fokker-Planck solution Eq.* (3.4)*. The parameters of the Fokker-Planck solution are the same as those used in Fig. 3.1 (black curve), for the logarithmic scaling function we use the parameters $F_0 = 19.0$ pN and $V_0 = 0.0023$ m/s. Note that around $V \simeq 10^{-3}$ m/s, the viscous regime appears in the Fokker-Planck solution and the friction becomes linear in the velocity (dotted line).*

Further analysis of comparativity factor m

As discussed previously, the parameter m is mainly introduced to rationalize the relatively high mU_HB values obtained from the fits. In Fig. 3.4, we show fits for the spider silk data on a $\Phi = 11\%$ surface for various m values between $m = 1$ and $m = 12$. In the fitting process, the curves are forced to intersect as $F_\mathrm{f} \to 0$ and at $F_\mathrm{f}/N = 32.3$ pN in order to isolate the effect of varying m. The resulting curves look very similar except the high-force range close to where the effect of the corrugated potential vanishes altogether. We conclude that m by itself does not influence the dependence of the friction coefficient on the friction force and in particular also not the viscous friction coefficient per HB, γ_HB, in the linear-response limit. This, in turn, means that the collectiveness factor m

cannot be easily determined from friction data unless one has additional information on the equilibrium free energy of HB formation.

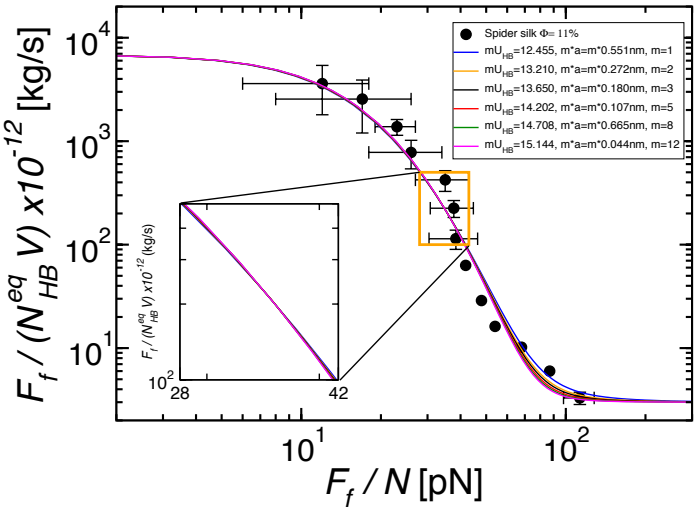

Figure 3.4.: *The spider silk peptide data, already shown in already the Fig. 3.1,* $F_f/(N_{HB}^{eq}V) \equiv \gamma_{HB}$*, are fitted with Eq.* (3.4) *and different* m *values. The inset shows the fitting functions close to the fixed intersection point at* $F_f/N = 32.3$ *pN.*

3.2. Cooperative hydrogen bond rupture

As we have just discussed in the previous paragraph, although the cooparivity of HB rupture manifest itself in the height of the energy barriers, our fit equation, Eq. 3.4, is not sensitive enough to determine the cooparativity factor m. However, as we have revealed in Chapter 2, there is a correlation between HB number (or HB number change) and stick-slip motion. Hence, a closer look at time traces of forces and of HB number can give clues about multiple HB breakages. Therefore, in Fig. 3.5, one typical spider silk trajectory on a $\Phi = 11\%$ polar surface is depicted. Here, time traces of (Fig. 3.5A) the displacement of the pulled terminal aa, (Fig. 3.5B) the instantaneous number of HBs, N_{HB}, and (Fig. 3.5C) the friction force per aa, F_{f}/N, are shown. Slip events in the displacement x correlate with sudden decreases in F_{f}/N and, as shown more clearly in the zoomed trajectories in Fig. 3.5D, with drops in the HB number, are quite similar to stick-slip phenomena in boundary lubrication [121]. In Fig. 3.5E, two snapshots of the peptide before and after a slip event are shown, surface-peptide HBs are marked by ellipses; one can discern that roughly 0.5 nm of displacement of the peptide is accompanied by roughly $\Delta N_{\mathrm{HB}} = N_{\mathrm{HB}}(t + \Delta t) - N_{\mathrm{HB}}(t) = -4$ HBs. Also, from these two snapshots and from Fig. 3.5, one can realize that the peptide chain can be in different states in terms of surface-peptide HBs. This means that the peptide is not completely stretched since, for certain time windows, it has less number of HB than the maximum possible $N_{\mathrm{HB}} \approx 5.5$ (see Fig. 2.5.

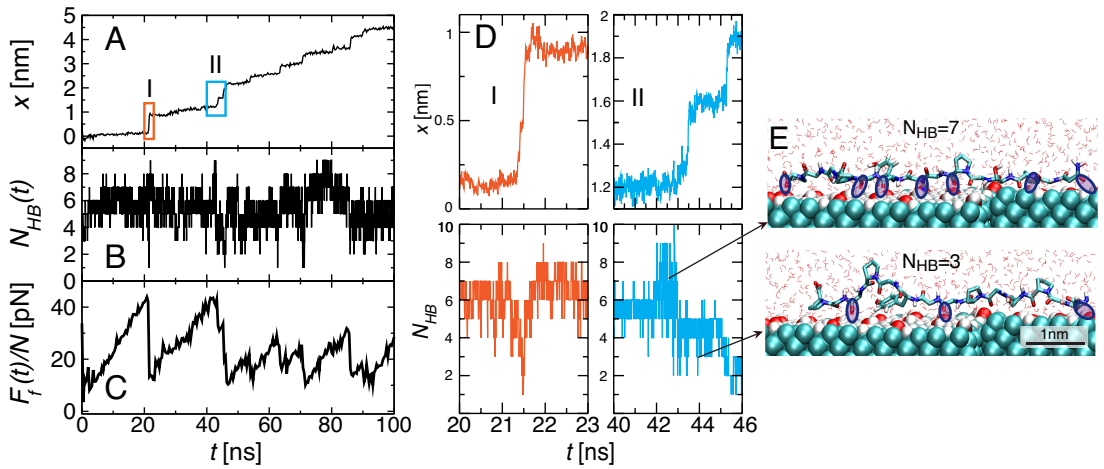

Figure 3.5.: *Simulation trajectory analysis for $N = 15$ spider silk on $\Phi = 11\%$ polar surface for pulling velocity V =0.05 m/s. A) Displacement of the terminal residue, B) surface-peptide HB number N_{HB}, C) friction force as a function of time. D) High-resolution trajectories for the two colored boxes indicated in (A). E) Peptide snapshots at two different times in the trajectory in (D). Surface-peptide HBs are marked by ellipses.*

Tracing the lifetime of a single hydrogen bond

To support our finding that 2-4 HBs rupture together, in Fig. 3.6 we focus on the motion of spider silk peptide on $\Phi = 11\%$ OH-covered surface again. Here in the top frame, three arbitrary jump events that manifest themselves in the displacement of the pulled group are marked and then zoomed in: As followed from Fig. 3.6, each jump in the position of the pulled group is accompanied by a decrease in total number of surface-peptide HBs N_{HB}. And at each jump, the peptide loses 2-3 HBs simultaneously. To emphasize this mechanism, also in Fig. 3.6, HBs existence maps are given: At the beginning of the studied time interval, existing HBs between *ith* amino acid and the polar surface are labelled with residue index of *ith* amino acid, e.g., amino acid index 6 in Fig. 3.6 means either donor or acceptor atom of 6th amino acid forms a HB with the polar diamond surface. Following, lifelines of labelled HBs are tracked until the end of the corresponding time interval. Each red tile represents the presence of a HB, and white ones's are for the absence. These maps confirm that whenever there is a forward motion, 2-3 HBs rupture together. Also, from these maps one can conclude that simultaneously ruptured HBs are close to each other along the peptide chain.

Distribution of hydrogen-bond-number change

To understand the cooperativity better, we analyse the distribution of the temporal change of the HB number , $N_{\mathrm{HB}}(t)$, $\Delta N_{\mathrm{HB}} = N_{\mathrm{HB}}(t + \Delta t) - N_{\mathrm{HB}}(t)$, for N=15 spider silk. In Fig. 3.7, various ΔN_{HB} distributions from the simulations (columns) are given for sampling intervals of $\Delta t = 8, 16$ ps and $\Delta t = 48$ ps. The normalized $P(\Delta N_{\mathrm{HB}})$ distributions (shown as bars) are obtained directly from our simulations. In Fig. 3.7, it

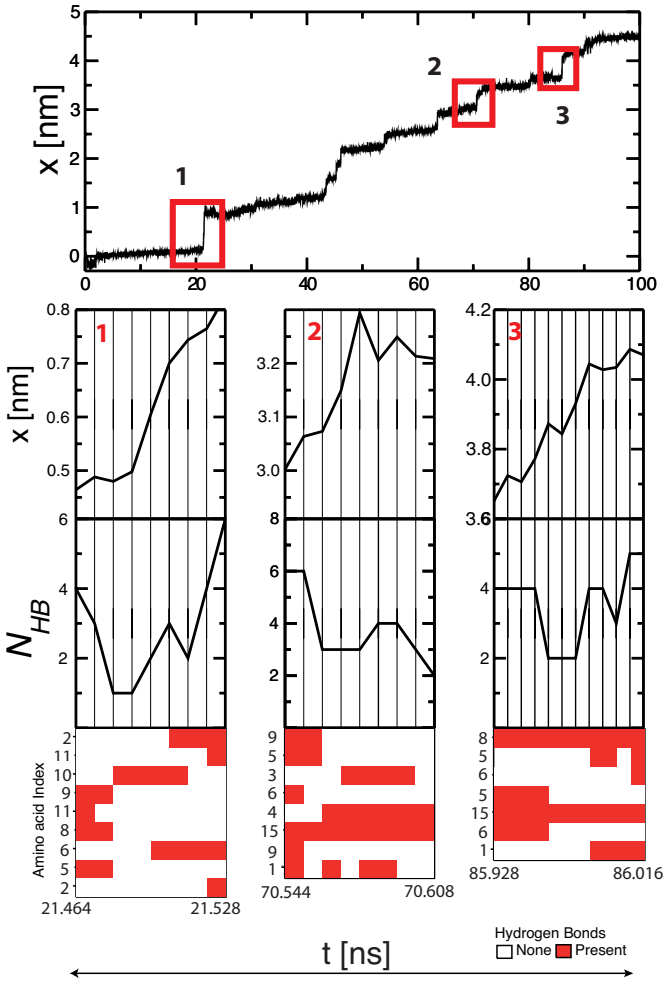

Figure 3.6.: *Three stick-slip events for spider silk peptide N=15 pulled with $V = 0.05$ m/s on $\Phi = 11\%$ OH-covered polar surface. x is the displacement of the pulled group. The time intervals, at which the sudden jumps in displacements and HB numbers show up, are zoomed in. Also, existing maps of HBs between ith amino acid and the surface for the given time interval are presented. For maps, the HBs that exist only at the beginning of the time interval are tracked until the end of the corresponding interval. The time scale between two adjacent vertical lines corresponds to 8 ps.*

is seen that changing the sampling time Δt does not change the distribution. To check whether the HB number change of $\Delta N_{\mathrm{HB}} > 1$ corresponds to the collective breaking of 2-4 HBs or whether the distribution can be explained by the uncorrelated fluctuation of HB numbers, we compare the simulation data with Poisson statistics, derived as following: Assume that HB breaking and forming are each described by a Poisson distribution

$$P(k;\lambda) = \frac{\lambda^k e^{-\lambda}}{k!}, \tag{3.6}$$

where k is the number of bond breaking or formation event and λ is the expectation value. Assuming further that HB breaking and formation are uncorrelated events, the distribution to see a net change of ΔN_{HB} follows as

$$P_{\mathrm{HB}}(\Delta N_{\mathrm{HB}};\lambda) = \sum_{m,k=0}^{\infty} \frac{\lambda^k e^{-\lambda}}{k!}\frac{\lambda^m e^{-\lambda}}{m!}\delta(\Delta N_{\mathrm{HB}} + k - m), \tag{3.7}$$

where the delta function enforces that $\Delta N_{\mathrm{HB}} = m - k$. The summation can be done, and we end up with

$$P_{\mathrm{HB}}(\Delta N_{\mathrm{HB}};\lambda) = e^{-2\lambda} I_{\Delta N_{\mathrm{HB}}}(\lambda), \tag{3.8}$$

where $I_{\Delta N_{\mathrm{HB}}}(\lambda)$ is the modified Bessel function of the first kind. These normalized probabilities are shown in Fig. 3.7 (diamonds). It turns out that the Poisson probabilities are very similar to what we obtain from our simulations, which means that the HB breaking and formation statistics are suggested to be of Poisson nature. The collectiveness we see in the dynamics is therefore not due to collectiveness in the HB breaking statistics (which would mean that a collection of m HBs are more prone to break together than one-by-one even when there is no pulling), but rather, the collectiveness seen in the friction data is produced by the coupling of peptide motion to HB bond breaking: only when a minimal number of HBs are broken, can the peptide move. This suggests that slip-producing HB breaking events, associated with $\Delta N_{\mathrm{HB}} \pm 3$ according to our friction analysis, make up only a small fraction of all HB breaking events.

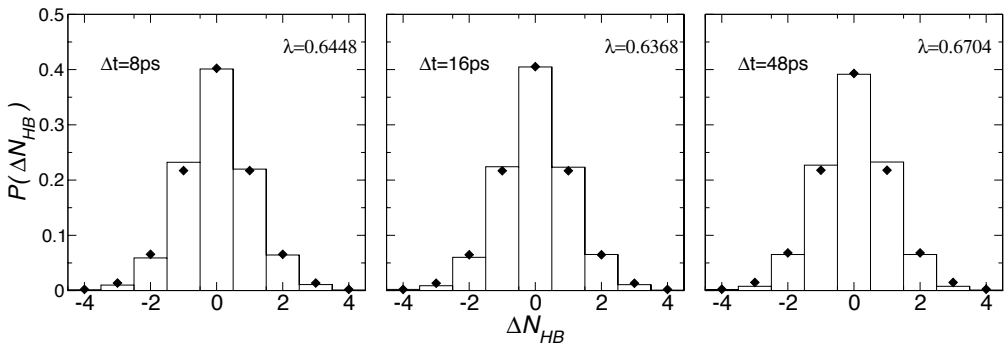

Figure 3.7.: *Normalized HB number-change distribution $\Delta N_{HB} = N_{HB}(t + \Delta t) - N_{HB}(t)$ for sampling time steps of $\Delta t = 8, 16$ ps and $\Delta t = 48$ ps for the N=15 spider silk peptide on a $\Phi = 11\%$ OH-covered polar surface. The pulling velocity is $V = 0.05$ m/s. Vertical bars denote the simulation data, diamonds denote predictions from a Poissonian analysis (see text).*

3.3. Conclusion and remarks

Based on solvent-explicit MD simulations for a peptide sliding over polar surfaces, performed for a wide range of pulling velocities from $V = 0.01$ m/s to 100 m/s, we have established the friction law for hydrogen bonded matter and in particular showed that

the friction force is proportional to the number of hydrogen bonds both in the viscous friction regime (where friction is proportional to sliding velocity) and in the non-linear regime for $V > V_0 \simeq 0.002$ m/s.

The viscous friction coefficient per HB turns out to be $\gamma_{\mathrm{HB}} \approx 10^{-8}$ kg/s and thus amounts to the Stokes friction of a sphere with an equivalent radius of roughly 1 μm moving in water. This means that at a biologically relevant velocity of $V \sim 1$ μm/s, the friction force of a single HB is only $F_{\mathrm{f}} \sim 10^{-14}$ N, so that the combined action of 100 HBs would be necessary to raise the force to 1 pN. The time for an assembly of N_{HB} HBs to diffuse over a length corresponding to the contour aN_{HB} is given by $\tau \simeq N_{\mathrm{HB}}^3 a^2 \gamma_{\mathrm{HB}}/(k_{\mathrm{B}}T)$. Taking $a = 0.2$ nm and $\gamma_{\mathrm{HB}} \simeq 10^{-8}$ kg/s we obtain $\tau \simeq N_{\mathrm{HB}}^3 \times 100$ ns, thus for $N_{\mathrm{HB}} = 5$ we obtain a diffusionial time in the order of 10 μs (note that our friction law is not valid for a single HB but only for N_{HB} beyond the cooperativity scale m). This finding is interesting in light of a puzzle in protein folding: while the typical times for the folding of structural motifs such as a 21-residue α helix [129] and the contact formation for 10-residue unstructured proteins [70, 127] are in the 10-100 ns range, protein folding times are typically much larger [130]. As shown above, HB friction associated with the iso-free-energetic diffusive escape from misfolded motifs can easily account for diffusional times in the μs scale.

We finally note that for assemblies larger than the cooperativity scale, HB friction should not be visualized as roughness in a 1D free energy landscape, rather, for proteins it is one contribution to internal friction in a diffusional protein folding picture [69]. HB friction will be most pronounced in β strands and other filamentous structures, since an initial misalignment will have to heal by diffusion. This might explain recent experiments on three-helix-bundle proteins, where mutations cause large changes in folding kinetics without major modifications in the free energy landscape [131].

An important factor determining the friction coefficient turns out to be the cooperativity factor m, since it appears exponentially[132]. For two rather stiff surfaces that can hydrogen-bond, the cooperativity will be higher than when the scaffolding matrices are very loose and flexible. In that sense, the setup chosen by us, one peptide on a stiff surface, besides being efficient from the simulation point of view, constitutes an intermediate case.

Chapter 4

Peptide friction in bundles

In foldable systems, e.g., in proteins or in RNA, friction arises from interplay of the surrounding solvent and internal resistance of the structure against deformations. The former has been studied by tuning the solvent viscosity, whereas the latter, internal friction, is still a source of debate [58, 60]. In equilibrium and non-equilibrium experiments, internal friction (or diffusion coefficient) manifest itself in the pre-factor of the rate equation, which also contains an Arrhenius factor. Hence, when energy barriers for corresponding transition are low, diffusion dominates the kinetics [70, 127]. However, folding/unfolding is a dynamic process, i.e., protein jumps between various intermediate states on the way to the folded state. During this search, individual monomers change their positions, possibly from less confined outer parts of the globule to the interior or vice versa, and dozens of bonds rotate. Conceivably, in such a situation, one expects that the related friction coefficient defined along a reaction coordinate should also be state-dependent [133, 134]. For instance, for proteins with their collapse preceding folding, a fast collapse is followed by a much slower dynamics to search for a correct path for the folded state. In that case, the number of native contacts increases as the final folded state is approached. If the reaction coordinate is defined as the number of any contacts, the corresponding friction coefficient increases a few orders of magnitude down as the native state of the protein is approached [135].

Usually in protein globule, internal friction is an interplay of various non-covalent interactions, i.e., intra-peptide HB or dispersive effect since in such structures, the relative orientations and positions of the monomers or peptide fragment can change fast. To concatenate on the detailed microscopic mechanism of the internal friction, we ask the question of how the confinement of a peptide chain by other peptides changes the dynamics, i.e., friction. We focus on the relative motion of short extended peptide fragments using prolonged Molecular Dynamics (MD) simulations in explicit water to infer the inter-peptide and water-peptide friction dynamics: Peptide chains were pulled parallel and also perpendicular to each other to discern any directional preferences in friction forces. Furthermore, to see how the nearest neighbour-chain interaction affects the dynamics, we stack peptide chains to create peptide bundles. By changing the number of

chains in the bundle, we modulate the confinement. By pulling one peptide out of the bundle with velocities down to the slowest possible MD velocities, $V \sim 10^{-3}$ m/s, we obtain friction forces. A simple stochastic theory supports our simulation results and extrapolates our data to vanishing force limits. We find that friction forces between peptide chains are proportional to inter-peptide HB number for slow velocities. Hence, friction coefficients are given for per HB to generalize the results beyond the glycine monomers used in this work.

Interlude: Description of model systems

In MD simulation setups, k polyglycine fragments with lengths N=10 and N=20 amino acids (AA) in contact with each other symmetrically in their extended configuration are solvated by roughly 1000 SPC (Single Point Charge) [104] water molecules prior to pulling as schematically shown in Fig. 4.2. Throughout this paper, all parallel configurations will be referred as *bundle*. Following, only one of the peptides is pulled from one of its AAs in parallel or perpendicular directions to the other $c-1$ chains, which are kept fixed from only one of their atoms (alpha carbon) to avoid dragging. Since we fix the positions of a single alpha carbon atom of non-pulled peptides, the effect of this position constraints is checked: chosen alpha carbon atom is varied or more than one atom are fixed, but no inconsistency in studied quantities, e.g., in HB number, is observed as long as the number of fixed atoms does not exceed 4 as shown in Fig. 4.1 The pulled and the

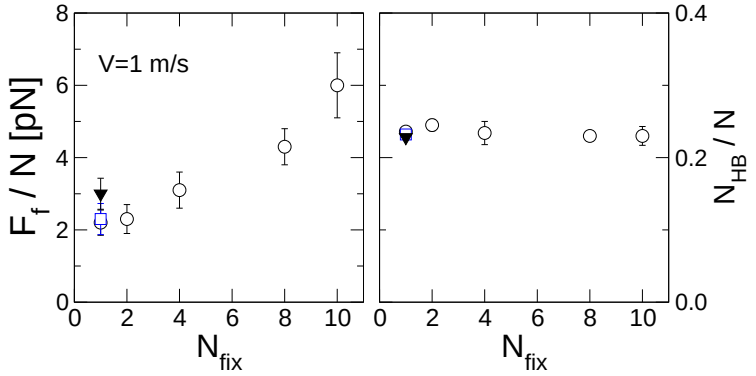

Figure 4.1.: *Rescaled friction forces and number of HBs between 2 parallel N=10 polyglycines as a function of the number of fixed atoms (open-circles), N_{fix}. One of the peptides (non-pulled) is fixed from its alpha carbon atoms via constraining potentials while the other one is pulled with a velocity of $V = 1$ m/s from a single amino acid. The data indicated by the square is the same data used in the main text in Fig. 2 (with a different fixed atom, which indicates that position of fixing does not affect the result). Data point indicated by a down-triangle is obtained via pulling both peptides in opposite direction with velocities $-V/2$ and $V/2$, instead of fixing one of the peptides and pulling the other one with a velocity V: Results for F_f/N and N_{HB}/N are in good agreement with the one-peptide pulling data.*

neighbouring peptide chains are fully periodic, i.e., there is a peptide bond between ith and Nth aas. To obtain a correct peptide bond, N is always taken as an even number

Table 4.1.: *The dimensions of simulation boxes used in our simulations except noted otherwise. Note that systems contain SPC water molecules.*

Peptide	N	System	$(L_x \times L_y \times L_z)$ [nm^3]
2 glycine	10	parallel	$3.5 \times 3 \times 3$
2 glycine	20	parallel	$7 \times 3 \times 3$
2 glycine	10	perpendicular	$3.5 \times 3.5 \times 3.5$
3 glycine	10	parallel	$3.5 \times 3 \times 3$
4 glycine	10	parallel	$3.5 \times 3.2 \times 3.2$
5 glycine	10	parallel	$3.5 \times 3.2 \times 3.2$
7 glycine	10	parallel	$3.5 \times 3.5 \times 3.5$

as can be rationalize in Fig. 4.2A. The sizes of the simulation boxes used for various setups are given in Table 4.1. The initial box dimensions in the directions parallel to the peptide-longitudinal axes are set to $N \times 0.35$ nm, which is roughly the equilibrium extension of the chains. During the simulations, the box length fluctuations are less than 1%. The pulling is performed by connecting a harmonic spring to the center of mass of a single aa, and then the other end of the spring is moved at constant velocities ranging between $V = 2 \times 10^{-3}$ m/s and $V = 50$ m/s as shown in Fig. 4.2A (we note that the lowest velocity is determined by computational capacity): From the average spring extension the average total friction force is deduced. The total friction force is given by the harmonic force $k\Delta x$ on the pulled aa, where k is the force constant of the spring, and Δx is the spring extension. The spring constant is chosen in a way that spring extensions are smaller than half of the box length in the pulling direction: the largest force constant is k=500 pN/nm, and the smallest is k=5 pN/nm. Durations of simulations vary between 10 ns and 2 μs depending on the pulling velocity to obtain long enough peptide displacements with an integration step of 2 fs. Also, each system is equilibrated at least for 1 ns prior to the pulling. Also, alternatively, in a small subset of simulations, we pull the two peptides in opposite directions at velocities $+V/2$ and $-V/2$ and thereby achieve the same relative pulling velocity V. The results shown in Fig. 4.1 are consistent with pulling only one peptide while others are fixed. Hence, we always pull only one of the peptides. For other MD details, same parameter given in Chapter 2 are used.

4.1. Parallel and perpendicular pulling of peptides

4.1.1. Parallel two-peptide systems

First of all, we discuss the relative motion of $k = 2$ parallel polyglycine chains as illustrated schematically in Fig. 4.2A. We pull one of peptides parallel to the fixed surrounding peptide exerting no force perpendicular to the pulling direction. During the pulling, the pulled peptide slides on the fixed one without any desorption since the stretching enhances adsorption [123]. Note that when the chains are non-stretched, they collapse on each other even if their initial configuration are stretched and adsorbed. In Fig. 4.3, we show the friction forces per monomer, F_{f}/N, and the hydrogen bond number between

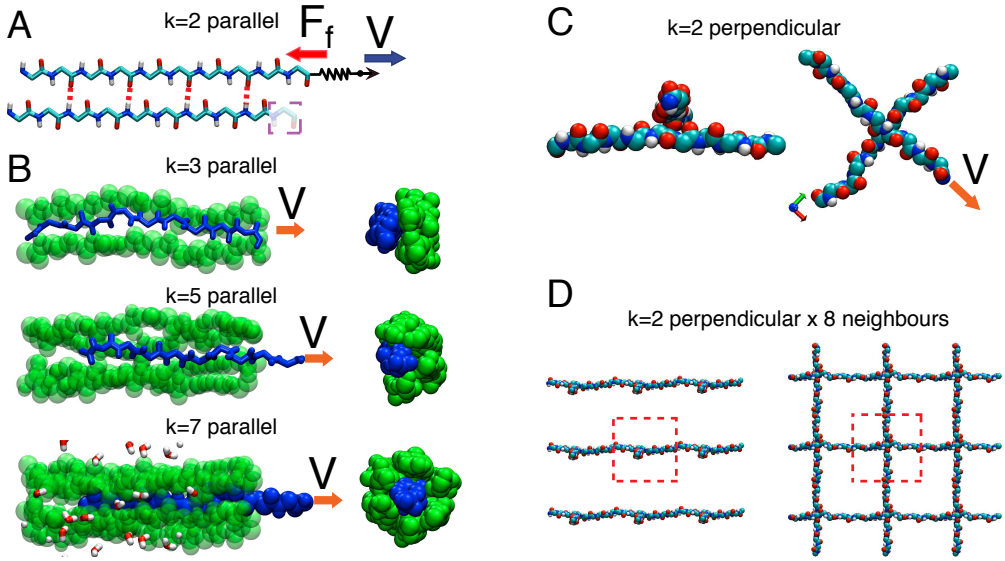

Figure 4.2.: *Illustration of peptide bundles made of periodic N=10 polyglycine chains A) Schematic picture of two-peptide, $k = 2$, parallel system. To obtain the friction forces, F_f, a spring is connected to one of polyglycine chains from a single amino acid, and other end is pulled with a constant velocity V. During the pulling, except noted otherwise, the non-pulled chains are kept fixed from one of their atoms. B) Parallel $k = 3, 5$ and $k = 7$ bundles. The pulled peptides are rendered by dark blue. For clarity, water molecules are not shown, except $k = 7$ case for which a few water molecule around the bundle are displayed for illustration. C) Perpendicular $k = 2$ system D) its periodic images. Original system is framed. All snapshots are generated using VMD.*

two peptides, N_{HB}/N, as a function of the pulling velocity, V, for N=10 (squares) and N=20 (diamonds) polyglycine. F_{f}/N data exhibit a viscous like regime, i.e., it is almost linear with V. However, a single linear fit (solid line) misses the data for $V > 10$ m/s as shown in Fig. 4.3A. This indicates a weak non-linear regime, and will be discussed in following section. If we temporarily consider only slow velocities, this fit gives a monomer friction coefficient $\gamma \equiv F/(NV) = 2.5 \times 10^{-12}$ kg/s, which is of the same order with the bulk water friction coefficient per monomer, $\gamma_0 \simeq 10^{-12}$ kg/s as shown in Chapter 2. Given the fact that $N_{\mathrm{HB}} \approx 2.3$ between two N=10 polyglycines and $N_{\mathrm{HB}} \approx 4.5$ between two N=20 chains, one might expect a more drastic change in the peptide-peptide friction force compared to that exerted on a single peptide in bulk water since HBs are observed to increase the friction for certain systems [45, 46]. However, HBs between two parallel polygycines are exposed to water, which considerably lowers the HB energy compared to vacuum phase [118]. Actually, in the following section, we will show how the isolation of polyglycines from water in bundles significantly increases the friction forces. Contrary to F_{f}/N, N_{HB}/N, which is defined via the Luzar-Chandler angle and distance criterion [108], exhibits a saturation behaviour for velocities below $V \sim 1$ m/s as shown in Fig. 4.3B. As the velocity is increased, N_{HB}/N decreases. This effect is due to decreasing time at the contact points necessary to reform HBs as the velocity is increased also observed in

Chapter 3 for HB between the polar surface and the pulled peptides. Similar effect can be related to the inverse velocity dependencies of number of adhesive contacts (HBs) [8, 39]

Additionally, to see whether pulling of a periodic molecule has any side effects, particularly in HB number, we perform extensive simulations up to 1 μm and 100 ns at $V = 0$ for both parallel N=10 and N=20 two-peptide systems, respectively, after removing all position constrains on their single atoms; namely, both chains in couplets are completely free to diffuse. Two parallel polyglycine chains stay adsorbed to each other for entire simulation durations. The resulting $N_{\rm HB}/N$ data are shown on the very left side of Fig. 4.3B in a non-log scale and consistent with the pulling data obtained with $V < 1$ m/s.

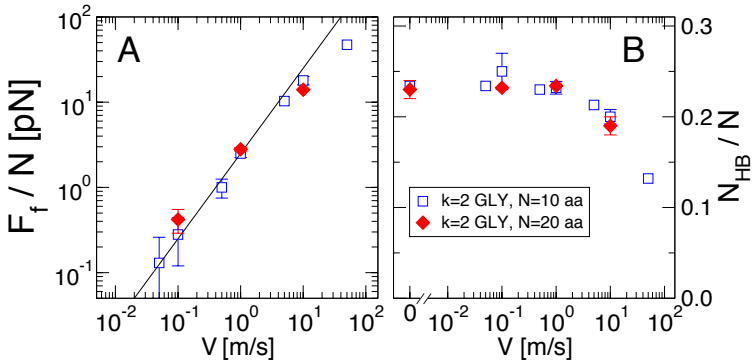

Figure 4.3.: *Friction forces and HB populations between two N=10 and N=20 polyglycine chains one of which is pulled parallel to the fixed chain. Non-pulled chain is kept fixed except $V = 0$ case by applying constraints on one of its atoms. The straight line has a slope of 1 and gives a monomer friction coefficient $\gamma \equiv F/(NV) \approx 2.5 \times 10^{-12}$ kg/s.*

4.1.2. Peptide bundles

In this section, we increase the number of polyglycines in paralel bundles to discern the effect of the nearest neighbouring peptides in friction forces. Since we do not find any difference between N=10 and N=20 polypeptides, we construct peptide bundles of $k = 3, 4, 5$ and $k = 7$ with N=10 polyglycines as illustrated in Fig. 4.2B from side and front (pulling) directions. The pulling is applied on one peptide (painted with dark blue in Fig. 4.2B) parallel to the bundle. Here note that for $k = 7$ bundle, the pulled chain is completely isolated from the surrounding water molecules. As shown in Fig. 4.4, increasing number of peptides in the bundle drastically increases the friction force, $F_{\rm f}/N$: The difference in $F_{\rm f}$ between $k = 2$ (squares) and $k = 7$ (open-circles) for velocities $V \sim 1$ m/s is roughly 2 orders of magnitude. Fig. 4.4 also shows that for $k = 3$ bundle (down-triangles), for velocities below $V \sim 1$ m/s, a linear regime appears similar to $k = 2$ case. For the high velocity regime, friction forces in all bundles tend to converge. Below $V < 10$ ms, for a fixed velocity $F_{\rm f}$ increases with rising k. This is related to the increase in total number of HBs between the pulled and non-pulled peptides, $N_{\rm HB}/N$, as displayed in Fig. 4.3B. As we increase the number peptides in the bundle, c, for a fixed velocity, $N_{\rm HB}/N$ follows this increase. More interestingly, if we rescale $N_{\rm HB}/N$ by the number of

neighbouring peptides, $c-1$, they almost drop on top of each other as shown in Fig. 4.3B. This indicates that each AA of non-pulled peptides, on average, contributes equally to the total HB number. However, almost 2 orders of magnitude difference in the friction force between the parallel $k = 2$ and $k = 7$ bundles cannot be explained by the increase in $N_{\rm HB}/N$. This difference is more easy to see in Fig. 4.5, in which we display the force per HB, $F/N_{\rm HB}$, as a function of the peptide number in the bundle, k, for three velocities $V = 0.1, 1$ m/s and $V = 10$ m/s: For the highest velocity, $V = 10$ m/s (squares), at which $N_{\rm HB}$ enters a decreasing mode as shown in Fig. 4.3B, increasing k has weak effect on $F/N_{\rm HB}$. However, as the velocity is decreased down to $V \sim 0.1$, m/s (circles), almost a 100-fold difference emerges between the friction forces in $k = 2$ and $k = 7$ bundle. On the other hand, $N_{\rm HB}/N$ for $k = 7$ is only 7-fold higher than that for $k = 3$. This notable effect due to increasing k can only be explained by collectivity of HBs, i.e., rupture of HBs in groups rather then one by one. As shown previously in Chapter 4, for surface-peptide systems, this trend can yield drastically high forces. In Section 4.2, we will discuss the possible effects of cooperativity and its relation with confinement in detail. Note that the results presented in Fig. 4.4 correspond to those parts of the trajectories where the structures are intact, i.e., bundles are not deformed.

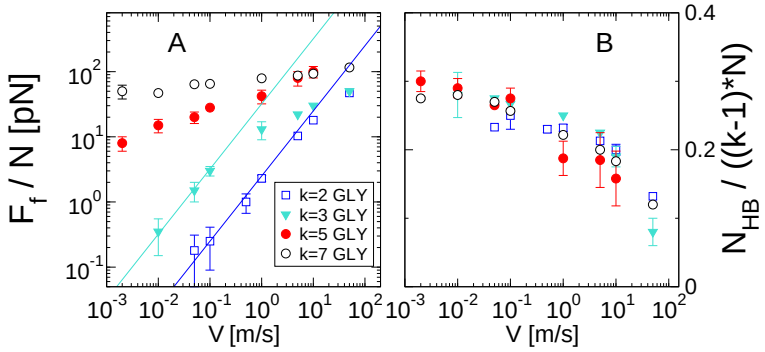

Figure 4.4.: *Friction forces and HB number for N=10 polyglycine bundles; A) Rescaled friction forces and B) HB populations in various parallel N=10 polyglycine bundles. One of the chains is pulled parallel to fixed chains which are kept fixed by one of their atoms.*

As we noted before, the pulled peptide moves either in semi-close cages, e.g., in $k = 5$ bundle or in fully-closed cages such as in $k = 7$ bundle. For pulling velocities, particularly above $V > 5$ m/s, we observe in our trajectories that in semi-closed cases, the bundles get deformed after 2-3 ns, and the pulled peptide reduces the number of neighbouring peptides as shown by snapshots in Fig. 4.6, ensuing a decrease in $F_{\rm f}$ and $N_{\rm HB}$. Therefore, while we deduce average forces $F_{\rm f}$ and average HB number $N_{\rm HB}$ given in Fig. 4.4, we stop considering the trajectories after the first distortion of the initial configuration is observed. In Fig. 4.6A, we explicitly show the time trace of friction force for $k = 5$ bundle at a velocity $V = 10$ m/s; For the first 2 ns, the semi-closed cage keeps its shape. Later, the pulled peptide slides out of its bearing, and the friction force also drops down. Resulting new configurations fluctuate between $k = 3$-like and $k = 4$ -like states as also shown with snapshots taken from the marked instants in Fig. 4.6. For comparison, in

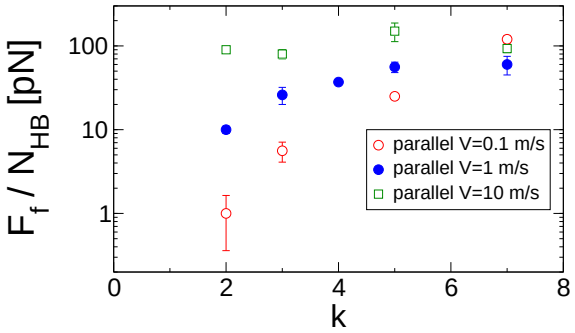

Figure 4.5.: *The ratio of the friction force and HB population data given in Fig. 4.4 for three different pulling velocities as a function of the number of N=10 polyglycine chains in bundles, k.*

Fig. 4.6A, we also display actual time traces of forces for $k = 2, 3$ and $k = 4$ cases, which also confirm the snapshots. One explanation for this behavior is that as the peptide is pulled with high velocities, the hydrophilic interactions, namely N_{HB}, between the pulled peptide and other non-pulled peptides decreases. As a result, hydrophilic interactions among non-pulled peptides is favoured since they do not move relative to each other. We should note that during the course of our simulations, for $V > 5$ m/s, the deformed $k = 5$ bundle never heals back. Also, Fig. 4.6B shows the running averages of the time traces of N_{HB} with 50 ps block sizes. Consistently, when $k = 5$ bundle is deformed towards $c < 5$-like bundles, N_{HB} also drops down in accord with the friction force. But this is not of concern for the low-velocity data, which will form the main result of this paper.

4.1.3. Perpendicular two-peptide systems

As shown in Fig. 4.2C, we also pull two peptide chains perpendicular to each other to infer the effect of peptide orientation in friction. Similar to parallel pulling, the N=10 polyglycine peptide is pulled from a single AA in a way that two peptides stay orthogonal to each other. In Fig. 4.7, the data for both parallel and perpendicular couplets are compared for various pulling velocities. It turns out that friction forces per monomer are almost equal for parallel and perpendicular cases. However, there is significant difference in N_{HB}/N since in perpendicular geometry the contact between two peptides is established via 1 AA or 2 aas.

Also, in perpendicular pulling, the pulled peptide chain desorbs off the other peptide and after a finite time, the peptide either adsorbs back to the same peptide or to the mirror image of the latter in the adjacent periodic box. This results in temporarily zero HB number, and a purely solvent friction force since two peptides have no contact. Therefore, to average the number of HBs between two peptides, time blocks with $N_{\mathrm{HB}}(t) = 0$ are not taken into account. For the same reason, to keep the peptides attached, we applied normal forces, $F_N = 0.12$ pN and $F_N = 1.2$ pN per aa, in opposite directions on both chains (normal to the surface formed by two chains). This data is also given in Fig. 4.7A and B: applied normal forces do not yield a drastic effect in the friction forces neither for $F_N = 0.12$ pN (triangles) nor for $F_N = 1.2$ pN (filled-squares).

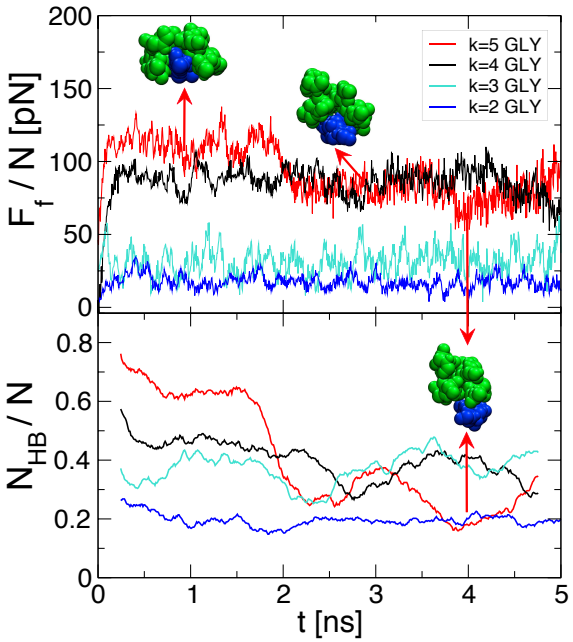

Figure 4.6.: *The time traces of the friction forces and of running averages of HB populations at $V = 10$ m/s for parallel $k = 2$ couplet and $k = 3, 4$ and $k = 5$ bundles made of N=10 polyglycine chains, one of which is pulled parallel to other fixed $c-1$ chains. There is no force acting laterally on the peptide chains, i.e., pulling is performed only in the $\hat{x}-$direction. Snapshots show the various deformed states of $k = 5$ bundle and are taken from the instants marked by arrows. The running averages are calculated for each 50 ps.*

However, N_{HB}/N increases slightly with rising normal forces up to $N_{\mathrm{HB}}/N \approx 0.1$ as shown in Fig. 4.7B. This value indicates that if the peptides are kept attached, the connection of two perpendicular peptides is established on average roughly via 1 HB. From Fig. 4.7A, if we assume a naive linear response, the slope of linear fits give friction coefficients per monomer $\gamma \approx 2.5 \times 10^{-12}$ kg/s for parallel and $\gamma \approx 1.5 \times 10^{-12}$ kg/s for perpendicular couplets. On the contrary, Fig. 4.7B imposes a more than 5-fold difference in N_{HB}/N between parallel and perpendicular cases; again if friction forces scale with N_{HB}/N, one expects a higher friction force for the parallel case. A simple explanation is that although, in the parallel case, N_{HB}/N is higher, in both parallel and perpendicular alignments, HBs break and reform in a similar manner, i.e., one by one, since for two perpendicular peptides, $N_{\mathrm{HB}} \approx 1$. This can be understood best if a single HB rupture is considered to be analogous to the barrier jump problem. Suppose that the barrier has a height of U. Following, the life time of a HB is given, by $\tau \approx \tau_0 exp(U/k_{\mathrm{B}}T)$ under zero external force. However, simultaneously breaking of more than 1 HB corresponds to a higher barrier height since the entire molecule displaces only if all barriers are crossed at once. Consequently, this results in an exponentially increasing life time, i.e., slower dynamics. Hence, comparable friction coefficients of perpendicular and parallel cases already hint that in both cases energy levels are similar and that the N_{HB}/N is not the

only determining factor in peptide friction, but also how HBs break, i.e., collectively or one by one, significantly alters the dynamics. In the following sections, we will discuss the effect of multiple-HB breakage also for $c > 2$ systems in detail.

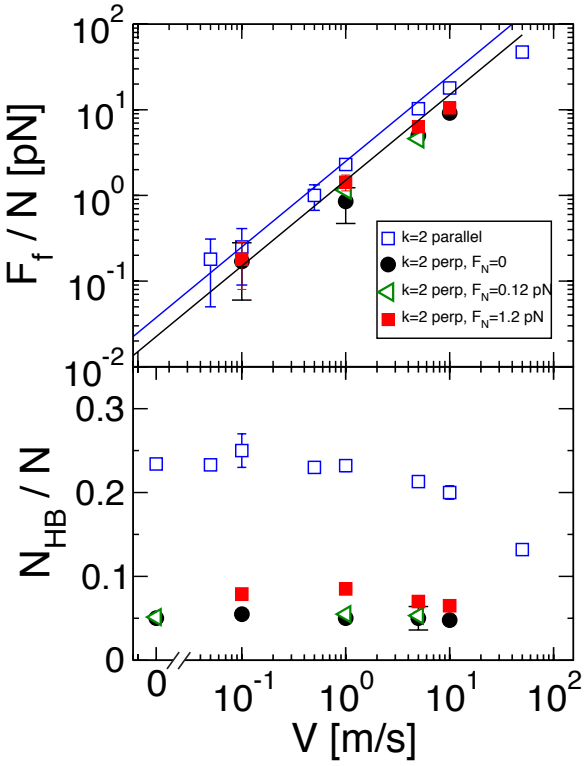

Figure 4.7.: *Friction forces and HB populations between two N=10 polyglycine chains one of which is pulled perpendicular or parallel to the fixed chain. Non-pulled chain is kept fixed except $V = 0$ case by applying position constraints on one of its atoms. The solid and dashed lines have slopes of $\gamma \equiv F/(NV) \approx 2.5 \times 10^{-12}$ kg/s and $\gamma \equiv F/(NV) \approx 1.5 \times 10^{-12}$ kg/s, respectively.*

4.2. Confinement dependent friction coefficients

So far, we have presented the friction forces for our bundle systems for various velocities, which are a few orders of magnitude higher than experimentally adapted velocities. Hence, to be able compare our results with experimental findings and interpret our results in meaningful manner, a friction coefficient per monomer as $\gamma \equiv F/(NV)$ can be defined straightforwardly. However, such a definition will limit our results only for glycine monomers, and naturally more polar or non-polar monomers will not obey such a friction coefficient. For this reason, we define the friction coefficient for per HB as given in Fig. 3.1

$$\gamma_{\mathrm{HB}} \equiv F_{\mathrm{f}}/(V N_{\mathrm{HB}}^{\mathrm{eq}}), \tag{4.1}$$

which is shown in Fig. 4.8 as a function of rescaled friction force F_f/N for all parallel bundles. Here note that instead of N_{HB}, we use N_{HB}^{eq} since for $V < 5$ m/s, $N_{HB} \approx N_{HB}^{eq}$ as can be seen in Figs. 4.3 and 4.4. For parallel c=2 and c=3 bundles, indicated by the same color code used before, the HB friction coefficients, γ_{HB}, reach a linear level, namely they are independent of the force, particularly for $F_f/N < 10$ pN. The plateaus appeared below $F_f/N < 10$ pN confirm that in our simulations for parallel $k = 2$ and $k = 3$ bundles, we accomplish the linear-response level. On the other hand, for $k = 5$ bundle, even with the slowest velocity of $V = 0.002$ m/s we have, γ_{HB} value still cannot reach its plateau. To observe the onset of the linear-response regime, velocities lower than $V = 0.002$ m/s are required, and pulling with slow rates (order of 10^{-6} m/s) is generic limitation in non-equilibrium MD simulations [77, 101, 119]. However, to be able to estimate the friction coefficient at the limit of $F_f \to 0$, we make use of the theoretical approach given in Chapter 4 by Fig. 3.4.

In Fig. 4.8, the Fokker-Planck solution, Eq. (3.4), is used to fit the data for all bundles by using various sets of a and U_{HB} values. It turns out that FP solutions can describe both slow-force plateau and large force regimes of parallel $k = 2$ and $k = 3$ cases accurately. Extrapolations of these curves to the limit of $F \to 0$ give $\gamma_{HB} = 10^{-11}$ kg/s and $\gamma_{HB} = 70 \times 10^{-12}$kg/s for parallel $k = 2$ and $k = 3$ bundles, respectively. Note that for high force regimes, each curve saturates at different values due to the first term in Eq. (3.4). Note that current non-linear fit for $k = 2$ can encompass the data much better than the linear fits in Figs. 4.3 and 4.4. For the $k = 5$ bundle, the FK fit with $mU_{HB}/k_BT = 13.8$ and $a = 0.45$ nm catches the change of the slope towards a linear-response plateau and extrapolates a value of $\gamma_{HB} \simeq 4 \times 10^{-9}$ kg/s as shown in Fig. 4.8. This result is very close to the value obtained via pulling the peptides on polar surfaces discussed in Chapter 4. For the most crowded bundle, $k = 7$, data cannot reach the linear level. However, still after fitting the slope, an estimate for bottom limit of the friction coefficient can be given as $\gamma_{HB} \simeq 10^{-6}$ kg/s. As can be realized from Fig. 4.8 that, as k is increased, to fit our data, the barrier heights, mU_{HB}, have to be increased almost 10-fold from going parallel $k = 2$ to $k = 7$ bundles. Two reasons for the increment in the barrier heights can hypothesized: i) as bundles grow in peptide number, the inter-peptide HBs are gradually isolated from the solvent, which leads to an alteration in the HB energy. This can more clearly seen in Fig. 4.9 in which we give hydrophobic, hydrophilic and total surface accessible area (SAS) as a function of k (see Appendix B.1 for the SAS algorithm). This figure shows that for crowded bundles, the contact with water is almost zero. For instance, in aqueous environment, the single HB energy ranges between $U_{HB} = 2-3k_BT$, whereas in vacuum, it rises up to $U_{HB} = 10k_BT$ [118]. Particularly, in $k = 5$ and $k = 7$ bundles, there happen HB breakages in the absence of water, which requires a higher mU_{HB}. ii) For increasing k, HB collectivity, which we take into account in Eq. (3.4) by defining m, also increases. These two effects are coupled to each other in mU_{HB}. Hence, it is difficult to discern their separate contributions to the energy landscape. However, parallel $k = 2$ and maybe $k = 3$ cases can be exceptional since due to orientations of the polyglycine chains, majority of HB breakages between the pulled and non-pulled chains should occur in the presence of water as can seen in the snapshots in Fig. 4.2

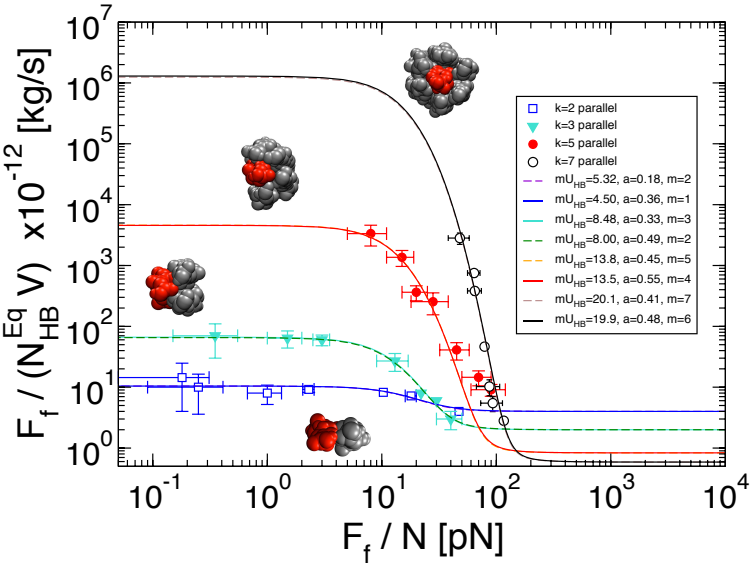

Figure 4.8.: *Comparison of the simulation data for the friction coefficient per equilibrium-HB-number, $\gamma_{HB} = F_f/(VN_{HB}^{eq})$, with the Fokker-Planck solution given in Eq. (3.4) as function of F_f/N. The bundles are constructed with periodic $N = 10$ polyglycine chains, and N_{HB}^{eq} =2.5, 5, 12 and N_{HB}^{eq} =17 for $k = 2, 3, 5$ and $k = 7$ bundles, respectively, and the solvent viscosity $\gamma_0 = 10^{-12}$ kg/s (see Chapter 2). Corresponding representative snapshots for each bundle are also shown from the front (pulling direction) view; the pulled chains are rendered with red. Notice that there are two indistinguishable fits for each data set (dashed and solid lines) on top of each other.*

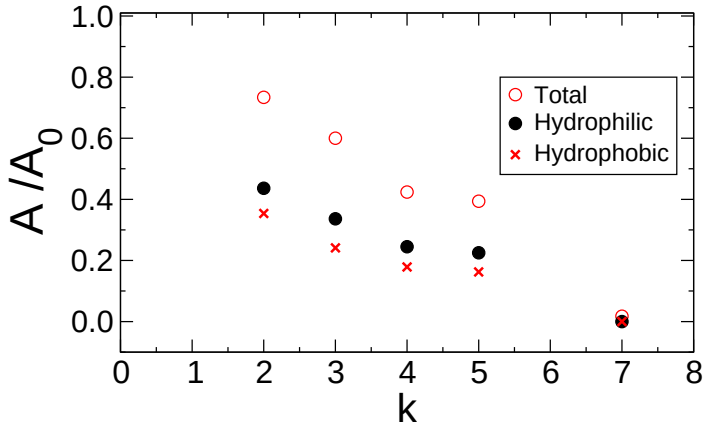

Figure 4.9.: *Rescaled hydrophobic and hydrophilic solvent accessible surface (SAS) [136] areas of the pulled peptide in contact with other parallel N=10 polyglycine in bundles as a function of bundle parameter k (number of peptides in the bundle). A_0 is the SAS for a single N=10 polyglcine in water. Pulling velocity $V = 1$ m/s. Note that when $k = 7$, the pulled peptide has no contact with water. See text for details.*

(see Fig. 4.9 for SAS). In that case, comparison of barrier heights $mU_{\mathrm{HB}} \approx 4k_{\mathrm{B}}T$ and $mU_{\mathrm{HB}} \approx 8k_{\mathrm{B}}T$, which are used to obtain the fits in Fig. 4.8 for parallel $k = 2$ and $k = 3$ bundles, respectively, might be interpreted by choosing $m = 1$ and $m = 2$, respectively. These numbers suggest that for parallel $k = 2$ couplet, $m = 1$ HB break whereas for $k = 3$ bundle, $m = 2$ HBs break in unison. On the other hand, although we give some m values to fit the $k = 5$ and $k = 7$ data, they do not necessarily reflect the nature of HB ruptures in the systems. For instance, $mU_{\mathrm{HB}}/k_{\mathrm{B}}T = 17.6$ can arise due to collective rupture of $m = 2$ HBs with vacuum energies $U_{\mathrm{HB}}/k_{\mathrm{B}}T \approx 9$, or similarly within $k = 5$ bundle, multiple HBs with various energies (in aqueous or vacuum environments) might act together. In fact, our fit equation, Eq. (3.4), which is used to obtain $F_{\mathrm{f}} \to 0$ limit, has a very weak dependence on m. Hence, m does not change the zero-force limit, namely γ_{HB}.

Another fit parameter appeared in Fig. 4.8 is the lattice constant of the model potential. For the m values we choose here, for all curves, they correspond to roughly the size of AA backbone, 0.35 nm. However, as mentioned before, the limit of γ_{HB} for vanishing forces and high enough barriers is independent of a. Also, in Fig. 4.8, we present the fits for all bundles using $m = c$. As we have mentioned, choosing a different m does change the zero-force limit.

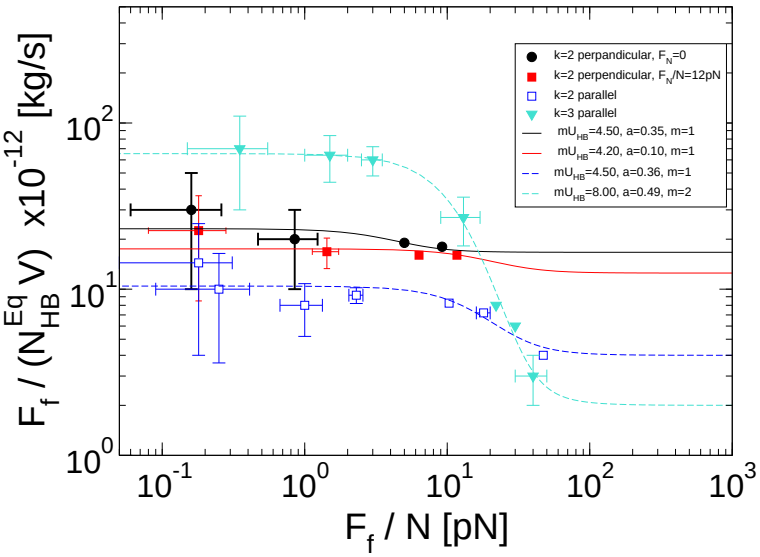

Figure 4.10.: *Comparison of the simulation data for the friction coefficient per equilibrium-HB-number, $\gamma_{HB} = F_f/(V N_{HB}^{eq})$, with the Fokker-Planck solution given in Eq. (3.4) as function of F_f/N. The parallel and perpendicular bundles are constructed with periodic $N = 10$ polyglycine chains, and N_{HB}^{eq} =2.5 and N_{HB}^{eq} =5 for parallel $k = 2$ and $k = 3$ bundles, whereas N_{HB}^{eq} =0.5 and N_{HB}^{eq} =0.8 for $k = 2$ perpendicular cases. The solvent viscosity $\gamma_0 = 10^{-12}$ kg/s (see Chapter 2)*

Another way to infer the collectivity of HBs and understand previously selected m values for bundles is to compare them with the perpendicular pulling, in which collectivity is expected to be weaker due to geometry. Since in the perpendicular orientation, two

peptides cannot have more than 2 HBs (data not shown), naturally m must be $m \leq 2$ as well. In Fig. 4.10, we compare perpendicular cases, $F_{\mathrm{N}} = 0$ (spheres) and $F_{\mathrm{N}}/N = 1.2$ pN (filled-squares), with parallel $k = 2$ (open squares) and $k = 3$ (triangles) bundles. For both perpendicular cases, data extrapolates a value of $\gamma_{\mathrm{HB}} \simeq 20 \times 10^{-12}$ kg/s, which is slightly higher than γ_{HB} of the parallel $k = 2$ bundle but lower than that of $k = 3$ bundle. Also the barrier heights to obtain the fits for perpendicular cases (black and red curves) and $k = 2$ parallel case (blue curve) are all at around $mU_{\mathrm{HB}}/k_{\mathrm{B}}T \approx 4$, which suggest that this parallel $k = 2$ and perpendicular cases have similar energy levels. This brings us to the conclusion that m values are of equivalent for these two systems, and $m \leq 2$ (remind that that for $k = 3$ case, $m = 2$ and $mU_{\mathrm{HB}} = 8k_{\mathrm{B}}T$).

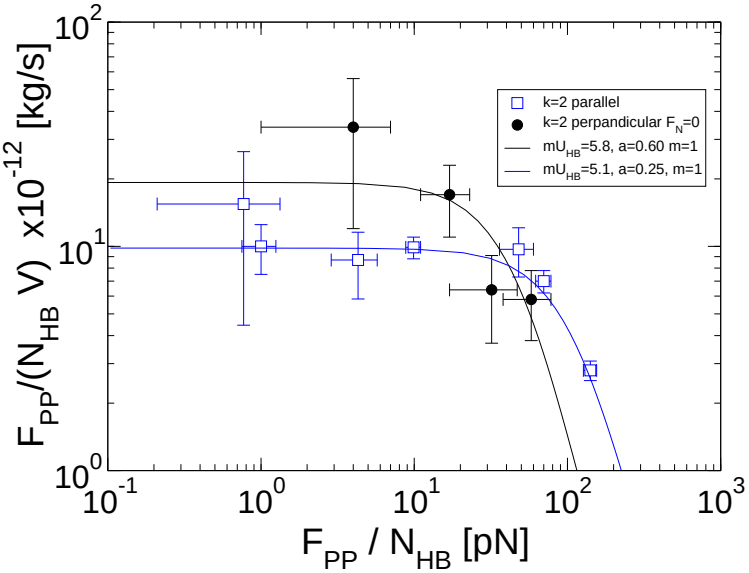

Figure 4.11.: *Comparison of the simulation data for the friction coefficient per equilibrium-HB-number, $\gamma_{HB} = F_{PP}/(VN_{HB})$, with the Fokker-Planck solution given in Eq.* (4.2) *as function of F_f/N obtained by considering only inter-peptide force F_{PP}. Note that for $V < 1$ m/s, $F_{PP} \approx F_f$ for all cases. The parallel and perpendicular bundles are constructed with periodic $N = 10$ polyglycine chains, and N_{HB}^{eq} =2.5 for parallel $k = 2$, and N_{HB}^{eq} =0.5 for perpendicular cases. The solvent viscosity $\gamma_0 = 10^{-12}$ kg/s (see Chapter 2)*

Alternative fitting for parallel $k = 2$ and perpendicular case

We also compare perpendicular and parallel $k = 2$ cases by separating the solvent friction force, F_{sol} and the friction force between two peptides, F_{PP}. For slow velocities $V < 1$ m/s, due to high force fluctuations of low forces (see Tables B.1 and B.2 in the Appendix section), we are unable to give accurate values for individual components. However, after comparison of F_{sol} and F_{PP} for $V > 1$ m/s and for $V < 1$ m/s, we concluded that the inter-peptide friction force roughly dominates the total friction force for $V < 1$ for all bundles (see Tables B.1 to B.4 in the Appendix section). In Fig. 4.11, we give the HB

friction coefficient, but this time, it is defined as $\gamma_{\mathrm{HB}}^{\mathrm{PP}} \equiv F_{\mathrm{PP}}/(VN_{\mathrm{HB}})$, as a function of $F_{\mathrm{PP}}/N_{\mathrm{HB}}$. Again, we can use Eq. 3.4 to fit our the data, but Eq. 3.4, compasses both solvent and surfaces forces. On the other hand, we eliminate the solvent friction force from the total force to define $\gamma_{\mathrm{HB}}^{\mathrm{PP}}$. Hence, for more accurate description of the data in Fig. 4.11, the first term on the right hand of Eq. 3.4, the solvent term, is dropped. In that case, Eq. 3.4 can be rewritten as

$$\gamma_{\mathrm{HB}}^{\mathrm{PP}} \approx \frac{\gamma_0}{m}\Psi\left(\frac{maF_{\mathrm{PP}}}{k_{\mathrm{B}}TN_{\mathrm{HB}}^{\mathrm{eq}}}, \frac{mU_{\mathrm{HB}}}{k_{\mathrm{B}}T}\right). \tag{4.2}$$

In Fig. 4.11, above equation is used the fit data: very similar to Fig. 4.10, barrier heights at around $mU_{\mathrm{HB}} \simeq 5k_{\mathrm{B}}T$ can describe both parallel $k = 2$ and perpendicular data quite well.

4.3. Conclusion and remarks

In Fig.4.12, we summarize our results: vanishing force limits obtained via extrapolation of the Fokker-Planck fits in Fig.4.8 are given as a function of k. Here for entire k range, we use the same value of $U_{\mathrm{HB}} = 2.85k_{\mathrm{B}}T$. However, as we noted before, this value should be considered more like an effective HB energy. Fig.4.12 shows that the HB friction coefficient spans a range of 5 orders of magnitude, depending on the confinement level. For comparison, we also added the $\gamma_{\mathrm{HB}} = 10^{-8}$ kg/s value obtained in Chapter 3 for N=11 pulled on a polar surface. The energy barrier of $mU_{\mathrm{HB}} = 14k_{\mathrm{B}}T$ used in Fig. 3.1 corresponds to $k \times 2.85k_{\mathrm{B}}T$ with $k \approx 4.9$.

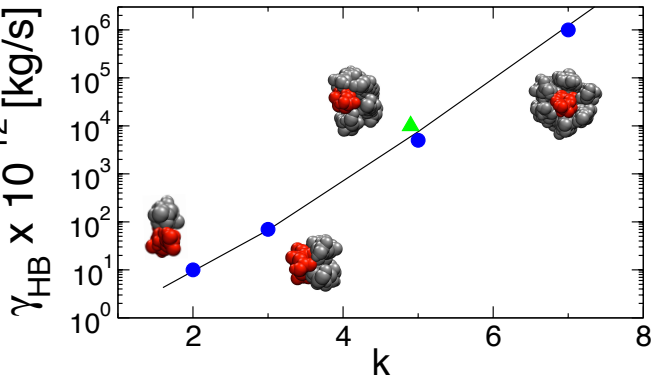

Figure 4.12.: *$\gamma_{HB} = F_f/(VN_{HB}^{eq})$ for parallel bundles obtained via extrapolation of the curves given in Fig. 4.8 as function of the bundle parameter k. The straight line is vanishing force limit given in Eq.* (3.5) *with $U_{HB} = 2.85k_BT$. The data indicated by the triangle is from Fig. 3.1 (triangle) for the peptide-surface system. Note that the barrier height reported in Chapter 4, $mU_{HB} = 14k_BT$ corresponds to $k = 14/2.85 \approx 4.9$.*

Using fully atomistic MD simulations, we obtain friction coefficients for inter-peptide hydrogen bonds as a function of a confinement parameter, k, which is the number of

parallel and perpendicular periodic polyglycine chains in a bundle. Our confinement dependent HB friction coefficient has a range from $\gamma_{\mathrm{HB}} \simeq 10^{-11}$ kg/s for parallel or perpendicular pairs of polyglycines to $\gamma_{\mathrm{HB}} \simeq 10^{-6}$ kg/s for a denser bundle. As k value is increased, the pulled polyglycine is isolated from the solvent due to surrounding peptide chains. Since k is the number of nearest neighbouring (non-bonded) contacts, consequently, k-dependent γ_{HB} can be considered as a position dependent friction coefficient along the corresponding reaction coordinate. Since the friction coefficient is related to the diffusion coefficient, Fig. 4.12 imposes that confinement can slow down the dynamics in the system at least 5 orders of magnitude, from solvent exposed case to completely buried state, at which there is no contact with the solvent.

Also, note that though γ_{HB} for parallel or perpendicular pairs of polyglycines are of the same order, parallel motion has slightly lower friction coefficient, which can favour parallel stacking of peptides more than perpendicular alignments.

This wide spectra of γ_{HB} can also explain the difference between the folding rates of fast folders, such as alpha-helices, and of larger complexes [127]. Additionally, our smallest $\gamma_{\mathrm{HB}} \simeq 10^{-6}$ kg/s value underlines the slow folding phase of large complexes after their initial collapse [137, 138]. Note that friction (or diffusion) coefficient influences the folding kinetic particularly in the presence of flat or low energy barriers, and related to the internal friction of a protein [131].

In polymeric solutions and melts of HB forming chains, inter-peptide friction might affect the viscoelastic properties significantly [139]. As we demonstrated here, parallely aligned multi chains can bear high resistive forces. This is consistent with the high strength observed in glycine-rich complexes [140].

Chapter 5

Peptide mobilities at hydrophobic surfaces

Hydrophobic interactions, which play an important role in protein folding/unfolding processes or in molecular aggregation, can be summarized as the tendency of non-polar units to assemble and form clusters. This complex phenomenon between non-polar molecules depends on variety of parameters, such the size of units, temperature or pressure, i.e., for small solutes with dimension ~ 0.1 nm, entropic effects, or contrarily, for larger solutes, enthalpic effects dominate the hydrophobic effect [141]. Moreover, in the formation of amphiphilic structures, such as micelles, hydrophobic interactions participate in stabilizing the structures. Most of the underlying principles of hydrophobic interactions are understood, at least qualitatively, but still there are controversial issues to quantify these interactions, particularly, their role on folding [142] or misfolding [143] mechanisms. One of the examples is the formation of amyloid fibrils causing Alzheimers' disease: peptide fragments vastly different in sequences come together to form beta-sheet structures [144], which hierarchically yield larger complexes. This suggests that in fibril formation non-specific HBs, i.e., due to backbone groups, and hydrophobic interactions act together.

A subtopic of hydrophobic interaction is the interaction of molecules with non-polar (hydrophobic) surfaces. The interaction with a planar non-polar surface is basically the high-curvature limit of a non-polar solute in water. Unlike the interaction of two relatively small non-polar solutes, non-polar surfaces can hydrophobically attract and interact even with mildly non-polar molecules. For a large class of proteins, the more hydrophobic the surface, the stronger proteins adhere the surface [145]. As a result of strong adsorption on the surface, structured proteins can change their conformations. For instance, an adsorbed protein on a non-polar surface can undergo a reversible denaturation from folded to unfolded state [125, 145].

Furthermore, by tuning the hydrophobicity level of a surface, 2D motion and or motility of polypeptides can be controlled. This is rather important in designing smart surfaces, on which specific molecules can be transmigrated to specific targets across the surface [25]. Another practical aspect of understanding the nature of hydrophobic interactions of

biomolecules is to construct durable body implants, which should interact with tissues without intoxication as if they are a part of the related organ.

In this chapter, we narrow down the topic, and we rather focus on unstructured and pre-adsorbed polypeptides. Since, equilibrium is not issue on non-polar surfaces [56, 123], MD simulation can be introduced safely to understand the quasi-equilibrium motion of various homo-peptides, polyglycine, polyasparagine and polyleucine as well as hetero-peptides such as also spider silk peptide at H-terminated diamond surfaces. In this chapter, friction data previously presented in Chapter 2 will be analysed in more detail using stochastic Fokker-Planck solution given in Chapter 3. Furthermore, conformation of pulled peptide fragments, surface effects and friction contributions and the dissipation mechanisms will be discussed in great detail. We should also underline 2 points i) although the high attraction capacity of non-polar surfaces hamper to observe purely hydrophobic surfaces in nature (due to the same reason, performing experiments on hydrophobic surfaces are equivalently difficult), still a peptide chain on a non-polar surface is an ideal model system to elucidate the detailed nature of 2D surface-peptide interactions ii) Reader should be reminded that, as mentioned before in Chapter 2, we knowingly use the term 'non-polar' for our hydrophobic surfaces since there are no polar groups on the surface. Technically, by changing interaction parameter (of the Lennard-Jones potential), even a flat surface can be made non-polar or polar [146].

5.1. Scaling dependence of monomeric mobility

In Fig 5.1A, we compare the monomer mobilities (inverse friction, see Eq. 2.1) for N=15 spider silk on non-polar surfaces and in water bulk reported by Serr et al. [57] as a function of the friction force per monomer. For all systems, the scaling of N^{-1} is used regardless of the peptide being in bulk or on the non-polar surface. Here we give mobilities instead of friction coefficient unlike previous chapter since the diffusion coefficient can be related to the mobility via $D = k_{\mathrm{B}}T\mu$. From Fig 5.1A, it is clear that non-polar surface mobilities are of the order of bulk mobility with the exception of non-polar data from Serr et al. [57] (gray squares). The reason of the difference between current non-polar and Serr et al. data becomes clear if we fit the data by using the Fokker-Planck description also used before in Chapter 3. For the surface potential, again, a periodic potential in the form of $\tilde{U}(x) = \tilde{U}_0/2[\cos(2\pi x) - 1]$ is preferred, where $\tilde{U}_0 = U_0/k_{\mathrm{B}}T$: for data sets of Serr et al. [57] given in Fig 5.1A, a curve obtained with $\tilde{U}_0 = 3$, $a = 6$ nm describes their data very well. Here we should underline that in these simulations the gap between two adjacent periodic diamonds of sizes 6 nm in the pulling direction manifests itself in the lattice coefficient. Other way of saying, this gap generates a potential with a wavelength of 6 nm. Therefore, their mobilities are lower than the results of the current work (brown down-triangles), where the diamond is gapless in all directions. Extrapolation of bulk and non-polar surface data shown in Fig 5.1A to the limit of $F_{\mathrm{f}} \to 0$ ($V \to 0$), which is relevant to the linear-response limit, gives a non-polar surface monomer mobility, for both our simulations and for Serr et al. [57] bulk data $\mu \simeq 100 \pm 30 \times 10^{10}$ s/kg (note that they predicted $\mu \simeq 90 \pm 30 \times 10^{10}$ s/kg). For the lowest pulling velocities, we should

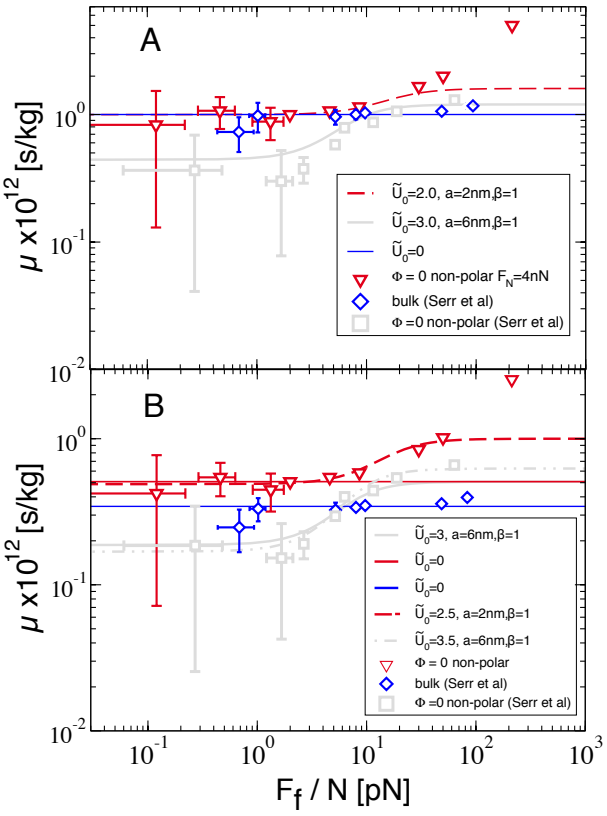

Figure 5.1.: *A) Monomer mobilities of spider silk peptide on the non-polar surface and in bulk water obtained via pulling simulations are compared with the numerical solution of Fokker-Planck equation given in Eq. A.7. The surface potential is given by Eq. A.1. The number of monomers, $N = 15$. For all cases $F_N = 0$. For mobility calculations Eq. 2.1 is used, and data for non-polar surface (grey squares) and for bulk are taken from Serr et al. [57]. The diamonds used for non-polar surface data have dimensions of $8nm \times 8nm \times 1.8nm$. For the monomer mobility μ, the scaling law N^{-1} is used for all cases. B) Same data presented in (A) except this time scaling laws are taken as $N^{-3/5}$ for bulk, $N^{-3/4}$ for the non-polar surface.*

emphasize that due to the very low friction forces, the peptide changes its conformation rapidly as we discussed in Chapter 2 and moves along $\hat{y}$-direction as well (due to the surface anisotropy, which will be discussed next). For the same reason, at low velocities, error bars in the force data also get larger, and to decrease the error bars, much longer simulations should be conducted. However, within the error bars and by considering overall range of data points, our extrapolation is well-founded.

In Fig 5.1A, the scaling law N^{-1} has been used for non-polar surface and for bulk. This yields that, considering motion of the whole peptide, the chain exhibits equal mobilities (or diffusion coefficient) in bulk and on non-polar surface. However, that does not mean that motion of individual monomers shares this property. Therefore, in Fig 5.1B, unlike in

Fig 5.1A , we use scaling laws obtained in Figs 2.6 and 2.3 : $N^{-3/5}$ for bulk and $N^{-3/4}$ for the non-polar surface to get more insight about the effect of surface on monomer mobilities. As shown in Fig 5.1B, the peptide monomer is more mobile on the non-polar surface compared to the bulk as $F_f \to 0$; the monomer mobilities are $\mu \simeq 35 \pm 5 \times 10^{10}$ s/kg and $\mu \simeq 50 \pm 15 \times 10^{10}$ s/kg for bulk and the non-polar surface, respectively. That might be attributed to two factors: i) The non-zero slip length of the diamond surface: A slip length of 2 nm for the diamond [146] allows peptide monomers to move faster on the non-polar surface ii) The less water-peptide contact area of the adsorbed peptide at the surface: When the peptide chain is adsorbed on the surface, it loses a certain amount of contact area with water, and during its motion less amount of water dragged compared to the bulk motion. Our findings suggest that the surface dispersive forces compensates the absence of solvent forces (or cannot in the cases the non-polar mobility is higher than that of bulk). Note that if the Serr et al. [57] data is revised with scaling laws used for our data, it also gets smaller (grey squares in Fig 5.1B).

Finite size effect: Deviations at high pulling velocities

We would like to discuss briefly a finite size effect that emerges particularly when the peptide is pulled with high velocities, $V > 10$ m/s, or equivalently $F_f \approx 10$ pN. As recognized in Fig 5.1A and B, the surface monomer mobilities increase abruptly above $F_f/N > 10$ pN. This is because, at high pulling velocities, the peptide induces an artificial shear flow in the $\hat{x}$-direction, namely the relative velocity of surrounding water in the pulling direction is higher than it has to be. Since the simulation box is periodic in all directions, this induced flow decreases the solvent friction. To illustrate this effect, in Fig 5.2A, we give velocity autocorrelation functions for N=15 spider silk peptide with respect to the water cluster around the peptide. The water cluster is defined in a way that it contains all water molecules around the peptide within the radius of 1 nm. This cluster is dynamic, i.e., as the peptide moves, water molecules can enter or exit this cluster. In an ideal case, the normalized autocorrelation function should decay fast since individual water molecules are not dragged by the peptide to distances longer then the box dimensions. However, as shown in Fig 5.2, for $V = 1000$ m/s (F_f/N=200 pN) and $V = 100$ m/s (F_f/N=50 pN), the velocities are very correlated unlike $V = 10$ m/s (F_f/N=10 pN) case. If we make a rough estimate by taking the decay time as the time at which autocorrelation function decays down to e^{-1}, the decay time is roughly 80 ps for $V = 100$ m/s, and during this time window, the peptide moves 8 nm. This distance is also the length of the simulation box in $\hat{x}$-direction. Therefore, when the peptide reaches the next periodic box, there will be still a flow generated by the previous image of the peptide. And this effect increases the mobility artificially, i.e, decreases the solvent friction since it depends on the relative velocity of the solvent with respect to the peptide. Also in Fig 5.2 for $V = 50$ m/s, we presented the friction forces for two different heights of the simulation box. It turns out that the smaller box height is, the higher the friction force is. This indicates that, when the upper image of the diamond (due to periodicity) is closer to the original system, the induced water flow in $\hat{x}$-direction diminishes.

Our non-polar data (brown triangles) in Fig. 5.1A and B can also described by a

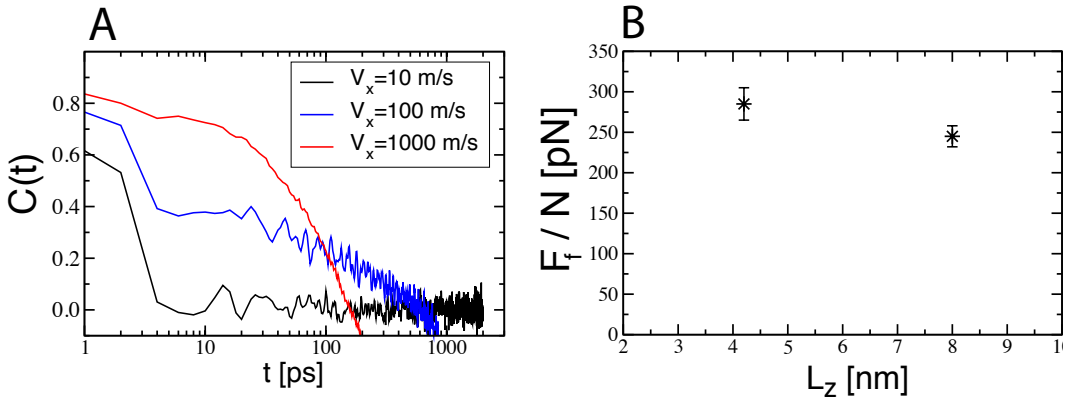

Figure 5.2.: *Finite size effect due to high pulling velocities. A) The normalized autocorrelation function of the peptide velocity with respect to a group of water molecules for different pulling velocities in $\hat{x}$-direction . These water molecules are within the range of 1 nm with respect to the peptide. The longer decay length (the time correlation function drops a factor of e), the higher velocity of the artificial flow in the next periodic box. The system is the N=15 spider silk on the non-polar diamond. Note that $V = 10$ m/s simulation is much longer than other 2 simulations. For other two velocities, statistics is not sufficient for longer times. B) The total friction force for with N=15 spider silk peptide versus the height of the simulation box in $\hat{z}$-direction for $V = 50$ m/s on the non-polar diamond surface. The diamond slabs have dimensions of $8nm \times 8nm \times 1.8nm$. The size of fully stretched peptide is around 4.5 nm.*

potential height of $\tilde{U}_0 = 0$ (solid lines) as long as the data points above $F \simeq 10$ pN are neglected. For this alternative fitting, the conformation of the peptide on the surface should be considered as a limiting factor: Pulling should not disturb the peptide chain under consideration of the linear response. This leads, with simple scaling arguments, If the chain has an unperturbed radius R_0, to a pulling force of $F_\mathrm{f} \approx k_\mathrm{B}T/R_0$ not to stretch the peptide completely. For our cases $R_0 \approx 1$ nm, which corresponds, with $k_BT = 4.14$ pNnm, a friction force of around $F \approx 4$ pN. Hence, above this force, the peptide feels the pulling and is stretched. However, we should underline that neglecting the data above $F \simeq 4$ pN does not affect the zero-force (linear-response) mobility estimates presented in Fig. 5.1A and B.

5.2. Effect of monomer size on mobility

In Fig. 5.3, the monomer mobilities obtained from terminal pulling simulations for N=11 polyglycine, polyasparagine, polyleucine and N=15 spider silk peptide on the non-polar surface are given with the scaling law $N^{-3/4}$. The monomer mobilities deduced from home-peptide chains show a similar behavior to the previously presented spider silk data, also shown in Fig. 5.1B. Among these three homo-peptides on the non-polar surface, the mobility of the glycine has the highest mobility. Using the exact solution of Fokker-Planck solution, Eq. A.7, as in spider silk case, the non-polar surface mobilities given in Fig 5.3 can be described with $\tilde{U}_0 = 0$, if the data for $F_\mathrm{f} \geq 10$ pN are not taken

into account. Extrapolated zero-force mobilities have an order of glycine > asparagine > leucine on the non-polar surface. As shown in Fig 5.3, the spider silk (averaged) monomer mobility is closer to the glycine mobility (black open-right triangle) since spider silk is mainly composed of glycine. Interestingly, the only asparagine bulk mobility value (black square) in Fig 5.3 for $V = 1$ m/s is almost equal to the non-polar surface mobility for the same velocity. This means that the bulk diffusion coefficient of asparagine is almost equal to that on the non-polar surface unlike spider silk for which non-polar monomer mobility is higher as shown in Fig 5.1B.

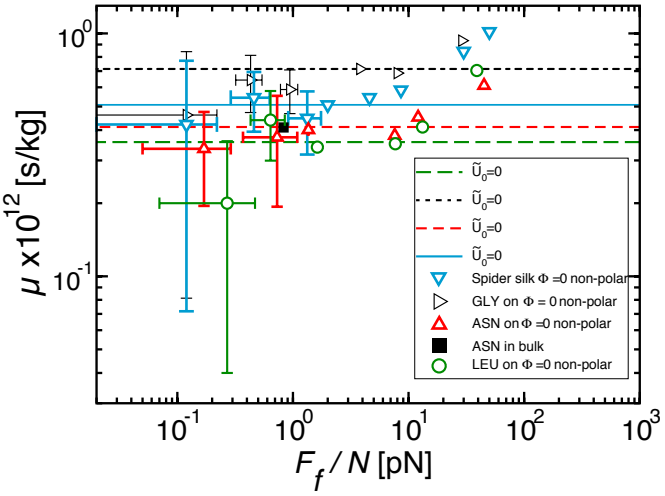

Figure 5.3.: *Monomer mobilities of N=11 polyglycine (GLY), polyasparagine (ASN), polyleucine (LEU) homo-peptides and N=15 spider silk obtained from pulling simulations on the non-polar surfaces and in bulk. The scaling laws are taken as $N^{-3/5}$ and $N^{-3/4}$ for bulk and non-polar surfaces, respectively. For all cases $F_N = 0$. For mobility calculations Eq. 2.1 is used. The lines are fits with $\tilde{U}_0 = 0$ by using Eq. A.7.*

Additionally, the order in the mobilities for the homo-peptides is consistent with their adsorption forces on the non-polar surface: We performed vertical pulling simulations for $N = 11$ chains with a velocity $V_z = 0.1$ m/s. Resulting forces in the $\hat{z}$-direction are shown in Fig. 5.4. It turned out that leucine monomers have the highest plateau force (F_z =90 pN) compared to glycine and asparagine, whereas glycine's (F_z = 40 pN) and asparagine's (F_z =50 pN) are close to each other. This indicates a correlation between adhesion and friction. However, we should note that adhesion energies at polar surfaces are similar to those at non-polar surfaces [57]. Our findings here underline that at least the correlation holds only when non-polar surfaces are considered.

5.3. Underlying dissipation mechanisms

As we have shown in previous sections in Figs. 5.1 and 5.3, on hydrophobic surfaces, the surface mobility is very close to the bulk mobility. Main reason to this is the low surface

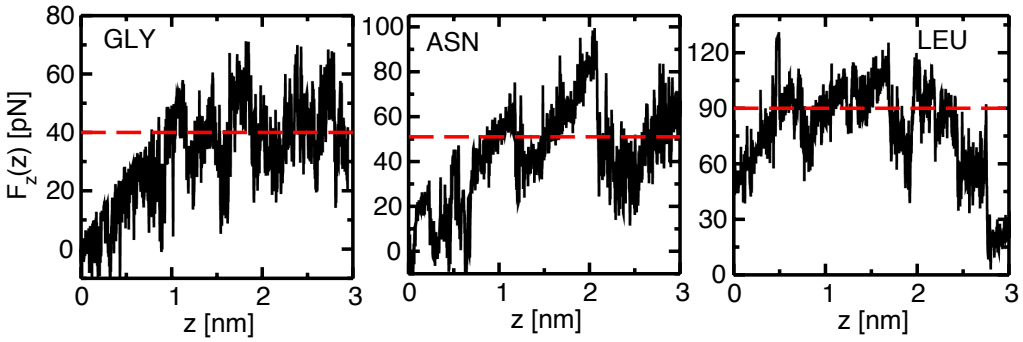

Figure 5.4.: *Vertical spring force as a function of the tip position for N=11 GLY, ASN and LEU chains on the non-polar surface with a pulling velocity of V_z =0.1 m/s. Lines indicate averages. The sudden decrease for polyleucine is due to the desorption of the entire molecule.*

contribution to the total friction force as we display in Fig. 5.5 for N=15 spider silk. For comparison, we also show the surface contributions on $\Phi = 11\%$ OH-covered surfaces. It is clear that for the velocity ranges considered here, solvent is the main source of dissipation on hydrophobic surfaces. For velocities above $V = 10$ m/s, the solvent effect in friction further increases regardless of the surface being polar or non-polar.

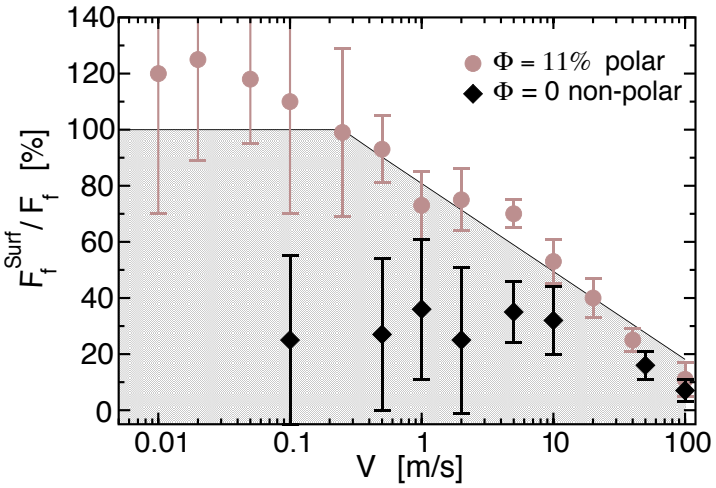

Figure 5.5.: *Average surface contribution to the friction force acting on N=15 spider silk peptide on $\Phi = 11\%$ OH covered polar and non-polar large surfaces. $F_N = 0$ for all cases. The peptide is pulled from the terminal group.*

Not only for spider silk, also for other homo-peptides, the same dissipation mechanism works. However, as we mentioned before, there is an apparent order in the surface mobilities: glycine has the smallest mobility whereas leucine and asparagine have almost equal mobilities for the given range of pulling velocities as can be seen in Fig. 5.3. Actually, at the first glance, this order of mobilities at the non-polar surface resembles to that in bulk water: The smaller the hydrodynamic radius, the lower the friction force via Stokes

relation $F_{\mathrm{f}} = V/6\pi\eta R_{\mathrm{HD}}$, where η is solvent viscosity. However, although asparagine and leucine have equal number of heavy atoms (non-hydrogen atoms, see Fig. 2.1), leucine is hydrophobic, and asparagine is hydrophilic. This means that while asparagine side chains form HBs with water, leucine side chains repel water. To understand why leucine and asparagine exhibit almost equal friction forces, we compare in Fig. 5.6A, the average distance between their side chains and the diamond surface: The leucine side chains are more closer to the surface than asparagine side chains. This confirms that the more hydrophobic polyleucine is adsorbed on the non-polar surface. On the other hand, polyasparagine side chains prefer staying in bulk more as shown in Fig. 5.6A. Similarly, the surface contribution to the total friction force shown in Fig. 5.6B is consistent with vertical distance data: surface friction is slightly higher for the more adsorbed polyluecine compared to less adsorbed polyasparagine. Note that also, in Fig. 5.6A, it appears that polyasparagine gets closer to the surface as the velocity is increased: The reason of this is that the pulling from the terminal group favours the adsorption by decreasing the effective Kuhn length perpendicular to the pulling direction [123].

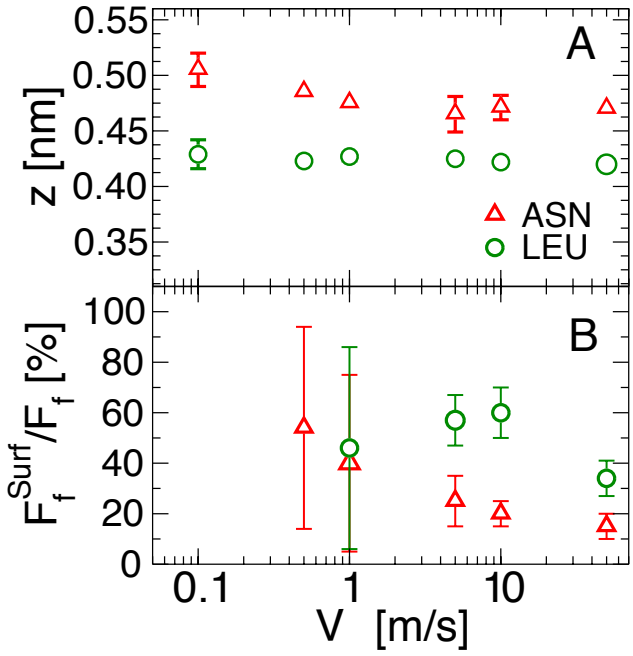

Figure 5.6.: *A) The average vertical distance between side chains and the diamond surface for $N = 11$ polyleucine and polyasparagine on the non-polar surface as a function of pulling velocity. The structures of the side chains are given in Fig. 2.1 with their related hydropathy index. B) Surface contribution to the friction force. $F_N = 0$ for all cases. Note that for velocities smaller than V =0.5 m/s, for some cases data are not shown due to the bad statistics.*

Since asparagine stays in the bulk more, it should interact with water more than leucine monomes do; in Fig. 5.7A, the sum of short range Coulomb and Leonard-Jones interactions between N=11 polyasparagine (polyleucine) and its surroundings for a cut-

off radius of r=0.8 nm is shown. As expected, asparagine-water interaction energy is 2-fold higher than those of leucine-water and glycine-water. In parallel, number of HB that N=11 polyasparagine forms with water is the maximum as displayed in Fig. 5.7B. On the other hand, leucine has the highest peptide-surface energy, which is responsible for its higher mobility compared to glycine and asparagine. However, the difference in the surface-peptide energies is not as emphasized as in surface-water energies. Also, it is worth to note that polar groups of leucine occluded by its own non-polar side chains lead a slightly smaller peptide-water HB number, N_{WP}, compared to glycine as shown in Fig. 5.7B.

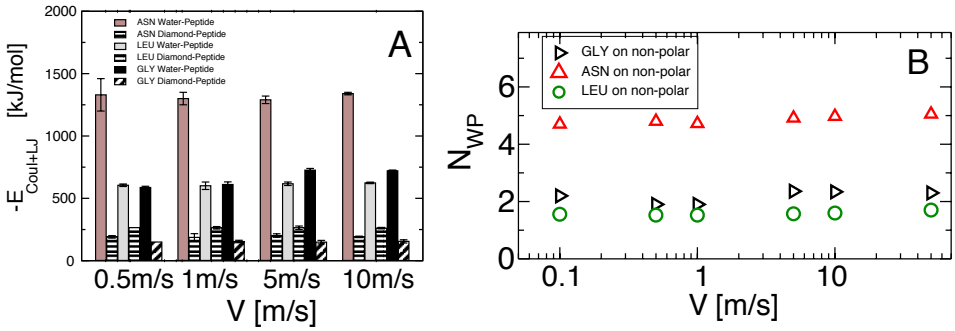

Figure 5.7.: *Interactions of homo-peptides with water: A) The sum of short range Coulomb and Leonard-Jones interaction energies for N=11 polyasparagine (ASN), polyleucine (LEU) and polyglycine (GLY) homo-peptides on the non-polar surface within a cut-off range of r=0.8 nm for pulling simulations. B) The number of HBs between water and the peptide per amino acid as a function of pulling velocity.* $F_N = 0$ *for all cases.*

5.4. Anisotropy of mobility on non-polar diamond surfaces

The non-polar diamond surface used in simulations is modelled in atomic level. As a result, this atomic-scale description of the surface creates a roughness. On the (001) surface of the non-polar diamond surface, this corrugation exhibits an anisotropy due to the channelled surface formed by surface carbon and hydrogen atoms. For the diamond surfaces, effect of the isotropy has been well studied for the friction between two planar surfaces: In MD simulations, two (001) diamond planes sliding on each other showed anisotropic friction [23]. A similar marked anisotropy in diamond friction has been observed in macroscopic level [147]. DFT (density functional theory) calculations for two diamond surfaces in contact have shown that interfacial shear stress (friction force per area) of H-terminated (001) diamond reveals anisotropy [42]. Not only for friction, but also the diffusion of adatoms on various metal surfaces, e.g., Rhenium on tungsten surfaces, shows anisotropic behaviour, i.e., adatoms moves along surface channels [24]. Naturally, reader might question the interest of planar-surface friction or atomic diffusion to the scopes of this work. Indeed, similar anisotropic motions were also reported for structured macromolecules moving on various nano-crystalline surfaces [148, 149]; when

the structure of the molecule moving on the surface registers with the surface structure, a higher mobility is observed in the direction where this registry is favoured. However, in case of unstructured short peptide chains, it is difficult to define registry points with the surface unlike a well defined geometry of a macromolecule since flexible peptide undergoes conformational transformations during its motion. One can also expect that these conformational fluctuations, which we focus in Chapter 2, lower the surface corrugation and result in an isotropic mobility even though the surface itself has an anisotropic structure. On the other hand, as shown previously, our non-polar surface mobilities are of the order of water bulk mobility. Therefore, even a weak anisotropy on the diamond surface can possibly affect the surface mobility.

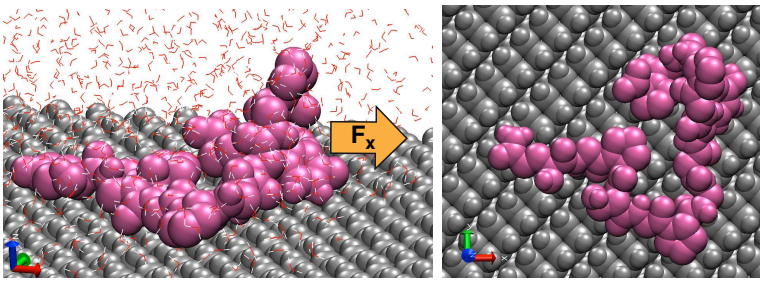

Figure 5.8.: *Snapshots of a N=15 spider silk driven by a lateral force of $F_x = 3.33$ pN per monomer in $\hat{x}$-direction at the non-polar (001) H-terminated diamond surface. For the side view, some of the water molecules are also displayed.*

To clarify all these points and see whether the motion of the peptide is anisotropic or not, we apply homogeneous forces on N=15 spider silk peptide in $\hat{x}$-direction as schematically illustrated in Fig. 5.8. Doing so, in an ideal case, the peptide should move in the direction of the applied force. Also note that applying force on the polypeptide while water is at rest, in principle, is reciprocal of applying a shear flow parallel to the diamond surface with zero force on the peptide. In Fig. 5.9, the mobilities obtained via the homogeneous force method on inelastic and elastic non-polar diamond surfaces versus the applied lateral force per monomer $F_{\mathrm{L}} \equiv F_{\mathrm{x}}$ are shown with the scaling $N^{-3/4}$. From Fig. 5.9, it is noticeable that there is a slight anisotropy with respect to the axis of symmetry of the diamond. This implies that, due to the surface anisotropy, the mobility matrix has non-diagonal elements and reads

$$\bar{\mu} = \begin{pmatrix} \mu_{xx} & \mu_{xy} \\ \mu_{yx} & \mu_{yy} \end{pmatrix}, \tag{5.1}$$

where μ_{ij} is the mobility in ith direction if the force is in jth direction. Since the molecule has no preference between $\hat{x}$ and $\hat{y}$-directions, $\mu_{ij} = \mu_{ji}$. The eigenvalues of the above matrix give the mobilities parallel $\mu_{\parallel}$ and perpendicular $\mu_{\perp}$ to the principle axes of the diamond surface as shown in Fig. 5.9. As can be rationalized from Fig. 5.9, when the peptide moves along the principle axis, namely parallel to the grooves on the surface, the mobility can be fitted using Eq. A.7 with $\tilde{U}_0 = 0$. On the other, if the peptide is moved

perpendicular to the principle axis, then $\tilde{U}_0 = 3.5$ and $a = 2$ nm describe the data well as shown in Fig. 5.9. However, regardless of the surface being elastic or inelastic, as $F \to \infty$ (or for high pulling rates) the anisotropy disappears, and $\mu_\perp \to \mu_\parallel$. This is expected since under high forces, the peptide moves faster and the surface contribution to the friction force also decreases (see Fig. 5.5) and so does the surfaces-stemmed anisotropy. Extrapolations of data shown in Fig 5.9 to the zero force limit give $\mu_\parallel \simeq 100 \pm 20 \times 10^{10}$ s/kg and $\mu_\perp \simeq 30 \pm 15 \times 10^{10}$ s/kg for $\mu_\parallel$ and $\mu_\perp$, respectively, on the non-polar diamond surface regardless of restraints on surface atoms.

For pulling simulations on non-polar surface shown so far, the peptides are pulled in the $\hat{x}$-direction (see Fig. 5.1). We observe same type of anisotropic peptide motion for the pulling simulations on the non-polar diamonds: When the peptide is pulled in $\hat{x}$-direction, it also slightly moves in the $\hat{y}$-direction. Actually, the peptide mobility in the $\hat{x}$-direction $\mu = 50 \pm 15 \times 10^{10}$ s/kg can be obtained from the combination of $\mu_\parallel$ and $\mu_\perp$ ($\mu_{comb} = 65 \pm 25 \times 10^{10}$ s/kg) as also shown in Fig. 5.9 with open brown triangles. Also, in Fig. 5.10, the displacements of pulled group obtained from homogeneous force simulations on elastic and inelastic diamond are given: Here anisotropy, which also diminishes as lateral force is increased, is clearly displayed.

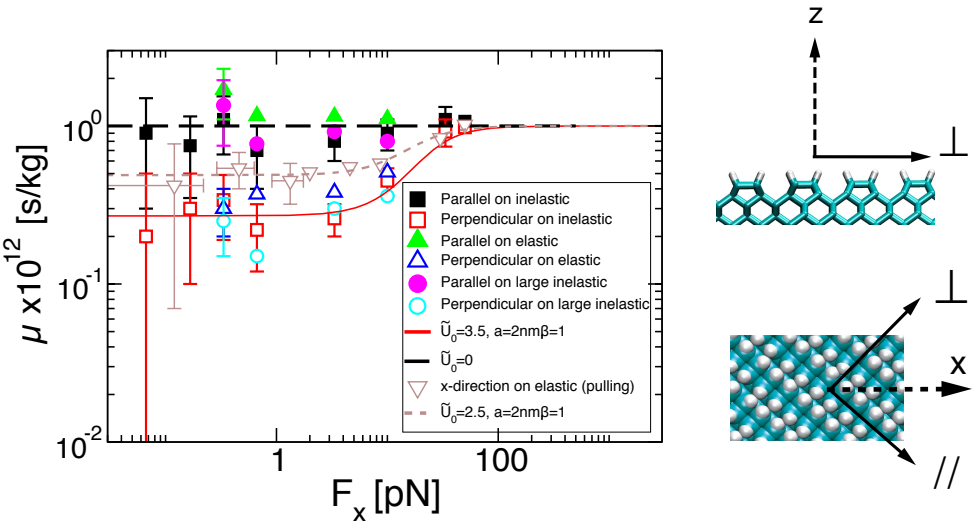

Figure 5.9.: *Parallel and perpendicular (to the axis of symmetry of the diamond surface) monomer mobilities obtained via homogeneous force simulations (except brown triangles, which are obtained with terminal pulling and are also shown in Fig. 5.1B) on the non-polar diamond surface versus applied lateral external force. The large diamond has dimensions of $8nm \times 8nm \times 1.8nm$. The scaling used is $N^{-3/4}$. The lateral force is only in $\hat{x}$-direction by applying equal force on each atom of the peptide. For inelastic diamond all bonded interactions are removed.*

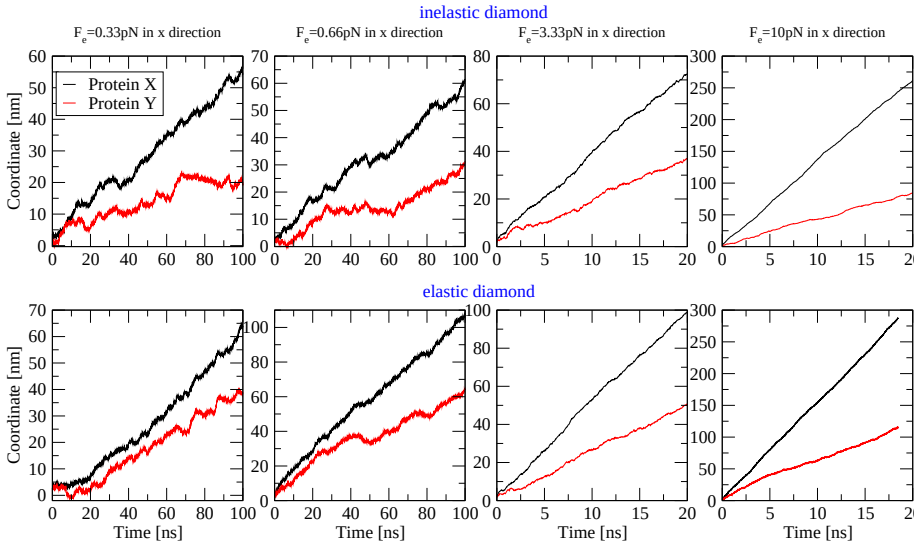

Figure 5.10.: *The center of mass displacements of N=15 spider silk in $\hat{x}$ and $\hat{y}$-directions obtained from homogeneous force simulations as a function of time under various lateral forces per amino acid on the non-polar diamond surface. The force is acted only in $\hat{x}$-direction by applying equal force on each atom of the peptide. For inelastic diamond all bonded interactions are removed.*

5.5. Conclusion and remarks

In this chapter, using MD simulations in explicit water, we demonstrate that the bulk mobility and the non-polar surface mobilities of various peptide chains are of equivalent. For MD simulations on non-polar surfaces, equilibration is not an issue [123], and mobilities mostly can reach the linear-response level. For the cases, in which non-linear effects arise, we introduce a non-linear solution obtained from the Fokker-Planck equation. Mobilities obtained via our simulations are in well agreement with experimental findings as shown in Table 5.1: For comparison, we also give mobilities on polar surfaces. For the polar surfaces the mobility is of the order of 10^8 s/kg whereas on the non-polar surface, the mobilities are closer to the bulk mobility value $\mu_0 \simeq 10^{12}$ s/kg. Accordingly, the non-polar mobilities followed from Einstein relation similar the water bulk case, i.e., the smaller the hydrodynamic radius, the larger the mobility: Glycine with lowest molecular mass is the most mobile on the non-polar surface. Also, hydrophobic leucine and hydrophilic asparagine monomers have similar mobilities with asparagine having slightly higher mobility on the non-polar surface. However, for asparagine the friction is due to the interaction with water while for leucine, non-polar surface play the role. This is consistent with the fact that the desorption force for leucine off the non-polar surface is higher than that for asparagine on non-polar diamond. Note that, as we discuss in Chapter 2, quantitative 2-fold difference between our results and experimental findings can be explained by the fact that SPC water model underestimates water viscosity a factor of 2 less [113].

However, we should note the adsorbed peptide loses some of its conformational entropy near the surface. This entropic contributions can change both the adsorption energy and the conformation of the peptide, which, in turn, can influence pulling forces from which we derived the mobilities. In Chapter 2, we demonstrate that pulling a peptide at slow enough velocities has a minor effect in the mobility,

We also display the surface anisotropy on the (001) surface of the H-terminated diamond surface: The mobility parallel to channels formed by surface atoms are at least factor of 4 less than that perpendicular to channels. This result can have significant importance, particularly, when similar surfaces are employed in simulations or in experiments to investigate 2D motion of various macromolecules. For instance, when a peptide is pulled by AFM, due to anisotropy, neighboring peptides can move towards the pulled peptide and alter the measured forces. This anisotropic mobility can also manipulate configuration of proteins at interfaces, e.g., in the high mobility direction, denaturation of the protein can be faster. On the other hand, surfaces with a weak anisotropy as we reported here, can be advantageous to assemble small molecules unidirectionally [24] or to initiate structure formation of more complex molecules [150].

Table 5.1.: *The monomer mobilities on various surfaces and in bulk. Simulation results are extrapolated to the limit of the linear response $F_f \to 0$. Note with SPC water viscosity correction of a factor of half, our bulk mobilities are in good agreement with experimental findings.*

Monomer mobilities for various peptides as $F_\mathrm{f} \to 0$ ($V \to 0$)					
Molecule	System	μ $[10^{10} s/kg]$	Method	Ref.	Scaling
asparagine	bulk water	40 ± 5	Sim.	This work	$N^{-3/5}$
asparagine[a]	bulk water	19	Exp.	[107]	$N^{-0.45}$
asparagine[b]	bulk water	20	Exp.	[110]	-
spider silk	bulk water	90 ± 30	Sim.	[57]	N^{-1}
spider silk	bulk water	35 ± 5	Sim.	[57] (revised)	$N^{-3/5}$
spider silk[a]	bulk water	21	Exp.	[107]	$N^{-0.45}$
glycine	non-polar diamond	71 ± 15	Sim.	This work	$N^{-3/4}$
asparagine	non-polar diamond	41 ± 10	Sim.	This work	$N^{-3/4}$
leucine	non-polar diamond	36 ± 10	Sim.	This work	$N^{-3/4}$
spider silk	non-polar diamond	50 ± 15	Sim.	This work	$N^{-3/4}$
spider silk	non-polar diamond	30 ± 10	Sim.	[57]	N^{-1}
spider silk	non-polar diamond	20 ± 5	Sim.	[57] (revised)	$N^{-3/4}$
glycine	polar diamond	$\simeq 10^{-3}$	Sim.	This work	N^{-1}
asparagine	polar diamond	$\leq 10^{-3}$	Sim.	This work	N^{-1}
spider silk	polar diamond	$\simeq 1.2 \times 10^{-3}$	Sim.	This work	N^{-1}
spider silk	polar diamond	< 1	Sim.	[57]	N^{-1}
PEG	hydrophobic SAM	8	Exp.	[25, 111]	$N^{-3/2}$
ds-DNA	on mica	0.17	Exp.	[53]	N^{-1}
LamB	on gold	$\simeq 5 \times 10^{-4}$	Exp.	[151]	N^{-1}

[a] Before applying the scaling law, polypeptide mobilities are calculated for asparagine with M=1683g/mol (N=15) and for spider silk with M=1298g/mol (N=15) from the scaling law given in ref [107]. [b] For a single asparagine monomer in solution at 25°C. Note that globular HSA protein shows different denaturation levels on different surfaces.

Chapter 6

Hydrodynamic response function with compressibility and finite slip

Based on the classical work by Stokes on the time-dependent response function for a sphere in a viscous incompressible medium [81, 152], several works reported the response function for a finite-size sphere including slip and compressibility [153–156], but the explicit flow field has not been given. For the cylindrical case, compressibility has not been considered at all [157, 158]. In the previous interpretation of microrheology measurements of complex fluids such as entangled polymer solutions, the dynamic response function of water has typically been considered featureless. In this section, we analyze the response function and flow profiles of a viscous compressible fluid at the basic geometries such as planes, spheres, cylinders in detail and show that the resulting behavior is quite rich, exhibiting resonant behavior both in the propagative as well as in the diffusive regime. Knowing the response function in principle allows to extract the slip length from experimentally measured spectral properties. The flow profile is important in situations where the hydrodynamic interaction between oscillating spheres or cylinders is probed and can help to rationalize hydrodynamic effects in confinement [159]. In addition, flows can be explicitly visualized with modern particle-image-velocimetry techniques, which would allow a direct comparison between theoretical and experimental results.

In the following sections, we will first derive the constitutive equations from basic principles, then after accepting certain assumptions, the Green's function for a point source will be obtained. Following, using the latter solution, velocity fields and response functions for planar, spherical and cylindrical geometries will be calculated explicitly.

6.1. Constitutive equations

Conservation of the i-th component of the momentum in an arbitrary finite volume V reads

$$\frac{d}{dt}\int_V \rho v_i d^3r + \int_{\partial V} \rho v_i v_j df_j = \int_V F_i d^3r + \int_{\partial V} \Pi_{ij} df_j, \tag{6.1}$$

where density ρ, velocity v_i, volume force F_i, stress tensor Π_{ij} are functions of both time t and position $\mathbf{r}$, i.e. $\rho(\mathbf{r},t)$, $v_i(\mathbf{r},t)$, $F_i(\mathbf{r},t)$, $\Pi_{ij}(\mathbf{r},t)$, and the Einstein summation convention is used throughout this paper. Using Gauss law, the local momentum conservation follows as

$$\frac{\partial \rho v_i}{\partial t} + \nabla_j \rho v_i v_j = F_i + \nabla_j \Pi_{ij}. \tag{6.2}$$

With the help of the continuity equation, $\partial\rho/\partial t + \nabla_j \rho v_j = 0$ and the material derivative acting on an arbitrary scalar field $A(\mathbf{r},t)$, defined as $DA/Dt = \partial A/\partial t + v_i \nabla_i A$, the Navier-Stokes equation in compact notation results

$$\rho \frac{Dv_i}{Dt} = F_i + \nabla_j \Pi_{ij}. \tag{6.3}$$

The symmetric stress tensor is divided into the diagonal pressure contribution and a part that depends on velocity gradients $\nabla_j v_i$. To lowest order, which defines a Newtonian liquid, one obtains

$$\Pi_{ij} + p\delta_{ij} = \zeta \delta_{ij} \nabla_k v_k + \eta \left(\nabla_i v_j + \nabla_j v_i - \frac{2}{3} \delta_{ij} \nabla_k v_k \right), \tag{6.4}$$

where η is the shear viscosity and ζ denotes the volume viscosity, which is often set to zero. The Navier Stokes equation becomes

$$\rho \frac{Dv_i}{Dt} = F_i - \nabla_i p + (\eta/3 + \zeta) \nabla_i \nabla_k v_k + \eta \nabla_k \nabla_k v_i. \tag{6.5}$$

Let us start out by a brief scaling analysis: Introducing scales for time, length, velocity, and density, T, L, V, ρ_0, respectively, and dividing the Navier-Stokes equation by $\eta V/L^2$ so that the viscosity terms are of order unity, the non-linear velocity term scales as the Reynolds number $\mathcal{R} \sim \rho_0 LV/\eta$, and the time-derivative term scales as $\mathcal{R}\,\mathcal{ST} \sim \rho_0 L^2/(\eta T)$. The Strouhal number is defined as $\mathcal{ST} \sim L/(VT)$ and measures the importance of the time-derivative term compared to the the non-linear term. Assuming water density $\rho_0 \simeq 10^3 kg/m^3$, water viscosity $\eta \simeq 10^{-3} kg/(ms)$, and typical length and velocity scales for biological or colloidal systems in the micron range, $L \simeq 10^{-6} m$, $V \simeq 10^{-6} m/s$, the Reynolds number is $\mathcal{R} \simeq 10^{-6}$ and thus the non-linear term is negligible for such situations. The Strouhal number on the other hand can be quite large, depending on the time scale considered. Assuming a time scale $T \simeq 10^{-6} s$, that means frequencies in the MHz range, the Strouhal number becomes $\mathcal{ST} \simeq 10^6$ and the time-derivative term scales of the order of unity, $\mathcal{R}\,\mathcal{ST} \simeq 1$, and thus cannot be neglected. Such short times scales are important in a number of situations. By neglecting the non-linear term but keeping the time-derivative, we are led to the so-called transient Stokes equation,

$$\rho \frac{\partial v_i}{\partial t} = F_i - \nabla_i p + (\eta/3 + \zeta) \nabla_i \nabla_k v_k + \eta \nabla_k \nabla_k v_i, \tag{6.6}$$

which serves as the starting point for all further investigations in this paper. This equation is discussed in classical texts in the incompressible regime, where the term proportional to $\nabla_k v_k$ is absent [81]. For the case of finite compressibility only few and quite recent studies have been reported [153–156].

In the next section we first calculate the Green's function of the transient Stokes Eq. (6.6). The Green's function includes compression and shear effects, both are damped (or screened) at frequency-dependent length scales. Interestingly, for water the screening length of compression waves (sound waves) is for typical kHz frequencies in the kilometer range and thus much larger than the wave length, i.e., compressional perturbations propagate. For much higher frequencies, the screening length becomes of the order of the wave length and compression perturbations do not propagate. The screening length of shear or vortex diffusion is always of the order of the perturbation wave length and thus shear perturbations never propagate. From the Green's function we construct the flow field at a plane, around a sphere and at a cylinder, using a generalized hydrodynamic boundary condition that includes a finite slip length b. We determine the pressure field and surface stress from which the forces acting on the bodies are derived. We find resonant features in the response functions, the scaling of which is analysed in detail.

6.2. Green's function approach for a point force

On the linear level we treat v_i, $\rho-\rho_0$, $p-p_0$, F_i as small quantities. Taking the divergence of the Stokes Eq. (6.6), one obtains on the linear level

$$\nabla_i\nabla_i p - \frac{\partial^2 p}{c^2\partial t^2} = \nabla_i F_i + (4\eta/3+\zeta)\nabla_i\nabla_i\nabla_k v_k. \tag{6.7}$$

In deriving this we have used the linearized continuity equation, $\rho_0\nabla_i(\partial v_i/\partial t) = -\partial^2\rho/\partial t^2$, the expression
$\partial^2\rho/\partial t^2 = c^{-2}\partial^2 p/\partial t^2$ valid in the adiabatic limit, and the definition of the speed of sound c via $\partial\rho/\partial p = c^{-2}$. We define fourier-transforms as

$$p(\mathbf{r},t) = \frac{1}{(2\pi)^3}\int d\omega d^3k\tilde{p}(\mathbf{k},\omega)e^{\imath(k_i r_i-\omega t)} \tag{6.8}$$

and similarly for v_i and F_i. Equations (6.6) and (6.7) become

$$-\imath\omega\rho_0\tilde{v}_i = \tilde{F}_i - \imath k_i\tilde{p} - (\eta/3+\zeta)k_i k_j\tilde{v}_j - \eta k_j k_j\tilde{v}_i \tag{6.9}$$

and

$$\left(\frac{\omega^2}{c^2} - k_i k_i\right)\tilde{p} = \imath k_i\tilde{F}_i - \imath(4\eta/3+\zeta)k_i k_i k_j\tilde{v}_j. \tag{6.10}$$

Equation (6.10) allows to express the pressure field in terms of the velocity field. Thus eliminating the pressure term in Eq. (6.9), one obtains an equation that only depends on velocity and external force. Straightforward solution of this algebraic equation is possible by decomposition of the velocity according to

$$\tilde{v}_i = \tilde{v}_i^T + \tilde{v}_i^L \tag{6.11}$$

into a transverse part defined by $k_i\tilde{v}_i^T = 0$ and a longitudinal part characterized by $k_i\tilde{v}_i = k_i\tilde{v}_i^L$. We define Green's functions for the transverse and longitudinal velocities as

$$\tilde{v}_i^T = \tilde{G}_{ij}^T\tilde{F}_j \tag{6.12}$$

and

$$\tilde{v}_i^L = \tilde{G}_{ij}^L \tilde{F}_j. \tag{6.13}$$

The transverse Green's function describes the velocity-field in the incompressible case and captures vorticity or shear effects; it has been derived by Stokes [81, 158] and is given by

$$\tilde{G}_{ij}^T = \frac{(\delta_{ij} - k_i k_j/k^2)/\eta}{k^2 + \alpha^2}, \tag{6.14}$$

where we have defined the length scale α^{-1} via

$$\alpha^2 = -\imath\omega\rho_0/\eta. \tag{6.15}$$

On the other hand, the longitudinal Green's function describes compression effects and reads

$$\tilde{G}_{ij}^L = \frac{k_i k_j \lambda^2}{\eta\alpha^2 k^2 (k^2 + \lambda^2)}, \tag{6.16}$$

where we have defined the length scale λ^{-1} via

$$\lambda^2 = \frac{-\imath\omega\rho_0}{4\eta/3 + \zeta + \imath\rho_0 c^2/\omega}. \tag{6.17}$$

The complete Green's function is defined by

$$\tilde{v}_i = \tilde{G}_{ij}\tilde{F}_j \tag{6.18}$$

and is obtained from the sum of transverse and longitudinal Green's functions

$$\tilde{G}_{ij} = \tilde{G}_{ij}^T + \tilde{G}_{ij}^L. \tag{6.19}$$

6.2.1. Transverse Green's function

The transverse Green's function in real space is obtained by straightforward back-fourier transformation and reads

$$G_{ij}^T = \frac{1}{4\pi\eta\alpha^2 r^3} \left\{ \delta_{ij} \left([1 + r\alpha + r^2\alpha^2] e^{-r\alpha} - 1 \right) + 3\hat{r}_i\hat{r}_j \left(1 - [1 + r\alpha + r^2\alpha^2/3] e^{-r\alpha} \right) \right\} \tag{6.20}$$

Note that Equation (6.20) is identical to Green's functions that are obtained for porous media [160]. For short distances, high viscosity or small frequencies, $r\alpha \ll 1$, the limiting behavior is

$$G_{ij}^T \simeq \frac{1}{8\pi\eta r} \left(\delta_{ij} + \hat{r}_i\hat{r}_j \right) \tag{6.21}$$

and corresponds to the static incompressible Green's function, the so-called Oseen Tensor. For large distances or high frequencies, $r\alpha \gg 1$, corresponding to the inviscous case, the limiting behavior is

$$G_{ij}^T \simeq \frac{1}{4\pi\eta r^3\alpha^2} \left(3\hat{r}_i\hat{r}_j - \delta_{ij} \right) \tag{6.22}$$

and exhibits a much faster decay (note that to leading order, the dependence on viscosity has dropped out). The decay constant α is separated into real and imaginary parts as

$$\alpha = \alpha_R + \imath\alpha_I. \tag{6.23}$$

By introducing the typical length scale a we obtain

$$a\alpha_R = -a\alpha_I = \sqrt{\omega/2\omega_0}, \tag{6.24}$$

where we have defined the vorticity frequency scale ω_0 as

$$\omega_0 = \frac{\eta}{a^2\rho_0}. \tag{6.25}$$

The inverse frequency ω_0^{-1} is the time vorticity needs to diffuse a certain distance a. For water with density $\rho_0 \approx 10^3 kg/m^3$ and viscosity $\eta \approx 10^{-3} kg/ms$, ω_0 ranges from $\omega_0 \simeq 1s^{-1}$ for $a \simeq 1mm$ to $\omega_0 \simeq 10^6 s^{-1}$ for $a \simeq 1\mu m$. In water, the decay length scales as $\alpha_R^{-1} \simeq 10^{-3}(\omega s)^{-1/2} m$ and thus is of the order of $\alpha_R^{-1} \simeq 1mm$ for a frequency $\omega = 1s^{-1}$ and $\alpha_R^{-1} \simeq 1\mu m$ for a frequency $\omega = 10^6 s^{-1}$.

6.2.2. Longitudinal Green's function

The longitudinal Green's function in real space reads

$$G_{ij}^L = \frac{1}{4\pi\eta\alpha^2 r^3}\left\{\delta_{ij}\left(1-[1+r\lambda]e^{-r\lambda}\right) -3\hat{r}_i\hat{r}_j\left(1-[1+r\lambda+r^2\lambda^2/3]e^{-r\lambda}\right)\right\}. \tag{6.26}$$

For short distances, low compressibility (i.e. high sound speed) or small frequencies, $r\lambda \ll 1$, the limiting behavior is

$$G_{ij}^L \simeq \frac{\lambda^2}{8\pi\eta r\alpha^2}\left(\delta_{ij}-\hat{r}_i\hat{r}_j\right). \tag{6.27}$$

In the incompressible case, characterized by an infinite sound velocity $c \to \infty$, one has $\lambda \to 0$ and thus the longitudinal Green's function vanishes. For large distances or high frequencies, $r\lambda \gg 1$, the limiting behavior is

$$G_{ij}^L \simeq -\frac{1}{4\pi\eta r^3\alpha^2}\left(3\hat{r}_i\hat{r}_j-\delta_{ij}\right) \tag{6.28}$$

and thus exactly cancels the asymptotic term from the incompressible Green's function given in Eq. (6.22); the large distance behavior of the total Green's function is thus determined by the next-leading order terms and will be discussed in the next section. The decay constant λ is separated into real and imaginary parts as $\lambda = \lambda_R + \imath\lambda_I$, where

$$a\lambda_R = \frac{\omega}{\omega_0}\sqrt{\frac{\sqrt{1+\left[\omega/(\omega_0\gamma)(4/3+\zeta/\eta)\right]^2}-1}{2\gamma\left(1+\left[\omega/(\omega_0\gamma)(4/3+\zeta/\eta)\right]^2\right)}} \tag{6.29}$$

and

$$a\lambda_I = -\frac{\omega}{\omega_0}\sqrt{\frac{\sqrt{1+\left[\omega/(\omega_0\gamma)(4/3+\zeta/\eta)\right]^2}+1}{2\gamma(1+\left[\omega/(\omega_0\gamma)(4/3+\zeta/\eta)\right]^2)}} \tag{6.30}$$

and we have defined the dimensionless parameter

$$\gamma = \frac{c^2}{a^2\omega_0^2} = \left(\frac{a\rho_0 c}{\eta}\right)^2. \tag{6.31}$$

Noting that a/c is the typical compression time scale associated with the time in which a propagating sound wave travels a distance a, γ turns out to be the squared ratio of the vorticity time scale ω_0^{-1} and the compression time scale a/c. Besides the volume viscosity ζ, the vorticity frequency scale ω_0 and the length scale a, γ is the only remaining parameter. The asymptotic behavior of the real and imaginary parts of λ are

$$a\lambda_R = \begin{cases} 2/3(\omega/\omega_0)^2\gamma^{-3/2} - \mathcal{O}[(\omega/\omega_0)^4] & \text{for} \quad \omega/(\omega_0\gamma) \ll 1, \\ \sqrt{3/8}(\omega/\omega_0)^{1/2} - \mathcal{O}[(\omega/\omega_0)^{-1/2}] & \text{for} \quad \omega/(\omega_0\gamma) \gg 1, \end{cases} \tag{6.32}$$

and

$$a\lambda_I = \begin{cases} -(\omega/\omega_0)\gamma^{-1/2} + \mathcal{O}[(\omega/\omega_0)^3] & \text{for} \quad \omega/(\omega_0\gamma) \ll 1, \\ -\sqrt{3/8}(\omega/\omega_0)^{1/2} - \mathcal{O}[(\omega/\omega_0)^{-1/2}] & \text{for} \quad \omega/(\omega_0\gamma) \gg 1. \end{cases} \tag{6.33}$$

The intrinsic frequency

$$\omega_0\gamma = \frac{c^2\rho_0}{\eta} \tag{6.34}$$

denotes the boundary between the propagating regime, realized for low frequencies $\omega < \omega_0\gamma$ and where compression perturbations lead to propagative waves, characterized by $\lambda_R^{-1} > \lambda_I^{-1}$ and a speed of sound $c \sim \omega\lambda_I^{-1}$, and the diffusive regime, realized for high frequencies $\omega > \omega_0\gamma$ and where compression perturbations are damped by viscosity effects, characterized by $\lambda_R \sim |\lambda_I| \sim \alpha_R \sim |\alpha_I|$. For water parameters and speed of sound $c \approx 10^3 m/s$, one obtains the intrinsic frequency $\omega_0\gamma \simeq 10^{12}s^{-1}$, i.e., for all realistic frequencies one has $\omega < \omega_0\gamma$ and thus propagating sound waves occur. For higher frequencies, the screening length of compression perturbations is identical to the shear waves. We note that the crossover frequency $\omega_0\gamma$ can be much lower for systems characterized by a higher compressibility or higher viscosity, e.g., liquids close to a critical point or polymers embedded in a solvent. The decay length in the propagative regime, $\lambda_R^{-1} \simeq (\omega_0/\omega)^2 a\gamma^{3/2}$, for water is given by $\lambda_R^{-1} \simeq 10^{15}\ (\omega s)^{-2}m$. For frequencies $\omega = 1s^{-1}$ and $\omega = 10^6 s^{-1}$, the screening lengths of compression waves are $\lambda_R^{-1} \simeq 10^{15}m$ and $\lambda_R^{-1} \simeq 10^3 m$, respectively, which means that for realistic frequencies this screening length is macroscopic. For non-aqueous systems, on the other hand, the screening length can become microscopic.

6.2.3. Total Green's function

The total Green's function reflecting both compression and shear effects is constructed by summing Eqs. (6.20) and (6.26) as

$$\begin{aligned} G_{ij} &= G_{ij}^T + G_{ij}^L \\ &= \frac{1}{4\pi\eta\alpha^2 r^3}\{\delta_{ij}([1+r\alpha+r^2\alpha^2]e^{-r\alpha} - [1+r\lambda]e^{-r\lambda}) \\ &-3\hat{r}_i\hat{r}_j([1+r\alpha+r^2\alpha^2/3]e^{-r\alpha} - [1+r\lambda+r^2\lambda^2/3]e^{-r\lambda})\}. \end{aligned} \tag{6.35}$$

According to Eqs. (6.32) and (6.33), for $\omega < \omega_0\gamma$ the screening length of compression waves λ_R^{-1} is larger than the screening length α_R^{-1} of shear waves and thus an intermediate distance range $\alpha_R^{-1} < r < \lambda_R^{-1}$ exists within which shear waves are screened and decay according to Eq. (6.22) but compression waves are unscreened and described by Eq. (6.27). For small distances, for which $r\lambda \ll 1$ and $r\alpha \ll 1$, the limiting behavior follows from summing up Eqs. (6.21) and (6.27)

$$G_{ij} \simeq \frac{1}{8\pi\eta r}\left(\delta_{ij}[1+\lambda^2/\alpha^2] + \hat{r}_i\hat{r}_j[1-\lambda^2/\alpha^2]\right). \tag{6.36}$$

Since the ratio $\lambda^2/\alpha^2 = (4/3+\zeta/\eta+\imath\omega_0\gamma/\omega)^{-1}$ is very small for water, one can neglect this contribution coming from the compression part. In the large-distance regime, for which $r\lambda \gg 1$ and $r\alpha \gg 1$, cancellation of the leading-order terms in Eqs. (6.22) and (6.28) takes place, by including second-leading order terms we obtain

$$G_{ij} \simeq \frac{1}{4\pi\eta\alpha^2 r^3}\left\{\delta_{ij}\left([r^2\alpha^2 - r\alpha]e^{-r\alpha} - r\lambda e^{-r\lambda}\right) - \hat{r}_i\hat{r}_j\left([r^2\alpha^2+3r\alpha]e^{-r\alpha} - r^2\lambda^2 e^{-r\lambda}\right)\right\}. \tag{6.37}$$

Here an interesting anisotropy of the hydrodynamic response exists: When the force is perpendicular to the connecting vector between source point and field point, one has $\hat{r}_j F_j = 0$ and thus

$$G_{ij}^{\perp} \simeq \frac{1}{4\pi\eta\alpha^2 r^3}\left(r^2\alpha^2 e^{-r\alpha} - r\lambda e^{-r\lambda}\right), \tag{6.38}$$

for the parallel contribution one obtains

$$G_{ij}^{\parallel} \simeq \frac{1}{4\pi\eta\alpha^2 r^3}\left(-4r\alpha e^{-r\alpha} + r^2\lambda^2 e^{-r\lambda}\right). \tag{6.39}$$

6.2.4. Surface stress

From the total Green's function for the velocity field one can calculate the Green's function for the stress tensor, denoted by Π_{ijk}, which is defined as

$$\Pi_{ij} = \Pi_{ijk}F_k. \tag{6.40}$$

For a more compact notation, we also define the gradient of the Green's function, G_{kij}, via

$$\nabla_k v_i = \nabla_k G_{ij} F_j = G_{kij}F_j. \tag{6.41}$$

From the constituting equation, Eq. (6.9), and the solutions given in Eqs. (6.14) and (6.16), the pressure follows as

$$p = \frac{\rho_0 c^2}{\imath\omega}\nabla_k v_k + p_0, \tag{6.42}$$

where p_0 is the constant background pressure. With the definition of the stress tensor, Eq. (6.4), the stress tensor Green's function follows as

$$\Pi_{ijk}/\eta = G_{ijk} + G_{jik} + (\alpha^2/\lambda^2 - 2)G_{llk}\delta_{ij}. \tag{6.43}$$

6.3. Velocity field of a plane

The Green's function for a compressible fluid given in Eq. (6.35) can be used to obtain the response function of bodies of different geometries by distributing a source field over the body surface. The simplest case is the response function of an oscillating plane of infinite extent. Here, perpendicular and tangential motions of the plane lead to a clear separation of compression and shear effects and the influence of surface slip is strikingly displayed. The Green's function of an infinite plane is obtained by the surface integral

$$G_{ij}^{pl}(z) = \int_S G_{ij}(x', y', z) dS(x', y'), \tag{6.44}$$

where S indicates the surface. Due to lateral translational invariance, $G_{ij}^{pl}(z)$ only depends on the vertical distance z from the plane and is given by

$$G_{ij}^{pl}(z) = \delta_{jz}\delta_{iz}\frac{\lambda e^{-|z|\lambda}}{\eta\alpha^2} + (\delta_{jx}\delta_{ix} + \delta_{jy}\delta_{iy})\frac{e^{-|z|\alpha}}{\eta\alpha}. \tag{6.45}$$

In the following we distinguish oscillations perpendicular and parallel to the surface plane.

6.3.1. Perpendicular motion

From Eq. (6.45), the velocity field caused by an oscillation perpendicular to the surface reads as

$$v_z^{pl,\perp}(z) \quad = \quad F_z^{pl} G_{zz}^{pl}(z) = \frac{F_z^{pl}}{\eta\alpha^2}\lambda e^{-|z|\lambda}, \tag{6.46}$$

where F_z^{pl} is the amplitude of the force acting on the plane per unit area, i.e. the pressure. Only motion in the z-direction is generated and exponentially damped away from the surface. Denoting the oscillation amplitude of the surface at the position $z = 0$ as V_z^{pl} and using the kinematic boundary condition,

$$V_z^{pl} = v_z^{pl,\perp}(0) = \frac{F_z^{pl}}{\eta\alpha^2}\lambda, \tag{6.47}$$

we define the perpendicular response function of the plane via

$$\mathcal{G}_{\perp}^{pl}(\omega) = \frac{F_z^{pl}}{V_z^{pl}} = \frac{\eta\alpha^2}{\lambda} \tag{6.48}$$
$$= \frac{\rho_0 c}{\sqrt{2}}\sqrt{\sqrt{1+(\frac{4\omega\eta}{3\rho_0 c^2})^2}+1} - \imath\frac{\rho_0 c}{\sqrt{2}}\sqrt{\sqrt{1+(\frac{4\omega\eta}{3\rho_0 c^2})^2}-1}.$$

Here and in the remainder of the paper, we have set the volume viscosity to zero, i.e. $\zeta = 0$. In the low frequency propagative regime, $\omega < \omega_0\gamma$, the response function shows the behavior

$$\mathcal{G}_{\perp}^{pl}(\omega) \simeq \rho_0 c\left[1 + 2\left(\frac{\omega}{3\omega_0\gamma}\right)^2 - \imath\frac{2\omega}{3\omega_0\gamma}\right] \tag{6.49}$$

while in the high-frequency limit, $\omega > \omega_0\gamma$, we find

$$\mathcal{G}_{\perp}^{pl}(\omega) \simeq \rho_0 c(1-\imath)\left(\frac{2\omega}{3\omega_0\gamma}\right)^{1/2}. \tag{6.50}$$

6.3.2. Parallel motion

For shearing motion parallel to the plane, the velocity field is given by

$$v_x^{pl,\parallel}(z) = F_x^{pl}G_{xx}^{pl}(z) = \frac{F_x^{pl}}{2\eta\alpha}e^{-|z|\alpha}. \tag{6.51}$$

Since no compression occurs, the parameter λ does not appear in this case. We apply the Navier boundary condition at the position of the surface,

$$b\frac{\partial v_x^{pl,\parallel}(z)}{\partial z}|_{z=0} = v_x^{pl,\parallel}(0) - V_x^{pl}, \tag{6.52}$$

which relates the fluid shear rate to the tangential velocity component of the fluid at the boundary via the slip length b. For $b = 0$ one has the no-slip boundary condition, finite b corresponds to variable amounts of surface slip. The response function due to the parallel plane oscillations reads

$$\mathcal{G}_{\parallel}^{pl}(\omega) = \frac{F_x^{pl}}{V_x^{pl}} = \frac{2\eta\alpha}{b\alpha+1}, \tag{6.53}$$

or in more explicit form by using Eq. (6.15)

$$\mathcal{G}_{\parallel}^{pl}(\omega) = 2\eta\frac{b\omega\rho_0/\eta + \sqrt{\omega\rho_0/2\eta} - \imath\sqrt{\omega\rho_0/2\eta}}{b^2\omega\rho_0/\eta + 2b\sqrt{\omega\rho_0/2\eta}+1}. \tag{6.54}$$

Note that in contrast to the perpendicular case, the static response for the parallel geometry is zero, i.e. the force needed to tangentially move a plane vanishes in the zero

frequency limit. This is expected since in the static limit $\omega \to 0$ the fluid is comoving with the plane as a whole and the dissipation (and thus the response function) vanishes. That the response for the perpendicular motion saturates at a constant value is due to the neglect of the convective non-linear term in the Navier-Stokes equation and signals a break down of the linearization approximation. In contrast, no convective term is present for the parallel motion case and thus the linear approximation is exact. As for the perpendicular case, if fluid is present on one side of the plane only, the response function is divided by a factor of two and coincides with Stokes' original result [81]. For small frequency the response becomes

$$\mathcal{G}_{\parallel}^{pl}(\omega) \simeq 2\eta(1-\imath)\sqrt{\omega\rho_0/2\eta}, \tag{6.55}$$

which is the same result obtained from the exact expression Eq. (6.54) in the limit of vanishing slip length, $b = 0$. For high frequencies, $\omega > \omega_b = \eta/(\rho_0 b^2)$, the behavior is distinctly different and we obtain

$$\mathcal{G}_{\parallel}^{pl}(\omega) \simeq 2\eta\left[b^{-1} - \imath b^{-2}(2\omega\rho_0/\eta)^{-1/2}\right]. \tag{6.56}$$

Comparison of Eqs. (6.55) and (6.56) shows that the real part of the response function saturates at a constant value for frequencies higher than ω_b, whereas the imaginary part of the response function exhibts a maximum around the crossover frequency ω_b and goes to zero both for very small and very high frequencies. The crossover frequency ω_b for water and a slip length of $b = 10nm$ as found for hydrophobic materials is of the order of $\omega_b \simeq 10^{10}s^{-1}$. We conclude that for aqueous fluids, very high frequencies and thus advanced experimental techniques are needed to probe the high-frequency slip regime. On the other hand, for fluids with large slip lengths or in confined media, the crossover occurs at lower and thus experimentally more easily accessible frequency scales.

Double-plane

Two infinitely extended parallel planes lie on xy plane. Fluid motion takes place at the space between two planar surfaces located at $z = 0$ and $z = D$. Both planes are allowed to oscillate in $\hat{x}$-direction with velocities V_1 and V_2, respectivel, and interaction of the planes with the fluid is defined via slip lengths b_1 and b_2. To write down the velocity field in between two parallel planes we can make use of the solution given in Eq. (6.51), then the general solution can be written as

$$v_x^{db,\parallel}(z) = Ae^{-\alpha|z|} + Be^{\alpha|z|}, \tag{6.57}$$

where A and B will be defined by Navier boundary conditions at $z = 0$ and $z = D$ as

$$\begin{aligned} b_1 \frac{\partial v_x^{db,\parallel}(z)}{\partial z}_{|_{z=0}} &= v_x^{db,\parallel}(0) - V_1, \\ -b_2 \frac{\partial v_x^{db,\parallel}(z)}{\partial z}_{|_{z=D}} &= v_x^{db,\parallel}(D) - V_2, \end{aligned} \tag{6.58}$$

then 2 resulting equations for 2 unknowns A and B

$$\begin{aligned} &B(b_1\alpha - 1) - A(b_1\alpha + 1) = -V_1, \\ &Be^{\alpha D}(b_2\alpha + 1) - Ae^{-\alpha D}(b_2\alpha - 1) = V_2. \end{aligned} \tag{6.59}$$

Substitution of

$$A = \frac{V_1 + B(b_1\alpha - 1)}{b_1\alpha + 1} \tag{6.60}$$

into Eq. (6.59) gives

$$A = \frac{V_1 e^{\alpha D}(b_2\alpha + 1) + V_2(b_1\alpha - 1)}{e^{\alpha D}[(b_2\alpha + 1)(b_1\alpha + 1) - (b_1\alpha - 1)(b_2\alpha - 1)e^{-2\alpha D}]} \tag{6.61}$$

$$B = \frac{V_1 e^{-\alpha D}(b_2\alpha - 1) + V_2(b_1\alpha + 1)}{e^{\alpha D}[(b_2\alpha + 1)(b_1\alpha + 1) - (b_1\alpha - 1)(b_2\alpha - 1)e^{-2\alpha D}]} \tag{6.62}$$

Final form of the Eq. (6.57) reads

$$v_x^{db,\parallel}(z) = \frac{V_1[(b_2\alpha + 1)e^{\alpha D - \alpha z} + (b_2\alpha - 1)e^{-\alpha D + \alpha z}] + V_2[(b_1\alpha - 1)e^{-\alpha z} + (b_1\alpha + 1)e^{\alpha z}]}{e^{\alpha D}[(b_2\alpha + 1)(b_1\alpha + 1) - (b_1\alpha - 1)(b_2\alpha - 1)e^{-2\alpha D}]}. \tag{6.63}$$

If we check the limits; for $b_1 = b_2 = V_2 = 0$ and $D \to \infty$

$$v_x^{db,\parallel}(z) = V_1 e^{-\alpha z}. \tag{6.64}$$

When $b_2 = V_2 = 0$ and $D \to \infty$

$$v_x^{db,\parallel}(z) = \frac{V_1 e^{-\alpha z}}{b_1\alpha + 1}. \tag{6.65}$$

Note that there is fluid only in upper side of the slab.

When $b_2 = b_1 = V_2 = 0$

$$v_x^{db,\parallel}(z) = \frac{V_1[e^{-\alpha z} - e^{-2D\alpha + \alpha z}]}{1 - e^{-2D\alpha}} = V_1 \frac{\sinh(D\alpha - \alpha z)}{\sinh(D\alpha)}. \tag{6.66}$$

If $V_2 = 0$, then the response function is

$$\begin{aligned} \mathcal{G}_1^{db,\parallel}(\omega) &= \frac{\Pi_{xz}}{V_1} = V_1^{-1}\eta \frac{\partial v_x^{db,\parallel}(x)}{\partial z}_{|z=0} \\ &= \end{aligned} \tag{6.67}$$

where Π_{xz} is the stress in the $\hat{x}$-direction in the surface-normal direction, and the indices 1 is for the bottom wall. For the limit of $\alpha \to 0$

$$\mathcal{G}_1^{db,\parallel}(\omega) \simeq -\frac{\eta}{(b_1 + b_2) + D}. \tag{6.68}$$

For $b_2 = 0$ and $D \to \infty$, the response function, Eq. (6.67), corresponds to Eq. (6.53). If only $b_2 = 0$, then Eq. (6.67) turns into

$$\mathcal{G}_1^{db,\parallel}(\omega) = -\frac{\eta\alpha[1 + e^{-2\alpha D}]}{[(b_1\alpha + 1) + (b_1\alpha - 1)e^{-2\alpha D}]}, \tag{6.69}$$

Note that this $\mathcal{G}_1^{wall}(w)$ is for the force exerted by the fluid on the slab; for the force on the fluid, "$-$" should be"$+$".

For the limit of $\alpha \to 0$, Eq. (6.69) becomes

$$\mathcal{G}_1^{db,\parallel}(\omega) \simeq -\frac{\eta}{b_1 + D}, \tag{6.70}$$

and as either $b_1 \to \infty$ or $D \to \infty$, the response is 0.

6.4. Velocity field of a sphere

To obtain the velocity field of an oscillating sphere, we use the singularity expansion of the point force Green's function [152]

$$G_{ij}^{sp} = \sum_{n=0}^{\infty} C_i(\nabla)^n G_{ij}. \tag{6.71}$$

For a sphere (or for the circular cross section of a cylinder), the first two even terms of above expansion are sufficient to describe the velocity field due the spherical symmetry. This leads for a sphere of radius a

$$G_{ij}^{sp} = (C_0 + C_2 a^2 \nabla_k \nabla_k) G_{ij} \tag{6.72}$$

so that the velocity field follows as $v_i^{sp} = F_j G_{ij}^{sp}$ and F_j is a source force. Note that the actual force acting on the sphere has to be calculated by integration of the surface traction over the sphere surface. In the presence of slip, the boundary condition at the sphere surface splits into the kinematic condition

$$6\pi\eta a \hat{r}_i G_{ij}^{sp} = \hat{r}_j \tag{6.73}$$

for $|\mathbf{r}| = a$, which defines the sphere velocity as $V_i^{sp} = F_i/6\pi\eta a$ such that in the steady (zero-frequency) limit, the source force F_i equals the actual force on the sphere. The Navier boundary condition for the tangential stress reads

$$b(\nabla_k G_{ij}^{sp} + \nabla_i G_{kj}^{sp})\hat{r}_k \mathcal{P}_{li} = (G_{ij}^{sp} - \delta_{ij}/6\pi\eta a)\mathcal{P}_{li} \tag{6.74}$$

for $|\mathbf{r}| = a$, where the projection operator is defined as $\mathcal{P}_{li} = (\delta_{li} - \hat{r}_l \hat{r}_i)$. The boundary conditions fix both coefficients C_0 and C_2 and the result for G_{ij}^{sp} reads

$$\begin{aligned} G_{ij}^{sp} &= \frac{1}{4\pi\eta\alpha^2 r^3} \Big\{ \delta_{ij} \left(E_1[1 + r\alpha + r^2\alpha^2]e^{-r\alpha} - E_2[1 + r\lambda]e^{-r\lambda} \right) \\ &\quad -3\hat{r}_i\hat{r}_j \left(E_1[1 + r\alpha + r^2\alpha^2/3]e^{-r\alpha} \; -E_2[1 + r\lambda + r^2\lambda^2/3]e^{-r\lambda} \right) \Big\} \end{aligned} \tag{6.75}$$

with the coefficients

$$E_1 = \frac{2}{3} e^{\tilde{\alpha}} \frac{(1+2\tilde{b})(3+3\tilde{\lambda}+\tilde{\lambda}^2)}{(2+2\tilde{\lambda}+\tilde{\lambda}^2)(1+\tilde{b}(3+\tilde{\alpha}))+(1+\tilde{\alpha})(1+2\tilde{b})\tilde{\lambda}^2/\tilde{\alpha}^2}, \tag{6.76}$$

$$E_2 = \frac{2}{3} e^{\tilde{\lambda}} \frac{(1+2\tilde{b})(3+3\tilde{\alpha}+\tilde{\alpha}^2)+\tilde{b}\tilde{\alpha}^2(1+\tilde{\alpha})}{(2+2\tilde{\lambda}+\tilde{\lambda}^2)(1+\tilde{b}(3+\tilde{\alpha}))+(1+\tilde{\alpha})(1+2\tilde{b})\tilde{\lambda}^2/\tilde{\alpha}^2}, \tag{6.77}$$

Here, we have defined the dimensionless slip length $\tilde{b} = b/a$ and the dimensionless decay constants $\tilde{\alpha} = a\alpha$ and $\tilde{\lambda} = a\lambda$. In Fig. 6.1 the real part of the velocity vector field $\mathbf{v}^{sp}$ is represented for different parameters in the xy plane with the force applied to the right (x-direction). Within the rows the rescaled frequency ω/ω_0 is constant, within the columns the parameter γ stays constant. The color scale corresponds to the velocity magnitude, while the arrows denote the velocity direction. For all parameter combinations we have $\omega/(\omega_0\gamma) < 1$ and are thus in the propagating wave regime. The discussion is simplified by defining the rescaled propagation wave length

$$\tilde{\Lambda} = \frac{\Lambda}{a} = \frac{c}{\omega/(2\pi)} = \frac{2\pi\gamma^{1/2}\omega_0}{\omega}, \tag{6.78}$$

which follows from Eq. (6.33) in the limit $\omega/(\omega_0\gamma) < 1$. For the parameter combinations on the diagonal we have $\tilde{\Lambda} \simeq 3$, in accord with the wavelength found by visual inspection. In the lower left picture the wave length is $\tilde{\Lambda} \simeq 1.2$, while in the upper right corner we have $\tilde{\Lambda} \simeq 9$ and thus a full wave length does not fit in the graph. To connect to aqueous systems, in water $\gamma = 10^4$ and $\gamma = 10^5$ correspond to radii $a \approx 10^{-7}m$ and $a \approx 10^{-6}m$, respectively. The rescaled frequencies $\omega/\omega_0 = 172$ and $\omega/\omega_0 = 535$ correspond for a radius $a \approx 10^{-6}m$ and water parameters to oscillation frequencies $\omega \simeq 10^8 s^{-1}$ and $\omega \simeq 10^9 s^{-1}$, respectively. To gain global insight into the flow profiles at an oscillating sphere, we in Fig. 6.2 plot the real parts of the normalized velocity profile for an oscillating force acting along the x-direction, in the upper row we show $V^{sp}(x, y = 0)$, i.e. the radial flow profile in the direction of the applied force, in the lower row we show $V^{sp}(x = 0, y)$, i.e. the tangential flow profile. Results are shown for the rescaled wavelengths $\tilde{\Lambda} = 0.2, 1$ and 5 and for frequencies in the propagating and the diffusing wave regimes, i.e. for $\omega/(\omega_0\gamma) < 1$ as well as $\omega/(\omega_0\gamma) > 1$, respectively. Indeed, propagating waves are clearly distinguished from diffusing waves for the radial velocity component (upper row), for the tangential flow component (bottom row) the difference is less pronounced. The other interesting observation is that for spheres small compared to the propagation wave length, i.e. for $\tilde{\Lambda} = 5$, the amplitude of the velocity field away from the sphere (which in the figure is rescaled by the flow velocity at the sphere surface) is much smaller than for a large sphere. This has to do with destructive interference effects from waves emanating from different regions of the sphere surface.

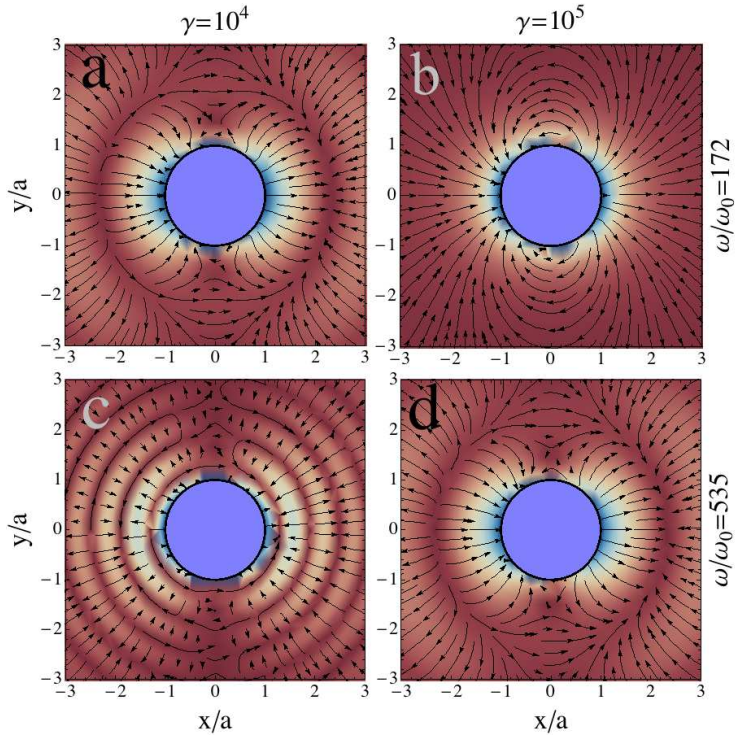

Figure 6.1.: *The Real part of the velocity field of a sphere, $v_i^{sp} = F_j G_{ij}^{sp}$, oscillating in x-direction in the xy plane for no slip, $b = 0$. Combinations for two different values of γ and ω/ω_0 are considered. The arrows indicate the direction of the velocity field, while the color denotes the velocity magnitude; the darker (red) the regions are, the smaller the velocity magnitude is. For water, γ values of 10^4 and 10^5 correspond to radii of $10^{-7}m$ and $10^{-6}m$.*

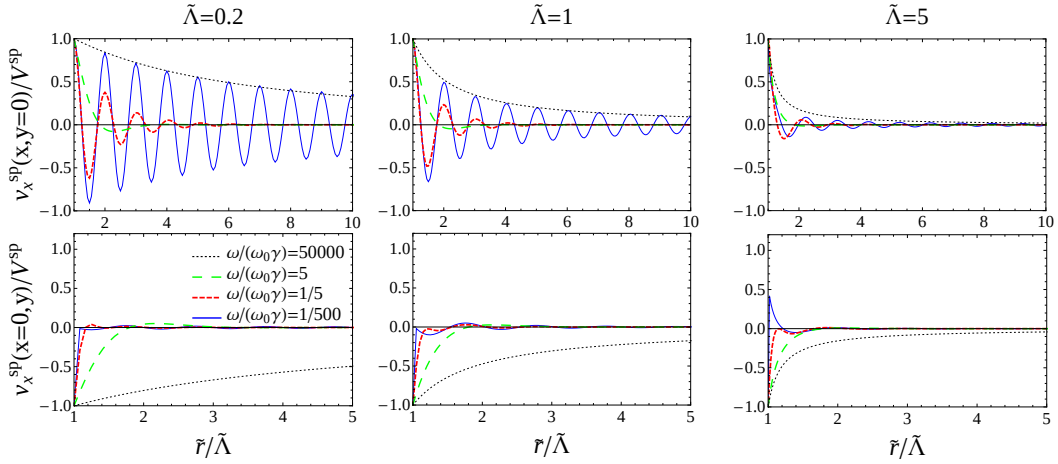

Figure 6.2.: *Normalized amplitude of the real part of the velocity field of a sphere for various values of $\omega/(\omega_0\gamma)$ and $\tilde{\Lambda}$ with no-slip boundary condition, $b = 0$. The upper row shows $V^{sp}(x, y = 0)$, i.e. the radial flow profile in the direction of the applied force, the lower row shows $V^{sp}(x = 0, y)$, i.e. the tangential flow profile. The oscillating force acts along the x-direction.*

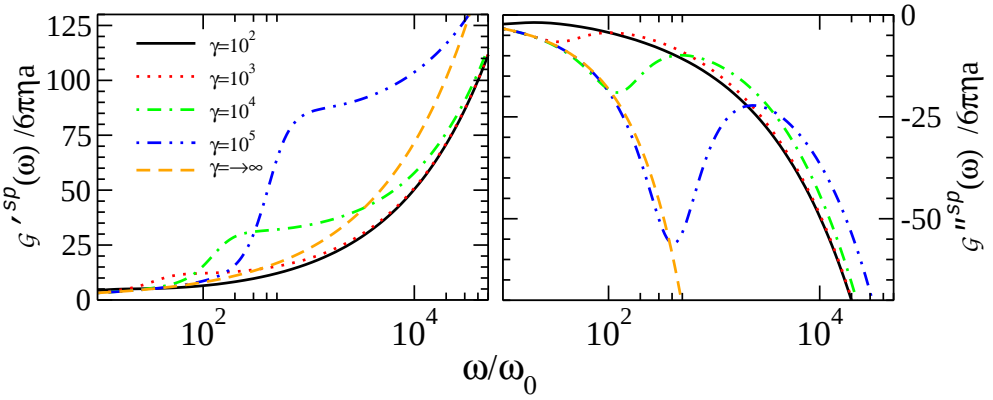

Figure 6.3.: *Real and imaginary parts of the rescaled response function of a sphere,* $\mathcal{G}^{sp}(\omega) = \mathcal{G}'^{sp}(\omega) + \imath\mathcal{G}''^{sp}(\omega)$*, for no-slip boundary condition,* $\tilde{b} = 0$*, given by Eq. (6.84), as a function of the rescaled frequency* ω/ω_0 *for different values of* γ*. The volume viscosity* ζ *is set to* 0*. Note that for the given scale, curves for* $\gamma = 10^2$ *and* $\gamma \to 0$ *are indistinguishable.*

6.4.1. Surface stress at a sphere

The expression for the stress-tensor Green's function given in Eq. (6.43) also applies to the spherical case. The derivative of the sphere Green's function reads

$$\begin{aligned} G^{sp}_{kij} \;=\; & \frac{1}{4\pi\eta r^4\alpha^2}\Big\{\delta_{ij}\hat{r}_k\left(-E_1[3+3r\alpha+2r^2\alpha^2+r^3\alpha^3]e^{-r\alpha}+E_2[3+3r\lambda+r^2\lambda^2]e^{-r\lambda}\right) \\ & -3(\delta_{ki}\hat{r}_j+\delta_{kj}\hat{r}_i)\left(E_1[1+r\alpha+r^2\alpha^2/3]e^{-r\alpha}-E_2[1+r\lambda+r^2\lambda^2/3]e^{-r\lambda}\right) \\ & +3\hat{r}_k\hat{r}_i\hat{r}_j\left(E_1[5+5r\alpha+2r^2\alpha^2+r^3\alpha^3/3]e^{-r\alpha}\right. \\ & \left.-E_2[5+5r\lambda+2r^2\lambda^2+r^3\lambda^3/3]e^{-r\lambda}\right)\Big\}. \end{aligned} \tag{6.79}$$

The frequency-dependent hydrodynamic force on a spherical particle follows by projection of the stress tensor on the surface and integration over the sphere surface,

$$F^{sp}_i = -6\pi\eta a V^{sp}_j \int d^3r\hat{r}_k\Pi_{kij}\delta(|r|-a), \tag{6.80}$$

where V^{sp}_j is the frequency-dependent velocity amplitude. The corresponding response function $\mathcal{G}^{sp}(\omega)$ follows as

$$\delta_{ij}\mathcal{G}^{sp}(\omega) = \frac{F^{sp}_i}{V^{sp}_j} = -6\pi\eta a\int d^3r\hat{r}_k\Pi_{kij}\delta(|r|-a). \tag{6.81}$$

In the calculation the identities $\int d^3r\delta_{ij}\delta(|r|-a) = 4\pi a^2\delta_{ij}$ and $\int d^3r\hat{r}_i\hat{r}_j\delta(|r|-a) = 4\pi a^2\delta_{ij}/3$ are used. The response function follows as

$$\mathcal{G}^{sp}(\omega) = \frac{2}{3}E_1e^{-a\alpha}(1+a\alpha)+\frac{1}{3}E_2e^{-a\lambda}(1+a\lambda) \tag{6.82}$$

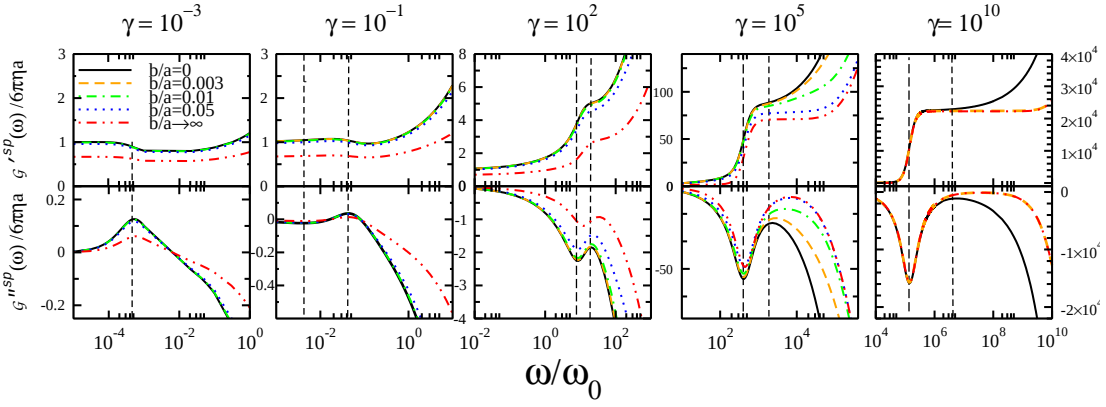

Figure 6.4.: *Real and imaginary parts of the rescaled response function of a sphere,* $\mathcal{G}^{sp}(\omega) = \mathcal{G}'^{sp}(\omega) + \imath\mathcal{G}''^{sp}(\omega)$*, given by Eq. (6.83), as a function of the rescaled frequency,* ω/ω_0 *for various normalized slip lengths,* $\tilde{b}$ *and different values of* γ*. For water,* γ *values of* $10^{-3}, 10^{-1}10^{2}, 10^{5}$ *and* 10^{10} *correspond to radii* $a = 10^{-12}m, 10^{-10}m, 10^{-8}m, 10^{-6}m$ *and* $10^{-4}m$*, respectively. The vertical dashed lines denote the resonant frequency for vanishing slip length,* $\tilde{b} = 0$*. The volume viscosity* ζ *is set to* 0*.*

or, in more explicit form, as

$$\mathcal{G}^{sp}(\omega) = \frac{4\pi\eta a}{3}\frac{(1+\tilde{\lambda})(9+9\tilde{\alpha}+\tilde{\alpha}^2)(1+2\tilde{b})+(1+\tilde{\alpha})(2\tilde{\lambda}^2(1+2\tilde{b})+\tilde{b}\tilde{\alpha}^2(1+\tilde{\lambda}))}{2+2\tilde{\lambda}+\tilde{\lambda}^2)(1+\tilde{b}(3+\tilde{\alpha}))+(1+\tilde{\alpha})(1+2\tilde{b})\tilde{\lambda}^2/\tilde{\alpha}^2}.$$

To investigate the asymptotic behavior of Eq. (6.83), we define real and imaginary parts according to

$$\mathcal{G}^{sp}(\omega) = \mathcal{G}'^{sp}(\omega) + \imath\mathcal{G}''^{sp}(\omega). \tag{6.83}$$

For the real part we obtain the asymptotic behavior

$$\frac{\mathcal{G}'^{sp}(\omega)}{6\pi\eta a} \simeq \begin{cases} \text{for} \quad \omega \to 0 \\ \qquad \frac{1+2\tilde{b}}{1+3\tilde{b}} + \frac{(1+2\tilde{b})^2\sqrt{\omega/\omega_0}}{\sqrt{2}(1+3\tilde{b})^2} + \mathcal{O}[\omega/\omega_0], \\ \text{for} \quad \omega \to \infty \\ \qquad \frac{2}{9}\sqrt{\frac{2}{3}}\sqrt{\omega/\omega_0} + \frac{4(3+4\tilde{b})}{27\tilde{b}} + \mathcal{O}[(\sqrt{\omega/\omega_0})^{-1}], \end{cases}$$

and for the imaginary part we obtain

$$\frac{\mathcal{G}''^{sp}(\omega)}{6\pi\eta a} \simeq \begin{cases} \text{for} \quad \omega \to 0 \\ \qquad -\frac{(1+2\tilde{b})^2\sqrt{\omega/\omega_0}}{\sqrt{2}(1+3\tilde{b})^2} + \frac{\omega/\omega_0\left(9-2\gamma+63\tilde{b}+18\tilde{b}^2(8+\gamma)+18\tilde{b}^3(6+\gamma)\right)}{18(1+3\tilde{b})^3\gamma} + \mathcal{O}[(\omega/\omega_0)^{3/2}], \\ \text{for} \quad \omega \to \infty \\ \qquad -\frac{2}{9}\sqrt{\frac{2}{3}}\sqrt{\omega/\omega_0} + \frac{-24+32\left(-3+\sqrt{3}\right)\tilde{b}+\left(-96+\sqrt{3}(64+3\gamma)\right)\tilde{b}^2}{54\sqrt{2}\sqrt{\omega/\omega_0}\tilde{b}^2} + \mathcal{O}[(\omega/\omega_0)^{-1}]. \end{cases}$$

As $\omega \to 0$, the real part of the response function goes to $6\pi\eta a$ for $\tilde{b} \to 0$ and $4\pi\eta a$ for $\tilde{b} \to \infty$, the standard steady-state results [81]. The compressibility effects (which are

parameterized by the parameter γ) are rather mild and only show up in higher order corrections.

As the normalized slip length $\tilde{b}$ goes to zero, which corresponds to the no-slip boundary condition, equation (6.83) turns into

$$\mathcal{G}^{sp}(\omega) = \frac{4\pi\eta a}{3}\frac{(1+\tilde{\lambda})(9+9\tilde{\alpha}+\tilde{\alpha}^2)+2\tilde{\lambda}^2(1+\tilde{\alpha})}{2(1+\tilde{\lambda})+(1+\tilde{\alpha}+\tilde{\alpha}^2)\tilde{\lambda}^2/\tilde{\alpha}^2}. \tag{6.84}$$

In the incompressible limit, when $\tilde{\lambda} \to 0$, Eq. (6.84) crosses over to $\mathcal{G}^{sp}(\omega) = 6\pi\eta a(1 + a\alpha + a^2\alpha^2/9)$, the well-known Stokes result [81].

In the limit of $b \to \infty$, the perfect slip case as realized for bubbles, Eq. (6.83) reads

$$\mathcal{G}^{sp}(\omega) = \frac{4\pi\eta a}{3}\frac{(1+\tilde{\lambda})(18+18\tilde{\alpha}+3\tilde{\alpha}^2+\tilde{\alpha}^3)+4(1+\tilde{\alpha})\tilde{\lambda}^2}{(2+2\tilde{\lambda}+\tilde{\lambda}^2)(3+\tilde{\alpha})+2(1+\tilde{\alpha})\tilde{\lambda}^2/\tilde{\alpha}^2}. \tag{6.85}$$

Again taking the incompressible limit, corresponding to $\tilde{\lambda} \to 0$, Eq. (6.85) reduces to

$$\mathcal{G}^{sp}(\omega) = 6\pi\eta a\frac{(2+2\tilde{\alpha}+\tilde{\alpha}^2/3+\tilde{\alpha}^3/9)}{(3+\tilde{\alpha})}, \tag{6.86}$$

which is Stokes' incompressible result for perfect slip boundary conditions.

Fig. 6.3 illustrates the effect of compressibility for zero slip, $\tilde{b} = 0$, corresponding to the result given in Eq. (6.84). The compressibility is tuned by changing γ from 10^2 (which is indistinguishable from the $\gamma = 0$ limit) to ∞, the higher γ, the more incompressible the liquid. What is remarkable is that both asymptotic limits, $\gamma = 0$ and $\gamma = \infty$, corresponding to a fluid of vanishing and infinite sound velocity, respectively, are finite and well-behaved, in agreement with the asymptotic expansion in Eqs. (6.84) and (6.84). Furthermore, the dependence of the response function on γ is non-monotonic.

In Fig. 6.4 the response function is shown for five different γ values, $\gamma = 10^{-3}, 10^{-1}, 10^2, 10^5$ and 10^{10}, which correspond to sphere radii of $a = 10^{-12}m$, $10^{-10}m$, $10^{-8}m$, $10^{-6}m$ and $10^{-4}m$ in water, respectively. These graphs reveal a pronounced dependence on the slip length, particularly for high frequencies. From the plots a double resonance behavior of the imaginary part is discerned. A sharp minimum is observed for high γ values, while for $\gamma \ll 1$, the minimum is less pronounced and the maximum is more visible. These extrema are defined by.

$$\frac{\partial \mathcal{G}''^{sp}(\omega)}{\partial\omega}|_{\omega^*} = 0. \tag{6.87}$$

Based on asymptotic analysis, the minimum ω^*_{min} obeys the scaling laws

$$\omega^*_{min} \simeq \begin{cases} \text{for} \quad \gamma \to 0 \\ \qquad \frac{1}{2}\omega_0\gamma^2 - \frac{23}{18}\omega_0\gamma^3 + \mathcal{O}(\gamma^4), \\ \\ \text{for} \quad \gamma \to \infty \\ \qquad \sqrt{2}\omega_0\gamma^{1/2} - 2.15822\ \omega_0\gamma^{1/4} + \mathcal{O}(1) \approx c/a, \end{cases} \tag{6.88}$$

and the maximum scales as

$$\omega^*_{max} \simeq \begin{cases} \text{for} \quad \gamma \to 0 \\ \quad \text{for} \quad b = 0 \\ \qquad \frac{6}{11}\,\omega_0\gamma - 0.54628\,\omega_0\gamma^{3/2} + \mathcal{O}(\gamma^2) \approx c^2\rho_0/\eta, \\ \quad \text{for} \quad b \neq 0 \\ \qquad \frac{6+18\tilde{b}}{11+30\tilde{b}}\,\omega_0\gamma + \mathcal{O}(\gamma^{3/2}), \\ \text{for} \quad \gamma \to \infty \\ \quad \text{for} \quad b = 0 \\ \qquad 2^{1/3}\omega_0\gamma^{2/3} - \frac{20}{9}\omega_0\gamma^{1/2} + \mathcal{O}(\gamma^{1/3}), \\ \quad \text{for} \quad b \neq 0 \\ \qquad \sqrt{3/2}\,\omega_0\gamma^{3/4} + \mathcal{O}(\gamma^{1/4}). \end{cases} \tag{6.89}$$

In Fig. 6.5, ω^*_{min}/ω_0 and ω^*_{max}/ω_0 as determined numerically from the solution of Eq. (6.87), dotted and broken lines, are compared to the asymptotic scaling laws (solid straight lines). The most pronounced features in Fig. 6.4 are obtained for ω^*_{min} for large γ and for ω^*_{max} for small γ, for which we now advance some simple scaling ideas. In fact, ω^*_{min} for large γ equals $\omega^*_{min} \sim \omega_0\gamma^{1/2} \sim c/a$ which is the inverse time a propagating compression wave needs to travel a distance corresponding to the sphere size a. This resonance can therefore be thought of as due to interference between waves emanating from different parts of the sphere. As γ decreases and reaches unity, this scaling law hits the boundary between the diffusive and propagative regimes, which scales as $\omega \sim \omega_0\gamma$, and thus the above scaling description of the resonance becomes invalid. The diffusive regime is indicated in Fig. 6.5 by a dark shading. In fact, in the limit of small γ a maximum shows up right at the boundary between the diffusive and propagative regime with the scaling $\omega^*_{max} \sim \omega_0\gamma$. This resonance-like feature is caused by interference effects between compression and shear effects, and related to the fact that compression waves are marginally propagative.

6.5. Velocity field of a cylinder

The Green's function approach is now applied to cylinders. This problem has been studied in the past for incompressible fluids by several authors [157, 158]. We consider a cylinder as illustrated in Fig. 6.6 of radius a aligned along the z-direction and treat oscillations parallel and perpendicular to the long axis.

We first derive the Green's function of a line source. To that end, we integrate the Green's function given in Eq. (6.35) over z as

$$G^{line}_{ij}(\sigma) \;=\; \int_{-\infty}^{+\infty} dz G_{ij}\,(x, y, z), \tag{6.90}$$

where $\sigma = x^2 + y^2$. After some algebra detailed in section C.1, the line Green's function can be expressed in terms of Bessel functions and separated into shear (transverse) and

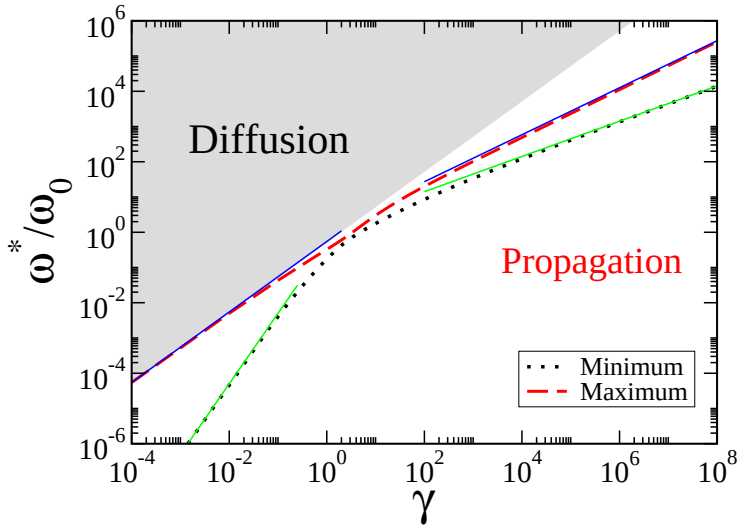

Figure 6.5.: *Rescaled resonance frequencies ω^*/ω_0 of a sphere for vanishing slip length, $b = 0$, as a function of γ. We distinguish a local maximum of the imaginary response function $\mathcal{G}''^{sp}(\omega)$ (broken line) from the local minimum (dotted line). Asymptotic laws given by Eqs. (6.88) and (6.89) are denoted by solid lines. The extrema are indicated by the vertical dashed lines in Fig. 6.4. The grey area denotes the diffusive regime, where compression perturbations are overdamped, while in the white area compression perturbations give rise to propagating waves.*

compression (longitudinal) contributions. The result is

$$G_{ij}^{line} = G_{ij}^{line,T} + G_{ij}^{line,L} \tag{6.91}$$

(see section C.1 for details). In the following sections, we explicitly calculate the Green's functions for parallel and perpendicular motions.

6.5.1. Perpendicular motion

We first consider motion perpendicular to the long axis. Similar to the singularity ansatz for the sphere, Eq. (6.72), we write the Green's function for the cylinder with finite radius as

$$\begin{aligned} G_{ij}^{cyl,\perp} &= D_0 G_{ij}^{line} + D_2 a^2 \nabla^2 G_{ij}^{line}, \\ &= E_1^{cyl} G_{ij}^{line,T} + E_2^{cyl} G_{ij}^{line,L}, \end{aligned} \tag{6.92}$$

Here, ∇^2 operator acts only in 2-dimension. Following, for perpendicular oscillations, Eq. (6.91) reduces to

$$\begin{aligned} G_{ij}^{line,T}(\sigma) &= \frac{\alpha}{2\pi\eta\alpha^2\sigma}\{\delta_{ij}[K_1(\alpha\sigma) + \alpha\sigma K_0(\alpha\sigma)] - \hat{r}_i\hat{r}_j[2K_1(\alpha\sigma) + \alpha\sigma K_0(\alpha\sigma)]\}, \\ G_{ij}^{line,L}(\sigma) &= \frac{\lambda}{2\pi\eta\alpha^2\sigma}\{-\delta_{ij}[K_1(\lambda\sigma)] + \hat{r}_i\hat{r}_j[2K_1(\lambda\sigma) + \lambda\sigma K_0(\lambda\sigma)]\}, \end{aligned} \tag{6.93}$$

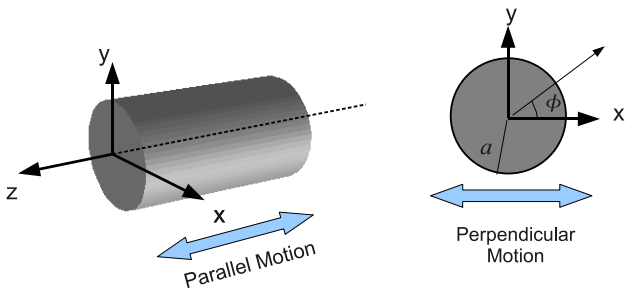

Figure 6.6.: *Illustration of a cylinder with radius a in cartesian coordinates. The parallel motion is defined along the z-direction. Contributions from the top and the bottom edges are neglected.*

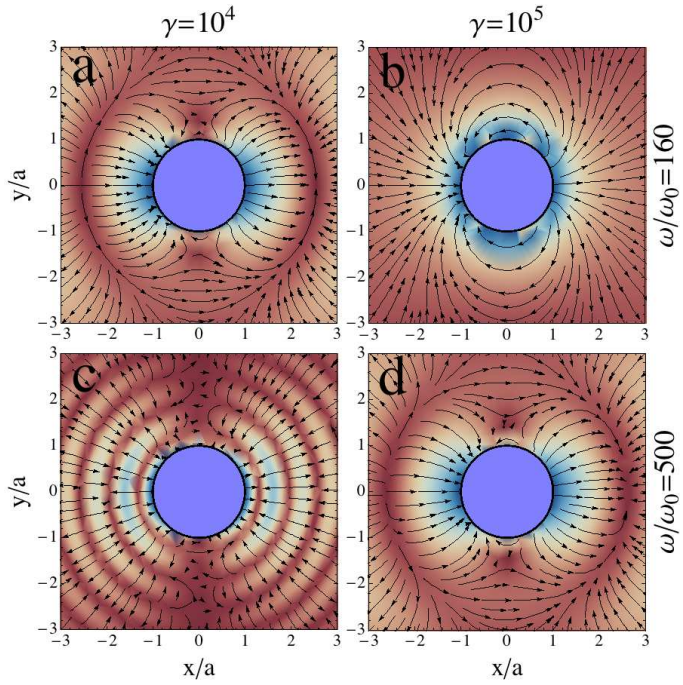

Figure 6.7.: *The real part of the velocity field of a perpendicularly oscillating cylinder, $v_i^{cyl,\perp} = F_j G_{ij}^{cyl,\perp}$, in the xy plane for no slip, $b = 0$. The oscillation is along the x-direction. The axes are normalized by the cylinder radius, and the arrows indicate the direction of the velocity vector. The darker (red) the regions are, the smaller the velocity magnitude is. Combinations for two different values of γ and ω/ω_0 are considered. For water, γ values of 10^4 and 10^5 correspond to radii of $10^{-7}m$ and $10^{-6}m$.*

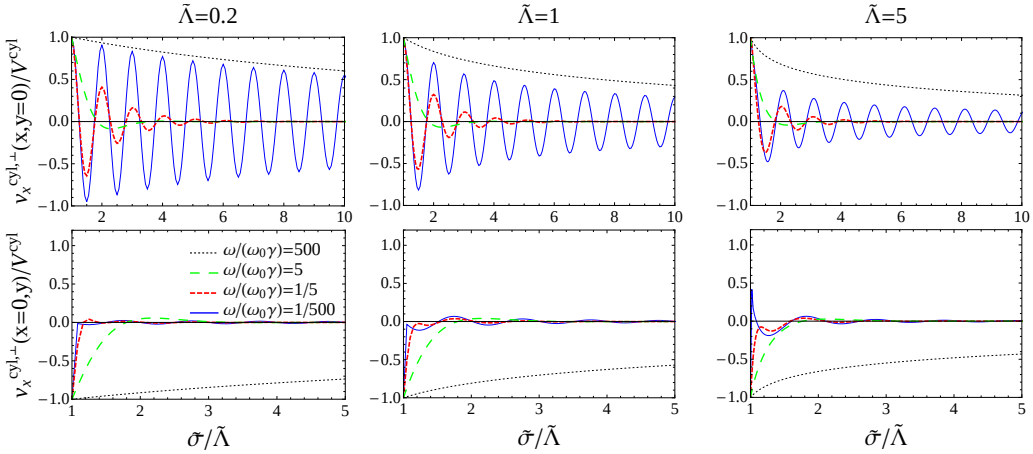

Figure 6.8.: *The normalized amplitude of the real part of the velocity field generated by a perpendicularly oscillating cylinder, for various values of* $\omega/(\omega_0\gamma)$ *and* $\tilde{\Lambda}$ *with no-slip condition,* $b = 0$*. The upper row shows* $V(x, y = 0)$*, i.e. the radial flow profile in the direction of the applied force, the lower row shows* $V(x = 0, y)$*, i.e. the tangential flow profile. The oscillating force acts along the x-direction and the distance is normalized by the wavelength given by Eq. 6.78.*

which has a similar structure as Eq. (6.75) (see section C.1 for the detailed calculation). The coefficients E_1^{cyl} and E_2^{cyl} are determined by the boundary conditions. The normal component of the velocity field at the cylinder surface satisfies

$$F_k \hat{r}_i G_{ij}^{cyl,\perp} = V_k^{cyl} \hat{r}_j \tag{6.94}$$

for $|\sigma| = a$, where V_k^{cyl} is velocity of the cylinder in perpendicular motion and F_k is the source with units of force per unit length. The Navier boundary condition for the tangential velocity component reads

$$b(\nabla_k G_{ij}^{cyl,\perp} + \nabla_i G_{kj}^{cyl,\perp})\hat{r}_k \mathcal{P}_{li} = (G_{ij}^{cyl,\perp} - \delta_{ij} F_k / V_k^{cyl})\mathcal{P}_{li}, \tag{6.95}$$

and holds for $|\sigma| = a$, where the projection operator is defined as $\mathcal{P}_{li} = (\delta_{li} - \hat{r}_l \hat{r}_i)$. Applying above conditions on $G_{ij}^{cyl,\perp}$ gives

$$\begin{aligned} E_1^{cyl} &= -\frac{2\pi\eta\alpha^2}{F_i/V_i^{cyl}} \frac{N_1 + N_2}{N_2 M_1 - N_1 M_2}, \\ E_2^{cyl} &= \frac{2\pi\eta\alpha^2}{F_i/V_i^{cyl}} \frac{M_1 + M_2}{N_2 M_1 - N_1 M_2}. \end{aligned} \tag{6.96}$$

After using recursion relations given in the appendix section, N_i and M_i can be expressed

in terms of Bessel functions as

$$\begin{aligned} M_1 &= -2(\alpha/a)\tilde{b}[2K_1(\alpha a)+\alpha a K_0(\alpha a)] - \tilde{b}\alpha^3 a K_1(\alpha a) \\ &\quad -(\alpha/a)[K_1(\alpha a)+\alpha a K_0(\alpha a)], \\ M_2 &= -(\alpha/a)K_1(\alpha a), \\ N_1 &= 2(\lambda/a)\tilde{b}[2K_1(\lambda a)+\lambda a K_0(\lambda a)] + (\lambda/a)K_1(\lambda a), \\ N_2 &= (\lambda/a)[K_1(\lambda a)+\lambda a K_0(\lambda a)]. \end{aligned} \tag{6.97}$$

In Fig. 6.7, we show the real part of the velocity field, $v_i^{cyl,\perp} = F_j G_{ij}^{cyl,\perp}$, for various fluid parameters. In the columns γ is constant while in the rows ω/ω_0 is constant. The color scale is a measure of the magnitude of the velocity, in the dark (red) regions the velocity is zero. For water γ values 10^4 and 10^5 correspond to radii of $10^{-7}m$ and $a \approx 10^{-6}m$, respectively. Since with the parameters chosen, all four systems belong to the propagative regime, the wave lengths discernable in the plots correspond to the predictions of Eq. (6.78).

In Fig. 6.8, the real part of the flow field of a cylinder in perpendicular motion is shown for various normalized wavelengths $\tilde{\Lambda} = 0.2, 1$ and 5, as in the sphere problem. For each $\tilde{\Lambda}$ value, velocity fields for different $\omega/(\omega_0\gamma)$ values $500, 5, 1/5$ and 500 are shown. The upper row shows $v_x^{cyl,\perp}(x, y = 0)$, i.e. the radial flow profile in the direction of the oscillation, the lower row shows $v_x^{cyl,\perp}(x = 0, y)$, i.e. the tangential flow profile. For $\omega/(\omega_0\gamma) = 1/500$, waves are clearly seen (black dotted line), however, as $\omega/(\omega_0\gamma)$ increases the number of waves observed goes down. As the rescaled wave length, $\tilde{\Lambda} = \Lambda/a$, increases, the amplitude of the velocity in the far field decreases because of interference effects, however, this effect is smaller than for the spherical case shown in Fig. 6.2.

6.5.2. Surface stress at a cylinder due to perpendicular motion

The stress Green's function defined in Eqs. (6.41) and (6.43) also holds for the cylindrical geometry. The force acting on the cylinder per unit length is calculated by the integration of the traction force over the perimeter of the cylinder

$$F_i^{cyl} = -F_j \int d^2 r \hat{r}_k \Pi_{kij} \delta(|r| - a), \tag{6.98}$$

where F_j is the source in the units of force per length. The cylindrical response function is defined as

$$\delta_{ij}\mathcal{G}_\perp^{cyl}(\omega) = \frac{F_i^{cyl}}{V_j^{cyl}} = -\frac{F_l}{V_j^{cyl}} \int d^2 r \hat{r}_k \Pi_{kil} \delta(|r| - a), \tag{6.99}$$

where we make use of the identities $\int d^2 \delta_{ij} \delta(|r| - a) = 2\pi a \delta_{ij}$ and $\int d^2 \hat{r}_i \hat{r}_j \delta(|r| - a) = \pi a \delta_{ij}$. The final result for the cylindrical response function reads

$$\delta_{ij}\mathcal{G}_\perp^{cyl}(\omega) = \frac{F_i/V_j^{cyl}}{2}\left(E_1^{cyl}\tilde{\alpha}K_1(\tilde{\alpha}) + E_2^{cyl}\tilde{\lambda}K_1(\tilde{\lambda})\right), \tag{6.100}$$

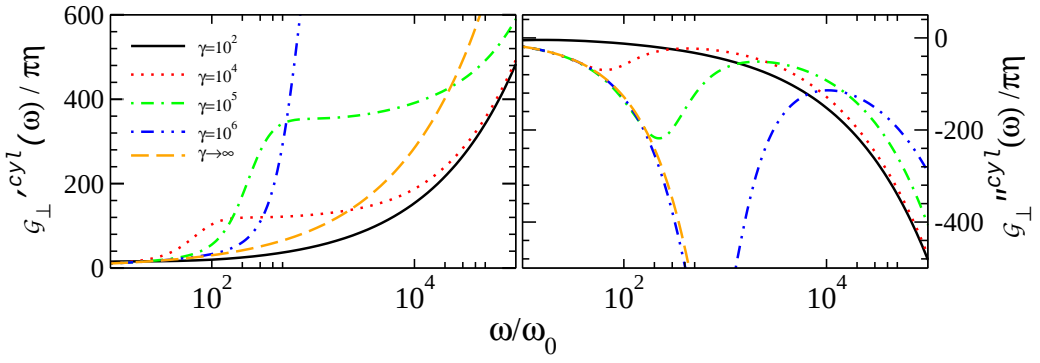

Figure 6.9.: *Real and imaginary parts of the response function of a cylinder for perpendicular motion given by Eq. (6.100) with no-slip boundary condition, $\tilde{b} = 0$, as a function of the compressibility parameter γ. The volume viscosity ζ is set to 0. Note that for the given scale, the curves for $\gamma = 10^2$ and $\gamma \to 0$ are indistinguishable.*

where $\tilde{\alpha} = a\alpha$ and $\tilde{\lambda} = a\lambda$. Note that the prefactor F_i/V_j^{cyl} cancels the inverse factor in E_1^{cyl} and E_2^{cyl}. In the incompressible limit, $\lambda \to 0$, and for the no-slip condition, $b = 0$, above equation crosses over to the known non-steady solution for the incompressible flow field at a cylinder [157], which is explicitly demonstrated in section C.4. The asymptotic behavior of $\mathcal{G}_\perp^{cyl}$ is obtained by asymptotic analysis of the modified Bessel function such as $K_0(x) \simeq -\ln x$ and $K_1(x) \simeq 1/x$ for $\omega \to 0$ and $K_n(x) \simeq e^{-x}/\sqrt{x}$ for $\omega \to \infty$. Using again the separation into real and imaginary parts as in Eq. (6.83), the asymptotic behavior follows as

$$\frac{\mathcal{G}_\perp'^{cyl}(\omega)}{\pi\eta} \simeq \begin{cases} \text{for } \omega \to 0 \\ -\frac{8}{(1+2\tilde{b})^2 ln(\omega/\omega_0)} + \frac{16\tilde{b}}{[(1+2\tilde{b})ln(\omega/\omega_0)])^2} + \mathcal{O}(\omega/\omega_0), \\ \text{for } \omega \to \infty \\ \sqrt{\frac{2}{3}}\sqrt{\omega/\omega_0} + \frac{3+4b}{3b} + \mathcal{O}[(\sqrt{\omega/\omega_0})^{-1}]. \end{cases} \tag{6.101}$$

$$\frac{\mathcal{G}_\perp''^{cyl}(\omega)}{\pi\eta} \simeq \begin{cases} \text{for } \omega \to 0 \\ -\frac{4\pi}{[(1+2\tilde{b})ln(\omega/\omega_0)]^2} + \mathcal{O}(\omega/\omega_0), \\ \text{for } \omega \to \infty \\ -\sqrt{\frac{2}{3}}\sqrt{\omega/\omega_0} + \mathcal{O}[(\sqrt{\omega/\omega_0})^{-1}]. \end{cases} \tag{6.102}$$

In contrast to the spherical case, the steady state solution obtained in the limit $\omega \to 0$ goes to zero logarithmically, whereas at high frequency a divergence as $\omega^{1/2}$ is found, identical to the the sphere case. Plots of $\mathcal{G}_\perp^{cyl}(\omega)$ are given in Figs. 6.9 and 6.10 for $\tilde{b} = 0$ and $\tilde{b} \neq 0$, respectively. Fig. 6.9 shows the effects of varying the compressibility parameter γ, Fig. 6.10 demonstrates the effect of varying slip length $\tilde{b}$ for given γ. For water, the γ values considered, $\gamma = 10^{-3}, 10^{-1}, 10^2, 10^6$ and 10^{10}, correspond to radii $a = 10^{-12}m, 10^{-10}m, 10^{-8}m, 10^{-6}m$ and $10^{-4}m$, respectively.

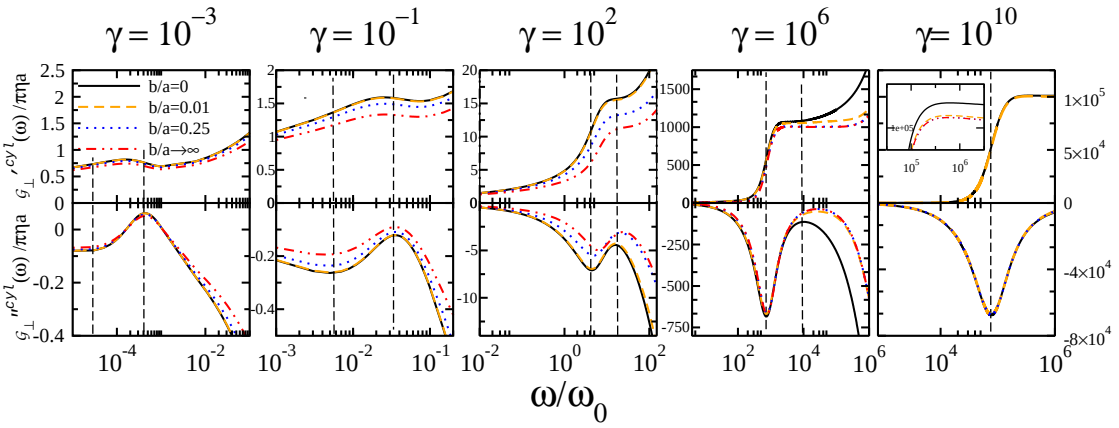

Figure 6.10.: *Real and imaginary parts of the rescaled response function of a cylinder in perpendicular motion given by Eq. (6.100) as a function of the rescaled frequency ω/ω_0 for various $\tilde{b}$ and γ values. For water, γ values of $10^{-3}, 10^{-1}, 10^{2}, 10^{6}$ and 10^{10} correspond to radii $a = 10^{-12}m, 10^{-10}m, 10^{-8}m, 10^{-6}m$ and $10^{-4}m$, respectively. The vertical dashed lines denote the resonance frequencies for vanishing slip length, $\tilde{b} = 0$. The volume viscosity ζ is set to 0.*

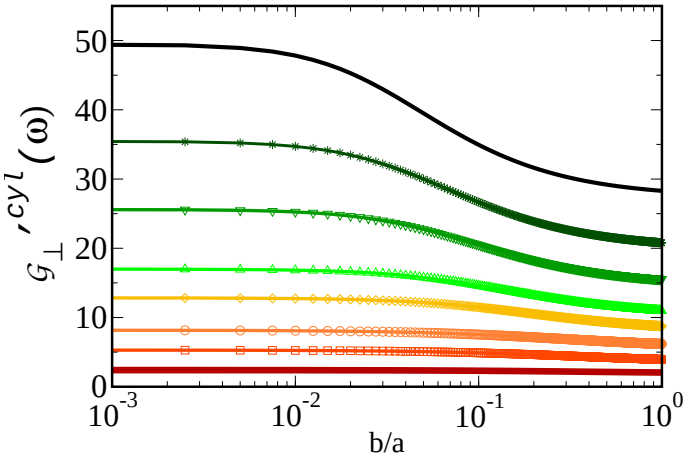

Figure 6.11.: *Real part of the response function $\mathcal{G}'^{cyl}_{\perp}(\omega)$ given by Eq. (6.100) for a cylinder oscillating perpendicular to its long axis as a function of the normalized slip length, $\tilde{b} = b/a$. The curves are for constant ω/ω_0 values of $10^{-1}, 1, 5, 50, 100, 250, 500$ and 10^{3} from bottom (red) to top (green), respectively. The compressibility constant is $\gamma = 10^{2}$. The volume viscosity ζ is set to 0.*

The effect of surface slip is illustrated in Fig. 6.11 which shows $\mathcal{G}'^{cyl}_{\perp}(\omega)$ versus $\tilde{b} = b/a$ for fixed $\gamma = 10^2$. Each curve corresponds to a fixed ω/ω_0 value between 10^{-1} and 10^3 from bottom (red) to top (green), respectively. At low frequency, $\mathcal{G}'^{cyl}(\omega)$ changes only little with varying slip length (curves at the bottom), but for higher frequency the slip length has a considerable effect on $\mathcal{G}'^{cyl}(\omega)$ (curves at the top).

As seen from the response functions in Figs. 6.9 and 6.10, also for the cylindrical geometry a resonant behavior is obtained. The asymptotic scaling of the resonance where the imaginary response shows a minimum obeys the asymptotic scaling laws

$$\omega^*_{min} \simeq \begin{cases} \text{for} & \gamma \to 0 \\ & -\omega_0 \gamma ln\gamma + \mathcal{O}(\gamma^2), \\ \text{for} & \gamma \to \infty \\ & 0.77129\ \omega_0 \gamma^{1/2} + \mathcal{O}(\gamma^{1/4}) \approx c/a, \end{cases} \tag{6.103}$$

and the maximum scales as

$$\omega^*_{max} \simeq \begin{cases} \text{for} & \gamma \to 0 \\ & 4.31252\ \omega_0 \gamma + \mathcal{O}(\gamma^{3/2}) \approx c^2 \rho_0/\eta, \\ \text{for} & \gamma \to \infty \\ & 2^{1/3} \omega_0 \gamma^{2/3} + \mathcal{O}(\gamma^{1/2}). \end{cases} \tag{6.104}$$

These function are displayed in Fig. 6.12. Except the logarithmic correction term for small γ, the result is identical to the sphere case.

6.5.3. Parallel motion

For parallel oscillations of the cylinder, the velocity field can be calculated directly from the line Green's function given in Eq. (6.91). The cylinder Green's function reads

$$G^{cyl,\parallel}_{zz} = C_0 G^{line}_{zz}, \tag{6.105}$$

where the coefficient C_0 is determined by the boundary condition at the cylinder surface. Using Integral functions given in section C.1, the line Green function for the parallel motion can be written as

$$G^{line}_{zz}(\sigma) \quad = \quad \frac{1}{2\pi\eta} K_0(\alpha\sigma) \tag{6.106}$$

and is independent of the compressibility parameter γ. Similar to a tangentially moved plane, the parallel motion of a cylinder generates only shear. The Navier-boundary condition at $\sigma = a$ reads

$$b \frac{\partial v^{cyl,\parallel}_z}{\partial \sigma} = (v^{cyl,\parallel}_z - V^{cyl}_z), \tag{6.107}$$

where V^{cyl}_z is the velocity of the cylinder, the fluid velocity field is $v^{cyl,\parallel}_z = F_z G^{cyl,\parallel}_{zz}$, and F_z is the source in units of a force per length. After some algebra and with the help of recursion relations introduced in section C.1, we obtain

$$C_0 = \frac{2\pi\eta}{F_z/V^{cyl}_z [b\alpha K_1(\alpha a) + K_0(\alpha a)]} \tag{6.108}$$

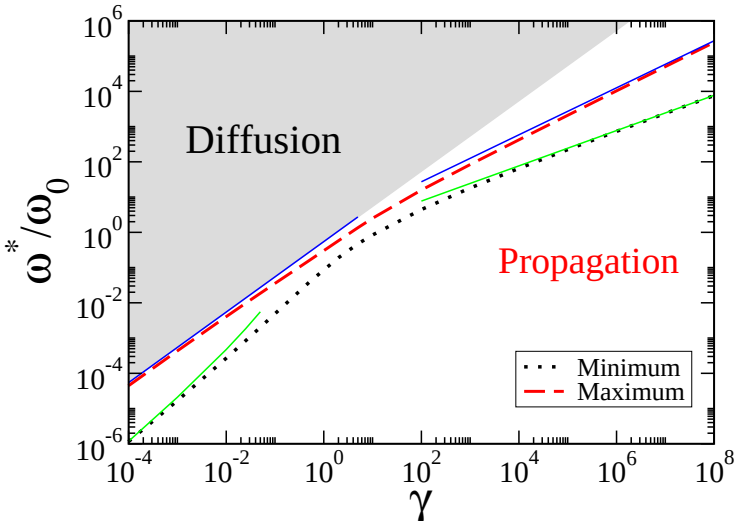

Figure 6.12.: *Rescaled resonance frequencies ω^*/ω_0 of a cylinder in perpendicular motion for vanishing slip length, $b = 0$, as a function of γ. We distinguish a local maximum of the imaginary response function $\mathcal{G}_\perp''^{cyl}(\omega)$ (broken line) from the local minimum (dotted line). Solid lines are scaling laws given in Eqs. (6.103) and (6.104). The extrema are indicated by the vertical dashed lines in Figure 6.10. The grey area denotes the diffusive regime, where compression perturbations are overdamped, while in the white area compression perturbations give rise to propagating waves.*

and thus according to equation (6.105)

$$G_{zz}^{cyl,\parallel}(\sigma) = \frac{K_0(\alpha\sigma)}{F_z/V_z^{cyl}[b\alpha K_1(\alpha a) + K_0(\alpha a)]}. \tag{6.109}$$

6.5.4. Surface stress at cylinder due to parallel motion

The force on the cylinder per unit length is calculated by integrating the surface traction over the perimeter of the cylinder

$$\begin{aligned} F_z^{cyl,\parallel} &= -\int_0^{2\pi}\int_0^a d\theta\sigma d\sigma \frac{\partial v_z^{cyl,\parallel}(\sigma)}{\partial\sigma}\delta(|\sigma| - a) \\ &= F_z C_0 \alpha a K_1(\alpha a). \end{aligned} \tag{6.110}$$

The response function due the parallel motion of the cylinder follows as

$$\mathcal{G}_\parallel^{cyl}(\omega) = \frac{F_z^{cyl,\parallel}}{V_z^{cyl}} = 2\pi\eta \frac{\tilde\alpha K_1(\tilde\alpha)}{\tilde b\tilde\alpha K_1(\tilde\alpha) + K_0(\tilde\alpha)}. \tag{6.111}$$

In the limit of infinite radius, $a \to \infty$, this response function turns into the response function of a tangentially oscillating plane given in Eq. (6.53), as expected and demonstrated in section C.3. In Fig. 6.13, above response function is illustrated for various

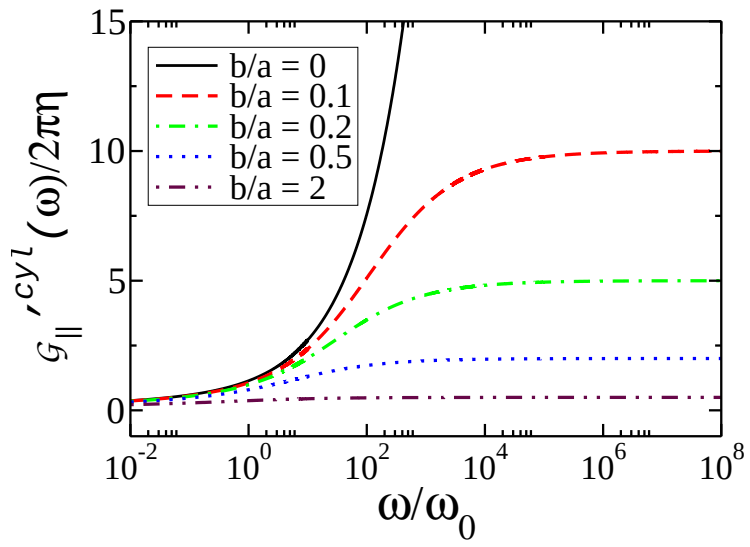

Figure 6.13.: *Real part of $\mathcal{G}_{\parallel}^{cyl}(\omega)$ given by Eq. (6.111), the response function for a cylinder oscillating parallel to its long axis for various slip lengths, $\tilde{b} = b/a$. Note that there is no dependence on the compressibility parameter γ.*

slip lengths. The asymptotic behavior of Eq. (6.111) in the limit $\omega \to 0$ reads

$$\mathcal{G}_{\parallel}^{cyl}(\omega) \simeq 2\pi\eta \left(\frac{4\tilde{b} - 2ln(\omega/\omega_0)}{(2\tilde{b} - ln(\omega/\omega_0))^2} - \imath \frac{\pi}{(2\tilde{b} - ln(\omega/\omega_0))^2} \right). \tag{6.112}$$

The ratio of the parallel response function given above and the perpendicular response function, Eq. (6.101), is $\mathcal{G}_{\perp}^{cyl}/\mathcal{G}_{\parallel}^{cyl} \simeq 2$ in the limit of $\omega \to 0$, in agreement with slender body theory [152]. On the other hand, the high frequency behavior of $\mathcal{G}_{\parallel}^{cyl}(\omega)$ is identical to that of a tangentially oscillating plane, Eq. (6.53), and given by

$$\mathcal{G}_{\parallel}^{cyl}(\omega) \simeq 2\pi\eta a \frac{\alpha}{b\alpha + 1}, \tag{6.113}$$

for a derivation see section C.3.

6.6. Conclusion and remarks

In this chapter, the response of a viscous compressible fluid to the motion of a plane, a sphere and a cylinder has been calculated as a function of surface slip length and frequency using a Green's function approach. We construct the flow fields around these objects in closed form. The response functions for the sphere and cylinder display a

resonant feature at a frequency $\omega^* \sim \omega_0 \gamma^{1/2} = c/a$ for high enough values of the parameter γ (i.e. for low enough values of the compressibility), where c/a is the inverse time sound needs to travel a typical distance a corresponding to the sphere or cylinder radius. For small frequencies a distinct resonance appears roughly at the boundary between the propagating and diffusive regimes. The effect of slip on the drag force is shown to be particularly important for high frequencies.

We have defined the frequency dependent response function $\mathcal{G}(\omega)$ (which corresponds to a frequency-dependent friction coefficient) in the linear-response limit and in the absence of inertia effects by $F_i(\omega) = \delta_{ij}\mathcal{G}(\omega)V_j(\omega)$, where $V_j(\omega)$ is the frequency dependent particle velocity and $F_i(\omega)$ the frequency dependent external force acting on the particle, e.g., for a harmonic trap with stiffness K, it reads $\imath K V_i(\omega)/\omega$. For a particle with a finite effective mass m_0, corresponding to the particle mass minus the mass of the displaced fluid, the equation of motion reads

$$-\imath\omega m_0 V_i(\omega) + \mathcal{G}(\omega)V_i(\omega) = F_i(\omega). \tag{6.114}$$

This shows that the imaginary part of the response function, $\mathcal{G}''(\omega)$, acts like an – in general frequency-dependent – additional mass of the particle, while the real part of the response function, $\mathcal{G}'(\omega)$, corresponds to the frequency dependent friction coefficient. The frequency dependent power dissipation reads
$\mathcal{P}(\omega) = Re(F_i(\omega)V_i(-\omega)) = \mathcal{G}'(\omega)|V_i^2(\omega)|$, which clearly shows that dissipation is a non-linear effect that does not influence response functions on the linear level. The real and the imaginary parts of the response function can be directly measured by micro-rheological methods [83, 84]. By external excitation of cylindrical geometries such as nanotubes or cantilevers, the slip length can be directly inferred from expressions for the response function given in Eqs. (6.100) and (6.111). Since the imaginary and real parts of the response function are related via Kramers-Kronig relation, probing either the real or imaginary part is sufficient to obtain the overall response function. Alternatively, by measuring the spectral density of particle thermal fluctuations, and invoking the fluctuation-dissipation theorem, one can also infer the complete response function. Note that in driven systems non-linear effects can in principle become important and lead to deviations from our linear analysis, equilibrium measurements based on particle fluctuations are by definition in the linear-response regime.

Viscoelastic effects can be easily taken into account in various standard models, the Maxwell model couples elasticity and viscosity in series and corresponds to a viscoelastic fluid. It can be incorporated into our framework by replacing the viscosity by a frequency dependent function

$$\eta(\omega) = \frac{\eta_0}{1 - \imath\omega\tau} \tag{6.115}$$

with a similar expression for the volume viscosity [93, 95, 155]. The viscoelastic time scale τ has empirically been found to be close to the vorticity time scale, i.e. setting $\tau \simeq \omega_0^{-1}$ can be viewed as a good approximation for simple fluids, but for more complex fluids pronounced deviations are of course expected. The expression Eq. (6.115) shows that viscoelastic effects only set in at high frequencies, but at these frequencies can drastically change the resultant behavior.

Chapter 7

Summary

In this thesis, we tried to highlight the certain aspects of the soft matter friction at he mesoscopic scales. As a major tool, we have addressed the issue of peptide friction on various surfaces as well as in the peptide bundles. Enlarged computer power allows us to simulate peptides sliding at prescribed velocities over 5 orders of magnitude down to $V \sim 10^{-3}$ m/s. Introducing a stochastic theory, our simulation data were extrapolated into the experimentally important linear-friction regime at even lower velocities. Our *in silico* setups are inspired from the single molecule AFM experiments to accomplish lateral pulling of short peptides.

In Chapter 2, using all-atom Molecular Dynamics (MD) simulations, the polypeptide friction was investigated on the polar (hydrophilic) and non-polar (hydrophobic) surfaces for various normal forces and pulling velocities. The friction force shows a non linear dependence on the normal force, which is in contradiction with the Amontons' law. The friction force on the polar surfaces is always higher than that on the non-polar surface due to the moderate hydrogen bonding between the polar surface and the peptide molecule. Furthermore, increasing the density of polar OH groups at the surface increases the friction force, however, this increase is limited to the HB formation capacity of the corresponding monomer.

Spurred by the finding in Chapter 2 that is, on average, the friction force per HB is almost constant for a given pulling velocity on polar surfaces, in Chapter 3, we defined a friction coefficient per HB, which is the ratio of the average friction force per HB and the pulling velocity. To describe our data, we made use of the Fokker-Planck equation and obtained an analytical form for the non-linear friction coefficient as a function of the friction force and the strength of the surface corrugation. The strength characterizes the HB-stemmed interaction between the pulled peptides and the polar surfaces. The analytical friction function fitted our high and intermediate-velocity data very well and allowed us to infer the much slower velocity regimes. We showed that, at the vanishing force limit, each HB has a friction response of $\gamma_{\mathrm{HB}} \simeq 10^{-8}$ kg/s if multiple HBs collectively resist against the rupture. Since the Fokker-Planck description allows to go below the crossover between the viscous and the thermal, i.e. logarithmic, regimes, for $V \to 0$, the

total friction force can be expressed as $F_{\mathrm{f}} = \gamma_{\mathrm{HB}} N_{\mathrm{HB}} V$, where N_{HB} is the HB number. For the peptide-surface system, i.e, the peptide being pulled on the polar surface, this collectivity imposes the rupture of 3-4 HBs in unison.

The HB friction coefficient obtained in Chapter 3 reflects the stiffness of the HB matrix. A stiffer matrix, e.g., two sliding polar surfaces, or contrarily, a softer matrix can lead to different HB friction coefficients. Hence, in Chapter 4, we focused on the friction between elongated peptide chains. One peptide was pulled out parallel to a bundle made out of parallelly stacked peptides. It turns out that the peptide-peptide matrix gives rise to a similar dynamics to the peptide-surface matrix as long as the pulled peptide keeps its contact with 4-5 peptides during its motion. Furthermore, the number of chains in the bundles was varied to obtain the confinement-dependent HB friction coefficients ranging from $\gamma_{\mathrm{HB}} \simeq 10^{-11}$ kg/s to $\gamma_{\mathrm{HB}} \simeq 10^{-6}$ kg/s. This high range is due to the coupled effect of the water-isolated HBs and the collective HB breakages/reformations.

We also focused on the motion of short peptides on the non-polar surfaces; since there are no HB between the surface and the peptides, friction is dominated by the solvent effects. In Chapter 5, we have leaned on the dissipation mechanisms beneath the peptide friction, and the interaction of peptides with water was discussed in detail. We also emphasized that the bulk water and non-polar surface mobilities are of almost equivalent mobilities. Finally, we showed that the (001) surface of the H-terminated diamond exhibits a strong anisotropic diffusion profile due to the channelled structure formed by the surface atoms.

Between Chapters 2 to 5, we focussed on the friction in the vicinity of water and a second interface. In Chapter 6, we turned our attention to the hydrodynamic friction; we first calculated the Green's function for a point force as a function of frequency in a compressible viscous fluid. Next, the flow fields for a planar, spherical and a cylindrical geometries were constructed for arbitrary surface slip length, and the frequency-dependent friction response functions were derived by calculating the surface stress. We showed that at the high frequency regime, response functions display resonance behaviours at frequencies characterized by the sound velocity and the characteristic system size. Those resonant features should be detectable experimentally by tracking the diffusion of particles, as well as by measuring the fluctuation spectrum or the response spectrum of the trapped particles. Since the response function depends sensitively on the slip length, in principle the slip length can be deduced from an experimentally measured response function.

For the future studies, the work we presented here can further be extended to shed light on the unknowns of the friction occurring at the mesoscopic scales. For instance, the effect of a very stiff matrix, i.e., two sliding polar surfaces with varying concentrations of polar groups, might yield a complete conformation of our hypothesis that the more collective the HB ruptures are, the higher the HB friction coefficient is. Additionally, the friction between peptide grafted surfaces may yield interesting results.

At the surface-peptide level, we considered a single adsorbed peptide chain. Same pulling methodology can be applied on a monolayer of adsorbed short peptides; a single adsorbed peptide can be pulled apart laterally or vertically to infer the desorption and the

friction forces in the presence of other adsorbed peptides. As we have shown here, in the case of the low friction, the non-equilibrium pulling would be much more advantageous compared to computationally expensive equilibrium free-drift simulations. Alternatively, for the latter case, synthetic polymers can also be chosen even though their friction dynamics, in essence, will not differ from organic monomers.

In this work, when we considered the inter-peptide friction, we used elongated periodic peptides. A more realistic picture may be to allow the peptides to collapse, and then pull one peptide out of the globule of collapsed peptides. Additionally, the dynamics of the peptide collapse from a stretched conformation may yield useful information about the initial stages of protein folding.

From our hydrodynamic calculations, we obtained the friction response for the translational motion. In principle, the rotational response functions will follow from a similar ansatz given in Fig. 6.72. Rotational frequency-dependent response function can be used to infer the findings of 2D microrheology experiments [100].

Parts of this thesis have been published or submitted to peer-reviewed journals, or manuscripts for submission process are in preparation. These are as follow

- A. Erbaş, D. Horinek, & R. R. Netz, Friction of hydrogen-bonded matter. *The Journal of American Chemical Society*, 134, 623, **2011**,
- A. Erbaş, R. Podgornik, & R. R. Netz, Viscous compressible hydrodynamics at planes, spheres and cylinders with finite surface slip. *The European Physical Journal E*, 32, 147, **2010**, (cover issue),
- A. Erbaş & R. R. Netz, Friction in peptide bundles, to be submitted,
- A. Erbaş & R. R. Netz, Stick-slip motion of a single polypeptide on polar surfaces, in preparation,
- A. Erbaş & R. R. Netz, Anisotropic peptide diffusion on H-terminated (001) diamond surface, in preparation.

Appendix A

A.1. Derivation of the Fokker-Planck friction coefficient

In this section, we derive the steady-state friction coefficient from the Fokker-Planck equation in the presence of an external force and a corrugated periodic potential. Consider a single particle moving in a 1D corrugated potential of the form of

$$U(x) = -U_{\mathrm{HB}} \left(\frac{1 - \cos(2\pi x/a)}{2} \right)^{\beta}, \tag{A.1}$$

where U_{HB} is the height of the potential, x is the position of the particle, and a is the periodicity of the potential. For the sake of generality, we add a steepness parameter β in the potential. In Fig. A.1A, we plot Eq. (A.1) for various values of β. Note that for all the fits shown in the main text, we always take $\beta = 1$.

Neglecting the particle inertia, the equation of motion reads

$$\gamma_0 \frac{dx}{dt} = -\frac{dU(x)}{dx} + F + \Gamma(t). \tag{A.2}$$

After rescaling, the equation can be written as

$$\dot{\tilde{x}} = \frac{d\tilde{x}}{d\tilde{t}} = -\frac{d\tilde{U}(\tilde{x})}{d\tilde{x}} + \tilde{F} + \tilde{\Gamma}(\tilde{t}), \tag{A.3}$$

where $\tilde{x} = x/a$ and $\tilde{U}(\tilde{x}) = U(\tilde{x})/k_{\mathrm{B}}T$ is the potential rescaled by the thermal energy $k_{\mathrm{B}}T$. $\tilde{F} = Fa/k_{\mathrm{B}}T$ and $\tilde{\Gamma} = \Gamma a/k_{\mathrm{B}}T$ are the rescaled external force and the rescaled Gaussian random force. $\tilde{\Gamma}(\tilde{t})$ obeys $\langle \tilde{\Gamma}(\tilde{0})\, \tilde{\Gamma}(\tilde{t}) \rangle = 2\delta(\tilde{t})$ and $\tilde{t} = t/\tau$ with $\tau = \gamma_0 a^2/(k_{\mathrm{B}}T)$. For the potential given in Eq. (A.1), the Fokker-Planck equation for the probability density $W(\tilde{x})$ reads

$$\frac{\partial W(\tilde{x})}{\partial \tilde{t}} = \frac{\partial}{\partial \tilde{x}} \left(\frac{d\tilde{U}(\tilde{x})}{d\tilde{x}} - \tilde{F} + \frac{\partial}{\partial \tilde{x}} \right) W(\tilde{x}) \tag{A.4}$$

and can be solved exactly for the stationary case [128]. The solution is

$$W(\tilde{x}) = \frac{e^{-\tilde{U}(\tilde{x})+\tilde{F}\tilde{x}}}{S} \times \left[\frac{\int_0^1 e^{\tilde{U}(\tilde{x}')-\tilde{F}\tilde{x}'} d\tilde{x}'}{1-e^{-\tilde{F}}} - \int_0^{\tilde{x}} e^{\tilde{U}(\tilde{x}')-\tilde{F}\tilde{x}'} d\tilde{x}' \right], \tag{A.5}$$

where S is a normalization constant. The average particle velocity $\langle \dot{x} \rangle$ can be calculated with the help of Eq. (A.3) as

$$\langle \dot{\tilde{x}} \rangle = \int_0^1 \dot{\tilde{x}} W(\tilde{x}) d\tilde{x} = -\int_0^1 \left[\frac{d\tilde{U}(\tilde{x})}{d\tilde{x}} - \tilde{F} \right] W(\tilde{x}) d\tilde{x}. \tag{A.6}$$

The normalized friction coefficient as a function of $\tilde{F}$ is given by

$$\begin{aligned} \frac{\gamma(\tilde{F})}{\gamma_0} &\equiv \frac{\tilde{F}}{\langle \dot{\tilde{x}} \rangle} = 1 + \Psi(\tilde{F}, \tilde{U}_{\mathrm{HB}}) \\ &\equiv \frac{\int_0^1 e^{-\tilde{U}(\tilde{x})+\tilde{F}\tilde{x}} d\tilde{x} \int_0^1 e^{\tilde{U}(\tilde{x})-\tilde{F}\tilde{x}} d\tilde{x}}{\tilde{F}^{-1}(1-e^{-\tilde{F}})} - \frac{\int_0^1 e^{-\tilde{U}(\tilde{x})+\tilde{F}\tilde{x}} \int_0^{\tilde{x}} e^{\tilde{U}(\tilde{x}')-\tilde{F}\tilde{x}'} d\tilde{x} d\tilde{x}'}{\tilde{F}^{-1}}, \end{aligned} \tag{A.7}$$

where $\Psi(\tilde{F}, \tilde{U}_{\mathrm{HB}})$ is the interaction-induced contribution to the friction and $\tilde{U}_{\mathrm{HB}} = U_{\mathrm{HB}}/k_{\mathrm{B}}T$. In the linear-response limit, as $\tilde{F} \to 0$, the viscous friction is given by

$$\frac{\gamma}{\gamma_0} \simeq \left[\int_0^1 e^{\tilde{U}(\tilde{x})} d\tilde{x} \int_0^1 e^{-\tilde{U}(\tilde{x})} d\tilde{x} \right]. \tag{A.8}$$

When $\beta = 1$, Eq. (A.8) can be written in a more compact form as

$$\frac{\gamma}{\gamma_0} \simeq \left[I_0(\tilde{U}_{\mathrm{HB}}/2) \right]^2, \tag{A.9}$$

where $I_0(x)$ is the modified Bessel function of the first kind. The $\tilde{U}_{\mathrm{HB}} \to 0$ limit of Eq. (A.9) follows from the expansion $I_0(x) \simeq 1 + x^2/4 + \mathcal{O}(x^4)$ as

$$\frac{\gamma}{\gamma_0} \simeq 1 + \frac{(\tilde{U}_{\mathrm{HB}})^2}{16} + \mathcal{O}(\left(\tilde{U}_{\mathrm{HB}}\right)^4). \tag{A.10}$$

The opposite limit, $\tilde{U}_{\mathrm{HB}} \to \infty$, can be obtained from the integral definition of $I_0(x)$ via saddle-point approximation as

$$I_0(x) = \frac{1}{\pi} \int_0^{\pi} e^{x\cos(t)} dt \simeq \frac{e^x}{2\pi} \int_{-\infty}^{\infty} e^{-xt^2/2} dt = \frac{e^x}{\sqrt{2\pi x}}. \tag{A.11}$$

Hence, the high barrier limit of Eq. (A.9) follows as

$$\frac{\gamma}{\gamma_0} \simeq \frac{e^{\tilde{U}_{\mathrm{HB}}}}{\pi \tilde{U}_{\mathrm{HB}}}. \tag{A.12}$$

Eqs. SA.8 to SA.12 indicate that the zero-force limit, i.e. the linear-response viscous limit, is only a function of the height of the barrier and not of the wavelength a. Choosing a different β only weakly affects the linear-response friction coefficient. To illustrate this, in Fig. A.1B, we present the inverse of the rescaled friction coefficient, given by the numerical solution of Eq. (A.8), as a function of β: It is evident that for β values away from the extreme values $\beta = 0$ and $\beta = \infty$, the linear-response limit of γ/γ_0 is quite insensitive to the precise value of β.

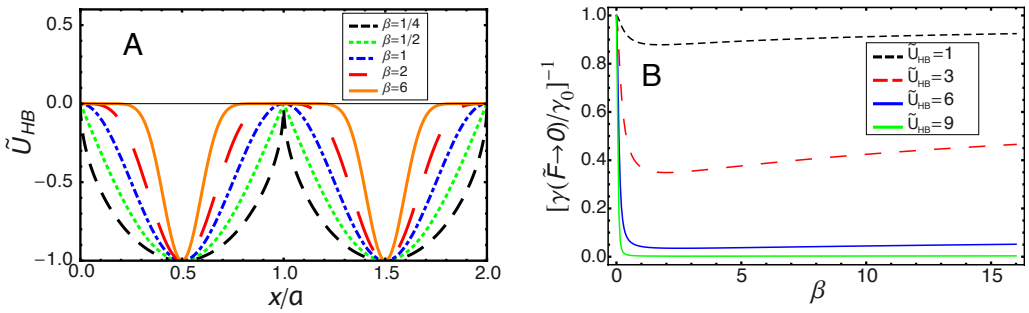

Figure A.1.: *Effect of various fit parameters on the friction coefficient as derived from the Fokker-Planck equation given in Eq.* (A.7). *A) The corrugated potential given in Eq.* (A.1) *as a function of x/a for various steepness parameters β, where a is the lattice constant. B) The friction coefficient in the linear-response limit, $\tilde{F} = Fa/k_BT \to 0$, given in Eq.* (A.8) *as a function of β for various potential heights $\tilde{U}_{HB}$.*

A.2. Derivation of the logarithmic scaling law from the Fokker-Planck equation

In this section, we will derive the heuristic logarithmic scaling law, given in the main text in Eq. (1), from the Fokker-Planck solution, Eq. (A.7), in conjunction with Eq.(3.4) In the derivation we assume $m\tilde{U}_{\mathrm{HB}} >> \tilde{F} = Fa/(k_{\mathrm{B}}T) > 1$. In this limit, we can simplify Eq. (A.7) and Eq.(3.4) to

$$\frac{1}{\langle\dot{\tilde{x}}\rangle} \simeq \frac{1}{m}\int_0^1 e^{-\tilde{U}(\tilde{x})+\tilde{F}\tilde{x}} \int_{\tilde{x}}^1 e^{\tilde{U}(\tilde{x}')-\tilde{F}\tilde{x}'} d\tilde{x}d\tilde{x}' = \frac{\mathcal{I}_3}{m}. \tag{A.13}$$

We define the three integrals

$$\begin{aligned} \mathcal{I}_1 &= \int_0^1 e^{-\tilde{U}(\tilde{x})+\tilde{F}\tilde{x}} d\tilde{x}, \\ \mathcal{I}_2(x) &= \int_x^1 e^{\tilde{U}(\tilde{x})-\tilde{F}\tilde{x}} d\tilde{x}, \\ \mathcal{I}_3 &= \int_0^1 e^{-\tilde{U}(\tilde{x})+\tilde{F}\tilde{x}} \mathcal{I}_2(\tilde{x}) d\tilde{x} \end{aligned} \tag{A.14}$$

that must be evaluated. Expansion of the total potential, $\tilde{U}(\tilde{x}) - \tilde{F}\tilde{x}$, around the minimum $\tilde{x} \approx 1/2$ yields

$$\tilde{U}(\tilde{x}) - \tilde{F}\tilde{x} \simeq -(m\tilde{U}_{\rm HB} + \tilde{F}/2) + (\tilde{x} - 1/2)^2\pi^2 m\tilde{U}_{\rm HB}, \tag{A.15}$$

and thus

$$\mathcal{I}_1 \simeq \frac{e^{m\tilde{U}_{\rm HB}+\tilde{F}/2}}{\sqrt{\pi m\tilde{U}_{\rm HB}}}. \tag{A.16}$$

For the integral $\mathcal{I}_3$ we use that the integrand is strongly peaked at $\tilde{x} \approx 1/2$ so that to leading order $\mathcal{I}_2(\tilde{x}) \simeq \mathcal{I}_2(1/2)$ can be used. The integral $\mathcal{I}_2(1/2)$ on the other hand is dominated by the contribution around $\tilde{x} \approx 1$. Expansion of the total potential, $\tilde{U}(\tilde{x})-\tilde{F}\tilde{x}$, around the local maximum at $\tilde{x} \approx 1$ yields

$$\tilde{U}(\tilde{x}) - \tilde{F}\tilde{x} \simeq -\tilde{F} - (\tilde{x} - 1)^2\pi^2 m\tilde{U}_{\rm HB}. \tag{A.17}$$

and with that

$$\mathcal{I}_2(1/2) \simeq \frac{e^{-\tilde{F}}}{2\sqrt{\pi m\tilde{U}_{\rm HB}}}. \tag{A.18}$$

To leading order we use

$$\mathcal{I}_3 \simeq \int_0^1 e^{-\tilde{U}(\tilde{x})+\tilde{F}\tilde{x}}\mathcal{I}_2(1/2)d\tilde{x} = \mathcal{I}_1\mathcal{I}_2(1/2) \simeq \frac{e^{m\tilde{U}_{\rm HB}}}{2\pi m\tilde{U}_{\rm HB}}e^{-\tilde{F}/2}. \tag{A.19}$$

Using $\langle\dot{\tilde{x}}\rangle \equiv \tilde{V} = m/\mathcal{I}_3$, inserting for the force acting on a cooperative unit the expression $\tilde{F} = aF/(k_BT) = maF_{\rm f}^{\rm surf}/(N_{\rm HB}^{\rm eq}k_BT)$, and using the short-hand notation $F_0 = 2k_{\rm B}T/(am)$ we obtain

$$\frac{F_{\rm f}^{\rm surf}}{N_{\rm HB}^{\rm eq}} \simeq F_0\ln(\tilde{V}/\tilde{V}_0) = F_0\ln(V/V_0), \tag{A.20}$$

where $\tilde{V}_0 = 2\pi m^2\tilde{U}_{HB}e^{-m\tilde{U}_{HB}}$, or $V_0 = (2\pi m^2U_{\rm HB}/(a\gamma_0))e^{-mU_{HB}/k_{\rm B}T}$ in un-rescaled variables, which is consistent with the scaling arguments given in the main text. Eq. (A.20) indicates that the logarithmic scaling given in the main text, Eq. (1), follows from the full Fokker-Planck solution in an intermediate range of forces. Note that the meaning of the length scale a_0 in the heuristic expression Eq. (1) in the main text has been changed slightly and according to the derivation in fact depends on the cooperativity factor m. In Fig. 3.3, we compare the logarithmic scaling with the full Fokker-Planck solution, Eq. (A.7), obtained from

$$\tilde{V}(\tilde{F}) \equiv \frac{\tilde{F}}{1+\Psi(\tilde{F})} \tag{A.21}$$

via inversion using the same parameter set, which we used in Fig. 3.1 of the main text. As seen in 3.3, the Fokker-Planck solution (black curve) crosses over to the viscous limit (indicated by a dotted line) at velocities $V \simeq 10^{-3}$ m/s, in agreement with the prediction in the main text via Eq. 2.2.

Appendix B

B.1. Solvent accessible surface (SAS) area algorithm

In the calculation of the SAS area, gromacs' build-in analysis tool, *g_sas* is used. This tool calculates the hydrophobic, hydrophilic and the total SAS of a molecular group according to the double cubic lattice method (DCLM) presented by Eisenhaber et al. [136]. Algorithm works as follows, n number of dots are assigned on the surface of each atom of a molecule as schematically depicted in Fig. B.1. If surfaces of two adjacent atoms overlap, the dots on these occluded surfaces are excluded (striped area in Fig. B.1). The remaining dots on the atom i, $n_{\mathrm{acc}}(i)$ are summed over all atoms of corresponding molecule to calculate surface area as

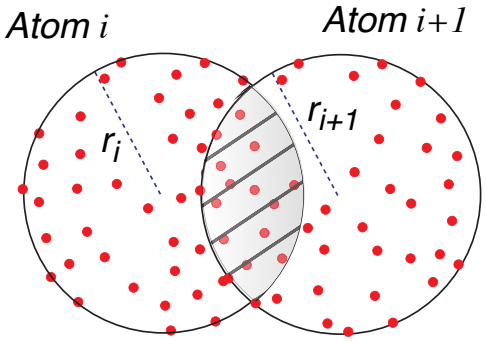

Figure B.1.: *Illustration for the algorithm used to calculate surface accessible area (SAS). Spheres represent two neighbouring atoms with a van der Walls radius of r_i. m number of dots are assigned on the surface each atom. Following, to calculate to SAS, dots occupied by two adjacent atoms are excluded (striped area). Remaining points are used to calculate the SAS for each atom through Eq.* (B.1).

$$A = 4\pi \sum_i r_i^2 \frac{n_{acc}(i)}{n}, \tag{B.1}$$

where r_i is the van der Waals radius of ith atom. As the number of assigned dots per sphere, n, is increased, accuracy of this method increases as well. In our calculation, $n =$

24, which is also default value in g_sas. In the calculation hydrophobic and hydrophilic SASs, atoms with charges less than $|q| = 0.2$e are contributed to the hydrophobic SAS area while others do add up in hydrophilic SAS.

B.2. Table of friction-force contributions in peptide bundles

In following tables, we present the separated force contributions for peptide bundle systems. Using, *rerun* option of GROMACS MD package, friction forces arising purely due to the inter-peptides, F_{PP}, and due to the water F_{Sol} are separated. All peptide systems are built of N=10 polyglycine chains. All systems contain SPC water. The total friction forces obtained from the spring deviations are of the opposite sign of the total friction force. Hence, F_{PP} and F_{Sol} are of minus signs given that motion of the pulled peptide is in the $+\hat{x}$-direction. Note for slow velocities, errors are larger than the corresponding value. When F_{PP} and F_{Sol} have opposite signs, related percentage cannot be calculated. These cases are indicated by a "?". If errors less than 6%, they are not given. Also if the errors are less than 6%, then they are not shown.

Table B.1.: *Peptide-peptide and the solvent contributions to the total friction force between* ***parallel k=2*** *N=10 polyglycine chains.*

V [m/s]	-F_{f} [pN]	F_{PP} [pN]	F_{Sol} [pN]	$\frac{F_{PP}}{F_{PP}+F_{Sol}}$[%]
0.05[1]	-1.8 ± 1.3	-4.2 ±5	2.7 ±11	?
0.1	-2.5 ± 1.6	-2.2 ±4	0.5± 5	?
0.5	-10 ± 3.3	-18 ±9	20±12	?
1	-24	-46 ±15	-7±30	%86± 78
5	-103	-108 ±25	-10±18	%91± 39
10	-180	-141 ±16	-30±18	%82±18
50	-470	-187 ±19	-300±35	%38± 6

Table B.2.: *Peptide-peptide and the solvent contributions to the total friction force between* ***perpendicular k=2*** *N=10 polyglycine chains.*

V [m/s]	-F_{f} [pN]	F_{PP} [pN]	F_{Sol} [pN]	$\frac{F_{PP}}{F_{PP}+F_{Sol}}$[%]
0.1	-2±3	1.5±5.3	2.7 ±18	?
1	-8.5±3.3	3±6.3	28±20	?
5	-50	-13±4	-36±25	%26±16
10	-96	-28±12	-70±18	%28±13

Table B.3.: *Peptide-peptide and the solvent contributions to the total friction force between* ***parallel k=3*** *N=10 polyglycine chains.*

V [m/s]	-F_{f} [pN]	F_{PP} [pN]	F_{Sol} [pN]	$\frac{F_{PP}}{F_{PP}+F_{Sol}}$[%]
0.01	-3.5 ±1.5	-12 ±4	9.3 ±3	?
0.05	-15 ±5	-26 ±7	4.7 ±10	?
0.1	-30 ±5	-60 ±10	38±5	?
1	-125	-156 ±10	33 ±8	?
5	-223 ±25	-258 ±72	28 ±32	?
10	-283	-260 ±60	-30 ±38	%89±31
50	-500	-260 ±35	-250 ±70	%51±10

Table B.4.: *Peptide-peptide and the solvent contributions to the total friction force between* ***k=5 parallel*** *N=10 polyglycine chains .*

V [m/s]	-F_{f} [pN]	F_{PP} [pN]	F_{Sol} [pN]	$\frac{F_{PP}}{F_{PP}+F_{Sol}}$[%]
0.01	-150±35	-152 ±27	-6.7 ±9	%96±28
0.05	-200±40	-193 ±30	-13±18	%94±26
0.1	-280	-297 ±25	14±18	?
1	-420±100	-387 ±25	50±35	?
5	-800±200	-600 ±42	-80±40	%88±12
10	-1010±200	-551 ±43	-70±52	%89±15

Appendix C

C.1. Calculation of the line Green's function

The Green's function resulting from Eq. (6.90) can be written in terms of integral functions $A_n(\alpha\sigma)$ defined as

$$\begin{aligned} A_n(\alpha\sigma) &= \int_0^{+\infty} \frac{e^{-\alpha\sqrt{\sigma^2+z^2}}dz}{(\alpha\sqrt{\sigma^2+z^2})^n} = \frac{1}{\alpha^n}\int_\sigma^{+\infty} \frac{e^{-\alpha r}dr}{r^{n-1}\sqrt{r^2-\sigma^2}} \\ &= \frac{1}{\alpha^n\sigma^{n-1}}\int_1^{+\infty} \frac{e^{-\alpha\sigma u}du}{u^{n-1}\sqrt{u^2-1}}, \end{aligned} \tag{C.1}$$

and similar for $A_n(\lambda\sigma)$. Note that $A_1(\alpha\sigma)$ and $A_0(\alpha\sigma)$ are connected to second order modified Bessel functions as $A_0(\alpha\sigma) = \sigma K_1(\alpha\sigma)$ and $A_1(\alpha\sigma) = K_0(\alpha\sigma)/\alpha$. Derivatives of $A_n(\alpha\sigma)$ are given by the recursion relation

$$\frac{\partial A_n(\alpha\sigma)}{\partial r_i} = -\frac{\hat{r}_i}{\sigma}\left[(n-1)A_n(\alpha\sigma) - A_{n-1}(\alpha\sigma)\right]. \tag{C.2}$$

Furthermore, A_n functions are related via

$$(n-1)A_n(\alpha\sigma) + A_{n-1}(\alpha\sigma) = \alpha^2\sigma^2[nA_{n+2}(\alpha\sigma) + A_{n+1}(\alpha\sigma)]. \tag{C.3}$$

Using Eqs. (C.1) and (C.3) in Eq. (6.91) gives the line Green's functions as

$$\begin{aligned} G_{ij}^{line,T}(\sigma) &= \delta_{iz}\delta_{jz}\frac{K_0(\alpha\sigma)}{2\pi\eta} \\ &\quad + \frac{\alpha}{2\pi\eta\alpha^2\sigma}\{(\delta_{ix}\delta_{jx}+\delta_{iy}\delta_{jy})[K_1(\alpha\sigma)+\alpha\sigma K_0(\alpha\sigma)] \\ &\quad - \hat{r}_i\hat{r}_j(\delta_{ix}\delta_{jx}+\delta_{iy}\delta_{jy}+\delta_{ix}\delta_{jy}+\delta_{iy}\delta_{jx}),[2K_1(\alpha\sigma)+\alpha\sigma K_0(\alpha\sigma)]\} \\ G_{ij}^{line,L}(\sigma) &= \frac{\lambda}{2\pi\eta\alpha^2\sigma}\{-(\delta_{ix}\delta_{jx}+\delta_{iy}\delta_{jy})K_1(\lambda\sigma) \\ &\quad + \hat{r}_i\hat{r}_j(\delta_{ix}\delta_{jx}+\delta_{iy}\delta_{jy}+\delta_{ix}\delta_{jy}+\delta_{iy}\delta_{jx})[2K_1(\lambda\sigma)+\lambda\sigma K_0(\lambda\sigma)]\}. \end{aligned} \tag{C.4}$$

C.2. Calculation of the cylinder response function for perpendicular motion

We start from Eq. (6.92), where here and in the following i and j can be either x or y. To calculate the effect of the ∇^2 operator, we use the following identities

$$\nabla^2(r_i r_j A_n) = 2\delta_{ij}A_n + \frac{r_i r_j}{\sigma^2}[(n-1)(n-5)A_n + (2n-7)A_{n-1} + A_{n-2}],$$
$$\nabla^2 A_n = \frac{1}{\sigma^2}[(n-1)^2 A_n + (2n-3)A_{n-1} + A_{n-2}]. \qquad \text{(C.5)}$$

Above identities give $\nabla^2 G_{ij}^{line,T} = \alpha^2 G_{ij}^{line,T}$ and $\nabla^2 G_{ij}^{line,L} = \lambda^2 G_{ij}^{line,L}$. Using these results in Eq. (6.92) gives

$$\begin{aligned} G_{ij}^{cyl,\perp}(\sigma) &= \underbrace{(D_0 + D_2 a^2\alpha^2)}_{E_1^{cyl}} G_{ij}^{line,T} + \underbrace{(D_0 + D_2 a^2\lambda^2)}_{E_2^{cyl}} G_{ij}^{line,L} \\ &= E_1^{cyl} G_{ij}^{line,T} + E_2^{cyl} G_{ij}^{line,L} \\ &= \frac{\alpha E_1^{cyl}}{2\pi\eta\alpha^2\sigma}\{\delta_{ij}[K_1(\alpha\sigma) + \alpha\sigma K_0(\alpha\sigma)] - \hat{r_i}\hat{r_j}[2K_1(\alpha\sigma) + \alpha\sigma K_0(\alpha\sigma)]\} \\ &\quad + \frac{\lambda E_2^{cyl}}{2\pi\eta\alpha^2\sigma}\{-\delta_{ij}K_1(\lambda\sigma) + \hat{r_i}\hat{r_j}\,[2K_1(\lambda\sigma) + \lambda\sigma K_0(\lambda\sigma)]\}. \qquad \text{(C.6)} \end{aligned}$$

The coefficients E_1^{cyl} and E_2^{cyl} are determined by boundary conditions Eqs. (6.94) and (6.95) at the cylinder surface. Using Eqs. (C.2) and (C.3), the coefficients E_1^{cyl} and E_2^{cyl} can be written as

$$E_1^{cyl} = -\frac{(2\tilde{b}+1)[2\tilde{\lambda}K_1(\tilde{\lambda}) + \tilde{\lambda}^2 K_0(\tilde{\lambda})]}{N_2M_1 - N_1M_2},$$
$$E_2^{cyl} = -\frac{(2\tilde{b}+1)[2\tilde{\alpha}K_1(\tilde{\alpha}) + \tilde{\alpha}^2 K_0(\tilde{\alpha})] + \tilde{b}\tilde{\alpha}^3 K_1(\tilde{\alpha})}{N_2M_1 - N_1M_2}, \qquad \text{(C.7)}$$

where the N_i and M_i coefficients, the final results for which are given in terms of Bessel functions in Eq. (6.97), are determined in terms of the A_n functions as

$$\begin{aligned} M_1 &= -2\alpha^3\tilde{b}[2A_3(\alpha a) + 2A_2(\alpha a) + A_1(\alpha a)] - \\ &\quad \tilde{b}\alpha^3 A_0(\alpha a) - \alpha^3[A_3(\alpha a) + A_2(\alpha a) + A_1(\alpha a)], \\ M_2 &= -\alpha^3[A_3(\alpha a) + A_2(\alpha a)], \\ N_1 &= 2\lambda^3\tilde{b}[2A_3(\lambda a) + 2A_2(\lambda a) \\ &\quad + A_1(\lambda a)] + \lambda^3[A_3(\lambda a) + A_2(\lambda a)], \\ N_2 &= \lambda^3[A_3(\lambda a) + A_2(\lambda a) + A_1(\lambda)], \qquad \text{(C.8)} \end{aligned}$$

where $\tilde{b} = b/a$. The denominator in the expressions for E_1^{cyl} and E_2^{cyl} is given by

$$\begin{aligned} N_2M_1 - N_1M_2 = & \left(\frac{2\pi\eta\tilde{\alpha}^2}{F_i/V_i^{cyl}}\right)^{-1} \Big\{\tilde{\lambda}\tilde{\alpha}(2\tilde{b}+1) \\ & \Big[\tilde{\alpha}K_0(\tilde{\alpha})\Big(K_1(\tilde{\lambda}) + \tilde{\lambda}K_0(\tilde{\lambda})\Big) + \tilde{\lambda}K_0(\tilde{\lambda})K_1(\tilde{\alpha})\Big] \\ & + \tilde{b}\tilde{\alpha}^3\tilde{\lambda}K_1(\tilde{\alpha})\Big(K_1(\tilde{\lambda}) + \tilde{\lambda}K_0(\tilde{\lambda})\Big)\Big\}, \end{aligned} \tag{C.9}$$

where $\tilde{\alpha} = a\alpha$ and $\tilde{\lambda} = a\lambda$.

C.3. Large-curvature limits of response functions

In the limit of $a \to \infty$, both cylindrical and spherical response functions are expected to converge towards combinations of the normal and tangential response functions obtained for a plane. This constitutes a sensitive test on the validity of our expressions.

Spherical response function: The complete response function of a spherical particle has been given in the main text by Eq. (6.83). For $a \to \infty$, Eq. (6.83) takes the form of

$$\lim_{a\to\infty} \mathcal{G}^{sp}(\omega) \simeq \frac{4\pi\eta a^2}{3} \frac{\lambda\alpha^2 + b\alpha^3\lambda + 2\lambda^2\alpha}{\lambda^2(b\alpha+1)},$$

and after some simplifications, above Eq. turns into

$$\lim_{a\to\infty} \mathcal{G}^{sp}(\omega) \simeq 4\pi a^2 \left(\frac{1}{3}\frac{\alpha^2\eta}{\lambda} + \frac{2}{3}\frac{\alpha\eta}{b\alpha+1}\right). \tag{C.10}$$

This shows that the response of a sphere in the infinite-radius limit, $a \to \infty$, is the weighted combination of the normal and the tangential planar response functions given in Eqs. (6.47) and (6.53) times the area of a sphere. Indeed, at an infinitely large sphere, the vectorial force $\vec{f}$ acting on each surface element can be considered as a combination of normal and tangential components,

$$f_j = \frac{\alpha^2\eta}{\lambda} V_i^{sp} \hat{r}_i\hat{r}_j + \frac{\alpha\eta}{b\alpha+1} V_i^{sp}(\delta_{ij} - \hat{r}_i\hat{r}_j), \tag{C.11}$$

where V_i^{sp} is the sphere velocity. Integration of this force over the spherical surface corresponds to

$$\overline{f_i} = \int dr^3 f_i \delta(|r| - a), \tag{C.12}$$

which straightforwardly leads to Eq. (C.10).

Cylindrical response function: The same analysis can be done for the parallel and the perpendicular response functions of the cylinder. The parallel component of the cylinder response function has been given in Eq. (6.111) as

$$\mathcal{G}_{\parallel}^{cyl} = 2\pi\eta \frac{\alpha K_1(\alpha a)}{b\alpha K_1(\alpha a) + K_0(\alpha a)}.$$

As $a \to \infty$, this equation crosses over to

$$\begin{aligned} \lim_{a\to\infty} \mathcal{G}_{\parallel}^{cyl} &= 2\pi\eta \frac{\alpha a K_1(\alpha a)}{K_1(\alpha a)(b\alpha + K_0(\alpha a)/K_1(\alpha a))} \\ &\simeq 2\pi a \frac{\alpha\eta}{b\alpha + 1} \end{aligned} \tag{C.13}$$

and thus equals the tangential response function of a plane, Eq. (6.53), times the circumference of the cylinder.

The perpendicular component of the cylinder response function can be treated similarly. Using the asymptotic behavior of the Bessel functions, $\lim_{x\to\infty} K_n(x) \simeq \frac{e^{-x}}{\sqrt{x}}$, the coefficients in Eq. (6.97) follow as

$$\begin{aligned} \lim_{a\to\infty} M_1 &\simeq \frac{-\alpha^2 e^{-a\alpha}}{\sqrt{\alpha a}} - \frac{b\alpha^3 e^{-a\alpha}}{\sqrt{\alpha a}}, \\ \lim_{a\to\infty} M_2 &\simeq 0, \\ \lim_{a\to\infty} N_1 &\simeq 0, \\ \lim_{a\to\infty} N_2 &\simeq \frac{\lambda^2 e^{-\lambda a}}{\sqrt{\lambda a}}, \end{aligned}$$

and yield in the limit $a \to \infty$

$$\begin{aligned} E_1^{cyl} &\simeq \frac{2\pi\eta}{F_i/V_i^{cyl}} e^{\alpha a} \frac{\sqrt{\alpha a}}{b\alpha + 1}, \\ E_2^{cyl} &\simeq \frac{2\pi\eta\alpha^2}{F_i/V_i^{cyl}} e^{\lambda a} \frac{\sqrt{\lambda a}}{\lambda^2}. \end{aligned} \tag{C.14}$$

Substitution of these coefficients into Eq. (6.100) gives the final form of the cylindrical response function in the infinite radius limit as

$$\lim_{a\to\infty} \mathcal{G}_{\perp}^{cyl}(\omega) \simeq 2\pi a \left(\frac{1}{2} \frac{\alpha^2\eta}{\lambda} + \frac{1}{2} \frac{\alpha\eta}{b\alpha + 1} \right), \tag{C.15}$$

which is again a weighted average of the tangential and normal planar response functions over the cylinder surface times the cylinder circumference.

C.4. Incompressible limit for cylinders

Analytical expressions for the response function of a cylinder in an incompressible nonsteady flow field have been given by various authors [157]. The limit of an incompressible fluid can be obtained from our more general results by taking the limit of $\lambda \to 0$ and constitutes another test of our results. Suppose that the cylinder oscillates in the x-direction with a frequency dependent velocity V_x^{cyl}. From Eq. (C.6) one can calculate

$v_x^\perp$ and $v_y^\perp$ with the no-slip condition by using $G_{xx}^{cyl,\perp}$ and $G_{xy}^{cyl,\perp}$. The velocity components can be explicitly written as

$$\begin{aligned} v_x^\perp(\sigma,\phi) &= V_x^{cyl}\left[\frac{2}{\alpha\sigma}A - \cos\phi^2 B + \frac{a}{\alpha\sigma^2}(2\cos\phi^2-1)C\right], \\ v_y^\perp(\sigma,\phi) &= V_x^{cyl}\sin\phi\cos\phi\left[-\frac{2}{\alpha\sigma}B + \frac{2a}{\alpha\sigma^2}C\right], \end{aligned}$$

where

$$\begin{aligned} A &= \frac{K_1(\alpha\sigma)}{K_0(\alpha a)} + \alpha\sigma\frac{K_0(\alpha\sigma)}{K_0(\alpha a)}, \\ B &= \frac{2K_1(\alpha\sigma)}{K_0(\alpha a)} + \alpha\sigma\frac{K_0(\alpha\sigma)}{K_0(\alpha a)}, \\ C &= \frac{2K_1(\alpha a)}{K_0(\alpha a)} + \alpha a, \end{aligned} \tag{C.16}$$

with the angle ϕ is defined in Fig. 6.6. Since $v_\sigma^\perp = v_x^\perp\cos\phi + v_y^\perp\sin\phi$ and $v_\phi^\perp = -v_x^\perp\sin\phi + v_y^\perp\cos\phi$, the velocity components in cylindrical components read as

$$\begin{aligned} v_\sigma^\perp(\sigma,\phi) &= V_x^{cyl}\cos\phi\left[\frac{a^2}{\sigma^2} - \frac{2K_1(\alpha\sigma)}{\alpha\sigma K_0(\alpha a)} + \frac{2aK_1(\alpha a)}{\alpha\sigma^2 K_0(\alpha a)}\right], \\ v_\phi^\perp(\sigma,\phi) &= V_x^{cyl}\sin\phi\left[\frac{a^2}{\sigma^2} - \frac{2K_0(\alpha\sigma)}{K_0(\alpha a)} - \frac{2K_1(\alpha\sigma)}{\alpha\sigma K_0(\alpha a)} + \frac{2aK_1(\alpha a)}{\alpha\sigma^2 K_0(\alpha a)}\right] \end{aligned} \tag{C.17}$$

and agree with the expressions derived previously in the incompressible limit [157].

C.5. Assumption of an isothermal liquid

In the hydrodynamic calculations presented in this paper, we neglect the heating and temperature variations through the medium due to the oscillatory motion of our geometries and assume an isothermal liquid. We first of all remark that the calculation we perform is exact on the linear layer and by that makes no assumption about the actual thermodynamic transformation type (e.g., adiabatic versus isothermal). There are also no corrections on the linear level due to dissipation effects. The question therefore is at which amplitudes the linear approximation breaks down and in what form this breakdown manifests itself. We split the discussion of this important question into several points:

i) The power spectrum of a body moving at velocity V and under force F_f is given by $P(\omega) = Re(F_i(\omega)V_i(-\omega))$. This can be written as $P(\omega) = \mathcal{G}'(\omega)|V^2(\omega)|$, which immediately shows that dissipation is quadratic in velocity (and thus beyond our linear approach) and proportional to the real part of the response function.

ii) Dissipation effects are best discussed in terms of the standard balance equation for the internal energy, which in the absence of external force reads

$$\rho\frac{du}{dt} = \Pi_{ij}\nabla_j v_i + \nabla_i(\kappa\nabla_i T), \tag{C.18}$$

where we used the internal energy per unit mass u, the stress tensor Π_{ij}, the temperature field T and the heat conduction coefficient κ. Changes in the internal energy density are due to viscous dissipation (first term on the right) and heat conduction (second term on the right). Note that viscous dissipation is quadratic in the velocity and thus beyond the linear analysis performed in our paper. Nevertheless, by means of dimensional analysis, i.e. assuming a typical length scale L_0, velocity scale V_0 and temperature scale T_0, one directly sees that both terms contribute equally at a typical temperature

$$T_0 \sim \frac{\eta V_0^2}{\kappa}. \tag{C.19}$$

For water with $\eta \simeq 10^{-3} kg/ms$ and $\kappa \simeq 0.6 J/msK$ one obtains for typical velocities $V_0 \simeq 10^{-6} m/s$ a threshold temperature of $T_0 \simeq 10^{-15} K$. This means that internal energy changes are predominantly due to heat flow for temperature variations above $T_0 \simeq 10^{-15} K$ and velocities compatible with the low-Reynolds number limit (for larger velocities one would have to worry about the neglect of non-linear terms in the Navier-Stokes equation). In a stationary situation, the internal energy change is zero, and thus the two terms on the right must balance, which shows that in this case the temperature changes are minimal for small velocities. For a cyclic process (like a sound wave) the two terms balance on average, which again shows that the induced temperature shifts are minimal.

iii) We now briefly discuss the question whether sound propagation is an adiabatic or an isothermal process and how that enters into our calculation. First of all, by linearizing the Navier Stokes equation and the continuity equation, one arrives at $\partial^2 \rho / \partial t^2 - \nabla^2 p = 0$, where for the present argumentation we have neglected the viscosity terms for simplicity. Expanding the equation of state to first order, one obtains $\rho - \rho_0 = c^{-2}(p - p_0)$, where we defined $c^{-2} = d\rho/dp|_{p_0}$. While the actual value of the sound velocity c does depend on whether the process is adiabatic or isothermal, the linear approximation for the equation of state works for both limits.

iv) In order to estimate to what extent heat flows during sound propagation, we write $du/dt \simeq \partial u/\partial t = c_p \partial T/\partial t$ (neglecting the difference between the substantial and partial time derivatives and using c_p although the pressure is not strictly constant) and obtain from Eq. C.18 in the absence of viscous effects $\rho c_p \partial T/\partial t \sim \kappa \nabla^2 T$. From dimensional analysis, the typical time scale τ_T for heat conduction over a length scale L_0 is

$$\tau_T \sim \rho_0 c_p L_0^2 / \kappa, \tag{C.20}$$

which has to be compared with the sound propagation time scale $\tau_{prop} \sim L_0/c$. For $\tau_T > \tau_{prop}$, or in other words for $\rho_0 c_p L_0 c/\kappa > 1$, one is in the adiabatic regime. In water, for a sound velocity of $c \simeq 1500 m/s$ and a heat capacaity of $c_p \simeq 4 kJ/kgK$ one has $\rho_0 c_p L_0 c/\kappa = 1$ for a length scale of $L_0 \simeq 10^{-10} m$, in air this length scale is $L_0 \simeq 10^{-7} m$. This means that in water, sound propagation is always adiabatic, in air deviations do occur at small wavelengths (i.e. high frequencies).

v) It remains to discuss how large the local temperature change due to a pressure change in a sound wave actually is. According to our previous arguments, we assume

the process is adiabatic. We therefore consider an isentropic process and thus obtain the temperature change as $dT = \partial T/\partial P|_S dP$.

From the internal energy and entropy change

$$\begin{aligned} dU &= -PdV + TdS \\ dS &= \frac{\partial S}{\partial T}|_V dT + \frac{\partial S}{\partial V}|_T dV \end{aligned} \tag{C.21}$$

Internal energy can be written as

$$\begin{aligned} dU &= -PdV + \frac{\partial S}{\partial T}|_V dT + \frac{\partial S}{\partial V}|_T dV \\ &= \frac{\partial S}{\partial T}|_V dT + \left(\frac{\partial S}{\partial V}|_T - P\right) dV \end{aligned} \tag{C.22}$$

using Maxwell identities

$$dU = \frac{\partial S}{\partial T}|_V dT + \left(\frac{\partial P}{\partial T}|_V - P\right) dV \tag{C.23}$$

Using the heat capacity $c_v = T\partial S/\partial T|_V$, the coefficient of thermal expansion, $\alpha = V^{-1}\partial V/\partial T|_P$ and the compressibility, $\kappa_T = -V^{-1}\partial V/\partial P|_T$, Eq. C.23 can be rewritten as

$$dU = c_v dT + \left(\frac{T\alpha}{\kappa_T} - P\right) dV. \tag{C.24}$$

By equating Eqs. C.21 and C.24, one obtains

$$TdS = c_v dT + \frac{T\alpha}{\kappa_T} dV. \tag{C.25}$$

Using the thermal coefficients given above, an identity for volume change can be written as $dV = -V\kappa_T dP + V\alpha dT$. If we plug this in to Eq. C.25 and use the assumption $dS = 0$ then

$$dT\left(c_v + \frac{T\alpha^2 V}{\kappa_T}\right) = T\alpha V dP, \tag{C.26}$$

which yields

$$\frac{\partial T}{\partial P}|_S = \left(\frac{\rho c_v}{\alpha T} + \frac{\alpha}{\kappa_T}\right)^{-1}. \tag{C.27}$$

Using for the coefficient of thermal expansion, $\alpha = \simeq 3 \cdot 10^{-4} K^{-1}$ and the compressibility, $\kappa_T = -simeq 4.6 \cdot 10^{-10} m^2 N^{-1}$for water, one obtains

$$\frac{\partial T}{\partial P}|_S \simeq \frac{\alpha T}{\rho c_v} \simeq 2 \cdot 10^{-8} \frac{K}{J m^{-3}}, \tag{C.28}$$

where for water we used that $c_v \simeq c_p$. This shows that a pressure increase by 1 Pa (which corresponds to a heavy noise close to the tolerance limit of the human ear) only changes the temperature by $10^{-8} K$, which is a tiny amount. We conclude that temperature effects are for typical applications negligible in agreement with our discussion above based on the energy balance equation.

Bibliography

[1] M. Urbakh, J. Klafter, D. Gourdon, et al. The nonlinear nature of friction. Nature **430 (6999)**, 525 (2004)

[2] B. N. J. Persson. *Sliding friction.* physical principles and applications (Springer Verlag, 2000)

[3] W. F. Brace, J. D. Byerlee. Stick-slip as a mechanism for earthquakes. Science **153 (3739)**, 990 (1966)

[4] F. P. Bowden, D. Tabor. *The Friction and Lubrication of Solids (Oxford Classic Texts in the Physical Sciences).* First edition (Oxford University Press, USA, 2001)

[5] J. H. Dumbleton. *Tribology of Natural and Artificial Joints* (North Holland, 1981)

[6] D. Dowson. *History of Tribology* (Longman, London and NY, 1979)

[7] R. R. Netz. Prof. netz, commented in this talk that in da vinci's original book, sketches for torture and friction machineries are next to each other. Molecular Kinetics '11 Conference, Berlin, September 4th - 6th (2011)

[8] T. Baumberger, C. Caroli. Solid friction from stick–slip down to pinning and aging. Advances in Physics **55 (3-4)**, 279 (2006)

[9] J. Gao, W. Luedtke, D. Gourdon, et al. Frictional forces and Amontons' law: from the molecular to the macroscopic scale. The Journal of Physical Chemistry B **108 (11)**, 3410 (2004)

[10] L. Bureau, C. Caroli, T. Baumberger. Frictional dissipation and interfacial glass transition of polymeric solids. Phys. Rev. Lett. **97 (22)**, 225501 (2006)

[11] K. Busuttil, M. Geoghegan, C. Hunter, et al. Contact mechanics of nanometer-scale molecular contacts: Correlation between adhesion, friction, and hydrogen Bond thermodynamics. Journal of the American Chemical Society (2011)

[12] G. He, M. Müser, M. Robbins. Adsorbed layers and the origin of static friction. Science **284 (5420)**, 1650 (1999)

[13] E. Riedo, I. Palaci, C. Boragno, et al. The 2/3 power law dependence of capillary force on normal load in nanoscopic friction. Journal of Physical Chemistry B-Condensed Phase **108 (17)**, 5324 (2004)

[14] G. Gao, P. Mikulski, J. Harrison. Molecular-scale tribology of amorphous carbon coatings: effects of film thickness, adhesion, and long-range interactions. Journal of the American Chemical Society **124 (24)**, 7202 (2002)

[15] J. Ringlein, M. Robbins. Understanding and illustrating the atomic origins of friction. American journal of physics **72**, 884 (2004)

[16] Y. Sang, M. Dubé, M. Grant. Thermal effects on atomic friction. Physical Review Letters **87 (17)**, 174301 (2001)

[17] E. Riedo, E. Gnecco. Thermally activated effects in nanofriction. Nanotechnology **15**, S288 (2004)

[18] B. Persson. Theory of friction: Stress domains, relaxation, and creep. Physical Review B **51 (19)**, 13568 (1995)

[19] B. Luan, M. Robbins. The breakdown of continuum models for mechanical contacts. Nature (2005)

[20] B. Bhushan, J. Israelachvili, U. Landman. Nanotribology: friction, wear and lubrication at the atomic scale. Nature (1995)

[21] I. Szlufarska, M. Chandross, R. W. Carpick. Recent advances in single-asperity nanotribology. Journal of Physics D: Applied Physics **41 (12)**, 123001 (2008)

[22] A. Erbaş, A. Tuncer, B. Yücesoy, et al. Phase diagrams and crossover in spatially anisotropic d = 3 Ising, XY magnetic, and percolation systems: exact renormalization-group solutions of hierarchical models. Physical review. E, Statistical, nonlinear, and soft matter physics **72 (2 Pt 2)**, 026129 (2005)

[23] M. Perry. Universal aspects of the atomic-scale friction of diamond surfaces. The Journal of Physical Chemistry (1995)

[24] E. Ruckenstein, R. Tsekov. Diffusion of atoms and dimers on metal surfaces. The Journal of Chemical Physics (1994)

[25] P. Burgos, Z. Zhang, R. Golestanian, et al. Directed single molecule diffusion triggered by surface energy gradients. ACS nano **3 (10)**, 3235 (2009)

[26] B. Maier, J. Rädler. Conformation and self-diffusion of single DNA molecules confined to two dimensions. Physical Review Letters **82 (9)**, 1911 (1999)

[27] M. Reguzzoni, M. Ferrario, S. Zapperi, et al. Onset of frictional slip by domain nucleation in adsorbed monolayers. Proceedings of the National Academy of Sciences **107 (4)**, 1311 (2010)

[28] M. H. Muser. First principles-based theory of collective creep. Proceedings of the National Academy of Sciences **107 (4)**, 1257 (2010)

[29] Z. Yang, H. P. Zhang, M. Marder. Dynamics of static friction between steel and silicon. Proceedings of the National Academy of Sciences **105 (36)**, 13264 (2008)

[30] M. Müser. How static is static friction? In *Proceedings of the National Academy of ...* (2008)

[31] O. Braun, A. Naumovets. Nanotribology: Microscopic mechanisms of friction. Surface Science Reports **60 (6-7)**, 79 (2006)

[32] G. Gao, R. J. Cannara, R. W. Carpick, et al. Atomic-scale friction on diamond: A comparison of different sliding directions on (001) and (111) surfaces using MD and AFM. Langmuir **23 (10)**, 5394 (2007)

[33] R. W. Carpick, M. Salmeron. Scratching the surface: Fundamental investigations of tribology with atomic force microscopy. Chemical Reviews **97 (4)**, 1163 (1997)

[34] Y. Mo, K. T. Turner, I. Szlufarska. Friction laws at the nanoscale. Nature **457 (7233)**, 1116 (2009)

[35] M. Enachescu, R. Van Den Oetelaar, R. Carpick, et al. Atomic force microscopy study of an ideally hard contact: the diamond (111)/tungsten carbide interface. Physical Review Letters **81 (9)**, 1877 (1998)

[36] F. Kühner, M. Erdmann, L. Sonnenberg, et al. Friction of single polymers at surfaces. Langmuir **22 (26)**, 11180 (2006)

[37] M. Rief, H. Grubmüller. Force spectroscopy of single biomolecules. ChemPhysChem **3 (3)**, 255 (2002)

[38] N. Maeda, N. Chen, M. Tirrell, et al. Adhesion and friction mechanisms of polymer-on-polymer surfaces. Science **297 (5580)**, 379 (2002)

[39] C. Drummond, J. Israelachvili, P. Richetti. Friction between two weakly adhering boundary lubricated surfaces in water. Physical Review E **67 (6)**, 066110 (2003)

[40] M. Heuberger, C. Drummond, J. Israelachvili. Coupling of normal and transverse motions during frictional sliding. The Journal of Physical ... (1998)

[41] G. Luengo, M. Heuberger, J. Israelachvili. Tribology of shearing polymer surfaces. 2. Polymer (PnBMA) sliding on mica. The Journal of Physical Chemistry B **104 (33)**, 7944 (2000)

[42] G. Zilibotti, M. Righi. Ab initio calculation of the adhesion and ideal shear strength of planar diamond interfaces with different atomic structure and hydrogen coverage. Langmuir (2011)

[43] E. Riedo, F. Lévy, H. Brune. Kinetics of capillary condensation in nanoscopic sliding friction. Physical Review Letters **88 (18)**, 185505 (2002)

[44] L. Ciliberto, L. Bocquet, E. Charlaix, et al. Moisture-induced ageing in granular media and the kinetics of capillary condensation. Nature **396**, 735 (1998)

[45] J. Chen, I. Ratera, J. Park, et al. Velocity dependence of friction and hydrogen bonding effects. Physical Review Letters **96 (23)**, 236102 (2006)

[46] P. Dickrell, S. Pal, G. Bourne, et al. Tunable friction behavior of oriented carbon nanotube films. Tribology Letters **24 (1)**, 85 (2006)

[47] I. M. Sivebaek, V. N. Samoilov, B. N. J. Persson. Frictional properties of confined polymers. The European Physical Journal E **27 (1)**, 37 (2008)

[48] R. Cannara, M. Brukman, K. Cimatu, et al. Nanoscale friction varied by isotopic shifting of surface vibrational frequencies. Science **318 (5851)**, 780 (2007)

[49] A. Schallamach. A theory of dynamic rubber friction. Wear **6 (5)**, 375 (1963)

[50] A. Ruina. Slip instability and state variable friction laws. Journal of Geophysical Research (1983)

[51] E. Perret, A. Leung, H. Feracci, et al. Trans-bonded pairs of E-cadherin exhibit a remarkable hierarchy of mechanical strengths. Proceedings of the National Academy of Sciences of the United States of America **101 (47)**, 16472 (2004)

[52] P. Robert, A.-M. Benoliel, A. Pierres, et al. What is the biological relevance of the specific bond properties revealed by single-molecule studies? Journal of Molecular Recognition **20 (6)**, 432 (2007)

[53] D. Pastré, O. Piétrement, A. Zozime, et al. Study of the DNA/ethidium bromide interactions on mica surface by atomic force microscope: influence of the surface friction. Biopolymers **77 (1)**, 53 (2004)

[54] F. Kuehner, J. Morfill, R. A. Neher, et al. Force-induced DNA slippage. Biophysical Journal **92 (7)**, 2491 (2007)

[55] V. Bormuth, V. Varga, J. Howard, et al. Protein friction limits diffusive and directed movements of kinesin motors on microtubules. Science **325 (5942)**, 870 (2009)

[56] D. Horinek, A. Serr, M. Geisler, et al. Peptide adsorption on a hydrophobic surface results from an interplay of solvation, surface, and intrapeptide forces. Proceedings of the National Academy of Sciences **105 (8)**, 2842 (2008)

[57] A. Serr, D. Horinek, R. R. Netz. Polypeptide friction and adhesion on hydrophobic and hydrophilic surfaces: a molecular dynamics case study. Journal of the American Chemical Society **130 (37)**, 12408 (2008)

[58] T. Cellmer, E. R. Henry, J. Hofrichter, et al. Measuring internal friction of an ultrafast-folding protein. Proceedings of the National Academy of Sciences **105 (47)**, 18320 (2008)

[59] Julius, Lennart, Dzubiella, et al. Peptide dynamics simulations in light and heavy water: Zooming in on internal friction-draft. Proceedings of the National Academy of Sciences (2012). To be published

[60] K. W. Plaxco, D. Baker. Limited internal friction in the rate-limiting step of a two-state protein folding reaction. Proceedings of the National Academy of Sciences of the United States of America **95 (23)**, 13591 (1998)

[61] B. Heymann, H. Grubmüller. Dynamic force spectroscopy of molecular adhesion bonds. Physical Review Letters **84 (26)**, 6126 (2000)

[62] A. Borgia, P. M. Williams, J. Clarke. Single-molecule studies of protein folding. Annual Review of Biochemistry **77 (1)**, 101 (2008)

[63] M. S. Kellermayer, S. B. Smith, H. L. Granzier, et al. Folding-unfolding transitions in single titin molecules characterized with laser tweezers. Science **276 (5315)**, 1112 (1997)

[64] A. D. Mehta, M. Rief, J. A. Spudich, et al. Single-molecule biomechanics with optical methods. Science **283 (5408)**, 1689 (1999)

[65] A. Bausch, K. Kroy. A bottom-up approach to cell mechanics. Nature Physics **2 (4)**, 231 (2006)

[66] C. Hyeon, G. Morrison, D. Thirumalai. Force-dependent hopping rates of RNA hairpins can be estimated from accurate measurement of the folding landscapes. Proceedings of the National Academy of Sciences **105 (28)**, 9604 (2008)

[67] P. Hänggi, P. Talkner, M. Borkovec. Reaction-rate theory: fifty years after Kramers. Reviews of Modern Physics **62 (2)**, 251 (1990)

[68] R. Zwanzig. Diffusion in a rough potential. Proceedings of the National Academy of Sciences **85 (7)**, 2029 (1988)

[69] J. Bryngelson, P. Wolynes. Intermediates and barrier crossing in a random energy model (with applications to protein folding). The Journal of Physical Chemistry **93 (19)**, 6902 (1989)

[70] A. Moeglich, K. Joder, T. Kiefhaber. End-to-end distance distributions and intrachain diffusion constants in unfolded polypeptide chains indicate intramolecular hydrogen bond formation. Proceedings of the National Academy of Sciences **103 (33)**, 12394 (2006)

[71] M. Geisler, S. Xiao, E. M. Puchner, et al. Controlling the structure of proteins at surfaces. Journal of the American Chemical Society (2010)

[72] M. Rief, M. Gautel, F. Oesterhelt, et al. Reversible unfolding of individual titin immunoglobulin domains by AFM. Science **276 (5315)**, 1109 (1997)

[73] G. A. Jeffrey. *An introduction to hydrogen bonding* (Oxford University Press, USA, 1997)

[74] S. Keten, M. Buehler. Geometric confinement governs the rupture strength of H-bond assemblies at a critical length scale. Nano Letters **8 (2)**, 743 (2008)

[75] U. Seifert. Rupture of multiple parallel molecular bonds under dynamic loading. Physical Review Letters **84 (12)**, 2750 (2000)

[76] E. Evans. Probing the relation between force-lifetime-and chemistry in single molecular bonds. Annual Review of Biophysics and Biomolecular Structure **30 (1)**, 105 (2001)

[77] M. Sotomayor, K. Schulten. Single-molecule experiments in vitro and in silico. Science **316 (5828)**, 1144 (2007)

[78] A. Kushner, J. Vossler, G. Williams, et al. A biomimetic modular polymer with tough and adaptive properties. Journal of the American Chemical Society **131 (25)**, 8766 (2009)

[79] P. Cordier, F. Tournilhac, C. Soulié-Ziakovic, et al. Self-healing and thermoreversible rubber from supramolecular assembly. Nature **451 (7181)**, 977 (2008)

[80] K. Wiemers, J. Kauffman. Dielectric friction and rotational diffusion of hydrogen bonding solutes. The Journal of Physical Chemistry A **104 (3)**, 451 (2000)

[81] G. Stokes. On the effect of the internal friction of fluids on the motion of pendulums. Transactions of the Cambridge Philosophical Society **9**, 8 (1851)

[82] J. I. Veysey, N. Goldenfeld. Simple viscous flows: From boundary layers to the renormalization group 1–107 (2008)

[83] F. Amblard, A. Maggs, B. Yurke, et al. Subdiffusion and anomalous local viscoelasticity in actin networks. Physical Review Letters **77 (21)**, 4470 (1996)

[84] F. Ziemann, J. Rädler, E. Sackmann. Local measurements of viscoelastic moduli of entangled actin networks using an oscillating magnetic bead micro-rheometer. Biophysical Journal **66 (6)**, 2210 (1994)

[85] I. Cohen, T. Mason, D. Weitz. Shear-induced configurations of confined colloidal suspensions. Physical Review Letters **93 (4)** (2004)

[86] T. Mason, K. Ganesan, J. Van Zanten, et al. Particle tracking microrheology of complex fluids. Physical Review Letters **79 (17)**, 3282 (1997)

[87] F. Gittes, B. Schnurr, P. Olmsted, et al. Microscopic viscoelasticity: shear moduli of soft materials determined from thermal fluctuations. Physical Review Letters **79 (17)**, 3286 (1997)

[88] M. Gardel, M. Valentine, J. Crocker, et al. Microrheology of entangled F-Actin solutions. Physical Review Letters **91 (15)**, 158302 (2003)

[89] K. Moloni, M. Buss, R. Andres. Tapping mode scanning force microscopy in water using a carbon nanotube probe. Ultramicroscopy **80 (4)**, 237 (1999)

[90] C. Li, T. Chou. Mass detection using carbon nanotube-based nanomechanical resonators. Applied Physics Letters **84**, 5246 (2004)

[91] W. Zhang, K. Turner. Frequency dependent fluid damping of micro/nano flexural resonators: Experiment, model and analysis. Sensors and Actuators A: Physical **134 (2)**, 594 (2007)

[92] N. Cappallo, C. Lapointe, D. Reich, et al. Nonlinear microrheology of wormlike micelle solutions using ferromagnetic nanowire probes. Physical Review E **76 (3)**, 031505 (2007)

[93] R. Zwanzig, M. Bixon. Hydrodynamic theory of the velocity correlation function. Physical Review A **2 (5)**, 2005 (1970)

[94] D. Bedeaux, P. Mazur. A generalization of Faxen's theorem to nonsteady motion of a sphere through a compressible fluid in arbitrary flow. Physica-Section A **78** (1974)

[95] H. Metiu, D. Oxtoby, K. Freed. Hydrodynamic theory for vibrational relaxation in liquids. Physical Review A **15 (1)**, 361 (1977)

[96] D. Huang, C. Sendner, D. Horinek, et al. Water Slippage versus Contact Angle: A Quasiuniversal Relationship. Physical Review Letters **101 (22)**, 226101 (2008)

[97] J. H. Walther, T. Werder, R. L. Jaffe, et al. Hydrodynamic properties of carbon nanotubes. Physical review. E, Statistical, nonlinear, and soft matter physics **69 (6)**, 062201 (2004)

[98] W. Tang, S. Advani. Drag on a nanotube in uniform liquid argon flow. The Journal of Chemical Physics **125**, 174706 (2006)

[99] M. J. Comstock, T. Ha, Y. R. Chemla. Ultrahigh-resolution optical trap with single-fluorophore sensitivity. Nature Methods **8 (4)**, 335 (2011)

[100] S. Q. Choi, S. Steltenkamp, J. A. Zasadzinski, et al. Active microrheology and simultaneous visualization of sheared phospholipid monolayers. Nature Communications **2**, 312 (2011)

[101] H. Grubmüller, B. Heymann, P. Tavan. Ligand binding: molecular mechanics calculation of the streptavidin-biotin rupture force. Science **271 (5251)**, 997 (1996)

[102] E. Lindahl, B. Hess. GROMACS 3.0: a package for molecular simulation and trajectory analysis. Journal of Molecular Modeling **7**, 306 (2001)

[103] W. Scott, P. Hünenberger, I. Tironi, et al. The gromos biomolecular simulation program package. The Journal of Physical Chemistry A **103 (19)**, 3596 (1999)

[104] H. Berendsen, J. Postma, W. van Gunsteren, et al. Interaction models for water in relation to protein hydration. Intermolecular Forces **331** (1981)

[105] K. Feenstra, B. Hess, H. Berendsen. Improving efficiency of large time-scale molecular dynamics simulations of hydrogen-rich systems. Journal of Computational Chemistry **20 (8)**, 786 (1999)

[106] T. Darden, D. York, L. Pedersen. Particle mesh ewald: An $nlog(n)$ method for ewald sums in large systems. The Journal of Chemical Physics **98 (12)**, 10089 (1993)

[107] J. Danielsson, J. Jarvet, P. Damberg, et al. Translational diffusion measured by PFG-NMR on full length and fragments of the Alzheimer Aβ (1-40) peptide. Determination of hydrodynamic radii of random coil peptides of varying length. Magnetic Resonance in Chemistry **40 (13)**, S89 (2002)

[108] A. Luzar, D. Chandler. Hydrogen-bond kinetics in liquid water. Nature **379 (6560)**, 55 (1996)

[109] M. Germann, T. Turner, S. Allison. Translational diffusion constants of the amino acids: Measurement by NMR and their use in modelling the transport of peptides. The Journal of Physical Chemistry A **111 (8)**, 1452 (2007)

[110] L. Longsworth. Diffusion measurements, at 25 ^{o} C , of aqueous solutions of amino acids, peptides and sugars. Journal of the American Chemical Society **75 (22)**, 5705 (1953)

[111] S. Sukhishvili, Y. Chen, J. Muller, et al. Surface diffusion of poly (ethylene glycol). Macromolecules **35 (5)**, 1776 (2002)

[112] T. Desai, P. Keblinski, S. Kumar. Polymer chain dynamics at interfaces: Role of boundary conditions at solid interface. The Journal of Chemical Physics **128**, 044903 (2008)

[113] B. Hess. Determining the shear viscosity of model liquids from molecular dynamics simulations. The Journal of Chemical Physics **116**, 209 (2002)

[114] Y. von Hansen, M. Hinczewski, R. R. Netz. Hydrodynamic screening near planar boundaries: Effects on semiflexible polymer dynamics. The Journal of Chemical Physics **134 (23)**, 235102 (2011)

[115] C. Sendner, R. Netz. Hydrodynamic lift of a moving nano-rod at a wall. Europhysics Letters **79**, 58004 (2007)

[116] S. Sque, R. Jones, P. Briddon. Hydrogenation and oxygenation of the(100) diamond surface and the consequences for transfer doping. Physica Status Solidi(a) **202 (11)**, 2091 (2005)

[117] A. Filippov, J. Klafter, M. Urbakh. Friction through dynamical formation and rupture of molecular Bonds. Physical Review Letters **92 (13)**, 135503 (2004)

[118] A. Fersht, J. Shi, J. Knill-Jones, et al. Hydrogen bonding and biological specificity analysed by protein engineering. Nature **314 (6008)**, 235 (1985)

[119] Q. Li, Y. Dong, D. Perez, et al. Speed dependence of atomic stick-slip friction in optimally matched experiments and molecular dynamics simulations. Physical Review Letters **106 (12)**, 126101 (2011)

[120] D. Gourdon, J. Israelachvili. Transitions between smooth and complex stick-slip sliding of surfaces. Physical Review E **68 (2)**, 021602 (2003)

[121] P. Thompson, M. Robbins. Origin of stick-slip motion in boundary lubrication. Science **250 (4982)**, 792 (1990)

[122] A. Lau, A. Prasad, Z. Dogic. Condensation of isolated semi-flexible filaments driven by depletion interactions. Europhysics Letters **87**, 48006 (2009)

[123] A. Serr, R. Netz. Enhancing polymer adsorption by lateral pulling. Europhysics Letters **78**, 68006 (2007)

[124] C. Kappel, H. Grubmüller. Velocity-dependent mechanical unfolding of bacteriorhodopsin is governed by a dynamic interaction network. Biophysical Journal **100 (4)**, 1109 (2104)

[125] E. P. Vieira, S. Rocha, M. Carmo Pereira, et al. Adsorption and diffusion of plasma proteins on hydrophilic and hydrophobic surfaces: Effect of trifluoroethanol on protein structure. Langmuir **25 (17)**, 9879 (2009)

[126] O. Dudko, G. Hummer, A. Szabo. Intrinsic rates and activation free energies from single-molecule pulling experiments. Physical Review Letters **96 (10)**, 108101 (2006)

[127] L. Lapidus, W. Eaton, J. Hofrichter. Measuring the rate of intramolecular contact formation in polypeptides. Proceedings of the National Academy of Sciences **97 (13)**, 7220 (2000)

[128] H. Risken, T. Frank. *The Fokker-Planck Equation: Methods of Solutions and Applications (Springer Series in Synergetics)*. 2nd ed. 1989. 3rd printing edition (Springer, 1996)

[129] S. Williams, T. Causgrove, R. Gilmanshin, et al. Fast events in protein folding: Helix melting and formation in a small peptide. Biochemistry **35 (3)**, 691 (1996)

[130] W. Yang, M. Gruebele. Folding at the speed limit. Nature **423 (6936)**, 193 (2003)

[131] B. G. Wensley, S. Batey, F. A. C. Bone, et al. Experimental evidence for a frustrated energy landscape in a three-helix-bundle protein family. Nature **463 (7281)**, 685 (2010)

[132] M. Müser, M. Robbins. Conditions for static friction between flat crystalline surfaces. Physical Review B **61 (3)**, 2335 (2000)

[133] R. B. Best, G. Hummer. Coordinate-dependent diffusion in protein folding. Proceedings of the National Academy of Sciences **107 (3)**, 1088 (2010)

[134] M. Hinczewski, Y. von Hansen, J. Dzubiella, et al. How the diffusivity profile reduces the arbitrariness of protein folding free energies. The Journal of Chemical Physics **132 (24)**, 245103 (2010)

[135] J. Chahine, R. J. Oliveira, V. B. P. Leite, et al. Configuration-dependent diffusion can shift the kinetic transition state and barrier height of protein folding. Proceedings of the National Academy of Sciences **104 (37)**, 14646 (2007)

[136] F. Eisenhaber, P. Lijnzaad, P. Argos, et al. The double cubic lattice method: efficient approaches to numerical integration of surface area and volume and to dot surface contouring of molecular assemblies. Journal of Computational Chemistry **16 (3)**, 273 (1995)

[137] C. Hyeon, D. Thirumalai. Mechanical unfolding of RNA hairpins. Proceedings of the National Academy of Sciences of the United States of America **102 (19)**, 6789 (2005)

[138] J. M. Fernandez. Force-clamp spectroscopy monitors the folding trajectory of a single protein. Science **303 (5664)**, 1674 (2004)

[139] L. Leibler, M. Rubinstein, R. Colby. Dynamics of reversible networks. Macromolecules **24 (16)**, 4701 (1991)

[140] M. Cetinkaya, S. Xiao, B. Markert, et al. Silk fiber mechanics from multiscale force distribution analysis. Biophysical Journal **100 (5)**, 1298 (2011)

[141] D. Chandler. Interfaces and the driving force of hydrophobic assembly. Nature **437 (7059)**, 640 (2005)

[142] P. R. ten Wolde, D. Chandler. Drying-induced hydrophobic polymer collapse. Proceedings of the National Academy of Sciences of the United States of America **99 (10)**, 6539 (2002)

[143] C. Dobson. Protein folding and misfolding. Nature **426 (6968)**, 884 (2003)

[144] G. Reddy, J. Straub, D. Thirumalai. Dry amyloid fibril assembly in a yeast prion peptide is mediated by long-lived structures containing water wires. Proceedings of the National Academy of Sciences **107 (50)**, 21459 (2010)

[145] J. Brash, T. Horbett. Proteins at interfaces. ACS symposium series (1995)

[146] F. Sedlmeier, J. Janecek, C. Sendner, et al. Water at polar and nonpolar solid walls. Biointerphases **3 (3)**, FC23 (2008)

[147] M. Schmitt, D. Paulmier. Influence of diamond crystal orientation on their tribological behaviour under various environments. Thin solid films (1999)

[148] R. Otero, F. Hümmelink, F. Sato, et al. Lock-and-key effect in the surface diffusion of large organic molecules probed by STM. Nature Materials **3 (11)**, 779 (2004)

[149] T. Trevethan, A. Shluger. Modeling the diffusive motion of large organic molecules on insulating surfaces. The Journal of Physical Chemistry C **112 (49)**, 19577 (2008)

[150] M. Geisler, T. Pirzer, C. Ackerschott, et al. Hydrophobic and hofmeister effects on the adhesion of spider Silk proteins onto solid substrates: An AFM-based single-molecule study. Langmuir **24 (4)**, 1350 (2008)

[151] C. So, C. Tamerler, M. Sarikaya. Adsorption, diffusion, and self-assembly of an engineered gold-binding peptide on Au (111) investigated by atomic force microscopy. Angewandte Chemie International Edition **48 (28)**, 5174 (2009)

[152] S. Kim, S. J. Karrila, Engineering. *Microhydrodynamics: Principles and Selected Applications* (Dover Publications, 2005)

[153] A. Guz. Vibrations of a sphere in the flow of a compressible viscous fluid. International Applied Mechanics (1993)

[154] P. Español. On the propagation of hydrodynamic interactions. Physica A: Statistical and Theoretical Physics **214 (2)**, 185 (1995)

[155] B. Felderhof. Backtracking of a sphere slowing down in a viscous compressible fluid. The Journal of Chemical Physics **123**, 044902 (2005)

[156] B. Felderhof. Effect of the wall on the velocity autocorrelation function and long-time tail of Brownian motion in a viscous compressible fluid. The Journal of Chemical Physics **123**, 184903 (2005)

[157] J. Holtsmark, I. Johnsen, T. Sikkeland, et al. Boundary layer flow near a cylindrical obstacle in an oscillating, incompressible fluid. The Journal of the Acoustical Society of America **26**, 26 (1954)

[158] C. Wang. On high-frequency oscillatory viscous flows. The Journal of Fluid Mechanics **32**, 55 (1968)

[159] H. Diamant. Hydrodynamic interaction in confined geometries. Journal of the Physical Society of Japan **78 (4)**, 1002 (2009)

[160] D. Long, A. Ajdari. A note on the screening of hydrodynamic interactions, in electrophoresis, and in porous media. The European Physical Journal E **4 (1)**, 29 (2001)

Acknowledgments

First of all, I would like to thank my advisor (Doktorvater) Prof. Dr. Roland R. Netz, who has been a great source of inspiration for me with his patience and pioneering guidance. During my Ph.D. studies in his group, he has helped to climb the stairs with firm and convenient steps, and I have acquired many skills from him that I will carry out throughout my life in academia. Prof. Netz has also been an elusive example that a good mentor and an excellent group leader can also organize marvellous parties.

I would like to thank also Prof. Dr. A Nihat Berker who gave me the idea to conduct my Ph.D. studies in Germany. It is always nice to be a member of this "mafia".

I am grateful to members of my examination committee, Prof. Dr. Ralf Metzler and the chair Prof. Dr. Matthias Rief, for their critical reading of this thesis and valuable comments.

My thanks and appreciations also go to my past and present colleagues in T37 in developing the projects and people who have willingly helped me out with their abilities.

Particularly, I owe thanks to Prof. Dr. Dominik Horinik for introducing and teaching me molecular dynamics simulations.

I would like to extend my sincere thanks also to Prof. Dr. Joachim Dzubiella for his short but precise scientific or non-scientific tips.

Off-science, I have had great time during my stay in Germany. Hence, I would like to thank all of my friends in TU München. My festival partner and good friend Immanuel Kalcher, the flying Dutchman, though he never does, except bike accidents, Douwe Jan Bonthuis, designated office-mate and cinema&politics critics Felix Sedlmeier (he also deserve a thank for the scripts), the best naked German (Bayerisch) Thomas Einert, eternal enemy Ioannis Daoutidis the Greek, the lady in Pink Nadine Schwierz, Yann von Hansen (he is not from Hansens, I guess); You all deserve my XXL size gratitudes. Thank you guys.

Also I would like to thank Dr. Maria Fyta, Dr. Michael Hinczewski, fresh father Dr. Emanuel Schneck, the poker gru Dr. Javier Madroñero and Dr. Matek Kanduč.

I would like to thank for the financial support TU München, FU Berlin, DPG, DPG and other foundations which sponsored this Ph.D. work.

Uzaklardan beni hep destekleyen ve özleyen annem Nesrin Erbaş'a, kardeşim Arzu'ya ve bana sonuna kadar güvenen dayım Tarık Candan'a tesşekkürü bir borç bilirim.

Uzun zamandır yanımda olan ve benden desteğini hiç esirgemeyen Başak Şenergin'i de kucak dolusu teşekkürler ediyorum.

Ich möchte unserer lieben Sekretärin Frau Sonja Ortner danken, dass sie mir durch den Dschungel der deutschen Bürokratie geholfen und mit mir täglich Deutsch zu sprechen geübt hat.

Finally, I would like to express my special gratitude to anyone whose names I forget to include here foolishly.